PONTIFÍCIA UNIVERSIDADE CATÓLICA
DO RIO DE JANEIRO

Fagner da Silva Moura

Copper(II) complexes derived from *N*-acylhydrazonic ligands as an antitumor alternative to platinum compounds: Synthesis, characterization, studies in solution and pharmacological potential

Tese de Doutorado

Thesis presented to the requirements for the degree of Doutor em Química in the Graduate Program in Chemistry, Department of Chemistry, PUC-Rio.

Advisor: Prof. Dr. Nicolás A. Rey

Rio de Janeiro, September 2024

PONTIFÍCIA UNIVERSIDADE CATÓLICA
DO RIO DE JANEIRO

Fagner da Silva Moura

Copper(II) complexes derived from *N*-acylhydrazonic ligands as an antitumor alternative to platinum compounds: Synthesis, characterization, studies in solution and pharmacological potential

Tese de Doutorado

Thesis presented to the Programa de Pós-Graduação em Química of PUC-Rio in partial fulfillment of the requirements for the degree of Doutor em Química. Approved by the

Examination Comittee:

Prof. Dr. Nicolás A. Rey
Advisor
Department of Chemistry – PUC-Rio

Prof. Dr. Lena Ruiz Azuara
UNAM (Mexico)

Prof. Dr. Ignacio Esteban León
UNLP (Argentina)

Prof. Dr. Roberto de Barros Faria
Institute of Chemistry - UFRJ

Prof. Dr. Marciela Scarpellini
Institute of Chemistry - UFRJ

Prof. Dr. Gláucio Braga Ferreira
Institute of Chemistry - UFF

Prof. Dr. Renan Lira de Farias
Department of Chemistry – PUC-Rio

Rio de Janeiro, September 9th, 2024

Fagner da Silva Moura

Graduated in Chemistry from the Federal University of Rio de Janeiro (UFRJ) in 2017, and obtained a master's degree in chemistry from the Federal University of Rio de Janeiro (UFRJ) in 2019.

Bibliographic data

Moura, Fagner da Silva

Copper(II) complexes derived from *N*-acylhydrazonic ligands as an antitumor alternative to platinum compounds : Synthesis, characterization, studies in solution and pharmacological potential / Fagner da Silva Moura ; advisor: Nicolás A. Rey. – 2024.
251 f. : il. color. ; 30 cm

Tese (doutorado)–Pontifícia Universidade Católica do Rio de Janeiro, Departamento de Química, 2024.
Inclui bibliografia

1. Química – Teses. 2. Complexos de cobre(II). 3. Câncer. 4. N-Acilhidrazonas. 5. HSA. 6. Química de coordenação. I. Rey, Nicolás Adrián. II. Pontifícia Universidade Católica do Rio de Janeiro. Departamento de Química. III. Título.

CDD: 540

In Memoriam of Josefa F. S. Moura: Her love and care will remain with me all the days of my life, eternally in my heart.

Acknowledgements

Agradeço a Deus pela vida, pelo seu amor, cuidado e fidelidade.

Além de toda bagagem científica e intelectual acumulada ao longo desses anos, certamente, as pessoas encontradas no caminho fizeram essa caminhada ser mais bela. Meus agradecimentos a todos esses encontros, que de uma forma direta ou indireta marcaram a minha trajetória.

Agradeço à minha mãe Josefa (*in memoriam*) que possibilitou tudo de melhor em minha vida. Meu amor e gratidão pela sua existência vai além das palavras e desta vida.

Agradeço à minha irmã Monique (*in memoriam*) pelo seu amor, cuidado e parceria.

Agradeço ao meu sobrinho Arthur, que mesmo depois de tanto tempo continua sendo o dono do meu sorriso mais sincero.

Agradeço a mim por ter chegado até aqui e, principalmente, pela fidelidade que mantenho aos meus sonhos.

Agradeço a minha mãe científica Dra. Annelise Casellato, eu poderia escrever mais uma tese para descrever minha gratidão por você. Foi com você que toda essa trajetória começou, foi nas suas aulas que a semente da curiosidade científica foi plantada em mim. Foi no seu laboratório que eu acertei, errei e escolhi o meu caminho. Obrigado por tudo, eu te amo. Agradeço demais pelas medidas de DRIFTS.

Agradeço ao meu pai científico Dr. Nicolás A. Rey pela oportunidade, orientação e aprendizado. A sua empolgação e perseverança em fazer Ciência sempre serão um referencial para mim. Suas ideias inundam o LABSO-Bio de motivação. Obrigado pela sua orientação humana, que nos momentos difíceis viu em mim algo além de uma mão de obra. Obrigado por tudo.

Agradeço a Dra. Daphne S. Cukierman por toda a ajuda, suporte e amizade. Não tenho dúvidas que sem você minha caminhada seria mais fatigante. O LABSO-Bio é um corpo onde o Prof. Nicolás é a cabeça, nós somos os membros e você é e sempre será o coração e a alma desse laboratório. Obrigado por tanto.

Agradeço ao Diogo Sousa pelo seu amor, companheirismo e paciência.

Agradeço ao LABSO-Bio, um laboratório que me acolheu e foi meu refúgio em muitos momentos. Gostaria de agradecer a todos os membros pela amizade e tolerância.

Agradeço demais aos meus ICs, meus parceiros de trincheira de todos os momentos. Carol, eu sou muito grato por ter encontrado a sua inefável amizade no meu caminho, a sua risada muda o meu astral e aquece meu coração. Obrigado pelo seu abraço que parece casa, eu te amo muito minha amiga. Ygor, agradeço a parceria, os momentos de descontração e a sua empolgação que me contagia. Vou me lembrar com muito carinho de vocês.

Agradeço a Babi por toda ajuda, suporte e amizade. Você alegrou meus dias e aliviou minhas dores. Eu tenho muito orgulho de você.

Agradeço ao Boris pelo companheirismo, ajuda e amizade. Você é o beta mais especial.

Agradeço a Dani, como pode em tão pouco tempo alguém ser tão especial? Obrigado pelos conselhos, ajuda e amizade. A sua luz iluminou meus dias.

Agradeço ao Matheus pela amizade, ajuda, suporte e por sempre me ouvir com paciência pronto para discordar de absolutamente tudo que vou dizer. Sua amizade foi um presente.

Agradeço a Anna Julia e Elisa, pela amizade, ajuda e bons momentos.

Agradeço aos amigos Roberta, Vitória, Henrique, Gabriel, Bia, Luis Fhernando, Fran e Leonny por tornarem meus dias mais leves e meu céu menos nublado.

Agradeço a todos os meus professores do CEFET/RJ UnED Nova Iguaçu, UFRJ e PUC-Rio que contribuíram para a minha formação pessoal e profissional.

Agradeço a todos os professores e funcionários do Departamento de Química da PUC-Rio que possibilitaram que esse trabalho pudesse ser desenvolvimento, especialmente aos técnicos Rodrigo, Sula, Maurício e Álvaro. Agradeço a Central Analítica Pe. Leopoldo Hainberger – CAPLH pelo uso dos equipamentos.

Agradeço ao Laboratório de Multiusuários do Departamento de Química Inorgânica - IQ-UFRJ e ao professor Luiz Fernanda Malta pelas medidas de TGA.

Sou muito grato por todas as colaborações que permitiram o desenvolvimento deste trabalho: Agradeço ao Dr. Jilder Serna (CBPF) por todas as medidas de EPR e pela camaradagem. Agradeço a Dra. Carolina Ligiero (UFF)

e Dra. Renata Diniz (UFMG) pelas medidas de DRX dos monocristais dos ligantes e complexos. Agradeço ao Prof. Dr. Nelson H. Morgon (Unicamp) pelos cálculos computacionais. Agradeço aos Dr. Maurício Yoguim (Unesp) e Prof. Dr. Aguinaldo de Souza (Unesp) pelos estudos de docking molecular envolvendo a proteína HSA. Agradeço ao Prof. Dr. Ignacio E. León (UNLP) pelos estudos de citotoxicidade e colaboração.

Agradeço a todos os membros da banca pela disponibilidade em avaliar este trabalho.

Agradeço aos órgãos de fomento Capes, pela concessão da bolsa de doutorado, CNPq e FAPERJ, pelo suporte financeiro que tornaram este estudo viável em todos os aspectos possíveis. Meu muito obrigado pelo apoio à Ciência no Brasil.

This study was financed in part by the Coordenação de Aperfeiçoamento de Pessoal de Nível Superior - Brasil (CAPES) - Finance Code 001

Abstract

Moura, Fagner da Silva; Rey, Nicolás Adrián (Advisor). **Copper(II) complexes derived from *N*-acylhydrazonic ligands as an antitumor alternative to platinum compounds: Synthesis, characterization, studies in solution and pharmacological potential.** Rio de Janeiro, 2024. 251p. Tese de Doutorado - Departamento de Química, Pontifícia Universidade Católica do Rio de Janeiro.

Cancer can be considered a collection of various diseases that collectively lead to an imbalance in the tissues from which they originate. The genesis of tumors is generally associated with mutations that accumulate within cells. The altered cell acquires an increased capacity of proliferation, undergoing clonal expansion and transmitting its genes to daughter cells. Disordered proliferation can form a solid and intricate mass of altered cells within the organ where the tumor originated.

Current cancer treatments focus on diagnosing the type of cell, its location and severity, guidance, selecting the best treatment options, and monitoring the progress. In the latter half of the 1960s, Rosenberg discovered the antitumor activity of cisplatin, which spurred the search for new metal-based anticancer agents. Despite this, few inorganic anticancer drugs have shown auspicious due to toxicity issues.

In this context, *N*-acylhydrazones and their copper(II) complexes have been suggested as promising compounds for achieving this objective. Copper(II) complexes have been presented in the literature as an alternative to platinum-based anticancer compounds, given that copper is an essential trace element with fewer side effects. In recent decades, many copper(II) coordination compounds exhibiting antitumor activity have been reported as promising active compounds against tumor cells, with some advancing to clinical trials, such as Casiopeínas®, which interact with cells in various ways.

Our research group has experience with copper(II) complexes exhibiting reported antitumor activity. Additionally, N,O-donor *N*-acylhydrazone ligands, both free and coordinated, have demonstrated biological activity as anticancer agents. This has motivated the design of a new generation of similar ligands to enhance antitumor activity. This work encompasses the synthesis, acquisition, and complete characterization of novel *N*-acylhydrazone ligands, which were thoroughly characterized, as well as their new copper(II) complexes obtained from three different starting salts. The study includes the reactivity, spectroscopic, electrochemical, and antiproliferative properties of a new generation of mono- and binuclear copper(II) complexes derived from these *N*-acylhydrazone ligands. Of the ten synthesized complexes, six showed reactivity towards human serum albumin (HSA), and three complexes derived from the ligand containing furan as a substituent had their antiproliferative activity evaluated, exhibiting greater activity than cisplatin.

Keywords: complexes, antitumor, hydrazone and copper(II)

Resumo Expandido em Português

Moura, Fagner da Silva; Rey, Nicolás Adrián (Orientador). **Complexos de cobre(II) derivados de ligantes *N*-acil-hidrazônicos como alternativa aos compostos de platina: Síntese, caracterização, estudos em solução e potencial farmacológico.** Rio de Janeiro, 2024. 251p. Tese de Doutorado - Departamento de Química, Pontifícia Universidade Católica do Rio de Janeiro.

Câncer pode ser considerado um conjunto de diversas doenças, que unidas, levam desequilíbrio aos tecidos dos quais se originaram. A gênese do tumor está associada, em geral, as mutações que as células sofrem e se acumulam em seu interior. A célula modificada adquire maior capacidade de proliferação, sofrendo expansão clonal transmitindo seus genes para as células filhas. A proliferação desordenada é capaz de formar uma massa sólida e intrincada de células alteradas dentro do órgão onde o tumor foi originado.

Os tratamentos atuais contra o câncer são voltados para o diagnóstico do tipo de câncer, sua localização e gravidade, orientação, a seleção de melhores opções de tratamento e o seu progresso. Na segunda metade da década de 1960, Rosenberg descobriu a atividade antitumoral da cisplatina, motivando a busca por novos agentes anticancerígenos baseados em metais. Apesar disso, poucos medicamentos anticancerígenos inorgânicos se mostraram promissores devido a problemas de toxicidade.

Diante desse escopo, derivados *N*-acilhidrazônicos e complexos de cobre(II) têm sido sugeridos como compostos promissores para atingir esse objetivo. Os complexos de cobre(II) têm sido apresentados na literatura como uma alternativa promissora aos compostos anticancerígenos de platina, uma vez que o cobre é um elemento traço essencial com menor efeito colateral. Nas últimas décadas, muitos compostos de coordenação de cobre(II) que apresentam atividade antitumoral foram relatados como promissores compostos ativos contra células tumorais, alguns deles avançando para testes clínicos, como é o caso das Casiopeínas® , apresentando diferentes formas de interação com a célula.

Diante disso, nosso grupo de pesquisa possui experiência em complexos de cobre(II) com atividade antitumoral já reportados. Além disso, ligantes N,O-doadores *N*-acilhidrazônicos livres e coordenados revelaram atividade biológica como agentes anticâncer. Isto motivou o design de uma nova geração de ligantes similares, na tentativa de potencializar a atividade antitumoral.

Este trabalho compreende a síntese, obtenção e caracterização completa de ligantes inéditos *N*-acilhidrazônicos que foram totalmente caracterizados, assim como seus novos complexos de cobre (II) obtidos a partir de três sais de partida diferentes, o estudo da reatividade, propriedades espectroscópicas, eletroquímicas e antiproliferativas de uma nova geração de complexos mono e binucleares de cobre(II) derivados desses ligantes *N*-acilhidrazônicos. Dos dez complexos sintetizados, seis deles apresentaram reatividade frente à HSA (albumina sérica humana), e três complexos tiveram sua atividade antiproliferativa avaliada, apresentando atividade maior que a cisplatina.

Palavras-chave: complexos, antitumoral, hidrazona e cobre(II)

Table of Contents

List of Acronyms and Abbreviations

Cas	®Casiopeins
CRGs	Cooperation response genes
DMF	Dimethylformamide
DMSO	Dimethyl sulfoxide
DNA	Deoxyribonucleic acid
DRIFTS	Diffuse Reflectance Infrared Fourier Transform Spectroscopy
Epa	Anodic potential
Epc	Cathodic potential
EPR	Electron Paramagnetic Resonance
ESCs	Embryonic stem cells
EtOH	Ethanol
GCE	Glassy Carbon Electrode
IC_{50}	Half maximal inhibitory concentration
HSA	Human Serum Albumin
HDI	Human Development Index
Hmb	5-methylsalicylaldehyde
ICP-OES	Inductively Coupled Plasma Optical Emission Spectrometry
Ipa	Anodic potential current
Ipc	Cathodic potential current
INCA	National Cancer Institute
***i*-PrOH**	Isopropyl alcohol
iPSCs	Induced pluripotent stem cells
IR	Infrared spectroscopy
MDA-MB-231	Triple-negative breast adenocarcinoma
MeCN	Acetonitrile
MeOH	Methanol
M.p	Melting Point
NMR	Nuclear magnetic resonance spectroscopy
ORTEP	Oak Ridge Thermal Ellipsoid Plot
PBS	Phosphate buffered saline
Ppm	Parts per million
ROS	Reactive oxygen species
SOD	Superoxide Dismutase
TASR	Truncated age-standardized incidence rates
$TBAPF_6$	Tetrabutylammonium hexafluorophosphate

TGA	Thermogravimetric analysis
UHF	Unrestricted Hartree-Fock
WHO	World Health Organization
XRD	X-ray diffraction

List of Figures

List of Tables

List of Appendix Figures

1. Introduction

1.1 Cancer: Statistics and Pathology

Cancer is a significant global public health issue. The 2020 pandemic caused by the 2019 coronavirus disease (COVID-19) led to delays in cancer diagnosis and treatment due to healthcare facility closures, disruptions in employment and health insurance, and fear of COVID-19 exposure. Although the impact was most pronounced during the peak of COVID-19, healthcare delivery has not fully recovered in many countries (Ghoshal *et al.*, 2022; Siegel *et al.*, 2023). The COVID-19 pandemic enforced worldwide confinement measures until late 2021, influencing cancer-related data. Medical facilities and research units diverted financial and personnel resources towards seeking suitable emergency medications for COVID-19 treatment, resulting in reduced attention to, and sometimes neglect of, other diseases. Therefore, cancer data collection likely lost priority within agencies during this period (Chhikara & Parang, 2023).

According to data Saloni Dattani (2023), cancer is the second leading cause of death globally, following cardiovascular diseases. In Brazil, according to the Brazilian National Cancer Institute José Alencar Gomes da Silva (INCA), excluding non-melanoma skin cancers, prostate cancer is the most common cancer among men in all regions of Brazil. Among women, breast cancer is the most frequent. Following prostate and breast cancer, cervical cancer in women and airway and lung cancer in men are the next most common types (e Vigilância, 2018).

1.1.1 Cancer Statistics

In 2022, it is estimated that over 19 million new cases of cancer occurred worldwide, resulting in more than 9 million confirmed deaths, accounting for 48% of the total new cancer cases diagnosed in 2012. Figure 1 depicts the new cancer cases worldwide in 2022. The proportion of confirmed deaths varied significantly by region, from 7.8% in Africa to 20.4% in Europe, 56.1% in Asia, and 0.76% in Oceania of the total fatal cases (Figure 2). Literature suggests that higher incidence in Europe and Asia may be attributed to their older populations, where cancer treatment in these patients can be more complex due to high levels of comorbidity, frailty, functional decline, and limited life expectancy affecting this age group (Observatory, 2024; Pilleron *et al.*, 2021; WHO, 2022).

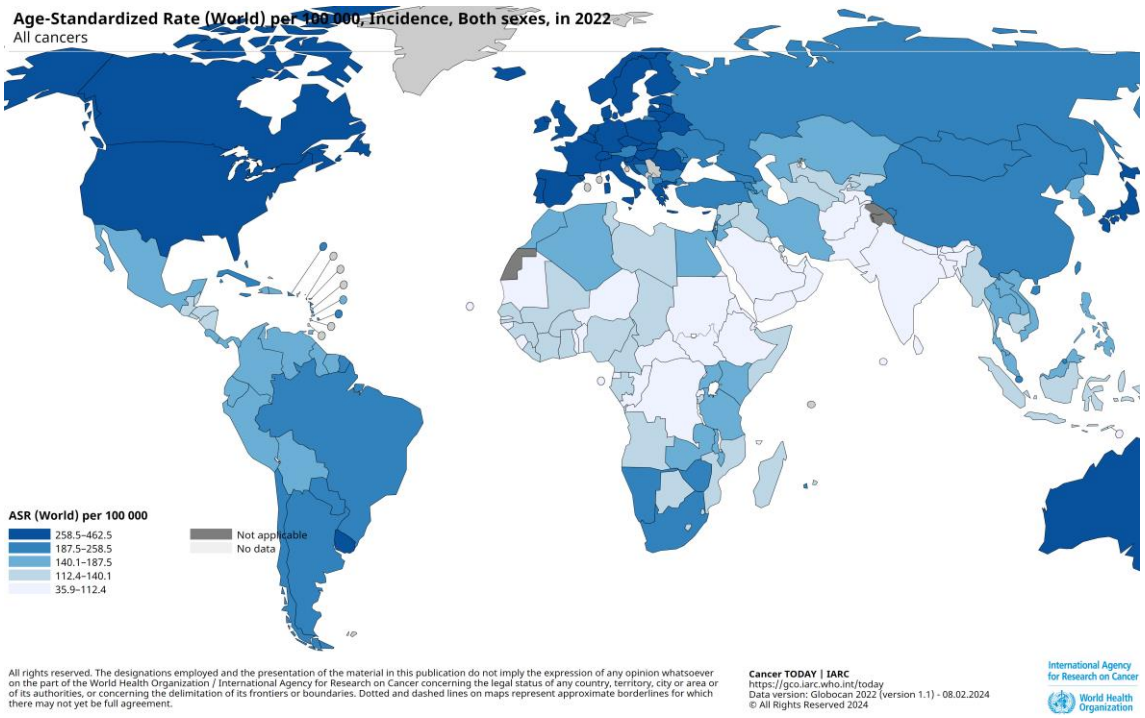

Figure 1. Truncated age-standardized incidence rates (TASR) in people aged 0 to 80+ years for both sexes combined in the world in 2022. Obtained from the WHO web page.

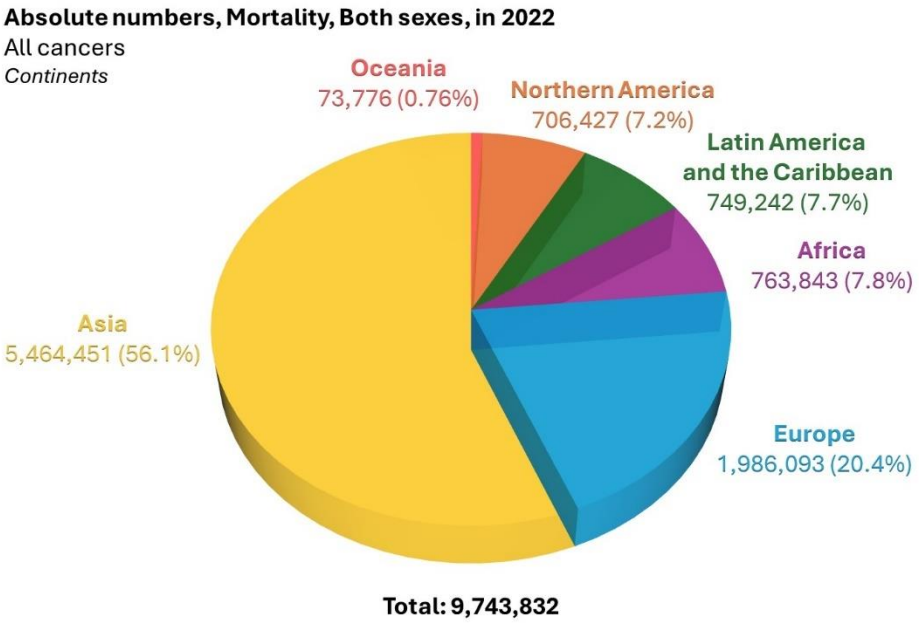

Figure 2. Graph that represents the total deaths as a percentage of the total number of new cancer cases in the world in people aged 0 to 80+ years for both sexes in 2022. Modified from the WHO web page.

The 2017 INCA data aligns with findings from the World Health Organization in 2022, wherein lung cancer emerged as the most common among men (15.2% of total new cases), followed by prostate cancer (14.2%) and colorectal cancer (10.4%). Among women, breast cancer is the most prevalent (23.8% of total new cases), followed by lung cancer (9.4%) and colorectal cancer (8.9%) (Observatory, 2024; WHO, 2022).

In Brazil, the scenario is distinctive due to significant social inequality, with a concentration of financial resources in certain regions facilitating better access to information, healthcare, and education. This leads to higher cancer reporting rates and clearer diagnosis and treatment pathways. States with higher Human Development Index (HDI) in Brazil show increased notification of malignant neoplasms, as indicated by projected INCA data for the upcoming triennium (2023-2025) (de Oliveira Santos *et al.*, 2023).

1.1.2 Pathology

According to the WHO, "cancer is a generic term for a large group of diseases characterized by the disorderly growth of cells beyond their usual boundaries, which can invade adjacent parts of the body and/or spread to other organs." The WHO uses terms such as malignant tumors and malignant neoplasms, among others, to denote cancer (WHO, 2022).

Cancer can develop in all tissues of the body WHO (2022) and encompasses numerous cytological and molecular subtypes, each requiring specific treatment approaches. According to the WHO, the most common types of cancer in men include lung, prostate, colorectal, stomach, and liver cancers, whereas in women, breast, colorectal, lung, cervical, and thyroid cancers are most frequent (WHO, 2022).

Cancer originates from transformed normal cells. Proto-oncogenes are initially inactive genes in normal cells responsible for encoding proteins that assist in regulating cellular growth, differentiation, and signal translation (Luo & Elledge, 2008). When proto-oncogenes are activated, they become oncogenes, which drive the malignancy of normal cells (Almeida *et al.*, 2005). Proto-oncogenes can be activated in various tissues, causing altered cells to behave atypically and multiply uncontrollably (Weinberg, 1983).

Uncontrolled cell proliferation increases the demand for nutrients, leading to the formation of new blood vessels (angiogenesis) that nourish tumor cells. This unregulated cell growth can result in the accumulation of mass, forming malignant tumors. Additionally, cells may detach from the original tumor and migrate to neighboring tissues, potentially entering blood or lymphatic vessels and disseminating throughout the body, reaching distant organs from the tumor's site of origin, a process known as metastasis (Almeida *et al.*, 2005).

Different genetic alterations enable the transformation of a normal cell into a cancerous one. However, the most relevant process involves oncogenic mutations (cancer-causing) in critical genes, which render the cell insensitive to signals that normally inhibit growth or promote cell death (Almeida *et al.*, 2005). Tumor suppressor genes are normal genes that help control cell division, repair DNA, or induce apoptosis. Cellular transformation is linked to the combination of two important factors: the inactivation of tumor suppressor genes and the activation of oncogenes. The majority of genetic alterations (about 80%) are associated with the environment. Here, environment refers to the natural surroundings in which an individual resides, as well as occupational, social/cultural (lifestyle and habits), and consumption environments, such as food and medications (Luo & Elledge, 2008).

Literature reports that a single oncogene is insufficient to transform normal cells into cancerous ones; conversely, cooperation between two distinct oncogenic mutations can drive the oncogenic process. McMurray *et al.* (2008) examined the cooperation between two significant oncogenic mutations in human cancers (Ras and p53). p53 is a gene transcription factor that responds to cellular stressors such as DNA damage, oxygen scarcity, or the presence of oncogenes (like mutant Ras) to halt proliferation and promote programmed cell death (apoptosis). It functions as a tumor suppressor gene (McMurray *et al.*, 2008). Ras proteins participate in signal transmission to stimulate cellular differentiation and proliferation, expressed by the Ras gene. Mutations in this gene can transform it into an oncogene. While the GTPase Ras protein and the transcription factor p53 individually have limited effects on cancer promotion, their cooperation is responsible for the transformation of normal cells into cancer cells. In Figure 3, the p53 mutation affects the expression of genes in group A, and the Ras mutation modifies the expression of genes in group B. When p53 and Ras mutations occur

in the same cell, they synergistically regulate a subset of genes (AB), known as cooperation response genes (CRGs), which are crucial mediators of tumor formation (Luo & Elledge, 2008; Montagner *et al.*, 2015).

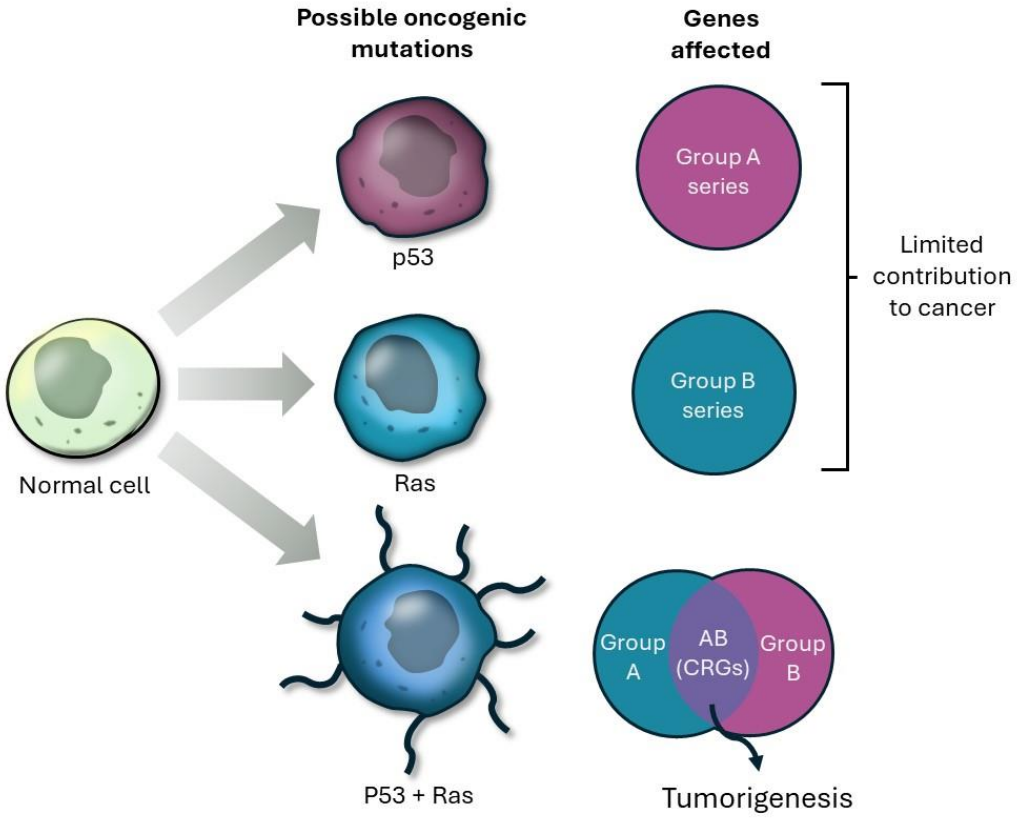

Figure 3. Scheme with oncogenic mutations involving the transcription factor p53 and the GTPase Ras protein. Modified from Luo & Elledge (2008).

Cancer cells are less specialized and functional compared to their normal counterparts. As the tumor grows uncontrollably, they replace the spaces of regular cells within tissues, leading to loss of function. Tissue malfunction can result in various detrimental effects on the organism, impairing the health and quality of life of oncology patients (de Oliveira Santos *et al.*, 2023; Montagner *et al.*, 2015)

1.1.3 Current cancer treatments

The literature reports a range of treatments for cancer, highlighting two categories: conventional and advanced therapies. Currently, worldwide, over half of all ongoing medical trials are focused on cancer treatment (Abbas & Rehman, 2018). These trials aim to diagnose cancer type, location, severity, guide treatment selection, and monitor progress. Traditional treatment methods include surgery, radiotherapy, and chemotherapy, while advanced therapies encompass hormonal therapy, anti-angiogenic therapy, stem cell therapies, immunotherapy, and dendritic cell-based immunotherapy (Charmsaz *et al.*, 2019).

Traditional cancer treatments, still widely recommended, come with both advantages and disadvantages. Surgical intervention is most effective during the early stages of disease progression (Moses *et al.*, 2003). Radiation therapy, however, can damage healthy cells, tissues, and organs (Arruebo *et al.*, 2011). Chemotherapy has significantly reduced cancer morbidity and mortality; however, most chemotherapeutic agents also harm healthy cells, and drug resistance remains a serious challenge (Mondal *et al.*, 2014; Shapira *et al.*, 2011).

Advanced treatments, like traditional ones, offer benefits and challenges. Stem cell therapy is still under experimental clinical trials, though its use in tissue regeneration has been explored (Naji *et al.*, 2019). Embryonic stem cells (ESCs), derived from the inner cell mass of embryos, have the potential to differentiate into various cell types, excluding placental cells (Takahashi & Yamanaka, 2006). Induced pluripotent stem cells (iPSCs) are another breakthrough, reprogrammed from adult cells, showing promise in cellular immunotherapy and anti-tumor vaccine development (Debela *et al.*, 2021; Li *et al.*, 2018; Ouyang *et al.*, 2019).

Targeted therapies involve medications or substances that interfere with molecules promoting tumor growth (Yadav, 2017). Unlike conventional chemotherapy, which affects healthy cells similarly to cancer cells, targeted therapies selectively disrupt cancer cell mechanisms like apoptosis induction, cell cycle arrest, and proliferation prevention (Valter *et al.*, 2017). These therapies have significantly increased survival rates, such as improving survival from 17% to 24% in advanced pancreatic cancer cases (Weber, 2006; Yadav, 2017).

Enzymes play critical roles in cancer cell signaling pathways. Specific targeted therapies inhibit these enzymes, such as DNA topoisomerases, to halt cancer cell growth. Molecules designed for targeted therapy bind to these

enzymes, acting as enzyme inhibitors. Mononuclear and dimeric copper(II) complexes have shown promise as DNA topoisomerase inhibitors, advancing to clinical trials. This underscores the potential of coordination chemistry, pioneered by Alfred Werner, in the pursuit of effective cancer treatments.

Some enzymes serve as signaling molecules for the growth of cancer cells. Certain targeted therapies inhibit these signaling enzymes, such as DNA topoisomerases, to impede cancer cell growth. The ideal molecules used in targeted therapy can bind to these enzymes, acting as enzymatic inhibitors. Mononuclear and dimeric copper(II) complexes have been reported in the literature as inhibitors of DNA topoisomerases, with some progressing to clinical trials (Citri & Yarden, 2006; Molinaro *et al.*, 2020). This suggests that in coordination chemistry, pioneered by Alfred Werner, there may lie the hope for a cure.

1.2 The rich chemistry of *N*-acylhydrazones: From structures to biological activity

Hydrazones are a class of organic compounds belonging to the Schiff bases family with the structure $R_1R_2C{=}NNH_2$. They can be obtained through the condensation reaction of an aldehyde or ketone with hydrazine (or substituted hydrazine) or hydrazides (H_2NNHR_1, where R_1 can be an acyl, sulfonyl, or phosphoryl group). In this work, the main focus will be on *N*-acylhydrazones (Verma *et al.*, 2014). These compounds contain the C=N bond, which is conjugated with a lone pair of electrons on the nitrogen atom, enabling them to act as ligands in complexation reactions as they can function as Lewis bases (Uppal *et al.*, 2011; Verma *et al.*, 2014). The nitrogen atoms in hydrazones are nucleophilic, with the amine nitrogen being the most reactive. The carbon atom, on the other hand, exhibits electrophilic and nucleophilic nature. The α-hydrogen of hydrazones is more acidic than that of acidic ketones (Uppal *et al.*, 2011). The combination of hydrazones with other functional groups, such as phenols and aromatic derivatives, allows for the synthesis of compounds with unique physicochemical properties (Verma *et al.*, 2014).

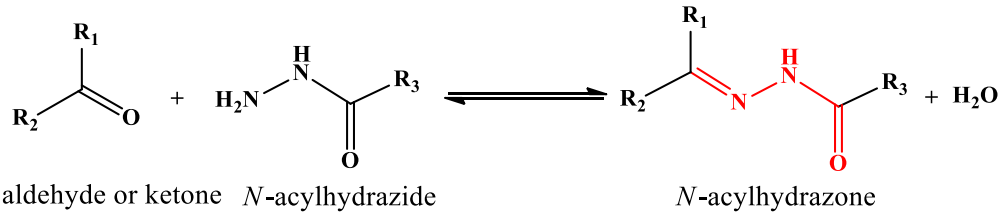

Figure 4. General scheme illustrating the obtaining of *N*-acylhydrazone from a condensation reaction.

1.2.1 Introduction to hydrazone chemistry

In addition to their widely documented pharmacological properties, hydrazones have emerged in medical biotechnology. Hydrazones are often combined with certain drugs and typically maintain neutrality at physiological pH (Wu & Senter, 2005). One of the primary biological activities of hydrazones is their anti-inflammatory effects. To achieve this anti-inflammatory effect, the hydrazine functional group reacts with aldehydes or ketones to form a new substituent group that provides chemical, thermal, and hydrolytic stability (Kajal *et al.*, 2014). Aryl, acyl, and heteroaryl hydrazones are known for featuring an additional donor site (C=O), making them versatile and flexible. This versatility has led to extensive exploration in the literature as effective chelating agents capable of forming a variety of coordination compounds with different transition metals (Kajal *et al.*, 2014).

Hydrazones possess two cleavable bonds, generally stable enough to allow transformations in other parts of the hydrazone molecule. The C=N bond is susceptible to hydrolytic, oxidative, and reductive cleavage, restoring the carbonyl group, while the N–N bond is predisposed to reductive cleavage to produce a primary amine (Enders *et al.*, 2000; Lazny & Nodzewska, 2010). *N*-acylhydrazones may exhibit keto-enolic tautomerism, utilizing the electron donor (the oxygen atom of the carbonyl group) along with the azomethine nitrogen atom (–N=) to coordinate with metal ions (Purandara *et al.*, 2019; Selvam *et al.*, 2019). Acylhydrazones can form intramolecular hydrogen bonds involving the hydrogen atom linked to the amino nitrogen (–NH–) and the oxygen atom (Sadhukhan *et al.*, 2019; Socea *et al.*, 2022).

Acylhydrazones exhibit geometric isomerism due to the imine group (N=CH–), existing in a mixture of *E* and *Z* isomers, where E predominates due to its greater stability over the *Z* isomer (Socea *et al.*, 2022). Theoretically, acylhydrazones can have four isomers, two of which are geometric isomers (*E*/*Z*) due to the C=N double bond, and two are conformational isomers (*syn/anti*) due to the N−N bond (Sadhukhan *et al.*, 2019; Socea *et al.*, 2022). In the case of *N*-aroylhydrazones, the *E* isomer is stabilized by an intramolecular hydrogen bond (Socea *et al.*, 2022).

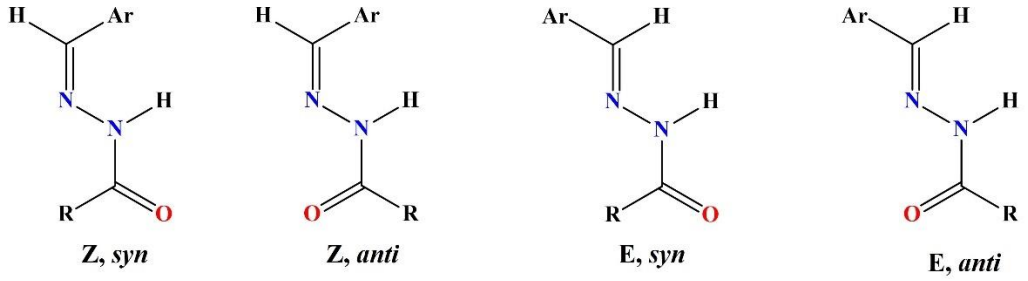

Figure 5. Isomers of acylhydrazone derivatives.

The mechanism for obtaining hydrazones through condensation reaction is widely documented in literature. One of the accepted mechanisms suggests nucleophilic addition to the carbonyl as the first reaction step, followed by proton transfer from the nitrogen that performed the nucleophilic attack. The reaction progresses as the oxygen molecule is protonated, forming a species that facilitates water elimination, leading to the formation of the iminium intermediate. In the final reaction step, the iminium ion is converted into the desired hydrazone through deprotonation by the conjugate base of the acid that protonated the oxygen earlier (Kölmel & Kool, 2017; Trost & Fleming, 1991). The mechanism is depicted in Figure 6, illustrating the general process of obtaining hydrazones through condensation reaction.

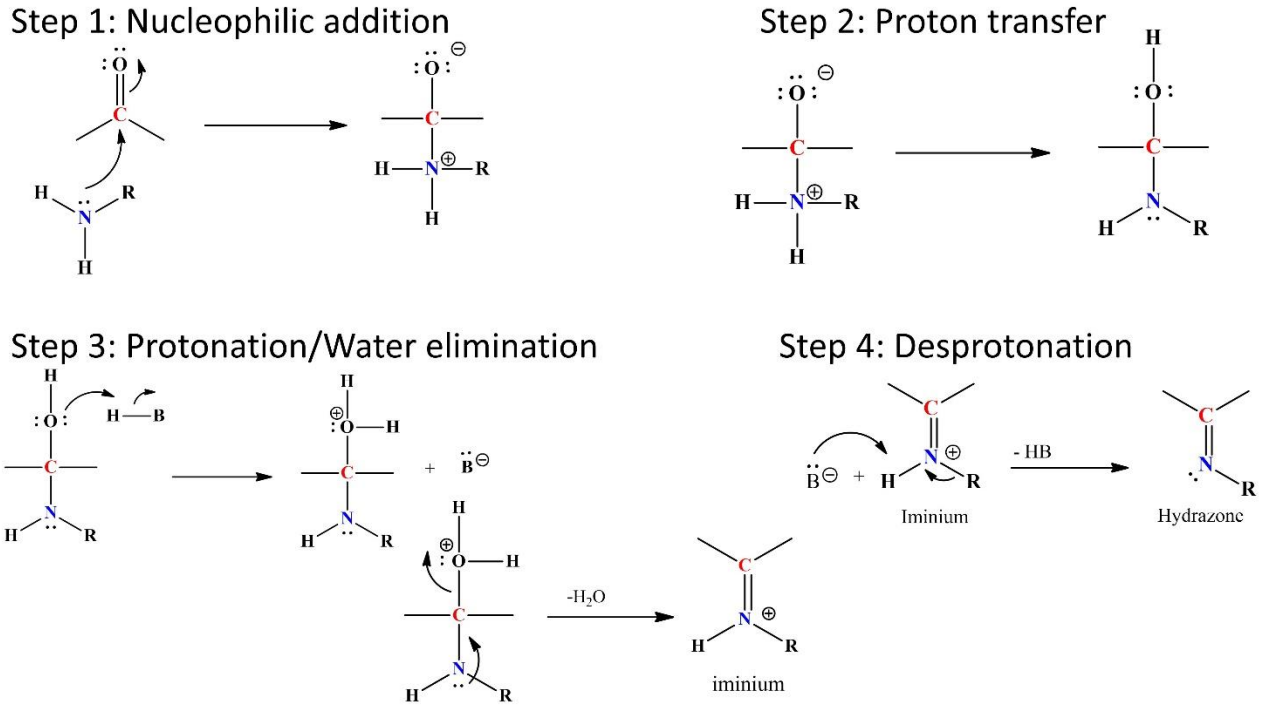

Figure 6. General mechanism for obtaining hydrazones from the condensation reaction.

Although the C=N bond provides stability to hydrazones, it is known that hydrolysis can occur when they are in solution, causing hydrazones to revert to their starting materials. Hydrolysis may be favored in protic solvents or depending on the structure of the hydrazones, which is why there are numerous reports in the literature and in our hydrazone group that demonstrate hydrazones capable of resisting hydrolysis and maintaining stability (Gamov *et al.*, 2023; Sahu *et al.*, 2023; Yang *et al.*, 2021). Figure 7 illustrates the mechanism of acid-catalyzed hydrolysis of a hydrazone, where the first step involves protonation of the azomethine nitrogen (Cukierman, 2021).

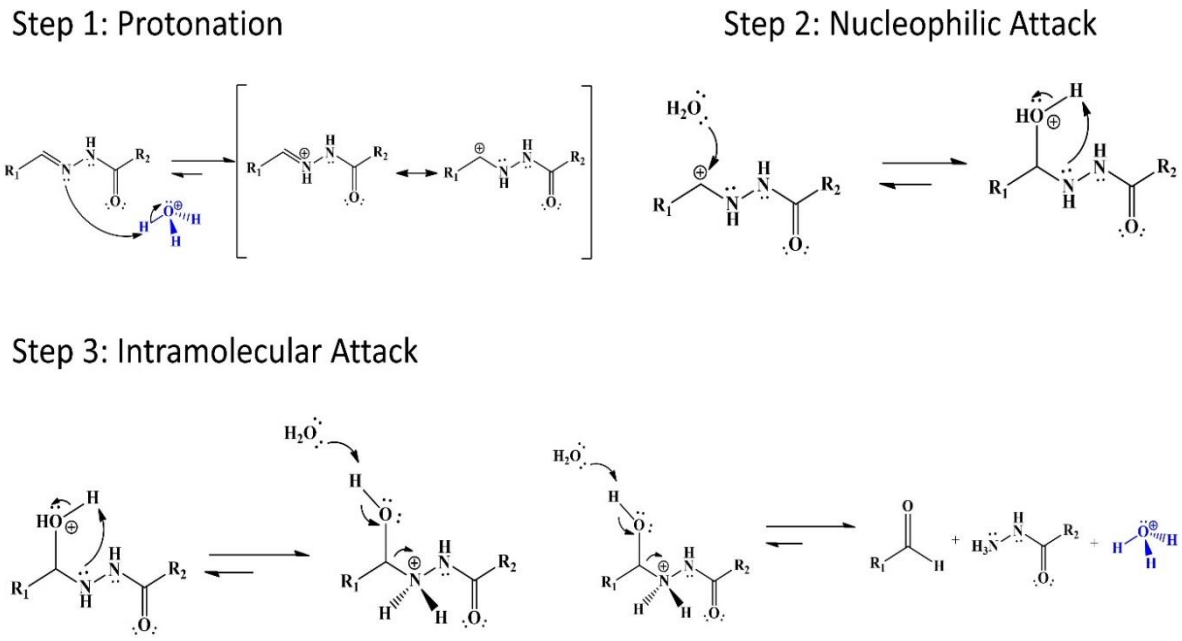

Figure 7. Mechanism of hydrolysis of hydrazones.

1.2.2 Biological activity of *N*-acylhydrazones

The discovery of new drugs is challenging because many fail in the early stages of clinical trials due to toxicity and lack of efficacy (Swinney & Anthony, 2011). Over the past two decades, the bioactive *N*-acylhydrazone group has been prominently featured in medicinal chemistry, identified in a large number of compounds targeting various molecular targets (Thota *et al.*, 2018). In recent years, several studies have been published on the chemistry and biological activity of *N*-acylhydrazones, making this topic crucial in the development of new therapeutically useful bioactive compounds (Pinheiro *et al.*, 2018; Thota *et al.*, 2018).

While many *N*-acylhydrazones have been reported in the literature with biological activity, few have been approved for clinical use, notable among them are the semicarbazones: nitrofurazone and nitrofurantoin (Figure 8) (Guay, 2001; Pinheiro *et al.*, 2018; Thota *et al.*, 2018). These two compounds are primarily used to combat bacterial infections. Nitrofurazone (1) is used as a topical antibacterial agent, and nitrofurantoin (2) is used orally to treat infections in the genitourinary tract (Guay, 2001; Thota *et al.*, 2018). The mechanism of action of these drugs is believed to be associated with the generation of highly reactive

electrophiles following reduction of nitrofuran by bacterial enzymes (nitroreductases), followed by reaction with nucleophiles (Pinheiro *et al.*, 2018).

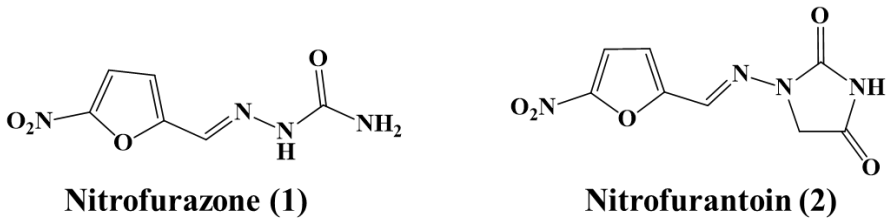

Figure 8. Structures of some *N*-acylhydrazones approved for clinical use.

Many anticancer drugs are undergoing clinical trials, and the intense search for new anticancer agents has led to the discovery of several hydrazones with antitumor activity (Rollas & Güniz Küçükgüzel, 2007). A recent study demonstrated that 5-bromo-1-methyl-N'-[(E)-(1-methyl-1H-indol-3-yl) methylidene]-1H-indole-3-carbohydrazide (Figure 9) exhibits antitumor activity in breast, cervical, and colon cancer cell lines, inducing cellular apoptosis. This action is mediated through adenosine monophosphate-dependent protein kinase A (cAMP), p53 protein, and stimulation of reactive oxygen species (ROS) and nitric oxide (NO) generation (Sreenivasulu *et al.*, 2019). Researchers also showed that (E)-1-(4-methoxybenzyl)-N'-(7-methyl-2-oxoindolin-3-ylidene)-1H-1,2,3triazole-4-carbohydrazide inhibits a kinase involved in the cell replication process, exerting an antiproliferative effect concurrently with increased ROS production, inducing apoptosis in cancer cell lines (Sreenivasulu *et al.*, 2019).

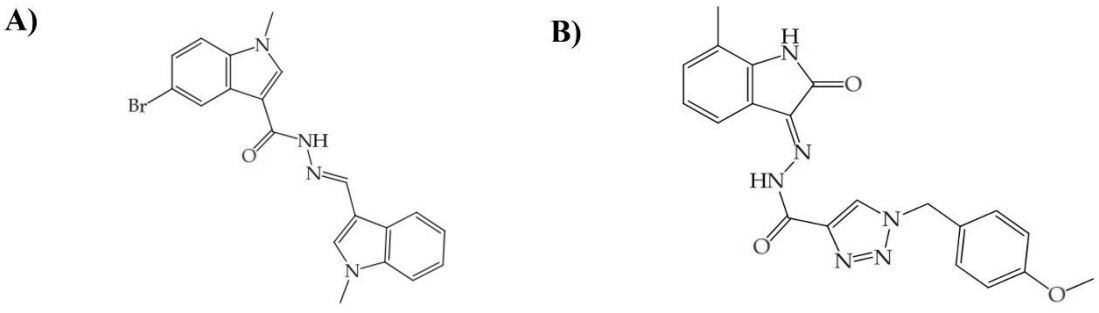

Figure 9. Structure of **A)** 5-bromo-1-methyl-N'-[(E)-(1-methyl-1H-indol-3-yl)methylidene]-1H-indole3-carbohydrazide **B)** (E)-1-(4-methoxybenzyl)-N'-(7-methyl-2-oxoindolin3-ylidene)-1H-1,2,3-triazole-4-carbohydrazide with antitumor action.

Numerous *N*-acylhydrazones have been reported as intermediates in heterocyclic reactions, owing to their structural variability which allows for the synthesis of compounds with diverse therapeutic indications (such as cytotoxic, antibacterial, antifungal, antiviral, antioxidant, antiparasitic, anti-inflammatory, anticonvulsant, and antihypertensive properties). Motivated by these and other studies, our research group has been dedicated over the past fifteen years to investigating the biological activities of different families of hydrazones, particularly in the context of managing Alzheimer's disease, Parkinson's disease, and cytotoxic activity. Additionally, we study the interaction of these molecules with various metal ions, whether in the formation of isolated coordination compounds or in solution studies (Cukierman, 2021; Cukierman *et al.*, 2018; Cukierman *et al.*, 2020; Cukierman *et al.*, 2017; Moura *et al.*, 2023; Rada *et al.*, 2019; Rada *et al.*, 2020).

1.3 Metals in Medicine

Some metal ions are vital for many functions in living organisms. Over the last few decades, metals have increasingly become important as diagnostic and therapeutic tools evolve to study and treat a variety of pathologies. Metals can easily become positively charged ions by losing electrons, allowing them to interact with biological molecules. The roles that metals play in biological systems are diverse, including oxygen transport, metabolism regulation, and serving as essential components of metalloenzymes. Metal ions also have structural roles, assisting biomolecules in achieving their functional conformation (Franz & Metzler-Nolte, 2019).

The literature reports that different coordination compounds have been used to control or treat various pathologies. Silver and antimony complexes have been employed as anti-infective agents: silver sulfadiazine is used as an antimicrobial, and both meglumine antimoniate and sodium stibogluconate are utilized for treating leishmaniasis. On the other hand, the iron chelator deferoxamine is used to treat malaria (Franz & Metzler-Nolte, 2019; Housecroft & Sharpe, 2005; Morrison *et al.*, 2020; 2022). Some iron and manganese coordination compounds derived from macrocyclic ligands (such as porphyrins) have been synthesized and evaluated by researchers, as they can potentially serve as superoxide scavengers, mimicking the enzyme superoxide dismutase (Roat-Malone, 2007).

Chemotherapy has been one of the main forms of cancer treatment. Chemotherapeutic agents induce a cytotoxic event that inhibits tumor progression. Chemotherapy aims for selective attack on tumor cells while preserving healthy cells; however, many chemotherapeutic agents damage healthy cells in addition to tumor cells (Roat-Malone, 2007).

In the 1960s, the anticancer activity of cisplatin (Figure 10) was discovered, marking it as one of the first coordination compounds used for cancer treatment. Cisplatin is responsible for curing more than 90% of testicular cancer cases and plays a pivotal role in treating ovarian, head and neck, bladder, cervical, melanoma, and lymphoma tumors (Chen *et al.*, 2009; de Oliveira Santos *et al.*, 2023; Lippard & Berg, 1994). The mechanism of action of cisplatin involves binding to DNA and subsequent interference with DNA replication. Following intravenous administration to the patient, cisplatin rapidly diffuses into tissues and strongly binds to plasma proteins, particularly albumin. Cisplatin's interactions with DNA can trigger cytotoxic processes leading to the death of both cancerous and healthy cells, indicating that cisplatin is less selective than other antitumor agents (Rosenberg *et al.*, 1967; Rosenberg *et al.*, 1965).

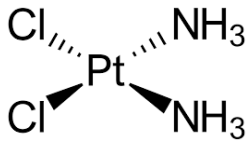

Figure 10. Cisplatin structure, *cis*-diaminodichloroplatinum(II).

Although cisplatin remains one of the most widely used treatments for cancer patients, often combined with other drugs, there are many reported side effects due to its low biocompatibility, as platinum is not a physiological metal. Besides nephrotoxicity and neurotoxicity associated with its use, damage to gastrointestinal mucosa is expected, and in many cases, the development of cellular resistance to the compound limits its use in cancer treatment. The metabolism of the drug by sulfur-containing proteins and peptides in the plasma and the repair of damaged DNA are some factors related to acquired resistance to cisplatin. Consequently, many new coordination compounds with anticancer activity, preferably less toxic and more selective than cisplatin, have been investigated (McMurray *et al.*, 2008; Montagner *et al.*, 2015; Rada *et al.*, 2019; Rada *et al.*, 2020). The literature reports a significant increase in the search for

new metal-based anticancer agents following the discovery of cisplatin's anticancer activity. However, few inorganic antineoplastic drugs have entered clinical study in recent decades, primarily due to issues of toxicity associated with lack of selectivity (Rada *et al.*, 2019; Rada *et al.*, 2020).

1.4 The bioinorganic chemistry of copper: An inorganic perspective on biological systems

When analyzing a biological system, there exists a clear boundary between organic and inorganic systems. On one side, essentials elements for life include C, H, N, and O, along with Na, Mg, K, Ca, Cl, P, and S. Among these, C, H, N, and O are responsible for the constitution of biomolecules such as lipids, amino acids, peptides, carbohydrates, proteins, and nucleic acids. P is important for ATP and DNA, and S allows for coordination capability in cysteine residues within proteins. On the other side, less abundant elements like Na, K, and Cl enable osmotic control and nervous action. Mg^{2+} is present in chlorophyll, and enzymes containing Mg^{2+} are involved in phosphate hydrolysis. The Ca^{2+} ion is crucial for structural functions such as bones, teeth, shells, and muscles, while the Fe^{2+} ion serves as the active site in hemoglobin, facilitating the transport of oxygen to cells (Housecroft & Sharpe, 2005).

In addition to the aforementioned elements, certain others known as trace metals (V, Cr, Mn, Fe, Co, Ni, Cu, Zn e Mo.) and trace non-metals (B, Si, Se, F, and I) hold significant relevance in biological systems. These elements constitute a minute fraction within living organisms (Housecroft & Sharpe, 2005). For some authors, Bevers *et al.* (2009); Hille (2002) , tungsten (W) is also considered biologically relevant because some metalloenzymes have this element in their active site.

1.4.1 Introduction to Bioinorganic Chemistry

Bioinorganic chemistry involves the study of metal species in biological systems. The essentiality of metal ions has been defined by several criteria:

a. Physiological deficiency occurs when the element is removed from the diet;

b. Deficiency is alleviated by adding the element back into the diet;

c. Specific biological functions are associated with the element;

d. High doses of these metal ions can cause toxic effects in the organism, eventually leading to lethality.

Beyond availability, physical-chemical properties such as ionic charge, ionic radius, ligand preferences, coordination geometry preferences, systemic kinetic control, and chemical reactivity justify the inclusion of these elements in biological systems (Housecroft & Sharpe, 2005; Lippard & Berg, 1994; Roat-Malone, 2007).

In general, the roles of metal ions in biological systems vary:

- Group 1 and 2 metals act as structural elements and in maintaining charge and osmotic balance.
- Transition metal ions occurring in a single oxidation state, such as Zn(II), function in superoxide dismutase and zinc fingers.
- Transition metals occurring in multiple oxidation states serve as electron carriers—e.g., iron ions in cytochromes or iron-sulfur clusters of the nitrogenase enzyme—and facilitate oxygen transport—e.g., iron ions in hemoglobin or copper ions in hemocyanin—and act as catalytic sites in enzyme catalysis—e.g., copper ions in superoxide dismutase or iron and molybdenum ions in nitrogenase (Housecroft & Sharpe, 2005; Lippard & Berg, 1994; Roat-Malone, 2007).

Table 1. List of essential metals and summary of where they can be found and their functions in biological systems Housecroft & Sharpe (2005).

Metal	Biological function
V	Enzymes (nitrogenases, haloperoxidases)
Cr	Essential in glucose metabolism in higher mammals (not yet proven)
Mn	Enzymes (phosphatases, mitochondrial superoxide dismutase, glycosyl transferase); photoredox activity
Fe	Electron transfer systems (Fe-S proteins, cytochromes); storage and transport of oxygen (hemoglobin, myoglobin, hemerythrin); Fe storage (ferritin, transferritin); Fe transport proteins (siderophores); in enzymes (e.g. nitrogenases, hydrogenases, oxidases, reductases)
Co	Vitamin B_{12} coenzyme
Ni	Enzymes (urease, some hydrogenases)
Cu	Electron transfer systems (blue copper proteins); storage and transport of oxygen (hemocyanin); Cu transport proteins (ceruloplasmin)
Zn	Acts as a Lewis acid (for example, in hydrolysis processes involving carboxypeptidase, carbonic anhydrase
Mo	Enzymes (nitrogenases, reductases, hydroxylases)

1.4.2 The Bioinorganic Chemistry of Copper

Copper has a variety of applications in bioinorganic chemistry, owing to its status as a transition metal with multiple oxidation states that facilitate a range of redox reactions, particularly relevant in biological systems. Copper's primary roles include electron transfer systems, such as those involving blue copper proteins, as well as the storage and transport of dioxygen (O_2) via hemocyanin. Ceruloplasmin is involved in the copper transport process within the body (Housecroft & Sharpe, 2005).

a) Blue copper proteins

Blue copper proteins constitute an important group of proteins involved in redox processes in biological systems. The ligands coordinated to copper ions modulate the ease with which the system can be oxidized or reduced. The Cu(I) ion is soft and prefers ligands containing sulfur (found in cysteine residues) or unsaturated ligands such as o-phenanthroline and 2,2'-bipyridine, which have large polarizable electron clouds. The Cu(II) ion, relatively hard or borderline, prefers ligands containing nitrogen (found in histidine residues), which are harder atoms. Typically, copper enzymes involved in redox reactions feature both types of ligands, allowing the metal centers to readily exist in both oxidation states (Roat-Malone, 2007). There are three classes of copper centers in blue copper proteins (Housecroft & Sharpe, 2005; Karlin & Tyeklar, 2012):

i) Type 1 center is characterized by intense absorption in the electronic spectrum with $\lambda_{max} \approx 600$ nm, and $\varepsilon_{max} \approx 100$ times greater than that of the aqueous Cu^{2+} ion, attributed to charge transfer from a coordinated cysteine to Cu^{2+}.

ii) Type 2 center exhibits typical electronic spectroscopy characteristics of the Cu^{2+} ion.

iii) Type 3 center shows absorption with $\lambda_{max} \approx 330$ nm, existing as a pair of antiferromagnetically coupled Cu(II) centers providing a diamagnetic system. The Cu_2 unit can function as a two-electron transfer center and is involved in O_2 reduction.

Blue copper proteins contain at least one Type 1 copper metal center, including plastocyanins and azurins. Plastocyanins are found in higher plants and blue-green algae. Azurins occur in some bacteria and are involved in electron transfer converting $[NO_3]^-$ to N_2 (Housecroft & Sharpe, 2005; Lippard & Berg, 1994; Roat-Malone, 2007). Type 1 enzymes sometimes have a distorted tetrahedral center, especially when the enzyme contains Cu(II) ions. In azurin, however, the Cu(II) ion adopts a trigonal bipyramidal geometry, while in both azurin and plastocyanin, copper(I) metal centers adopt trigonal geometry. For Type 2 and Type 3 copper centers, certain ligands may or may not bond with the metal center, depending on the metalloprotein and the oxidation state of the copper ion (Roat-Malone, 2007). Although blue copper proteins are involved in

electron transfer processes, the Franck-Condon principle ensures that no nuclear movement occurs during the electronic transition; thus, the geometry of the species before and after electron transfer is little changed. Consequently, the geometry of the active site of a redox metalloenzyme should approach the appropriate transition state for electron transfer (Housecroft & Sharpe, 2005; Lippard & Berg, 1994; Roat-Malone, 2007).

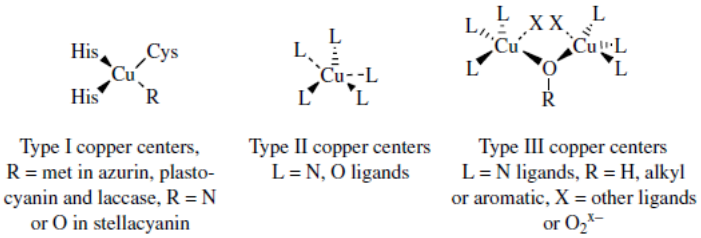

Figure 11. Type I, II, and III copper center geometries. Dotted lines indicate possible ligands.

b) Hemocyanin

Hemocyanins are copper-containing proteins that transport O_2 in mollusks and arthropods. Hemocyanin is a large multimeric protein (molar mass 4×10^5 to 9×10^6 Da) that binds molecular oxygen at Type III dinuclear copper sites (Housecroft & Sharpe, 2005; Roat-Malone, 2007). This metalloprotein transports O_2 by binding molecular oxygen as a peroxide ion at a dinuclear copper site, concomitantly oxidizing copper(I) to copper(II). The presence of Cu(II) in oxyhemocyanin imparts a blue color to species that utilize this metalloenzyme as their oxygen carrier. Oxyhemocyanin exhibits an intense optical transition at 340 nm and a weaker transition at 580 nm, both attributed to ligand-to-metal charge transfer bands (Lippard & Berg, 1994; Roat-Malone, 2007).

The deoxy form of hemocyanin is colorless and contains Cu(I), while oxygen binding results in the blue Cu(II) form. In deoxyhemocyanin, two Cu(I) ions, with variable internuclear distances depending on the species studied, are each trigonally coordinated by three histidines. A cavity exists between the two copper ions to accommodate the oxygen molecule (Housecroft & Sharpe, 2005; Roat-Malone, 2007).

Oxyhemocyanin features the $Cu_2(His)_6$ unit resembling the deoxy form. The O_2 unit is bound in a bridging mode with an O−O bond length of 140 pm, typical of that found in peroxide complexes. The O_2 binding site is formulated as Cu(II)−$[O_2]^{2-}$−Cu(II), indicating that electron transfer accompanies O_2 binding (Housecroft & Sharpe, 2005). Many model complexes have been studied in an effort to understand O_2 binding in hemocyanin; frequently, these model complexes involve imidazole or pyrazole derivatives to mimic histidine residues. One of the models closely resembling oxyhemocyanin is the dicopper(II) peroxide complex.

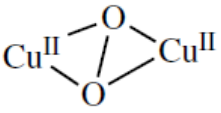

Figure 12. [Cu_2-μ-η^2: η^2 O_2] peroxo binding mode found in hemocyanin.

c) Superoxide Dismutase

Superoxide dismutase enzymes are functional dimers with a molecular weight of approximately 32 kDa. Each enzyme contains one copper ion and one zinc ion per subunit. These metalloenzymes catalyze the dismutation reaction of the biologically harmful superoxide radical ion, as described by the following reaction (Karlin & Tyeklar, 2012; Lippard & Berg, 1994; Roat-Malone, 2007):

$$\mathbf{2O_2^- + 2H^+ \rightarrow H_2O_2 + O_2}$$

The product of this reaction, H_2O_2, is also potentially harmful to the organism. Hydrogen peroxide is removed by the action of the metalloenzyme catalase, which contains an iron site, through the reaction:

$$\mathbf{2H_2O_2 \rightarrow 2H_2O + O_2}$$

In prokaryotes, it has been discovered that superoxide dismutases (SOD) exhibit redox activity from active sites containing manganese or iron, whereas those found in eukaryotes and some bacterial species feature copper-zinc active sites. This enzyme, predominantly located in mammalian liver, blood cells, and brain tissue, consists of two identical subunits, each containing one copper and one zinc atom. The primary role of SOD is believed to be the removal of the superoxide radical ion from the cytosol. In this capacity, SOD acts as an antioxidant, inhibiting aging and carcinogenesis (Karlin & Tyeklar, 2012; Lippard & Berg, 1994; Roat-Malone, 2007). Imbalances in SOD have been experimentally linked to various types of cancer, such as hepatocellular carcinoma (Huang *et al.*,

2000; Oberley & Buettner, 1979).

1.4.3 Copper(II) complexes with antitumor activity

Copper is a metal with unique properties, exhibiting different coordination numbers and capable of forming complexes with diverse geometric structures. Given its status as an important trace element in biological processes, copper complexes with antitumor activity are expected to reduce side effects compared to widely used platinum-based compounds (Hu *et al.*, 2017). Moreover, due to fundamental differences in the chemistry between copper and platinum complexes, diverse mechanisms of action can also be anticipated. These characteristics make copper complexes promising candidates for the discovery of new active compounds against tumors. The use of these metal complexes as a potential new therapeutic class for various diseases, including cancer, has been extensively discussed in the scientific community (Moura *et al.*, 2023; Rada *et al.*, 2019; Rada *et al.*, 2020).

The Casiopeínas®, developed in Mexico by the research group led by Prof. Dr. Lena Ruiz Azuara, represent a series of promising mononuclear copper(II) ternary complexes. These compounds have recently entered clinical phase testing for cancer, being the first copper-based complexes to reach such an advanced stage of development. This family of copper(II) coordination compounds was initially designed to target DNA damage induction. Consequently, the molecules were engineered with ligands positioned in the equatorial plane of the metal center to facilitate intercalation interactions with DNA. The design incorporated a copper atom, which, as an endogenous metal atom, was intended to mitigate the compound's toxicity. Another potential objective is the development of small cationic molecules to enhance solubility in biological environments. Additionally, the research explores whether the redox properties of the metal might be relevant in tumor cells. The research group prioritized the synthesis and characterization of these compounds, and it was in the 1990s that the name Casiopeínas® was adopted and preclinical studies commenced (Aguilar-Jiménez *et al.*, 2023; Ruiz-Azuara *et al.*, 2014).

The complex depicted in Figure 13, designated Cas III-ia, exemplifies this series. This complex has been shown to induce cell death via apoptosis and autophagy in the C6 glioma cell line in rats. Post-treatment with this complex, C6 glioma cells exhibited morphological features indicative of autophagy, accompanied by intracellular generation of reactive oxygen species (ROS), suggesting a significant role of these species in cell death (Aguilar-Jiménez *et al.*, 2023; Ruiz-Azuara *et al.*, 2014; Tan *et al.*, 2014).

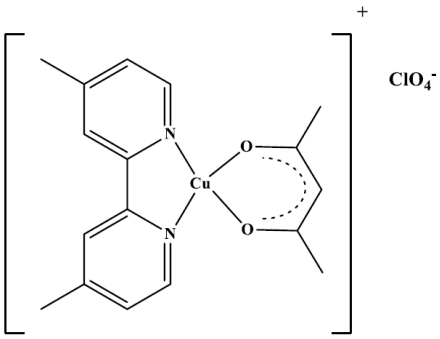

Figure 13. Structure of the mononuclear Cas III-ia complex.

Mononuclear complexes containing *N*-acylhydrazone ligands with antitumor activity have also been reported in the literature, with several studies published by Prof. Dr. Ignacio E. León's research group (Balsa *et al.*, 2021; Balsa, L. M. *et al.*, 2023; Balsa *et al.*, 2020; Balsa, M. L. *et al.*, 2023; Burgos-Lopez *et al.*, 2019). Figure 14 illustrates one of these promising compounds investigated by the group.

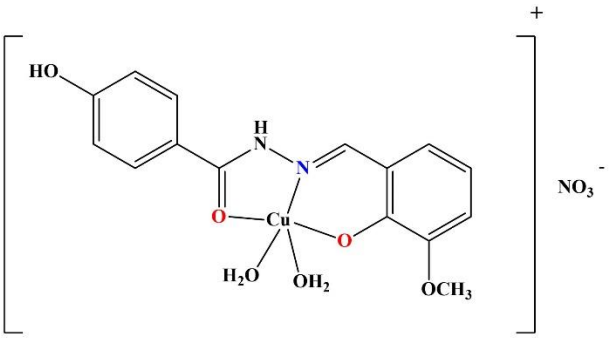

Figure 14. Mononuclear copper(II) complex derived from an *N*-acylhydrazonic ligand with antitumor activity.

The complex depicted in Figure 14 inhibits the viability of five human cancer cell lines, demonstrating greater potency than that observed for the free ligand and Cu(II) ion. The anticancer activity of this complex against the tested cells exceeds that reported for the reference metallodrug cisplatin. These findings

underscore the significant impact of coordination on the bioactivity of the complex (Burgos-Lopez *et al.*, 2019).

Binuclear copper(II) complexes have exhibited significant cytotoxic activity in vitro; in some cases, even better than cisplatin. Comparisons of the cytotoxic activity of copper(II) complexes with other derivatives containing cobalt, nickel, or zinc indicate that copper complexes show superior DNA cleavage activity. Furthermore, the addition of copper(II) ion to the ligands commonly enhances the antiproliferative activity compared to the free ligand (Fekri *et al.*, 2019; Ferreira *et al.*, 2016; Rossi *et al.*, 2005; Rossi *et al.*, 2002). Copper(II) coordination compounds, both mono- and binuclear, with ligands derived from coumarin, *N*-acylhydrazones, *N*-heterocycles, benzimidazoles, and Schiff bases have been extensively investigated and described. Some of them have demonstrated significant capability to induce apoptotic cell death (Liu *et al.*, 2022; Santini *et al.*, 2014).

1.5 Human Serum Albumin Protein (HSA)

Many drugs are low molecular weight chemical compounds, molecules that can be used in the treatment of various diseases. However, these drugs have some disadvantages such as rapid degradation, short circulation time, quick clearance, nonspecific distribution, and toxic accumulation in specific organ(s) (Sun & H Coy, 2011; Sun *et al.*, 2008). In diseases like cancer and immune disorders, disturbances often occur in specific tissues or organs. These characteristics demand that the drug used acts specifically, being delivered to a particular site selectively (Sun & H Coy, 2011; Sun *et al.*, 2008). Therefore, various strategies have been employed to target nonspecific low molecular weight drugs for site-specific delivery. One approach involves conjugating these drugs with monoclonal antibodies, peptides, and proteins. These carriers can achieve the goal of delivering drugs to the body more selectively. One such carrier is human serum albumin (HSA), which has been widely used for clinical treatments and drug delivery (Wang *et al.*, 2020).

The human albumin gene is located on the long arm of chromosome 4. HSA is produced in human hepatocytes and is the most dominant protein component of blood, constituting approximately 50% of all serum proteins (Bern *et al.*, 2015; Leblanc *et al.*, 2019). HSA serves multiple biological functions, exhibits antioxidant properties, regulates osmotic blood pressure, and can transport various hydrophobic endogenous or exogenous ligands, binding to fatty acids, amino acids, hormones, ions such as Ca^{2+}, Na^{+}, and K^{+}, water, and others (Wang *et al.*, 2020). HSA can transport drugs through covalent bonds, peptides/proteins, by fusing them to its C and N terminals (Larsen *et al.*, 2016; Wang *et al.*, 2020)

Human serum albumin (HSA) is a single chain consisting of 609 amino acids with a molecular weight of 66.5 kDa, as depicted in Figure 15. Its primary structure comprises an N-terminal, a C-terminal, and three homologous domains named domain I, II, and III (Wang *et al.*, 2020). Each of these domains has two helical subdomains (IA and IB, IIA and IIB, IIIA and IIIB), each containing 4 to 6 α-helices (Bern *et al.*, 2015; Wang *et al.*, 2020). These six subdomains form a three-dimensional structure. Unlike other blood proteins, HSA is not glycosylated. Additionally, HSA is highly soluble in water due to its negatively charged surface and is very stable in blood with a half-life of approximately 19 days, owing to its ability to diffuse in and out of blood vessels (Bern *et al.*, 2015; Foss *et al.*, 2016).

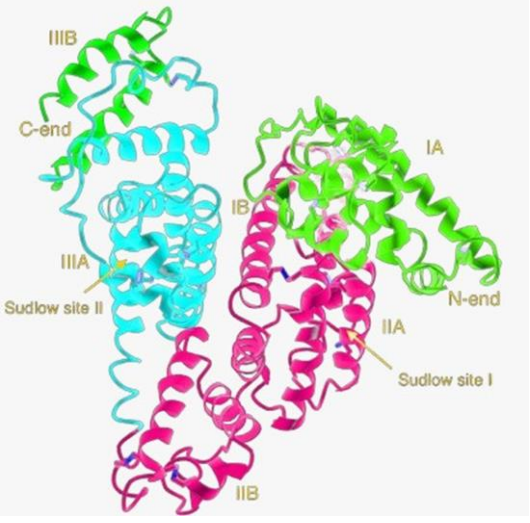

Figure 15. The crystal structure of human serum albumin (HSA) (PDB ID: 1AO6, MMDB ID:47931). The primary structure of HSA consists of one N-terminus, one C-terminus and three homologous domains (domain I, II, and III). Each of these domains has two subdomains (IA and IB, IIA and IIB, IIIA and IIIB), respectively and contains 4 to 6 α-helices, as well with both Sudlow site I and Sudlow site I/II shown. Figure modified from (Wang *et al.*, 2020).

Human serum albumin has an exceptional capacity to transport various ligands, primarily due to its hydrophobic pockets, which provides potential applications in drug delivery. According to Sudlow's nomenclature for albumin, there are two critical binding regions, as illustrated in Figure 15 (Sudlow site I and Sudlow site II), which represent two primary drug-binding sites in the 3D structure of albumin. Both Sudlow site I and Sudlow site II are located in the hydrophobic cavities of subdomain IIA and subdomain IIIA, respectively (Larsen *et al.*, 2016; Leblanc *et al.*, 2019) This unique structure of HSA provides key binding sites for various drugs. Voluminous heterocyclic anions (charged molecules) and dicarboxylic acids preferentially bind to Sudlow sites (Foss *et al.*, 2016).

The literature reports a number of studies demonstrating the use of HSA as a drug delivery vehicle in the body, due to its characteristics of long half-life, recirculation, accumulation in tumor tissues, and ease of diffusion through the epithelium (Foss *et al.*, 2016; Sand *et al.*, 2015). Albumin can pass through leakage from tumor blood vessels, and this characteristic allows albumin to transport anticancer agents to localized tumor regions. Thus, understanding the interaction of a new biologically active compound with HSA is strategically important (Foss *et al.*, 2016; Larsen *et al.*, 2016).

2. Work proposal and justification

The limitations and side effects associated with cisplatin have motivated the development of new chemotherapeutic agents with alternative mechanisms of action. *N*-acylhydrazone derivatives and their copper(II) complexes have been proposed as promising candidates to achieve this goal. Copper complexes offer several advantages over cisplatin. The copper is an essential metal to the human body and exhibits interesting properties, including multiple coordination numbers and very rich stereochemistry. Moreover, various mono- and dinuclear copper(II) complexes synthesized recently have demonstrated cytotoxic activity against cancer cells, positioning them as a new generation of potential chemotherapeutics. The literature reports some dinuclear copper(II) complexes capable of inducing apoptosis in cancer cells and exhibiting *in vitro* activity superior to cisplatin across different tumor cell lines (Aguilar-Jiménez *et al.*, 2023; Balsa *et al.*, 2021; Balsa, L. M. *et al.*, 2023; Balsa *et al.*, 2020; Burgos-Lopez *et al.*, 2019; Rada *et al.*, 2019; Rada *et al.*, 2020; Ruiz-Azuara *et al.*, 2014). Additionally, ONO-donor *N*-acylhydrazonic ligands, both free and in their coordinated form, have shown biological activity as anticancer agents. This has motivated the design of a new generation of similar ligands to enhance antitumor activity (Almeida *et al.*, 2005).

The design of the four bioinspired ligands was based on different criteria. The ligand **H_2L1**, which contains a pyridine substituent, was derived from isoniazid, a drug already used in the treatment of tuberculosis (Gegia *et al.*, 2017; LoBue & Moser, 2003). Heterocyclic aromatic rings with five members are of significant biological relevance, as reported in the literature (Alizadeh *et al.*, 2018; Gibson *et al.*, 1996); therefore, the furan substituent was incorporated into the structure of the ligand **H_2L2**. The 3-phenyl-isoxazole substituent was incorporated into the structure of ligand **H_2L3** due to the significant interaction with biomolecules and antiproliferative activity observed in complexes derived from similar ligands containing the same substituent, which have been previously synthesized by the group (Rada *et al.*, 2020). Additionally, the biological relevance of this substituent has been documented in the literature (Kumar & Jayaroopa, 2013; Walunj *et al.*, 2021). The methyl-imidazole substituent was incorporated into the structure of ligand **H_2L4** due to the presence of the imidazole group in the amino acid histidine.

This study encompasses the investigation of the reactivity, spectroscopic, electrochemical, and antiproliferative properties of a group of new mononuclear and dinuclear copper(II) complexes derived from phenol-based *N*-acylhydrazonic ligands. Different coordination compounds can be obtained from various starting salts. Therefore, in addition to synthesizing a new family of *N*-acylhydrazones, we aim to produce distinct copper complexes by varying the starting salts to observe possible structural modifications these compounds might undergo.

Following the syntheses, characterization, and reactivity studies for all the compounds toward the HSA, as well as their spectroscopic and electrochemical properties, the cytotoxicity of the compounds will be evaluated against human tumor and normal cell lines. The different ligands will be synthesized according to the literature (Rada *et al.*, 2019; Rada *et al.*, 2021; Rada *et al.*, 2020) from a commercial aldehyde and various (commercial or not) hydrazides, generating a new family of *N*-acylhydrazones (Figure 16), which will then be used as ligands in the synthesis of the copper(II) complexes.

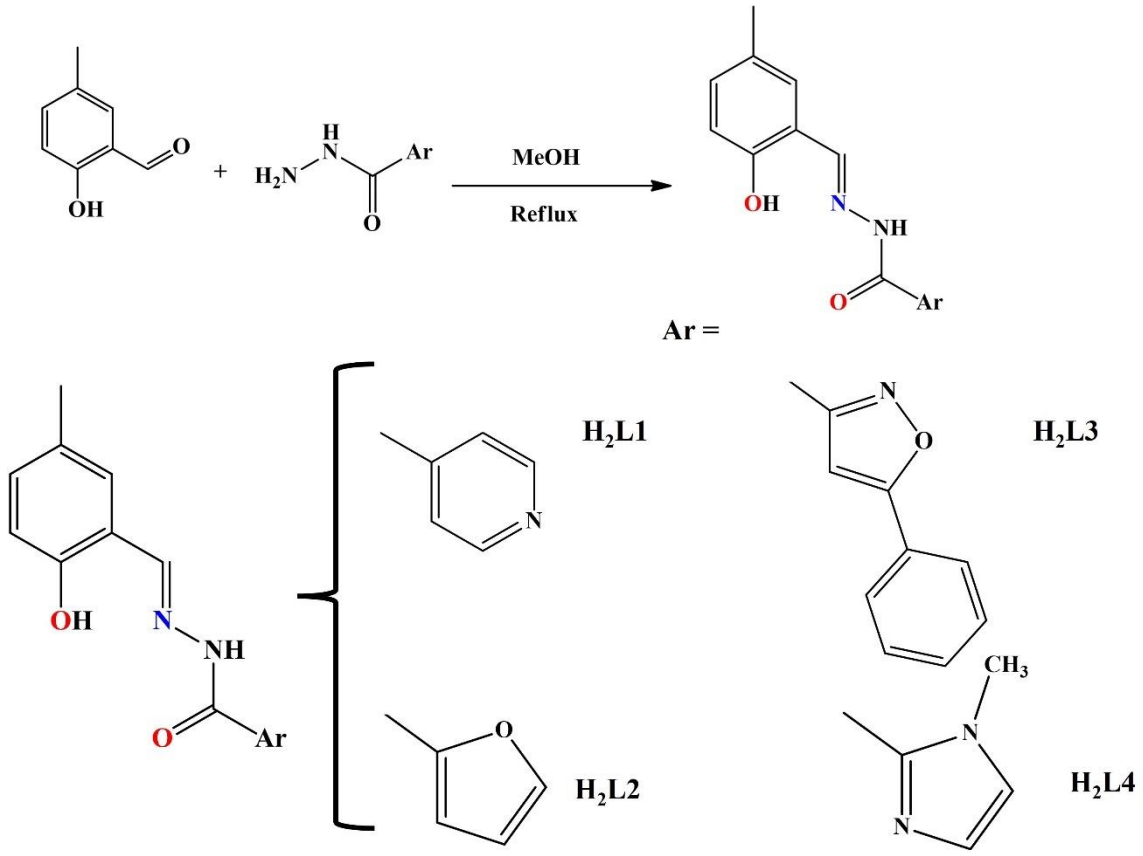

Figure 16. General scheme for the synthesis of the proposed phenol-based, tridentate *N*-acylhydrazonic ligands substituted with different Ar = aroyl groups.

3. Objectives

3.1 General objective

The primary objective of this study is to synthesize and characterize new *N*-acylhydrazonic ligands and their corresponding copper(II) complexes, as well as to explore their spectroscopic and electrochemical properties, their *in vitro* interaction with HSA and their cytotoxicity toward human tumor cell lines.

Additionally, the study aims to correlate structural and physicochemical properties of these compounds with the results obtained.

3.2. Specific objectives

- Design and synthesize a new group of bioinspired *N*-acylhydrazones and their Cu^{2+} complexes;
- Evaluate the various Cu^{2+} coordination compounds that can be obtained from the starting salts copper(II) chloride dihydrate, copper(II) perchlorate hexahydrate, and copper(II) nitrate trihydrate;
- Characterize the new ligands and their complexes through spectroscopic, electrochemical, and thermogravimetric techniques;
- Study the formation of the different complexes in solution and correlate these results with those obtained for the complexes in the solid state;
- Determine the pK_a values of the new synthesized ligands using electronic spectroscopy in the UV-Vis region;
- Investigate the interaction of ligands and complexes with the blood protein HSA *via* electronic spectroscopy in the UV-Vis region;
- Assess the cytotoxicity of the prepared compounds against both tumor and healthy human cells, comparing their activity with the one of cisplatin;
- Perform theoretical calculations to correlate the spectroscopic properties of the ligands and complexes with their chemical structures.

4. Methodology

4.1 Reagents and Solvents

Acetone, acetonitrile (MeCN), diethyl ether (Et_2O), dimethyl sulfoxide (DMSO), dimethylformamide (DMF), ethanol (EtOH), methanol (MeOH), isopropyl alcohol (*i*-PrOH), hydrochloric acid, barium sulfate, silver nitrate, monobasic sodium phosphate, potassium hydroxide, sodium hydroxide, potassium bromide, the supporting electrolyte tetrabutylammonium hexafluorophosphate, copper(II) perchlorate hexahydrate, copper(II) chloride dihydrate and copper(II) nitrate trihydrate, precursor 5-methylsalicylaldehyde (Hmb), 5-phenylisoxazole-3-carbohydrazide and human serum albumin (HSA) were obtained from Sigma-Aldrich; sodium chloride was purchased from Sigma-Aldrich / VWR PROLABO; furan-2-carbohydrazide and pyridine-2-carbohydrazide were obtained from Acros Organics and Sigma-Aldrich, respectively. All these chemicals were used without any type of treatment or further purification. The precursor 1-methylimidazole-2-carbohydrazide, on the other hand, was synthesized from the respective ester by the PhD student Hélcio Marcondes, under supervision of our collaborator, Prof. Cláudio Donnici (Departamento de Química – UFMG).

4.2 Synthesis of ligands

4.2.1 Ligand H_2L1

This ligand was synthesized by adding dropwise a methanolic solution (~15 mL) of 5-methylsalicylaldehyde (408 mg, 3 mmol) to 412 mg (3 mmol) of isoniazid dissolved in MeOH (15 mL). The mixture was stirred and refluxed for ~3 h. After the solution reached room temperature, the pH was evaluated at around 5-6. Yellow crystals suitable for XRD analysis were obtained from the stock solution after 2 days. The data regarding characterization agrees with analogous compounds already reported in the literature by the group.

M.p. = 209 ± 2 ºC, yield = 708 mg (2.7 mmol, 92%). Elemental analysis (%) – calculated for $C_{14}H_{13}O_2N_3$ (255.29 g mol^{-1}): C – 65.8, H – 5.1, N – 16.5; found: C – 65.0, H – 5.0, N – 16.6. ^{1}H NMR (DMSO-d_6, ppm): 12.26 (*s*, 1H, –N*H*–); 10.81 (*s*, 1H, –O*H*); 8.80 (*dd*, 2H,); 8.63 (*s*, 1H); 7.83 (*dd*, 2H,); 7.40 (*d*, 1H,); 7.13 (*dd*, 1H); 6.85 (*d*, 1H); 2.25 (*s*, 3H).

4.2.2 Ligand H_2L2

This ligand was prepared by adding dropwise a methanolic solution (about 15 mL) of 5-methylsalicylaldehyde (408 mg, 3 mmol) to 378 mg (3 mmol) of furan-2-carboxyhydrazide dissolved in MeOH (15 mL). The mixture was stirred and refluxed for ~3 h. After the solution reached room temperature, the pH was evaluated at around 5-6. Yellow crystals suitable for XRD analysis were obtained from the stock solution after 2 days. The data regarding characterization agrees with analogous compounds already reported in the literature.

M.p. = 150 ± 2 ºC, yield = 657 mg (2.5 mmol, 83%). Elemental analysis (%) – calculated for $C_{13}H_{12}O_3N_2 \cdot H_2O$ (262.29 g mol^{-1}): C – 59.5, H – 5.4, N – 10.7; found: C – 59.0, H – 5.3, N – 10.6. ^{1}H NMR (DMSO-d_6, ppm): 12.08 (*s*, 1H, –N*H*–); 10.88 (*s*, 1H, –O*H*); 8.60 (*s*, 1H, *H*7); 7.96 (*dd*, 1H, *H*12); 7.34 (*bs*, 1H, *H*5); 7.31 (*d*, 1H, *H*10); 7.10 (*dd*, 1H, *H*3); 6.83 (*d*, 1H, *H*2); 6.71 (*dd*, 1H, *H*11); 2.24 (*s*, 3H, *H*13). TGA: a two-step weight loss of approximately 6.7% (calcd 6.9%) is observed between 60 and 160 °C, consistent with one hydration water molecule.

4.2.3 Ligand H_2L3

This ligand was synthesized by adding dropwise a methanolic solution (~15 mL) of 5-methylsalicylaldehyde (408 mg, 3 mmol) to 378 mg (3 mmol) of 5-phenylisoxazole-3-carbohydrazide dissolved in MeOH (15 mL). The mixture was stirred and refluxed for ~3 h. After the solution reached room temperature, the pH was evaluated at around 5-6. White crystals suitable for XRD analysis were obtained from the stock solution after 4 days. The data regarding characterization agrees with analogous compounds already reported in the literature by the group.

M.p. = 190 ± 2 ºC, yield = 832 mg (2.5 mmol, 81%). Elemental analysis (%) – calculated for $C_{18}H_{15}O_3N_3$ (321.34 g mol^{-1}): C – 67.2, H – 4.7, N – 13.1; found: C – 65.9, H – 4.6, N – 12.8. ^{1}H NMR (DMSO-d_6, ppm): 12.54 (*s*, 1H, –N*H*–); 10.76 (*s*, 1H, –O*H*); 8.70 (*s*, 1H); 7.98 (*dd*, 2H); 7.50 (*dd*, 3H); 7.14 (*dd*, 1H); 7.10 (*dd*, 1H); 6.85 (*d*, 1H); 6.83 (*d*, 1H); 2.24 (*s*, 3H).

4.2.4 Ligand H_2L4

This ligand was prepared by adding dropwise a methanolic solution (about 15 mL) of 5-methylsalicylaldehyde (136 mg, 1 mmol) to 140 mg (1 mmol) of 1-methyl-imidazole-2-carbohydrazide dissolved in MeOH (15 mL). The mixture was stirred and refluxed for ~3 h. After the solution reached room temperature, the pH was evaluated at around 5-6. Yellowish crystals suitable for XRD analysis were obtained from the stock solution after 8 days. Characterization data agree with analogous compounds already reported in the literature by the group.

M.p. = 189 ± 2 ºC, yield = 219.5 mg (0.85 mmol, 85%). Elemental analysis (%) – calculated for $C_{13}H_{14}O_2N_4$ (258.28 g mol^{-1}): C – 60.4, H – 5.5, N – 21.7; found: C – 60.6, H – 5.3, N – 21.7. ^{1}H NMR (DMSO-d_6, ppm): 12.31 (*s*, 1H, –N*H*–); 11.12 (*s*, 1H, –O*H*); 8.66 (*s*, 1H); 7.45 (*dd*, 1H); 7.23 (*d*, 1H); 7.11 (*dd*, 2H); 6.83 (*d*, 1H); 3.99 (*s*, 3H); 2.24 (*s*, 3H).

4.3 Syntheses of copper(II) complexes

4.3.1 Copper(II) complexes derived from H_2L1

Attention!

Perchlorate salts of metal complexes containing organic ligands are potentially explosive and must be handled with care. Small quantities must be prepared.

Complexes **1A**, **1B** and **1C** were prepared from **H_2L1**, respectively, with the starting salts: copper(II) chloride dihydrate, copper(II) perchlorate hexahydrate and copper(II) nitrate trihydrate.

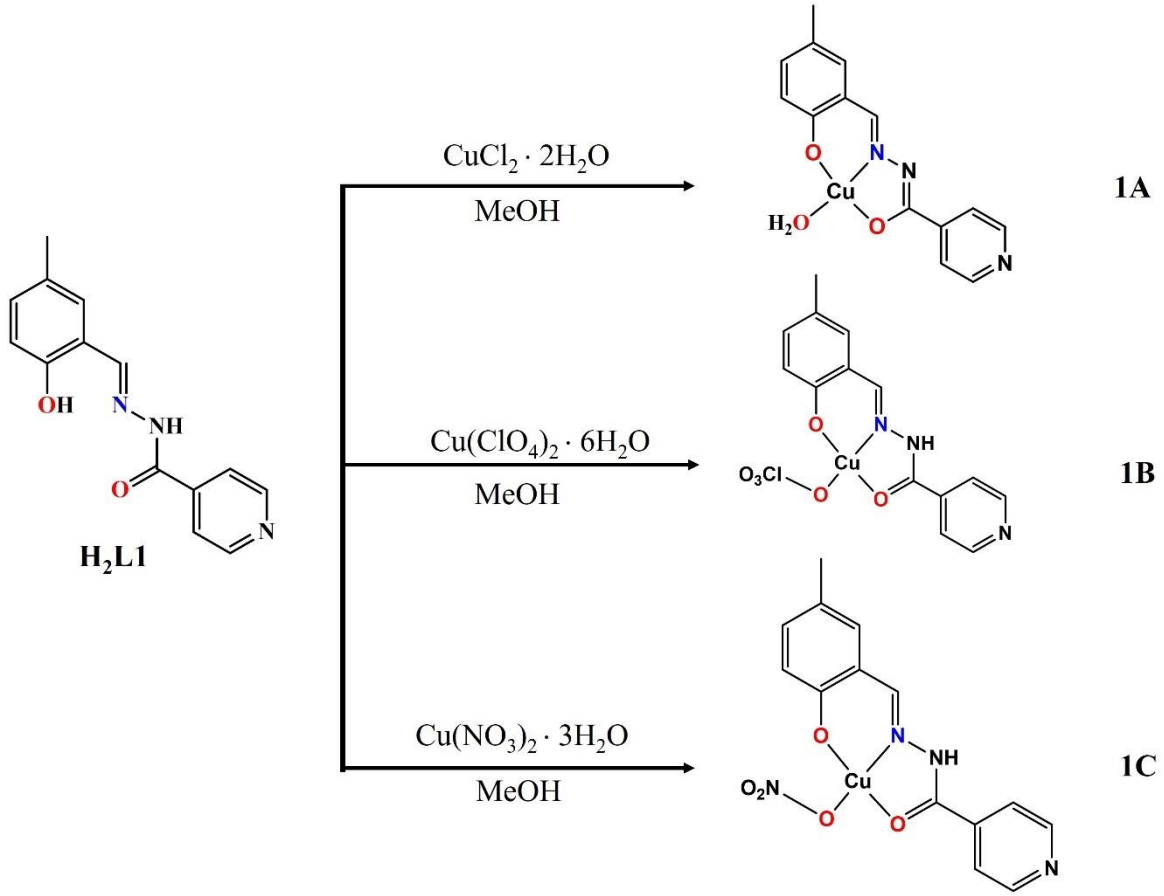

Figure 17. Synthetic scheme for complexes **1A, 1B** and **1C.**

Complex **1A** was synthesized by dissolving 1 mmol (250 mg) of **H_2L1** in 15 mL of MeOH, then adding 1 mmol (170 mg) of copper(II) chloride dihydrate. The mixture was stirred for 1 h at room temperature. A reddish precipitate was obtained. After 4 days, with slow evaporation of the solvent, a reddish powder was isolated. Figure 17 illustrates the synthesis of complex **1A**.

Yield = 290 mg (0.8 mmol, 82%). ICP-OES (% of metal) – calculated for $[Cu(C_{14}H_{11}O_2N_3)(OH_2)]$ (334.83 g mol^{-1}): Cu – 19.0; found: Cu – 19.4 ; TGA: Around 300 ºC there is a loss of mass of 72.5%, this loss is related to the organic fraction of the complex and water molecule. The 27.5% residue is suggested as copper(II) oxide, corresponding to 22.8% copper. With an error of 3.8% for the percentage of copper calculated for the suggested structure of the complex.

Complex **1B** was synthesized by dissolving 1 mmol (250 mg) of **H_2L1** in 15 mL of MeOH, then adding 1 mmol (370 mg) of copper(II) perchlorate hexahydrate. The mixture was stirred for 1 h at room temperature. A reddish precipitate was obtained. After 3 days, with slow evaporation of the solvent, a

reddish powder was isolated. Figure 17 illustrates the synthesis of complex **1B**.

Yield = 295 mg (0.4 mmol, 40%). ICP-OES (% of metal) – calculated for $[Cu(C_{14}H_{12}O_2N_3)ClO_4]$ (417.26 g mol^{-1}): Cu – 15.2; found: Cu – 16.6; TGA: The experiment was not carried out because the sample contains perchlorate.

Complex **1C** was synthesized by dissolving 1 mmol (250 mg) of **H_2L1** in 15 mL of MeOH, then adding 1 mmol (240 mg) of copper(II) nitrate trihydrate. The mixture was stirred for 1 h at room temperature. A reddish precipitate was obtained. After 4 days, with slow evaporation of the solvent, a reddish powder was isolated. Figure 17 illustrates the synthesis of complex **1C**.

Yield = 302 mg (0.43 mmol, 43%). ICP-OES (% of metal) – calculated for $[Cu(C_{14}H_{12}O_2N_3)NO_3]$ (379.81 g mol^{-1}): Cu – 16.73; found: Cu – 16.9; TGA: For complex **1C**, it was possible to observe a loss of mass of approximately 77% at around 380 ºC, this loss is related to the organic fraction of the complex. The 23.30% residue is probably copper(II) oxide, corresponding to 18.63% copper. This is in accordance with the structure suggested for the complex and close to that obtained through ICP-OES.

4.3.2 Copper(II) complexes derived from the H_2L2

Attention!

Perchlorate salts of metal complexes containing organic ligands are potentially explosive and must be handled with care. Small quantities must be prepared.

Complexes **2A**, **2B** and **2C** were prepared from **H_2L2**, respectively, with the starting salts: copper(II) chloride dihydrate, copper(II) perchlorate hexahydrate and copper(II) nitrate trihydrate.

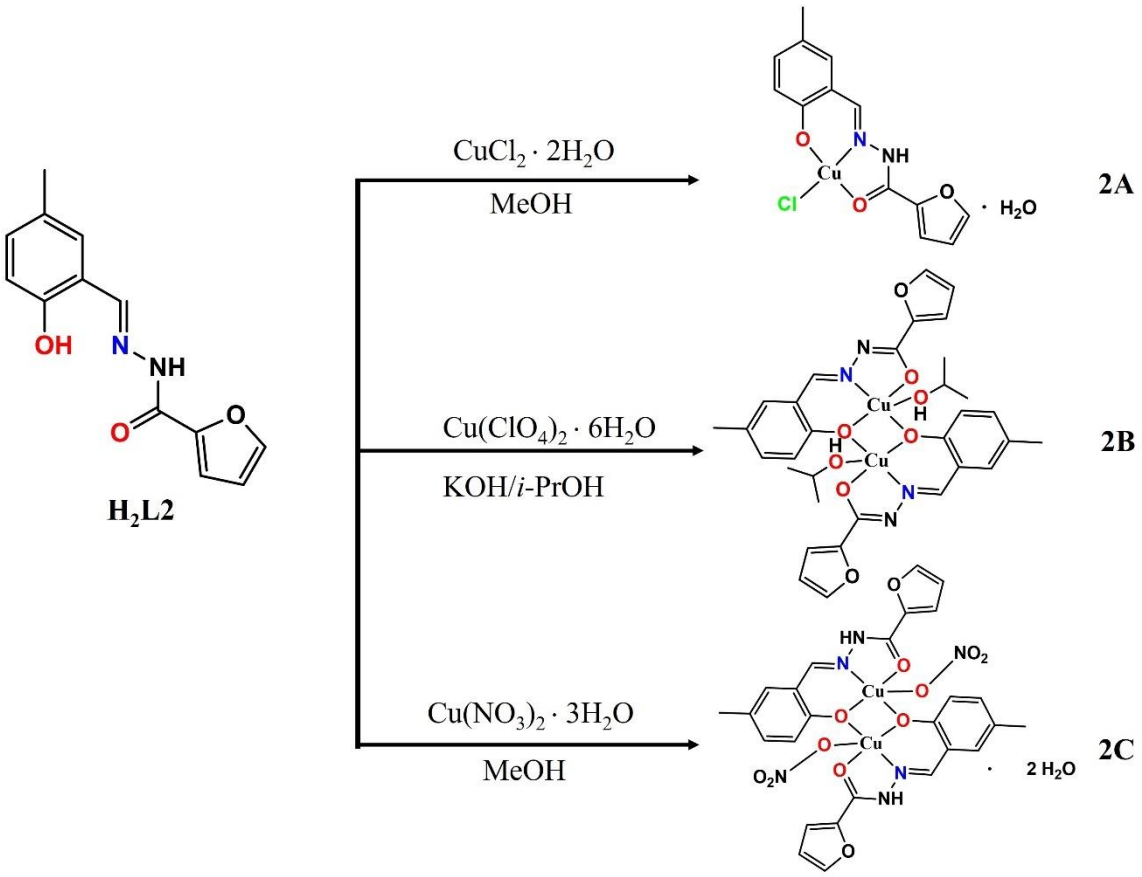

Figure 18. Scheme of the synthesis of complexes **2A, 2B** and **2C.**

Complex **2A** was synthesized by dissolving 0.2 mmol (52 mg) of **H_2L2** in 10 mL of MeOH, then adding 0.2 mmol (34 mg) of copper(II) chloride dihydrate. The reactants were stirred at room temperature for 1 h, affording a dark green solution. After a few days, dark green crystals suitable for XRD analysis were isolated. Figure 18 illustrates the synthesis of complex **2A**.

Yield = 59.0 mg (0.16 mmol, 80%). Elemental analysis (%) – calculated for $[Cu(C_{13}H_{11}O_3N_2)Cl]\cdot H_2O$ (360.28 g mol^{-1}): C – 43.3, H – 3.6, N – 7.8; found: C – 43.6, H – 3.7, N – 7.8. ICP-OES (%) – calculated: Cu – 17.6; found: Cu – 17.9. TGA: a weight loss of approximately 4.2% (calcd 5.0%) between 80 and 150 ºC, roughly agreeing with one hydration water molecule. Molar conductivity in DMF: 25.9 ohm^{-1} cm^2 mol^{-1}, consistent with the presence of a mixture of the neutral complex **2A** and its solvent-substituted derivative [Cu(HL)DMF]Cl (1:1).

Complex **2B** was prepared by dissolving 1.0 mmol (378 mg) of copper(II) perchlorate hexahydrate in 10 mL of methanol, then adding 1.0 mmol (262 mg) of **H_2L2** in 15 mL of MeOH. The reactants were stirred at room temperature for 1 h, resulting in a green solution. After a few days, a green solid was obtained, which, upon recrystallization in *i*-PrOH alkalinized with KOH, gave light green crystals suitable for XRD analysis. Figure 18 illustrates the synthesis of complex **2B**.

Yield = 330 mg (0.45 mmol, 45%). Elemental analysis (%) – calculated for $[Cu_2(C_{26}H_{22}O_6N_4)(C_3H_8O)_2]$ (731.75 g mol^{-1}): C – 52.5, H – 5.0, N – 7.7; found: C – 52.4, H – 4.8, N – 7.8. ICP-OES (%) – calculated: Cu – 17.4; found: Cu – 18.2. TGA: a weight loss of ~15.8% (calcd 16.4%) between 90-140 °C, consistent with the removal of two isopropanol molecules. Molar conductivity in DMF: 2.68 ohm^{-1} cm^2 mol^{-1}, in accordance with a non-electrolyte system.

Complex **2C** was prepared by dissolving 1.0 mmol (242 mg) of copper(II) nitrate trihydrate in 10 mL of MeOH, then adding 1.0 mmol (262 mg) of **H_2L2** in 15 mL of methanol. Reactants were stirred at room temperature for 1 h, resulting in a green solution. After a few days, green crystals suitable for XRD analysis were isolated. Figure 18 illustrates the synthesis of complex **2C**.

Yield = 310 mg (0.4 mmol, 80% for dimer). Elemental analysis (%) – calculated for $[Cu_2(C_{13}H_{11}O_3N_2)_2(NO_3)_2{\cdot}2H_2O]$ (773.60 g mol^{-1}): C – 40.4, H – 3.4, N – 10.9; found: C – 39.9, H – 3.0, N – 10.6. ICP-OES (%) – calculated: Cu – 16.4; found: Cu – 16.2. TGA: It is possible to observe three thermal events before the decomposition of the organic fraction of **2C**. In the region 100-160 ºC, a loss of 5.79% of mass is noted, suggesting that in this range the complex loses water and O_2 molecules derived from the thermal decomposition of the nitrate ion. The solid residue obtained corresponds to 20.8%, considering that this residue is CuO, it is calculated that the amount of copper in the sample is 16.6%. Molar conductivity in DMF: 160.41 ohm^{-1} cm^2 mol^{-1}, in accordance with a 2:1-type electrolyte, $[Cu_2(HL2)_2(DMF)_2](NO_3)_2$ (2:1).

4.3.3 Copper(II) complexes derived from the H_2L3

The complex 3A was prepared from the ligand **H_2L3**, using the starting salts copper(II) chloride dihydrate and copper(II) nitrate trihydrate. It was not possible to obtain a copper(II) complex from the starting salt copper(II) perchlorate hexahydrate.

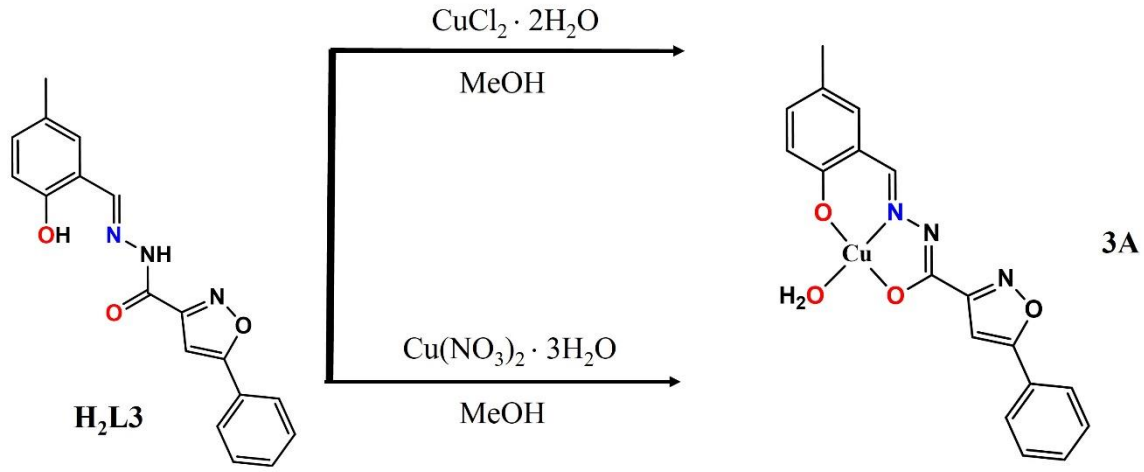

Figure 19. Synthetic scheme for complex **3A.**

The complex **3A** was synthesized *via* two analogous routes using different starting salts. In one route, 0.2 mmol (64.3 mg) of the ligand **H_2L3** was dissolved in 10 mL of MeOH, followed by the addition of 0.2 mmol (34.1 mg) of copper(II) chloride dihydrate. In the other synthetic route, the same quantities of **H_2L3** and methanol were mixed with 0.2 mmol (48.5 mg) of copper(II) nitrate trihydrate. The reactants were stirred at room temperature for 1 h, yielding a green solution. After 3 days, the complex precipitated and was isolated as an amorphous green solid. Figure 19 illustrates the synthesis of complex **3A**.

Yield = 46.0 mg (0.11 mmol, 55%). Elemental analysis (%) – calculated for $[Cu(C_{18}H_{13}O_3N_3)(OH_2)]$ (400.88 g mol^{-1}): ICP-OES (%) – calculated: Cu – 15.8; found: Cu – 16.1. TGA: At approximately 270 ºC, there was a loss of water corresponding to 3.2% (calc. 4.5%). Given the high temperature at which this thermal event occurs, it can be inferred that the water molecule was complexed, supporting the proposed structure. Residual mass corresponds to 20.6% copper(II) oxide, which indicates 16.6% copper, aligning with the percentage obtained from ICP-OES. This consistency suggests that the proposed structure is accurate. Molar conductivity in DMF: 3.2 ohm^{-1} cm^2 mol^{-1}, indicating a non-electrolytic complex, which is consistent with the suggested structure.

4.3.4 Copper(II) complexes derived from the H_2L4

Attention!

Perchlorate salts of metal complexes containing organic ligands are potentially explosive and must be handled with care. Small quantities should be prepared.

Complexes **4A**, **4B** and **4C** were prepared from **H_2L4**, respectively, with the starting salts: copper(II) chloride dihydrate, copper(II) perchlorate hexahydrate and copper(II) nitrate trihydrate.

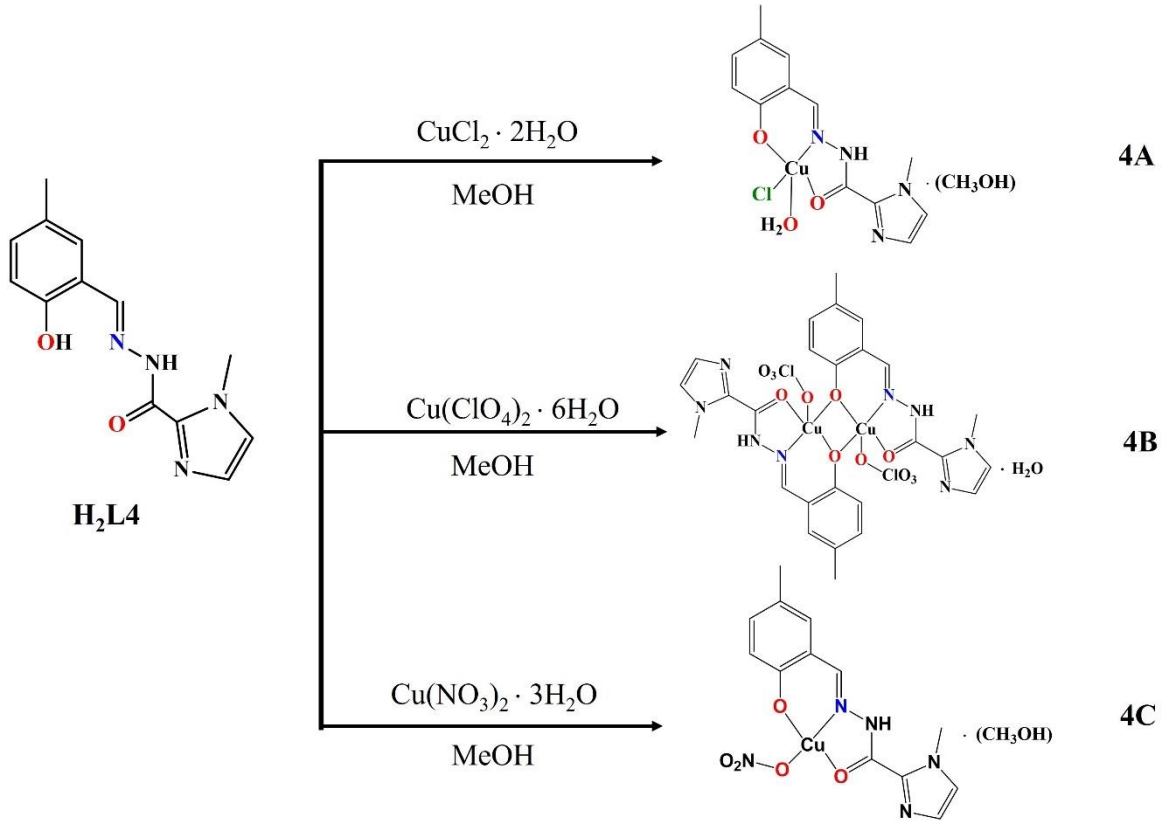

Figure 20. Synthetic scheme for complexes **4A, 4B** and **4C.**

Complex **4A** was synthesized by dissolving 0.2 mmol (51.7 mg) of **H_2L4** in 10 mL of methanol, and then adding 0.2 mmol (34.1 mg) of copper(II) chloride dihydrate. Reactants were stirred at room temperature for 1 h. Along the synthesis, the complex precipitated and was isolated as an amorphous light green solid. Figure 20 illustrates the synthesis of complex **4A**.

Yield = 48.0 mg (0.11 mmol, 59%). ICP-OES (% of metal) – calculated for $[Cu(C_{13}H_{13}O_2N_4)(Cl)(H_2O)]\cdot CH_3OH$ (406.32 g mol^{-1}): Cu – 15.6; found: Cu – 16.4. TGA: between 30-250 ºC there is one thermal event at around 220 ºC, which involves a mass loss of 10.6% (Corresponding to methanol, which is present as a

crystallization solvent, and a coordinated water molecule). The residual mass corresponds to 16.2% of metallic copper, in line with the percentage obtained through ICP-OES, indicating that the suggested structure is coherent. Molar conductivity in DMF: 65.3 ohm^{-1} cm^2 mol^{-1}, in good agreement with the suggested structure since it indicates a 1:1-type electrolyte complex, probably [Cu(HL4)DMF]Cl (1:1).

Complex **4B** was prepared by dissolving 1.0 mmol (375 mg) of copper(II) perchlorate hexahydrate in 10 mL of methanol, then adding 1.0 mmol (258 mg) of **H_2L4** in 15 mL of MeOH. The reactants were stirred at room temperature for 1 h. During the synthesis, the complex precipitated and was isolated as dark green solid. Figure 20 illustrates the synthesis of complex **4B**.

Yield = 532 mg (0.68 mmol, 68%). Elemental analysis (%) – calculated for $[Cu_2(C_{13}H_{13}O_2N_4)_2(ClO_4)_2 \cdot H_2O]$ (858.54 g mol^{-1}): C – 36.4, H – 3.3, N – 13.0; found: C – 36.6, H – 3.1, N – 12.6. ICP-OES (%) – calculated: Cu – 14.8; found: Cu – 14.7. TGA: The experiment was not carried out because the sample contains perchlorate. Molar conductivity in DMF: 144.8 ohm^{-1} cm^2 mol^{-1}, in good accordance with a 1:2-type electrolyte system, $[Cu_2(HL4)_2(DMF)_2](ClO_4)_2$.

Complex **4C** was prepared by dissolving 1.0 mmol (242 mg) of copper(II) nitrate trihydrate in 10 mL of methanol, then adding 1.0 mmol (258 mg) of **H_2L4** in 15 mL of MeOH. The reactants were stirred at room temperature for 1 h. Along the synthesis, the complex precipitated and was isolated as light green solid. Figure 20 illustrates the synthesis of complex **4C**.

Yield = 250 mg (0.60 mmol, 60%). Elemental analysis (%) – calculated for $[Cu(C_{13}H_{13}O_2N_4)NO_3] \cdot CH_3OH$ (414.86 g mol^{-1}): C – 40.5, H – 4.1, N – 16.9; found: C – 40.6, H – 3.5, N – 16.7. ICP-OES (%) – calculated: Cu – 15.3; found: Cu – 15.8. TGA: Three thermal events are observed in the range 30-400 ºC, the first (~30 ºC) with 7.4%, probably related to the loss of methanol and remaining moisture in the solid (7.7%). Another mass loss, of 8.4%, occurs at 170 ºC, and is possibly related to the loss of O_2 resulting from the thermal decomposition of nitrate (calcd. 7.7%). The loss at 310 ºC, of 28.8%, is related to the loss of NO_x from the decomposition of nitrate and part of the organic fraction. According to thermogravimetric analysis, 15.7% of solid residue was obtained for metallic Cu, in line with the percentage calculated from ICP-OES, indicating that the suggested structure is coherent in relation to elements' content. Molar conductivity in DMF:

55.2 ohm^{-1} cm^2 mol^{-1}, consistent with the suggested structure indicating a 1:1-type electrolyte complex: [Cu(HL4)DMF]NO_3 (1:1).

4.4 Physical Characterization Methods

4.4.1 Spectroscopic Studies

Absorption spectra over the wavelength range 800-250 nm were recorded in a Cary 100 (Agilent) spectrophotometer with a temperature-controlled module. Softwares were provided by the manufacturers.

The electronic spectra in the UV-VIS region of the compounds, in the solid state, were obtained by diffuse reflectance in a UV-Vis spectrophotometer, Shimadzu, model 2450, in diffuse reflectance mode (DRIFTS- Diffuse Reflectance Infrared Fourier Transform Spectroscopy) on barium sulfate tablets. barium, in the region of 250-850 nm. The analyzes were carried out in the instruments and research Laboratory of the Inorganic Chemistry Department - IQ-UFRJ in laboratory A628.

The ligands were characterized by 1D nuclear magnetic resonance spectroscopy (NMR). The spectra were recorded on a Bruker Avance III HD-400, Bruker Avance III nanobay 400 or Bruker Avance III nanobay 300 spectrometers and calibrated in reference to the residual peaks for DMSO-d_6 at 2.50 ppm (^{1}H). Coupling constants (*J*) are given in Hz and chemical shifts are reported in ppm. Spectra were processed by using the TopSpin 6.0 and MestReNova softwares.

Mid-infrared (MIR) spectra were acquired on a Perkin-Elmer Spectrum 400 FTIR spectrophotometer, at room temperature, in KBr pellets, with a resolution of 4 cm^{-1} in the 4000-400 cm^{-1} range. The spectra were processed by using the Perkin-Elmer Spectrum 10.03.09 software.

The EPR spectra of the studied complexes were recorded at 300 K (room temperature, solid state) or 77 K (liquid nitrogen, DMF solution) on a CW-Bruker EMX-Plus spectrometer with X-band cavity (9.5 GHz), employing microwave powers of 10 mW. Spectra were fitted through the OriginPro program using an Easyspin45 MATLAB routine. The tests were carried out at CBPF (Brazilian Center for Physical Research).

4.4.2 X-ray crystallography of single crystals

Crystallographic measurements for ligands **H_2L2**, **H_2L4** and complexes **2A** and **2C** were carried out in collaboration with Dr. Renata Diniz, from the Chemistry Department of the Federal University of Minas Gerais, Brazil. The crystallographic measurements for ligands **H_2L1**, **H_2L3** and complex **2B** were carried out in collaboration with Dra. Carolina Bastos Pereira Ligiero, from the Chemistry Institute of the Fluminense Federal University, Brazil. Single crystal data of ligands **H_2L2**, **H_2L4** and complexes **2A** and **2C** were collected with Mo *K*α radiation (λ = 0.71073 Å) in a Bruker D8 Venture diffractometer at 296 K, by the area detector Photon III. They were integrated with a narrow-frame algorithm in SAINT Bruker software, version V8.40B (Bruker, 1999). Absorption was corrected with the multi-scan method in SADABS, version 2016/2 (Krause *et al.*, 2015). The structure was solved using direct methods with ShelxS (Sheldrick, 2008) and refined with full-matrix least-square in ShelxL, (Sheldrick, 2015) both implemented in WinGX (Farrugia, 2012) and ShelxLE (Hubschle *et al.*, 2011) systems. Non-H atoms were located from the electron density map and anisotropically refined. Carbon-bound hydrogen atoms were ridden on their parent C with U_{iso}(H)= 1.2 or 1.5 U_{eq}. Hydrogens bound to oxygen atoms were refined freely and ridden on their parent atoms with U_{iso}(H)= 1.5 U_{eq}. On the other hand, the data regarding ligands **H_2L1**, **H_2L3** and complex **2B** were collected in a Rigaku-Oxford-Diffraction Sinergy equipment also using Mo *K*α radiation, at 293 K. Data collection, cell refinement and data reduction were performed using the CRYSALISPRO (CrysAlisPro, 2015) software. The structure was resolved by direct methods and refined by ShelxL (Sheldrick, 2015) program using OLEX2 (Dolomanov *et al.*, 2009) system, and all non-hydrogen atoms were refined with anisotropic thermal parameters. H atoms connected to carbon atoms were placed in idealized positions and treated by rigid model, with U_{iso}(H) = 1.2 Ueq (aromatic, CH and NH), and U_{iso}(H) = 1.5 U_{eq} (methyl group). Figures and data tables were prepared with Platon (Spek, 2009). Symmetry codes and data deviation were obtained by using the PLATON software. Distance and angles were calculated with MERCURY software.

4.4.3 Elemental Analysis CHNS and ICP-OES

Elemental analysis was performed to determine the CHNS content in ligands and complexes on a Thermo-Electron analyser equipment, model Flash EA 1112. Copper content in complexes was estimated with an inductively coupled plasma optical emission ICP-OES spectrometer Perkin-Elmer Optima 7300 DV. Samples were treated with nitric acid and diluted in water. Measurements were performed with the dye laser pulsed in the 324.7 nm line.

4.4.4 Thermogravimetric Analysis, Melting Point and Molar Conductivity Studies

Thermogravimetric curves were acquired in a Thermogravimetric Analyzer Perkin Elmer, Pyris 1 TGA. TGA scans were performed from 25 to 900 ºC at a heating rate of 10 ºC min^{-1}, under flowing dry air atmosphere. Curve optimization and calculations processed in the Pyris v 8.0.0.0172 software and simultaneous TGA/DTA equipment SHIMADZU model DGT-60, with a heating rate of 10 ºC min^{-1}, in a range of 25 to 900 ºC and carrier gas flow of 50 mL/min. As a reference material, alumina was used in the analyzes in an argon atmosphere in the instruments and research Laboratory of the Inorganic Chemistry Department - IQ-UFRJ, laboratory A628.

Attention: *Although no problems were observed in the syntheses with complexes derived from copper(II) perchlorate hexahydrate, precautions should always be taken when handling perchlorate salts, as they are potentially explosive. For this reason, no complex containing perchlorate in its structure was subjected to thermogravimetric analysis.*

The conductivity measurements were performed at room temperature in an electrical conductivity 650MA Analyser. In order to obtain a final concentration of 1×10^{-3} mol L^{-1}, the copper(II) complexes were dissolved in DMF.

The determinations of the melting points of the organic ligands were performed in a Fisatom model 431 apparatus, in triplicate.

4.4.5 Cyclic Voltammetry

Cyclic voltammetry experiments were performed at room temperature in a BASi Epsilon™ EC potenciostat/galvanostat. Experiments were carried out in DMF solution containing 0.1 mol L^{-1} $TBAPF_6$ as supporting electrolyte, under nitrogen atmosphere and at 25 °C, in a three-electrode cell. A 3.0 mm diameter Glassy Carbon Electrode was employed as the working electrode. Reference was the BASi MF-2052 Ag/AgCl (3 M NaCl) electrode, while the counter-electrode consisted of a platinum wire.

4.4.6 Complexation Studies

The assays involving the complexation study were monitored by UV-Vis under different conditions. All compounds were synthesized in methanol; therefore, complexation studies were carried out with the same solvent and conditions analogous to those of synthesis.

It was not possible to carry out the complexation study for the complexes derived from **H_2L1** due to the low solubility showed by them. The other systems, on the other hand, showed good solubility under the conditions evaluated.

For the complexes derived from **H_2L2**, a methanolic solution of the ligand with a concentration of 2×10^{-5} mol L^{-1} was used with successive additions of 0.05 equivalents of the respective Cu salts [copper(II) chloride dihydrate, copper(II) perchlorate hexahydrate and copper(II) nitrate trihydrate] in methanolic solution of concentration 3×10^{-4} mol L^{-1}. Especially in the case of the complexation study of complex **2B**, the 4×10^{-5} mol L^{-1} ligand solution was diluted with a methanolic sodium hydroxide solution of the same concentration in an attempt to simulate the synthesis conditions in which compound **2B** was obtained. The complexes derived from the **H_2L3** and **H_2L4** ligands had their complexation studies carried out under the same conditions as the complexes derived from the **H_2L2** ligand.

4.4.7 Determination of the Ligand's pK_a

The ligands had their pK_a values determined by UV-Vis measurements in different proportions of organic solvent and water. Solutions of the ligands **H_2L1**, **H_2L2** and **H_2L4** were prepared in a mixture of 10% methanol in deionized water with a concentration of 2×10^{-5} mol L^{-1}. The mixtures underwent pH variations with diluted hydrochloric acid and sodium hydroxide solutions. The **H_2L3** ligand had its pK_a evaluated in 30% DMF:water mixture (concentration: 2×10^{-5} mol L^{-1}).

4.4.8 Interaction Studies with HSA

Experimental interaction between HSA and the ligands **H_2L2** and **H_2L4** and their respective complexes were confirmed by UV-Vis spectroscopy (Cary 100). Solutions of the compounds were prepared at 2 x 10^{-5} mol L^{-1}. **H_2L2** and **2A** were dissolved in 1% MeOH/PBS (5 x 10^{-2} mol L^{-1}, pH 7.4), while the complexes **2B** and **2C**, in 2% MeOH/PBS. On the other hand, HSA stock solution (3 x 10^{-4} mol L^{-1}) was prepared in pure PBS. 3.0 mL of compound (ligand or complex) solution were placed in the cuvette and equal amounts (10 μL) of HSA were added at each titration point, followed by the obtainment of an UV-Vis spectrum. All measurements were carried out at room temperature (25 ºC).

4.4.9 Computational Methods

The computational calculations involving the ligand **H_2L2** and complexes **2A** and **2B** were conducted in collaboration with Prof. Dr. Nelson H. Morgon, from the Chemistry Institute, Campinas State University, Campinas, Brazil. The molecular geometries of the ligand, complexes **2A** and **2B** were fully optimized both in the gas phase and for a water solution, without symmetry constraints, using density functional theory (DFT). B3LYP exchange-correlation functional, along with the Pople 6-311++G(2d,p) basis set, was employed. Solvent effects were described implicitly using the SMD model. The D3 version of Grimme's dispersion corrections with Becke-Johnson damping was added. Methodology, in this case, referred to as B3LYP-GD3(BJ)/6-311++G(2d,p)/SMD(Water), calculation of UHF open-layer configuration. Energy minima were characterized by calculating harmonic vibrational frequencies, and corresponding infrared spectra were obtained at the previously described calculation level. The UV-Vis electronic spectra, in the previously obtained molecular geometries for the water

medium, were calculated through the TD-PBE0/6-311++G(3df,2p)-GD3(BJ)/SMD(Water) theory, considering 30 electronic states. All the electronic and molecular calculations were performed using the Gaussian16 program Frisch & Clemente .

4.4.10 Docking Studies on HSA

Molecular docking studies were conducted in collaboration with Dr. Maurício Yoguim and Prof. Dr. Aguinaldo de Souza (Department of Chemistry, Sao Paulo State University (UNESP), Bauru, Brazil). Initial molecular docking investigations focused on the three drug interaction sites (DS), located in regions IIA (DS1), IIIA (DS2), and IB (DS3). Additionally, studies were extended to the FA6 region, a site associated with fatty acids.

The crystallographic structures chosen for this study are similar to those present in the experimental conditions, i.e., HSA not containing fatty acids. All selections were obtained from the Protein Database (PDB). Thus, PDB 2bxe (Ghuman *et al.*, 2005) presents the structure of diflunisal (a nonsteroidal anti-inflammatory drug) in the DS1, DS2 and FA6 sites, with a resolution of 2.95 Å. The second structure chosen for this study was PDB 2bx8 (Ghuman *et al.*, 2005) which has the nonsteroidal anti-inflammatory drug azapropazone at DS1 and DS3 sites, with a resolution of 2.70 Å. The third selected structure was PDB 2vue, (Zunszain *et al.*, 2008) which shows a bilirubin molecule in the DS3 site and has a resolution of 2.42 Å.

The structures of **H_2L2** and its complexes **2A and 2B** were obtained through the GaussView 6 software (Dennington *et al.*, 2019) and analysed in the Discovery Studio Visualizer 2021 program (Systèmes, 2021) to verify if the input reading was correct, and then proceeded to the molecular docking studies.

Molecular docking was performed using GOLD 2022.3.0 software. This program executes ten runs using the chemscore_kinase calculation parameters, with a Goldscore scoring function based on **Equation 1**, where S (hb_ext) represents the energy of H bonds in the binding protein; S (vdw_ext), the energy of van der Waals protein-ligand or protein-complex interactions; and S (int) is a penalty for not taking into account the internal interactions of the ligand or coordination compound (Johnson *et al.*, 2010; Kozuch & Martin, 2013). In addition to determining the conditions of the function parameters, it is possible to

vary the study radius of the ligand or complex and also, when possible, change conditions such as protonation state, rotation or flexibilization of the amino acids involved in the interactions.

$$\text{Fit function} = \text{S (hb\_ext)} + 1.3750 \text{ x S (vdw\_ext)} + \text{S (int)}$$

(**Equation 1**)

Results were analyzed in the software Discovery Studio Visualizer 2021 software, (Systèmes, 2021) being examination initially performed visually in relation to the poses obtained in the calculations. Then, they were correlated with the energetic values obtained for the different conformers. After that, in the same software, the possible interactions of a chosen conformer in the protein region were determined.

4.4.11 Antiproliferative Activity Studies

Cytotoxicity studies were conducted in collaboration with the Prof. Dr. Ignacio E. León's research group at the CEQUINOR, Faculty of Exact Sciences, National University of La Plata, Argentina.

Cytotoxicity was assessed using the MTT assay for the ligand **H_2L2** and the complexes **2A**, **2B**, and **2C** in MDA-MB-231 cells (triple-negative breast adenocarcinoma). The clinically established agent cisplatin (CDDP) was used as a reference for antiproliferative activity, along with the clinical drug doxorubicin.

5. Results and discussion

5.1 Ligands

5.1.1 ^{1}H NMR

Ligands were firstly characterized by ^{1}H NMR spectroscopy in DMSO-d_6 solution. Hydrazones are a highly versatile group, finding applications in diverse fields, and exhibiting rich chemistry. Literature reports that hydrazones can exist in solution as a mixture of (*E*)/(*Z*) stereoisomers relative to the azomethine group, *anti*/*syn* conformations relative to the amide bond and, also associated with this latter group, undergo tautomerization, forming dynamic amido-iminol equilibria, as depicted in the Figure 21 (R stands for a generic substituent):

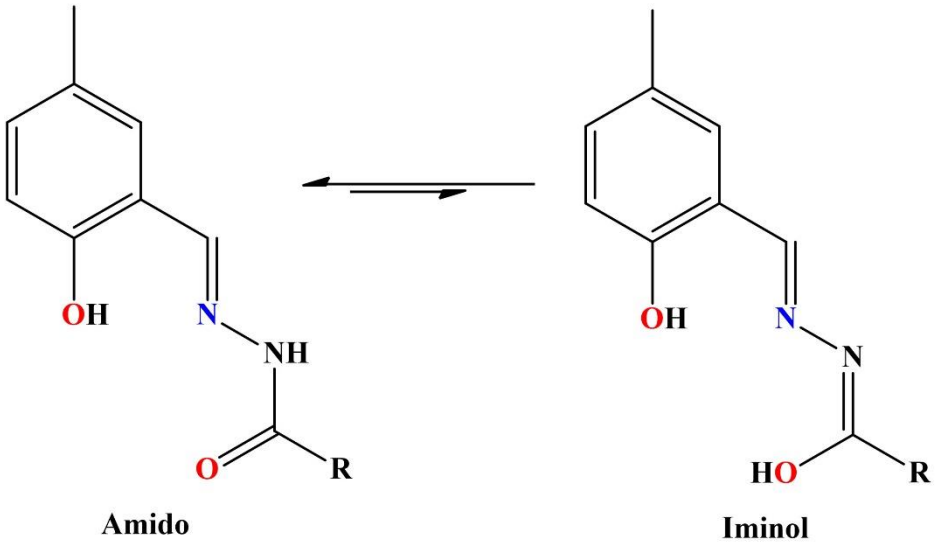

Figure 21. Scheme of the amido-iminol tautomerism present in the synthesized ligands.

In addition to the tautomers formed, and as stated above, the formation of (*E*) and (*Z*) stereoisomers can occur due to restricted rotation around the C=N bond. However, for the ligands studied, only the (*E*) isomer was obtained. In this configuration, the azomethine nitrogen can form an intramolecular hydrogen bond with the phenolic hydroxyl in the *para* position, thereby enhancing the stability of the (*E*) isomer compared to the (*Z*) isomer (Figure 22).

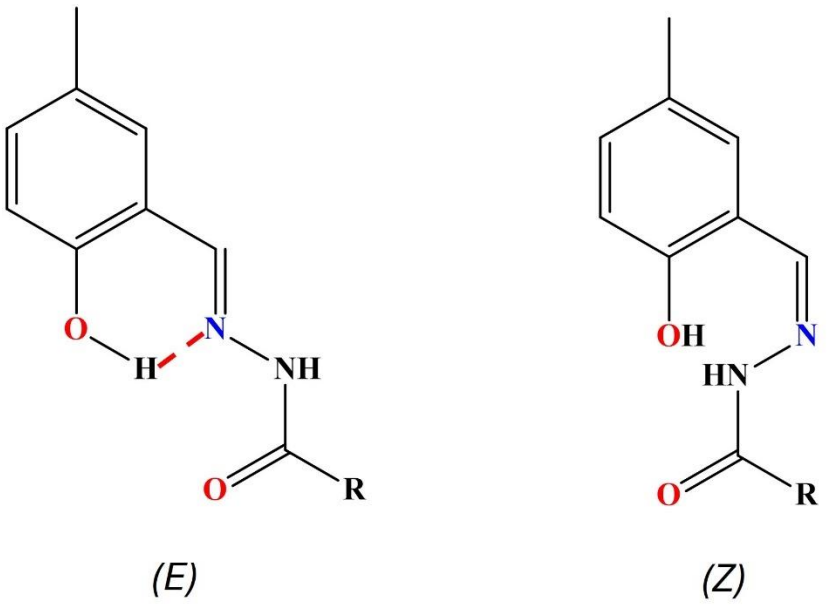

Figure 22. General structure of the stereoisomers *(E)* and *(Z)*, with the possibility of hydrogen bonding, for the synthesized ligands.

Figures 23-26 correspond to the ^{1}H NMR spectra of the ligands obtained. To assign their chemical shifts, the starting compounds already widely reported in the literature as well as the **H_2L2** ligand, the first to be published by us of this series, were employed (Broussy *et al.*, 2003; Eid *et al.*, 2021; Liang *et al.*, 2012; Manonmani *et al.*, 2000; Moura *et al.*, 2023; Yogeeswari *et al.*, 2011). The numbering of the hydrogen atoms does not correspond exactly to the numbering designated from the X-ray diffraction analysis.

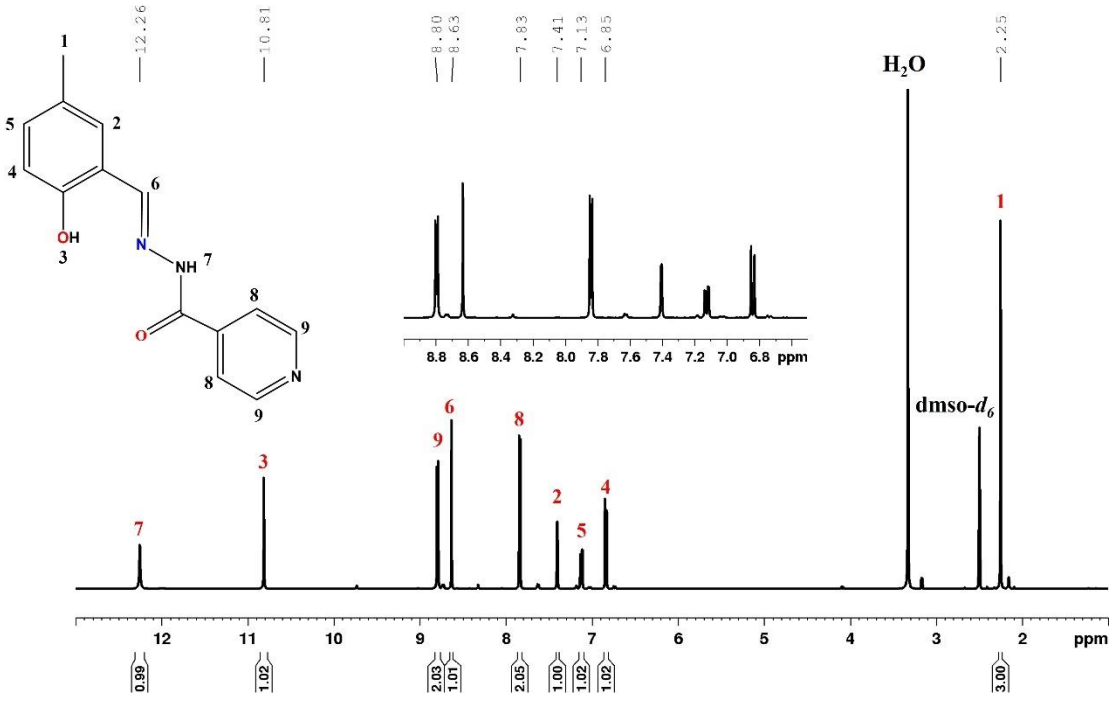

Figure 23. ^{1}H NMR spectra (400 MHz) of **H_2L1** in DMSO−d_6 at room temperature.

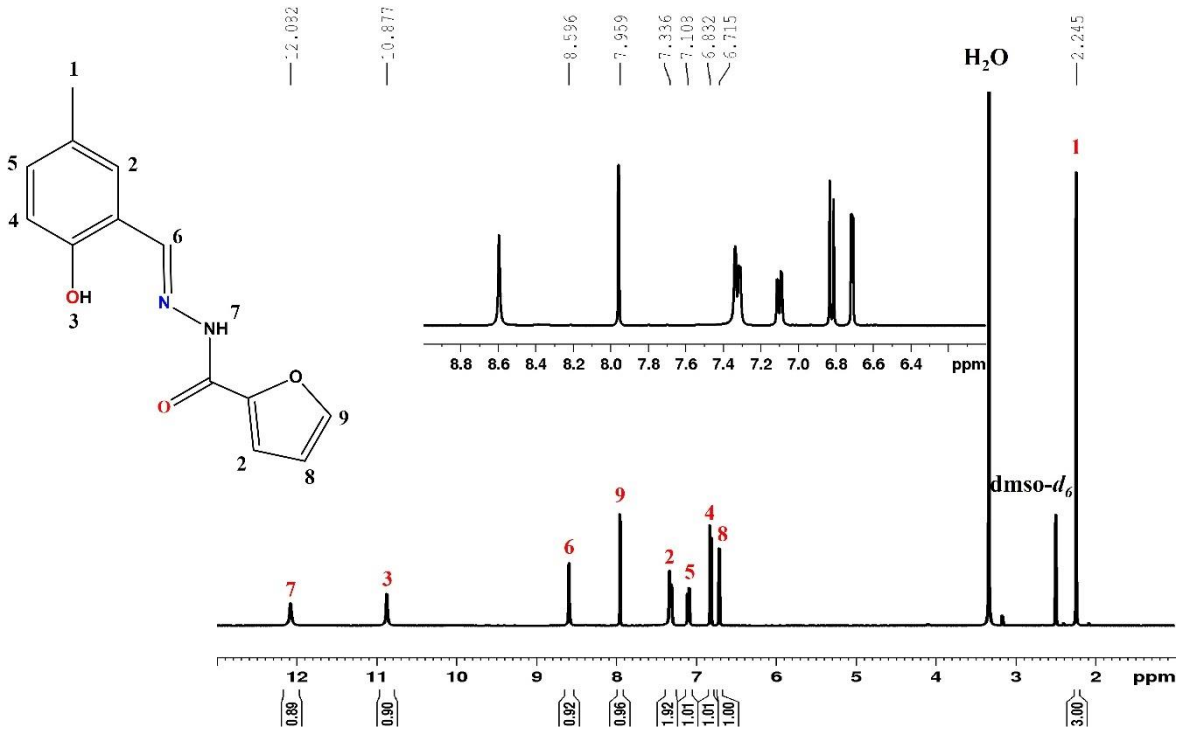

Figure 24. [1]H NMR spectra (400 MHz) of **H_2L2** in DMSO−d_6 at room temperature.

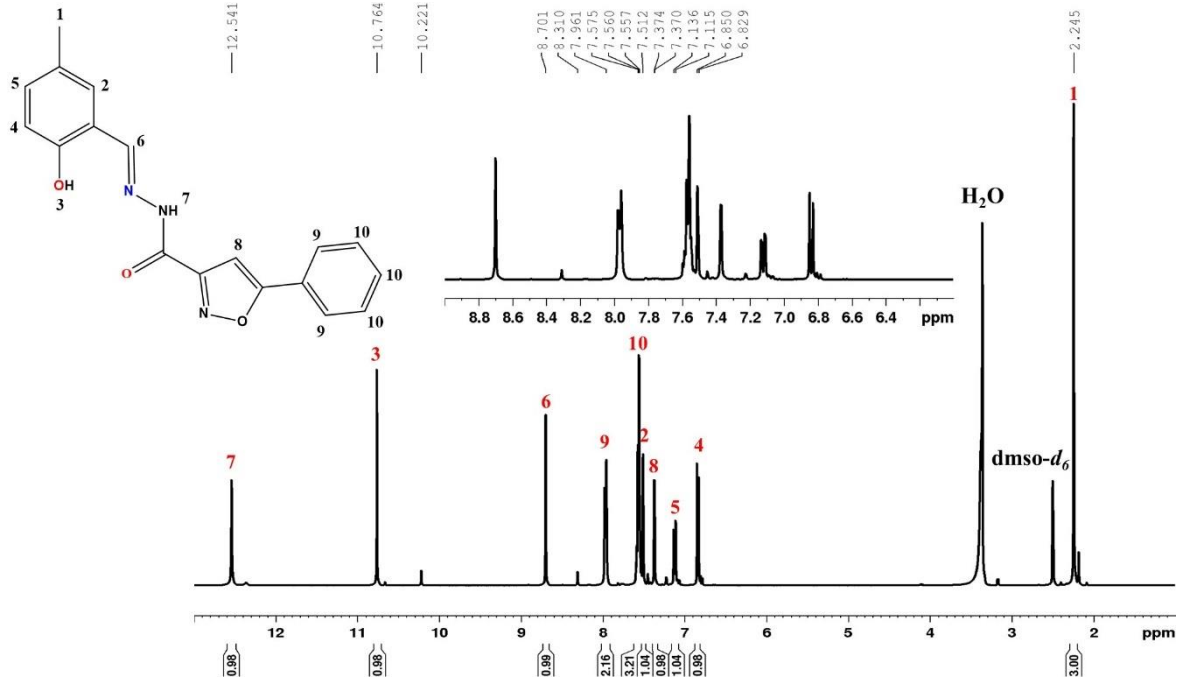

Figure 25. [1]H NMR spectra (400 MHz) of **H_2L3** in DMSO−d_6 at room temperature.

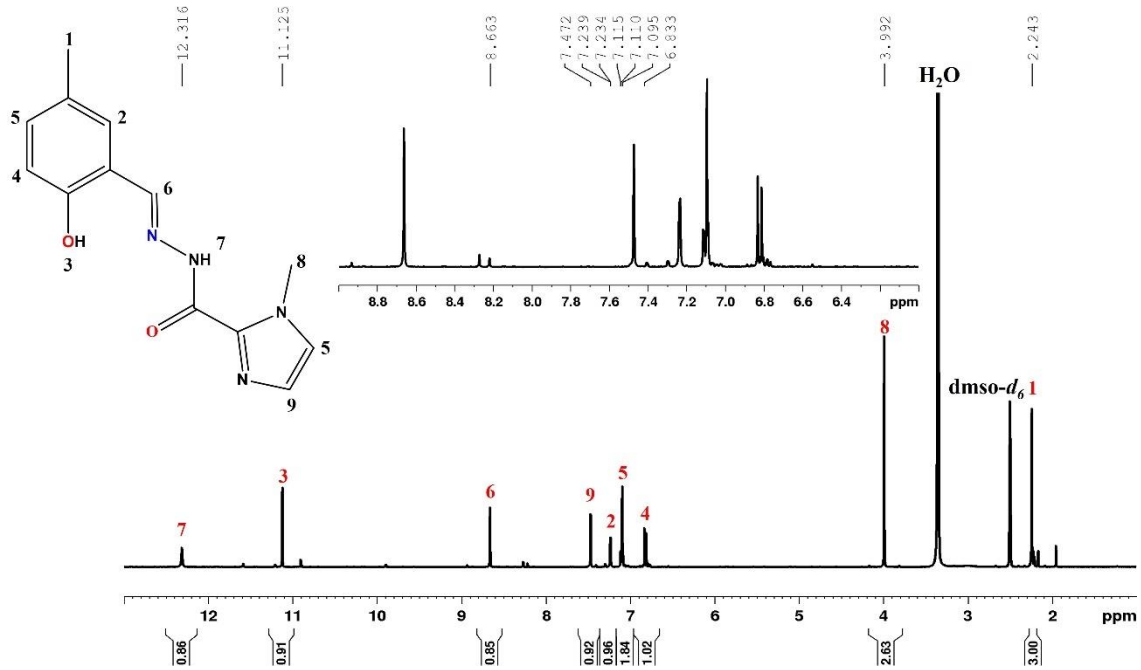

Figure 26. [1]H NMR spectra (400 MHz) of **H_2L4** in DMSO−d_6 at room temperature.

The [1]H NMR spectra obtained for the ligands confirm that the compounds predominantly exist in the amido tautomeric form, as evidenced by the observed chemical shift of the HN−C=O hydrogen. Table 2 correlates chemical shift values found with their respective assignments, along with the integrated areas obtained.

Table 2. [1]H (400 MHz) data for compounds **H_2L1, H_2L2, H_2L3** and **H_2L4** in DMSO-d_6 at room temperature.

H	**H_2L1** ***δ (ppm)***	**H_2L2** ***δ (ppm)***	**H_2L3** ***δ (ppm)***	**H_2L4** ***δ (ppm)***
1	2.25 (*s*, 3H)	2.24 (*s*, 3H)	2.24 (*s*, 3H)	2.24 (*s*, 3H)
2	7.40 (*d*,1H)	7.34 (*bs*, 2H)	6.83 (*d*, 1H)	7.23 (*d*, 1H)
3	10.81 (*s*, 1H)	10.88 (*s*, 1H)	10.76 (*s*, 1H)	11.12 (*s*, 1H)
4	6.85 (*d*, 1H)	6.83 (*d*, 1H)	6.85 (*d*, 1H)	6.83 (*d*, 1H)
5	7.13 (*dd*,1H)	7.10 (*dd*, 1H)	7.51 (*dd*, 1H)	7.11 (*dd*, 2H)
6	8.63 (*s*, 1H)	8.60 (*s*, 1H)	8.70 (*s*, 1H)	8.66 (*s*, 1H)
7	12.26 (*s*, 1H)	12.08 (*s*, 1H)	12.54 (*s*, 1H)	12.31 (*s*, 1H)
8	7.83 (*dd*, 2H)	6.71 (*dd*, 1H)	7.14 (*dd*, 1H)	3.99 (*s*, 3H)
9	8.80 (*dd*, 2H)	7.96 (*dd*, 1H)	7.98 (*dd*, 2H)	7.45 (*dd*, 1H)
10	----	----	7.57 (*dd*, 3H)	----

s: singlet, *d*: doublet, *dd*: doublet of doublets, *bs*: broad singlet

5.1.2 CHN Elemental Analysis

Elemental analyses were carried out with crystalline samples of the ligands isolated. The results obtained are listed in Table 3.

Table 3. Calculated and experimental elemental analyses of ligands **H_2L1, H_2L2, H_2L3** and **H_2L4.**

Ligands	**%C**		**%H**		**%N**	
	calculated	found	calculated	found	calculated	found
H_2L1	65.87	65.06	5.13	5.03	16.46	16.61
H_2L2	59.54	58.84	5.38	5.26	10.68	10.57
H_2L3	67.28	65.94	4.71	4.59	13.08	13.08
H_2L4	60.40	60.60	5.50	5.30	21.70	21.70

5.1.3 Melting Points

Melting points of the ligands were determined using crystalline samples, and there was no degradation of any of them. For **H_2L2**, it was possible to observe a slight change in the color of the ligand at around 100-110 ºC, possibly due to the loss of the hydration water molecule present in the structure. Table 4 displays the melting points obtained for the ligands studied.

Table 4. Melting points determined for the ligands studied.

Ligands	**H_2L1**	**H_2L2**	**H_2L3**	**H_2L4**
Melting Point (ºC)	209 ± 1	150 ± 2	190 ± 2	189 ± 2

5.1.4 Crystal Structure of Ligands by Single Crystal XRD

The crystallographic experimental details for the studied ligands, as well as the conclusions that can be drawn from their respective structures, are provided below:

Table 5. Experimental crystallographic details for ligands **H_2L1, H_2L2, H_2L3** and **H_2L4.**

Crystal	**H_2L1**	**H_2L2**	**H_2L3**	**H_2L4**
Chemical formula	$C_{14}H_{13}N_3O_2$	$C_{13}H_{14}O_4N_2$	$C_{18}H_{15}N_3O_3$	$C_{13}H_{14}O_2N_4$
***M*r (g mol^{-1})**	226.27	262.26	321.33	258.28
Crystal system, space group	Monoclinic, $P2_1/n$	Orthorhombic, $P2_12_12_1$	Monoclinic, $P2_1/n$	Monoclinic, $P2_1/c$
Temperature (K)	293	296	293	293
***a*, *b*, *c* (Å)**	8.5360(19), 16.005(3), 9.4686(19)	4.9316(2), 12.4514(5), 20.7391(9)	15.8412(7) 4.6432(2) 16.2474(7)	11.5982(6) 13.9605(7) 16.3869(7)
***V* (Å^3)**	1261.6(4)	1273.49(9)	1558.50(11)	2648.3(2)
Z	4	4	4	8
Radiation type	Mo *K*α	Mo *K*α	Mo *K*α	Mo *K*α
μ (mm^{-1})	0.622	0.103	0.096	0.091
Crystal size (mm)	0.20 × 0.24 × 0.68	0.72 × 0.14 × 0.12	0.10 × 0.20 × 0.66	0.47 × 0.38 × 0.17
R_{int}	0.050	0.043	0.135	0.0598
$R[F^2 > 2\sigma(F^2)]$, $wR(F^2)$, S	0.0494, 0.1369, 1.07	0.040, 0.126, 1.09	0.0650, 0.105, 1.04	0.0576, 0.1217, 1.016
Nº. of parameters	175	231	225	350
Δρmax, Δρmin (e Å^{-3})	-0.15, 0.20	0.147, –0.150	-0.25, 0.16	0.166, -0.170

Single crystals of the ligands suitable for X-ray diffraction were obtained. All of them were obtained in the (*E*)-isomeric form, displaying an *antiperiplanar* configuration stabilized by an intramolecular hydrogen bond between the phenolic group and the azomethine nitrogen, –HC=N–. The bond lengths and angles data obtained for the ligands can be found in the appendix (Appendix Table 1).

The ligand **H_2L1** crystallizes in a monoclinic system, space group $P2_1/n$, with four ligands *per* unit cell. The structure of **H_2L1** is depicted in Figure 27. It was obtained in its anhydrous state. An intramolecular hydrogen bond is observed between the phenolic hydrogen (O1−H) and the nitrogen (N1) of the azomethine group (HC=N). Figure 28 illustrates the intermolecular H bonds in the network of **H_2L1** and Table 6 exhibit H-bonding parameter. Each molecule can form two intermolecular hydrogen bonds, involving the hydrogen attached to N2, the amide nitrogen (HNCO), and pyridine nitrogen N3 of a neighboring molecule as the hydrogen acceptor, resulting in a zigzag chain that runs parallel to the *b* crystallographic axis.

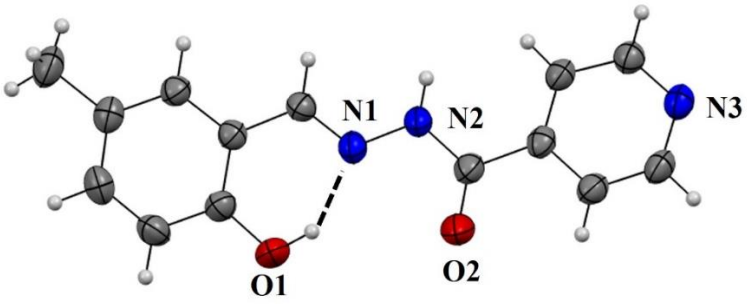

Figure 27. Crystal structure representation of **H_2L1.** For the sake of simplicity, only the atoms more important for the discussion are labeled. Ellipsoids drawn at the 50% probability level.

Table 6. H-bonding geometric parameters for **H_2L1.**

H_2L1				
D−H···A	**D−H (Å)**	**H···A (Å)**	**D···A (Å)**	**D−H···A (º)**
O1−H1···N1[a]	0.87(2)	1.826(18)	2.5852(19)	111.3(14)
N2−H2···N3[b]	0.86	2.1900	3.023(2)	165.00

Symmetry code: a: x,y,z; b: -1/2+x,1.5-y,-1/2+z

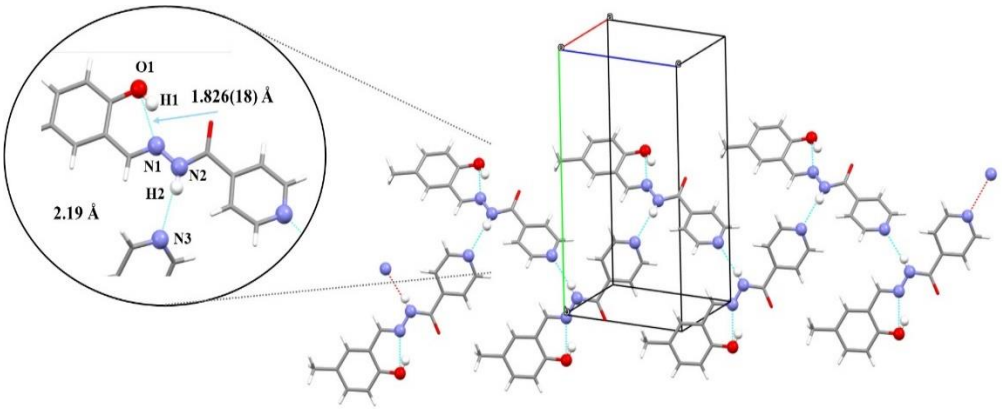

Figure 28. Hydrogen bond interactions in the crystal networks of compound **H_2L1.**

The *N*-acylhydrazone **H_2L2** crystallizes in the orthorhombic system, space group $P2_12_12_1$, with four molecules in the unit cell. The corresponding ORTEP structure view is shown in Figure 29.

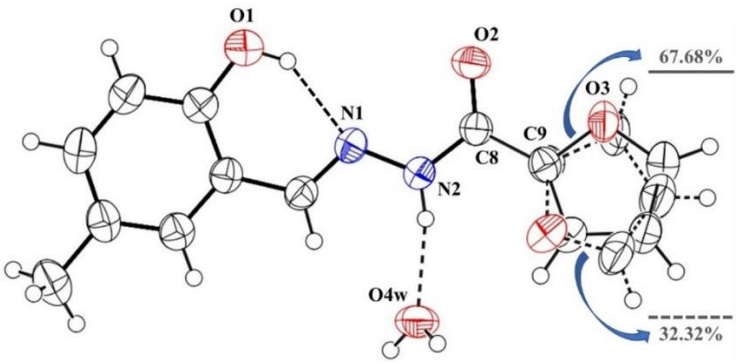

Figure 29. Crystal structure representation of **H_2L2.** For clarity, only the atoms more important for the discussion are labeled. Ellipsoids drawn at the 50% probability level.

Each molecule contains one hydration water molecule, with water oxygen engaged in intermolecular H bonding with the hydrogen of the N−H bond in the hydrazone. A positional disorder in the furan ring is observed, resulting from free rotation around the C8−C9 bond, a characteristic previously noted by our research group in a copper complex of a hydrazonic ligand containing the furan ring as well (Cukierman *et al.*, 2023). The hydrogen bonds present in the **H_2L2** ligand occur between the crystallization water molecules (Figure 30). These bonds connect to another **H_2L2** molecule, forming a chain linkage in a lamellar arrangement that extends parallel along the crystallographic *a*-*b* axis. The hydrazone oxygen (O2) forms two bifurcated hydrogen bonds with different water molecules (H4A and H4B from distinct water molecules), while the hydrogen atom opposite the furan oxygen (O3B) engages in conventional hydrogen bonds with water molecules, the table 7 exhibit H-bonding parameters. The major fraction (67.7%) exhibits the oxygen O3 pointing in the same direction as O2, while the minor component (32.3%) shows O3 pointing in the opposite direction. In both cases, the ring is nearly coplanar with the molecular structure.

Table 7. H-bonding geometric parameters for **H_2L2.**

H_2L2				
D−H···A	**D−H (Å)**	**H···A (Å)**	**D···A (Å)**	**D−H···A (º)**
N2−H2A···O4[a]	0.86(3)	1.94(3)	2.786(3)	167.26(4)
O4−H4A···O2[b]	0.835(4)	2.041(4)	2.86(3)	166.72(4)
O4−H4B···O2[b]	0.87(4)	1.93(4)	2.789(3)	168.09(4)
O1−H1···N1[a]	0.85(4)	1.99(4)	2.722(3)	143.88(3)
O3B−H10A···O4[a]	0.86	2.93(1)	2.93(1)	50.81

Symmetry code: a: x,y,z; b: -x,1/2+y,1/2-z

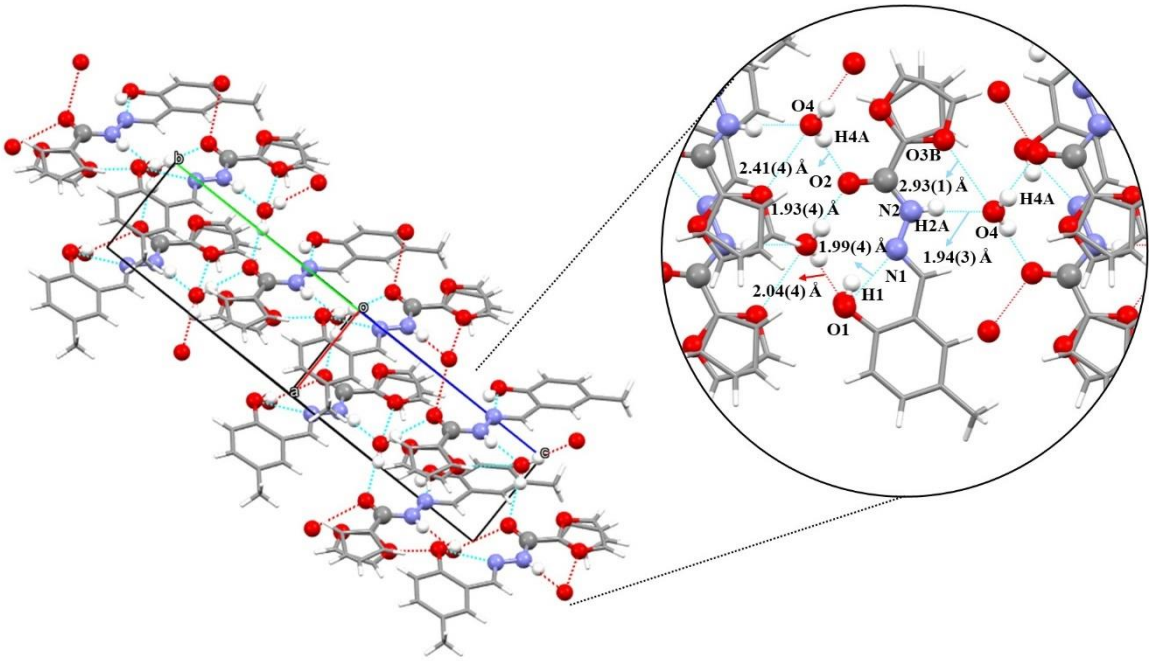

Figure 30. Hydrogen bond interactions in the crystal networks of compound **H_2L2.**

The ligand **H_2L3**, was crystallizes in the monoclinic system, space group $P2_1/n$, with four ligand molecules *per* unit cell. The crystal structure of this compound is shown in Figure 31.

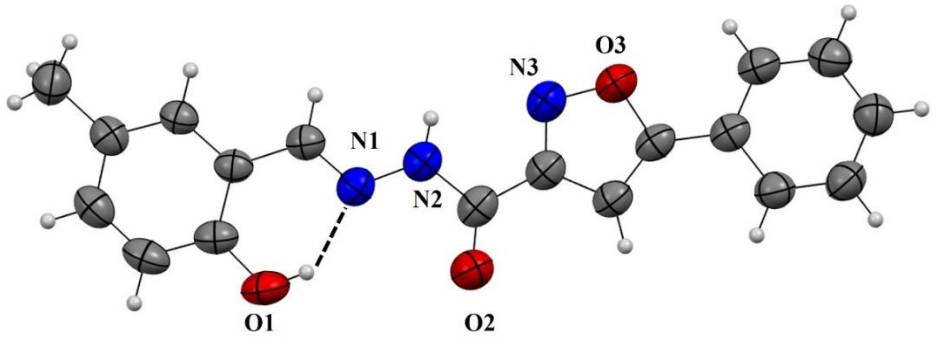

Figure 31. Crystal structure representation of **H_2L3.** For the sake of simplicity, only the atoms more important for the discussion are labeled. Ellipsoids drawn at the 50% probability level.

H_2L3 was obtained in its anhydrous form. The intramolecular interaction between the phenolic hydrogen (O1−H) and the nitrogen (N1) of the azomethine group (HC=N), with a distance of 2.610(3) Å (Figure 31). π-π stacking interactions could not be observed; however, ligand **H_2L3** exhibits non-conventional H bonds: O2···H10, where H10 is bonded to the isoxazole carbon C10, with a distance of 2.560(4) Å and a symmetry code of [–*x*,1–*y*,–*z*]; O1···H14, where H14 is bonded to the phenyl carbon C14, with a distance of 2.480(4) Å and a symmetry code of [–*x*,1–*y*,–*z*]; and an non-conventional intramolecular hydrogen bond between O3···H17, where H17 is bonded to the phenyl carbon C17, with a distance of 2.460(4) Å, table 8 exhibit H-bonding parameters.

Table 8. H-bonding geometric parameters for **H_2L3.**

H_2L3				
D−H···A	**D−H (Å)**	**H···A (Å)**	**D···A (Å)**	**D−H···A (º)**
O1−H1···N1[a]	0.84(3)	1.91(3)	2.610(3)	141(3)
N2−H2···N3[a]	0.846(19)	2.23(2)	2.642(3)	109.7(17)
C10−H10···O2[b]	0.93(1)	2.5600(4)	3.451(3)	160(4)
C14−H14···O1[b]	0.93(1)	2.4800(4)	3.288(3)	145(3)
C17−H17···O3[a]	0.93(1)	2.4600(4)	2.776(3)	100(2)

Symmetry code: a: x,y,z; b: -x,1-y,-z

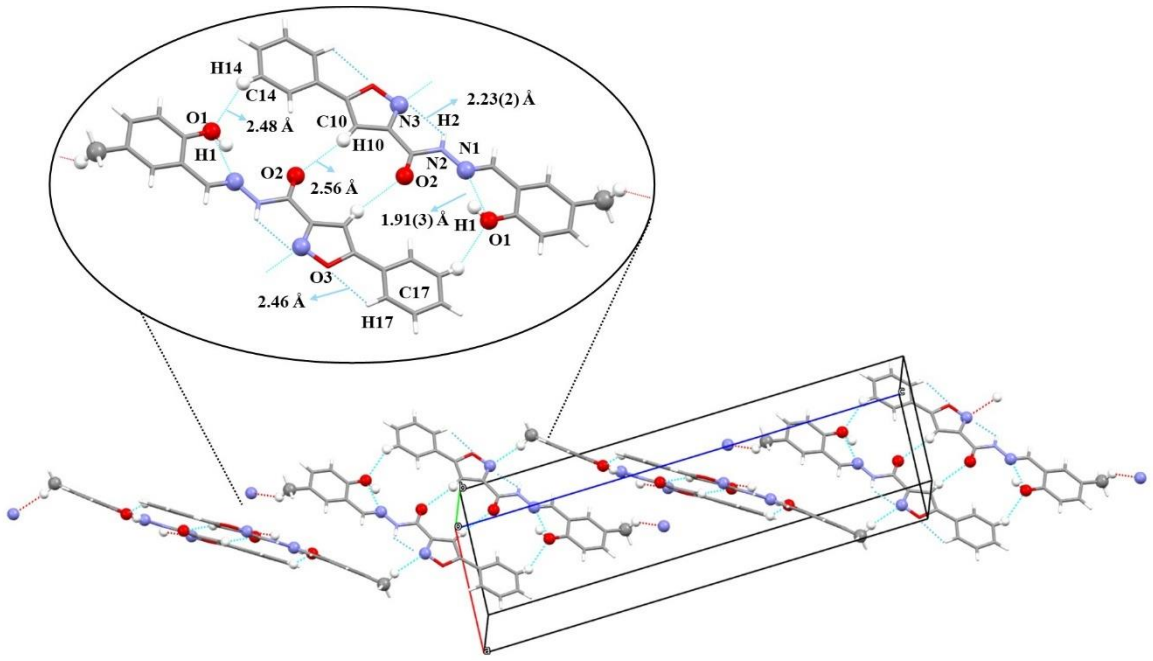

Figure 32. Hydrogen bond interactions in the crystal networks of compound **H_2L3.**

The ligand **H_2L4** crystallizes in the monoclinic system, space group $P2_1/c$, with eight ligand units arranged into dimers constituted by independent molecules *via* hydrogen bonding *per* cell. However, just one **H_2L4** molecular unit is depicted in Figure 33. **H_2L4** is anhydrous, as **H_2L1** and **H_2L3**.

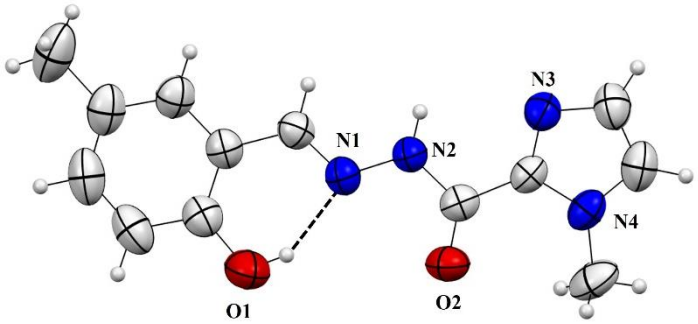

Figure 33. Crystal structure representation of **H_2L4.** For the sake of simplicity, only the atoms more important for the discussion are labeled. Ellipsoids drawn at the 50% probability level.

In addition to the observed intramolecular hydrogen bond, intermolecular cross H bonds are formed between the imidazole nitrogen N3 (H-acceptor) and the amide nitrogen N2 (H-donor), as in Figure 34A and 35. π-π stacking interactions were also observed between **H_2L4** molecules with a centroid of 8.343(2) Å, with the main difference between them being the torsion angle between the phenol and imidazole rings: 5.65° for the red molecules and 13.29° for the green ones (Figure 34B). Table 9 exhibit H-bonding parameters.

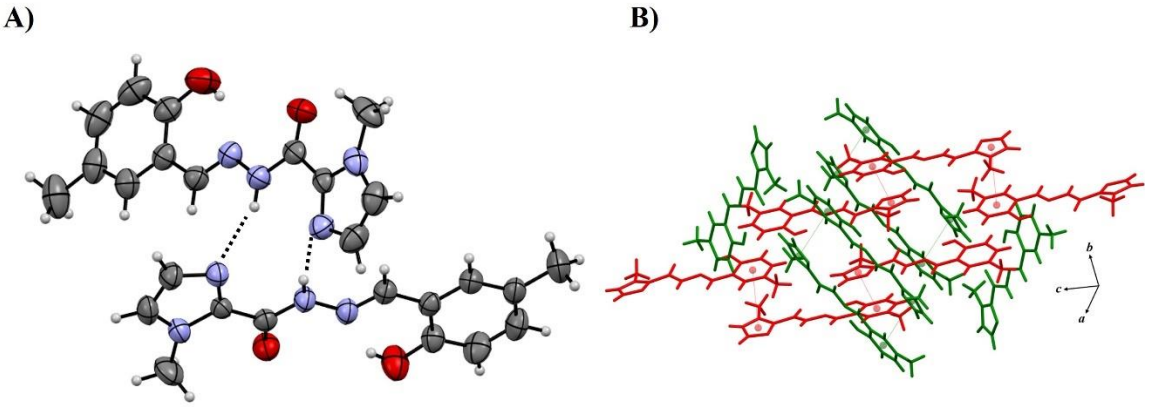

Figure 34. A) Simplified hydrogen bond interactions in **H_2L4. B)** π- π stacking interactions in **H_2L4.**

Table 9. H-bonding geometric parameters for **H_2L4.**

H_2L4				
D−H···A	**D−H (Å)**	**H···A (Å)**	**D···A (Å)**	**D−H···A (º)**
O1−H1···N1[a]	0.82(2)	1.91(3)	2.626(2)	146.0(2)
O3−H3···N5[a]	0.82(2)	1.90(2)	2.614(2)	145.0(2)
N2−H2···N7[a]	0.86(2)	2.20(2)	3.018(2)	159.0(2)
C14−H14···O1[a]	0.86(3)	2.20(2)	3.036(2)	164.0(4)

Symmetry code: a: x,y,z;

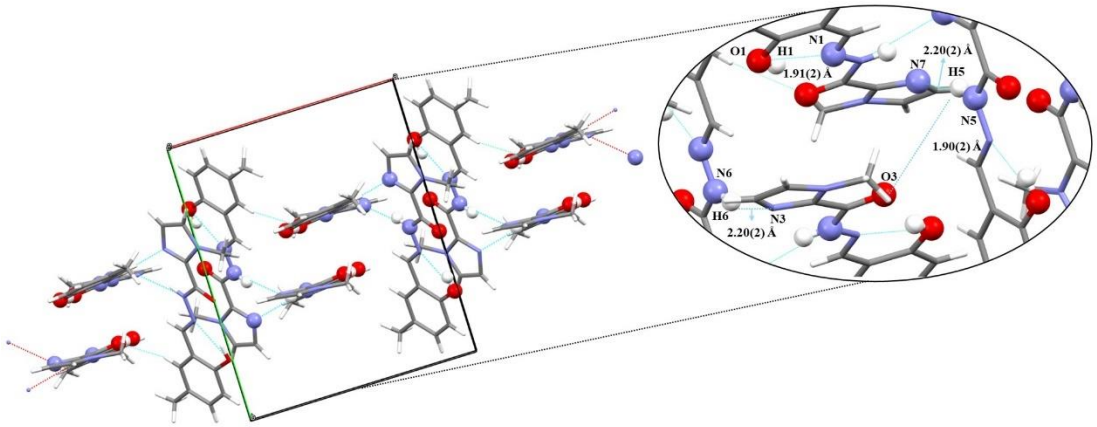

Figure 35. Hydrogen bond interactions in the crystal networks of compound **H_2L4.**

5.1.5 Determination of the Ligands' pK_a by Spectrophotometric Titration

All the synthesized *N*-acylhydrazonic ligands possess two common acidic sites: the phenolic O−H group and the N−H group of the amide group. Therefore, it is important to determine the pH range at which the ligand is predominantly deprotonated, as the ligand will act as a Lewis base both in the protonation and the complexation processes. It will coordinate the metal, which acts as a Lewis acid. The more deprotonated the ligand is, the more effective the complexation will be.

Although there are two acidic sites in the ligands considered, it was not feasible to titrate the two ionizable hydrogens separately. This is due to phenols having pK_a values around 8-10 and *N*-acylhydrazones having nearby pK_a values, of around 10-11 (Vitório *et al.*, 2015; Wu *et al.*, 2007). Therefore, both ionizable protons were titrated together, resulting in the determination of an apparent pK_a.

The pK_as of these *N*-acylhydrazones were obtained *via* spectrophotometric titration. Solutions containing 5% MeOH were prepared for ligands **H_2L1**, **H_2L2**, and **H_2L4** in ultrapure water, with a concentration of 2×10^{-5} mol L^{-1}. For **H_2L3**,

due to its lower water solubility, the pK_a was evaluated in a solution containing 30% DMF in ultrapure water, also at of 2×10^{-5} mol L^{-1}. Solutions 0.1 mol L^{-1} and 0.01 mol L^{-1} of HCl and NaOH were prepared for pH adjustments.

As the pH values increased, an intensification in the absorbance at around 400 nm was observed. This band corresponds to the deprotonation of the phenol group to phenolate, promoting a charge transfer from the basic oxygenated site to the ring, enhancing conjugation and therefore increasing absorbance. Moreover, the N−H group of the hydrazone moiety can also undergo deprotonation, further contributing to electronic density delocalization, which similarly contributes to the absorbance at around 400 nm for the different ligands evaluated. This band was then used to monitor ligand deprotonation and obtain the apparent pK_a values (as shown in Figures 36-39, in which the apparent pK_a values are denoted as pK_a').

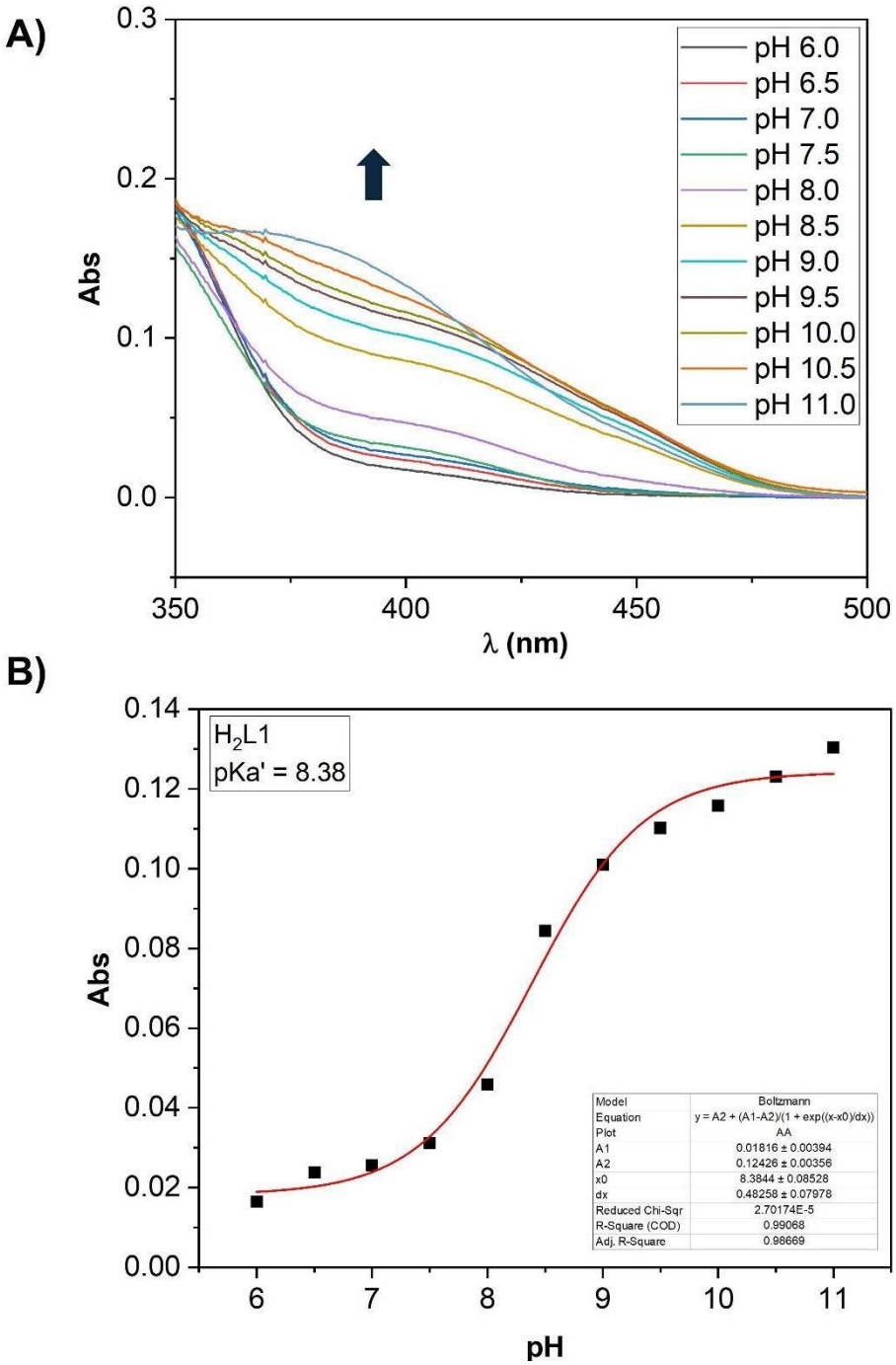

Figure 36. A) UV-Vis spectrum of the **H_2L1** ligand in 5% MeOH:H_2O at different pHs in the range of 350-500 nm with a concentration of 2×10^{-5} mol L^{-1}. **B)** Relationship of pH with the different absorbances of the 400 nm band.

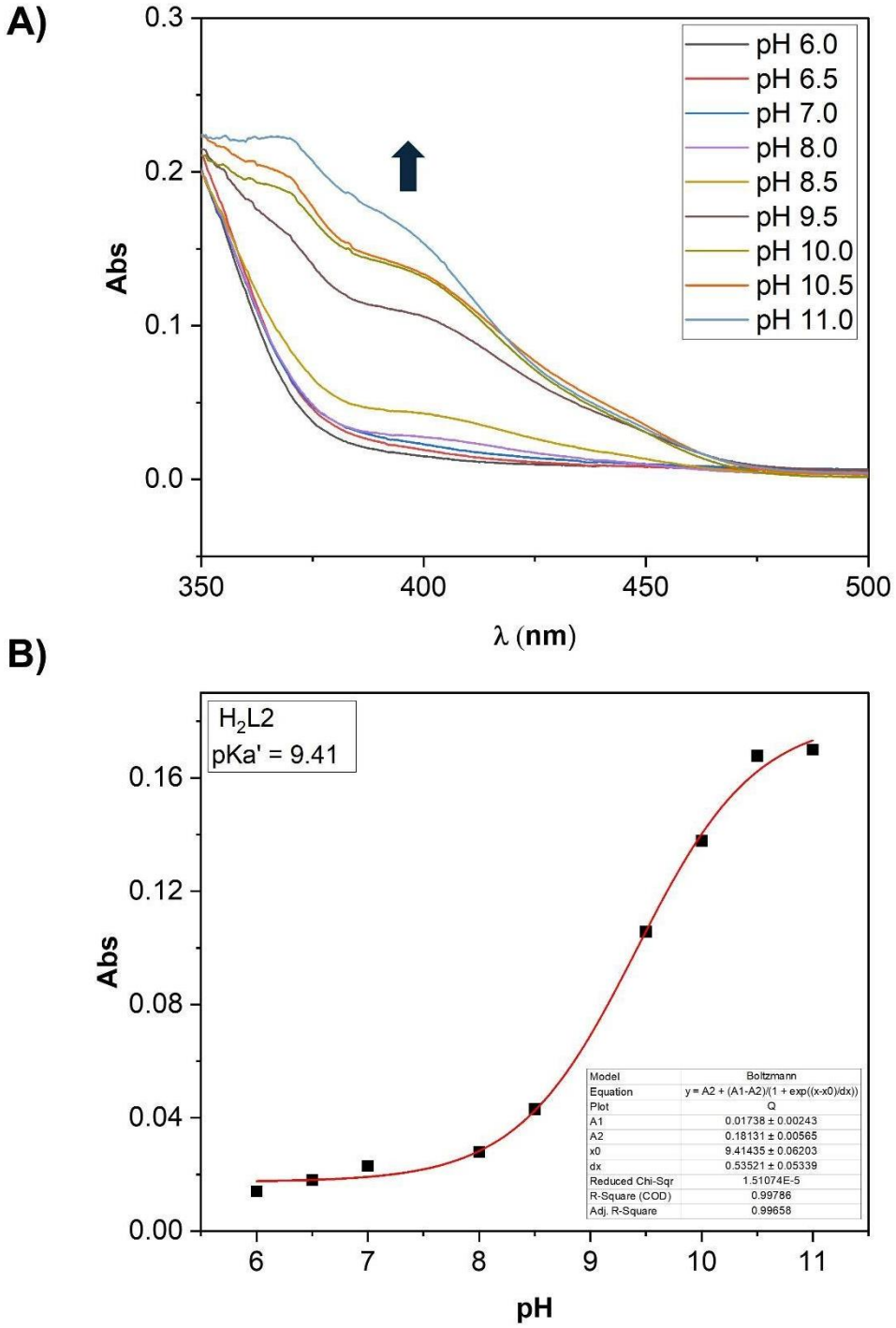

Figure 37. A) UV-Vis spectrum of the **H_2L2** ligand in 5% MeOH:H_2O at different pHs in the range of 350-500 nm with a concentration of 2×10^{-5} mol L^{-1}. **B)** Relationship of pH with the different absorbances of the 405 nm band.

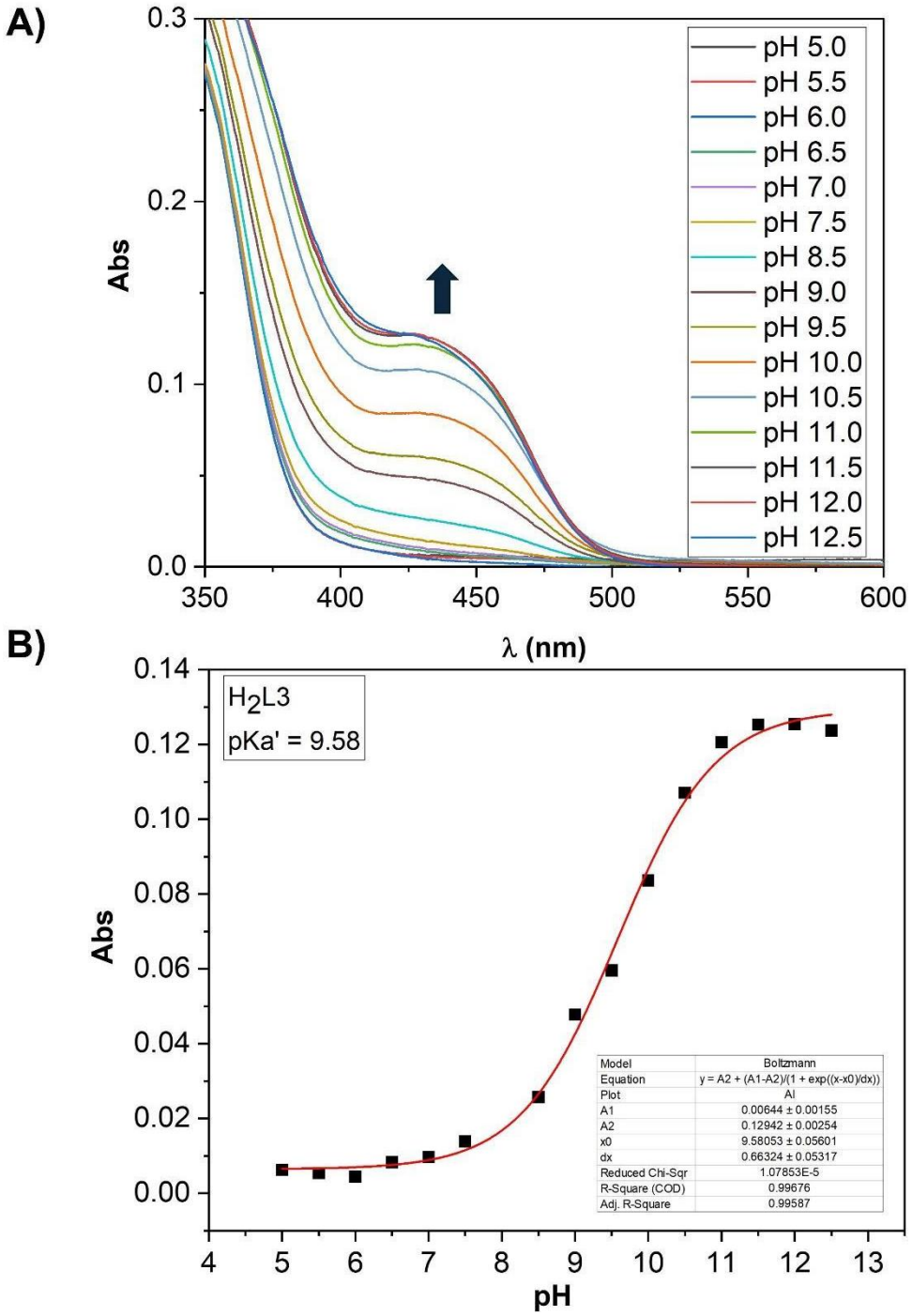

Figure 38. A) UV-Vis spectrum of the **H_2L3** ligand in 30% DMF:H_2O at different pHs in the range of 350-600 nm with a concentration of 2×10^{-5} mol L^{-1}. **B)** Relationship of pH with the different absorbances of the 430 nm band.

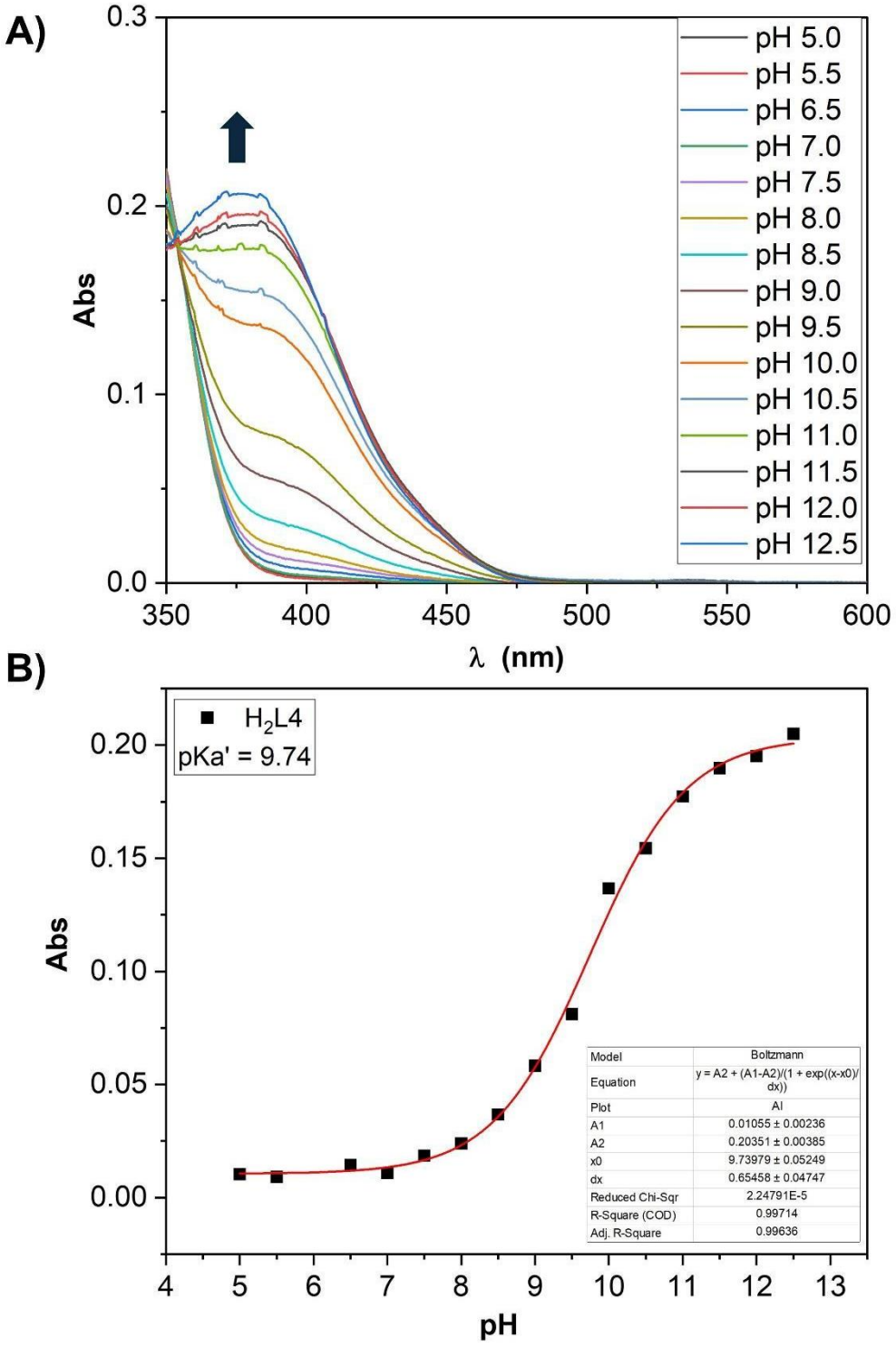

Figure 39. A) UV-Vis spectrum of the **H_2L4** ligand in 5% MeOH:H_2O at different pHs in the range of 350-600 nm with a concentration of 2×10^{-5} mol L^{-1}**. B)** Relationship of pH with the different absorbances of the 398 nm band.

According to the data obtained represented in Figures 36, 37, 38 and 39, the decreasing order of acidity for the ligands is **H_2L1** > **H_2L2** > **H_2L3** > **H_2L4**.

5.1.6 Electrochemical Behavior of Ligands

The chemistry of hydrazones is highly diverse and rich, offering numerous possibilities. In terms of electrochemistry, the redox processes are dependent on the Schiff base (−C=N) or on the substituent group, if it exhibits redox activity (Lawrence *et al.*, 2019). Literature reports indicate that HOMO-LUMO orbitals of free hydrazones are influenced by the functionality of the iminic group (Bakir & Brown, 2011; Bakir *et al.*, 2017; Bakir *et al.*, 2015).

Electrochemical studies demonstrate that in non-aqueous media, the cyclic voltammetry profile of hydrazones exhibits an irreversible wave. The behavior of hydrazones is analogous to that observed in imines / Schiff bases (Lawrence *et al.*, 2019). Most authors attribute the first cathodic peak to the reduction of the −C=N fraction. Electron transfer can proceed *via* a rapid chemical reaction that may lead to the cleavage of the N−N bond in the hydrazone, resulting in a $C{=}N^{\bullet -}$ radical anion. Other reductions may involve proton coupling, potentially leading to the formation of amines (from the complete reduction of the C=N bond) and various species, depending on the nature of the substituent group (Bakir *et al.*, 2016; D Özel *et al.*, 2009; Tropol'skaya *et al.*, 1979).

Figure 40 presents the proposed general mechanism for the electrochemical reduction of hydrazones, suggesting that the mechanism may involve one or two electrons.

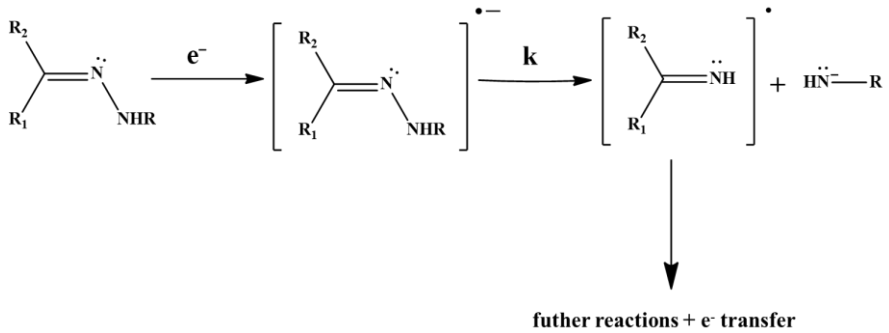

Figure 40. General mechanism of electrochemical reduction of hydrazones. Modified from Lawrence *et al.* (2019).

From the voltammograms of the obtained ligands and some correlations, it is possible to derive electrochemical parameters that can indicate the number of involved electrons (n), the redox mechanism, the transport process, and even the transfer coefficient (α) (Abbar & Nandibewoor, 2012).

The relationship between the square root of the scan rate and the peak current provides information about the type of transport process acting in cyclic voltammetry (Abbar & Nandibewoor, 2012). Analyzing this relationship for the studied ligands reveals a linear correlation, indicating that the system is diffusion-controlled (Abbar & Nandibewoor, 2012; Gosser, 1993). Also corroborated by the linear relationship between the logarithm of the potential and the logarithm of the scan rate, where the value of the slope coefficient being less than or almost equal to 0.5 suggests diffusion-controlled processes (Laviron *et al.*, 1980).

Table 10 presents the electrochemical parameters obtained for the studied complexes. The transfer coefficient (α) can be experimentally determined from a Tafel plot. The Tafel plot utilizes the relationship log Ip *versus* *E*p, at a scan rate of 100 $mV \cdot s^{-1}$, for the determination of electrochemical parameters (Compton & Banks, 2007; Muhammad *et al.*, 2016; van der Heijden *et al.*, 2024). The obtained slope can be related to the transfer coefficient (α) by the following relationship (Compton & Banks, 2007; Muhammad *et al.*, 2016):

$$|slope| = |\frac{\alpha F}{2.3RT}|$$

Where *F* = Faraday constant

R = Ideal gas constant

T = Temperature (K)

The number of electrons (n) can be estimated, once the transfer coefficient is known, from the relationship:

$$|E_p - E_{\frac{p}{2}}| = \frac{0{,}048}{\alpha n}$$

Where *E*p = Potential of the analyzed peak

*E*p/2 = Corresponds to the potential at which current is the half peak value

n = Number of electrons involved in the redox process

α = Transfer coefficient

Table 10. Estimated electrochemical parameters for the studied ligands. **H_2L2** is non-electroactive.

Ligands	**H_2L1**	**H_2L2**	**H_2L3**	**H_2L4**
E_{pc} (V *vs* Ag/AgCl)	–1.44	---	–1.71	–1.45
$E_{pc½}$ (V *vs* Ag/AgCl)	–1.29	---	–1.59	–1.35
α_c	0.15	---	0.18	0.86
n_c	2.08	---	2.10	0.59

Figures 42 and 43 (A and C, respectively) present cyclic voltammograms of ligands **H_2L1** and **H_2L3**, showing an irreversible profile, suggesting that the cathodic peaks observed at the potentials of –1.44 V and –1.71 V *vs*. Ag/AgCl, correspondingly, are associated with the reduction of the imine (C=N) present in *N*-acylhydrazonic ligands (Lawrence *et al.*, 2019).

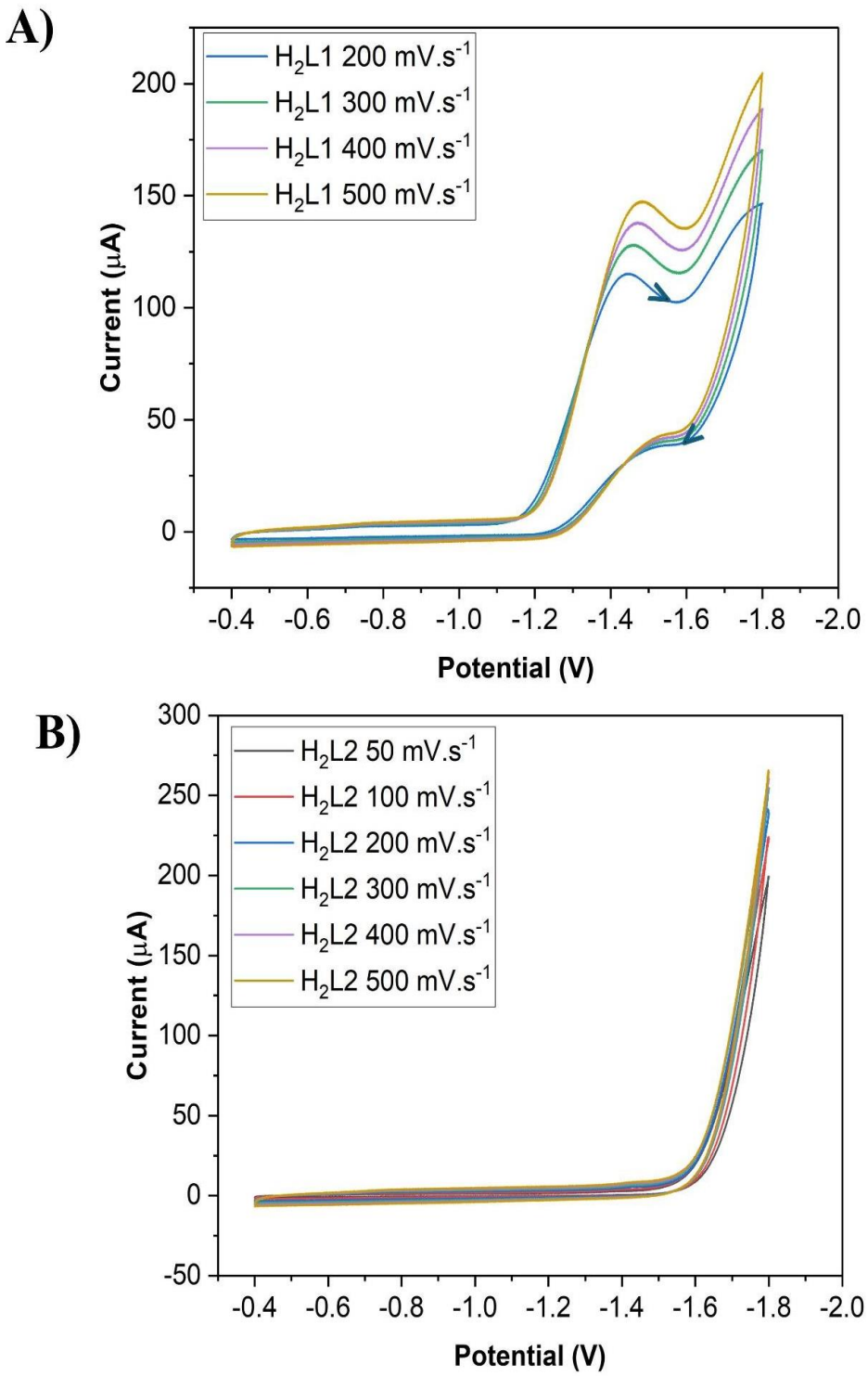

Figure 41. Representative cyclic voltammograms of ligands **(A) H_2L1** and **(B) H_2L2** at different scan rates, measured in DMF/0.1 mol L^{-1} $TBAPF_6$ (25 ºC), using a GCE as the working electrode.

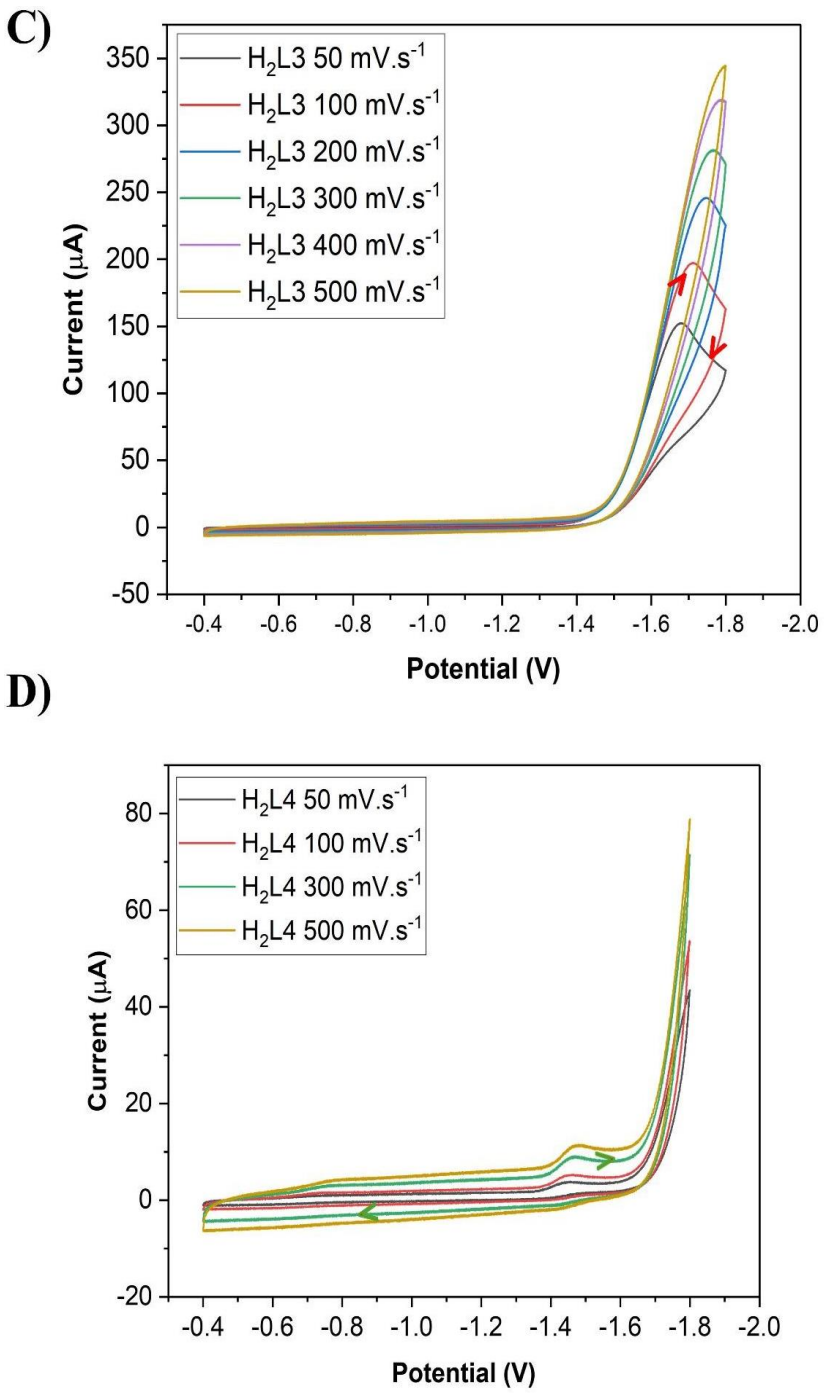

Figure 42. Representative cyclic voltammograms of ligands **(C) H_2L3** and **(D) H_2L4** at different scan rates, measured in DMF/0.1 mol L^{-1} $TBAPF_6$ (25 ºC), using a GCE as the working electrode.

Electrochemical studies conducted on ligands **H_2L1** and **H_2L3** indicate a two-electron reduction process, implying that the C=N group may be reduced to an amine on the electrode surface. The observed current values in the assay are significantly high for both ligands, which is consistent with the proposal that two electrons are involved in the reduction process.

Figure 41B displays the cyclic voltammogram of ligand **H_2L2**, where the ligand appears to be non-electroactive as no cathodic or anodic waves are seen within the studied potential range.

Figure 42D, on the other hand, shows the cyclic voltammogram of ligand **H_2L4**, which also exhibits an irreversible profile. The cathodic peak observed at the potential −1.45 V suggests reduction of the iminic group (C=N) in the studied ligand (Lawrence *et al.*, 2019). Electrochemical studies on ligand **H_2L4** (Figure 42D) indicate a single-electron reduction process, implying partial reduction of the C=N group on the electrode surface. This reduction *via* a single electron suggests the formation of a C=N$^{\bullet}$ radical rather than an amine on the electrode surface. The observed current values in the assay are considerably lower compared to those observed for **H_2L1** (Figure 41A) and **H_2L3** (Figure 42C), which is consistent with the suggestion of a single electron being involved in the reduction process.

5.2 H_2L1 Series

5.2.1 Synthesis of the Compounds belonging to the H_2L1 Series

The ligand was synthesized through a condensation reaction between 5-methylsalicylaldehyde and isoniazid with good yield. The complexes precipitated during the syntheses as reddish powders, with appreciable yield. Figure 43 depicts the synthesis scheme of the ligand and its respective complexes.

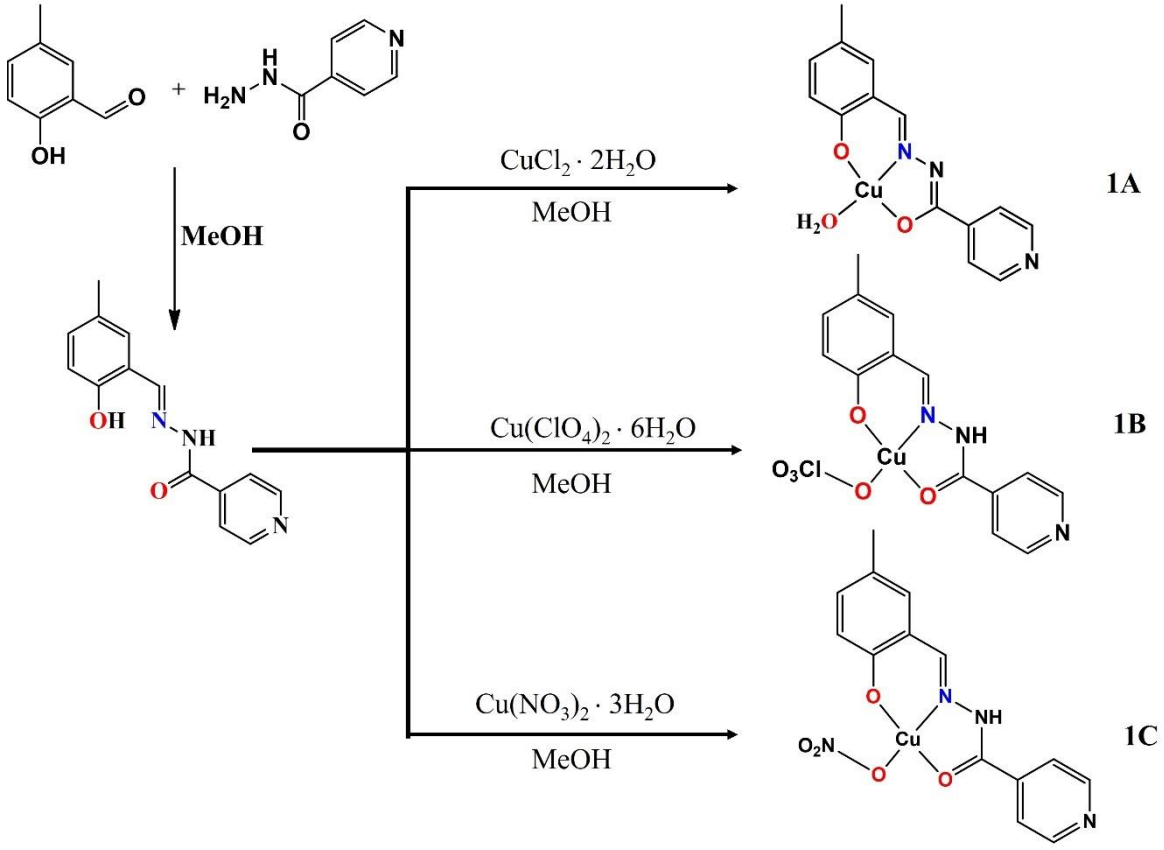

Figure 43. General synthetic scheme for the **H_2L1** ligand and complexes **1A**, **1B** and **1C**.

In the TGA analysis of complex **1A** (Figure 44), a significant mass loss of approximately 72.5% is observed at around 350-400 ºC, suggesting that within this range, the coordinated water molecule is lost along with the degradation of the organic fraction of **1A**. The remaining solid residue corresponds to 27.5%, and assuming it is CuO, we would have 22.8% of copper in complex **1A**.

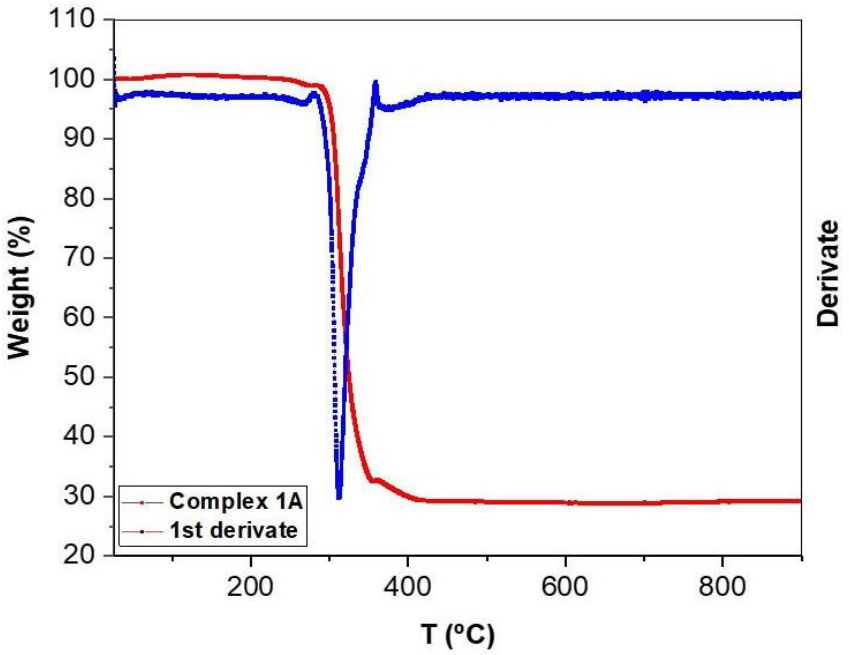

Figure 44. Thermogravimetric curve for the complex **1A.**

The obtained value of 22.8% of copper differs from the calculated value.

The absence of chloride ion in the coordination sphere of complex **1A** was confirmed through a test using a 1.0 mol L^{-1} aqueous solution of silver nitrate. A mixture of **1A** in methanol was prepared, and the insoluble fraction was filtered out. Drops of the aqueous silver nitrate solution were added to the remaining solution, and no precipitation was observed, indicating that the chloride ion does not participate in the coordination sphere and is not present as a counterion.

In the TGA of complex **1C** (Figure 45), a mass loss of approximately 4.95% is observed starting at around 120 ºC, suggesting that, within this range, the loss of the nitrate ion as NOx occurs (Fei *et al.*, 2019). At 400 ºC, degradation of the organic fraction is observed. The remaining solid residue, stable from 700 ºC on, corresponds to 23.46%, and assuming it is CuO, we would have 18.74% of the copper in **1C**. The obtained value of 18.74% differs from the calculated value by approximately 2.0%, suggesting that the proposed structure is reasonable.

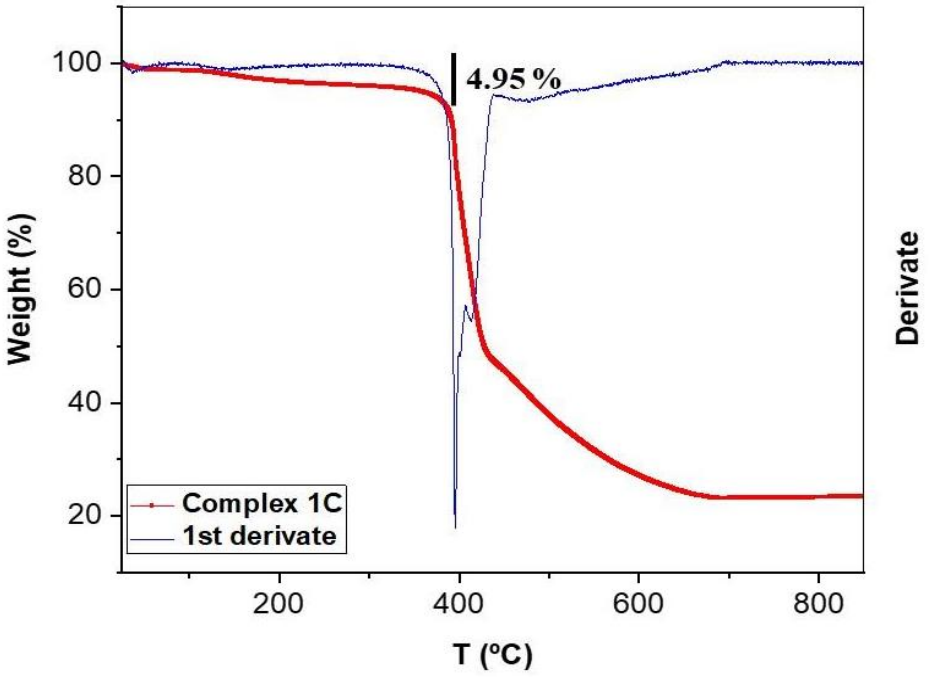

Figure 45. Thermogravimetric curve for the complex **1C.**

All the obtained complexes were highly insoluble in the tested solvents, including water, methanol, ethanol, isopropanol, acetone, acetonitrile, DMF, and DMSO. The low solubility of these compounds prevented any solution-based assays as well as the interaction studies with HSA.

5.2.1 Characterization of H_2L1 and their Complexes

5.2.1.1 Copper content (ICP-OES)

Assays using the ICP-OES were performed for all the complexes derived from **H_2L1**. The results are organized in Table 11.

Table 11. Relationship between the percentage of copper calculated and that found.

Complexes	**%Cu**	
	calculated	found
1A	19.0 %	19.4%
1B	15.2%	16.6 %
1C	16.7%	16.9 %

5.2.2.2 Infrared Vibrational Spectroscopy

The results obtained from infrared vibrational spectroscopy for compounds **1A**, **1B**, and **1C** were crucial in proposing a structure that aligns with the obtained data, as crystallization of these compounds was not achievable. Most of the bands present in the infrared spectrum of ligand **H_2L1** are still evident in its respective complexes. However, absorption shifts, band disappearances, and the appearance of new absorptions in the spectra of complexes **1A**, **1B**, and **1C** (Figures 46-48, respectively, and Table 12) suggest coordination.

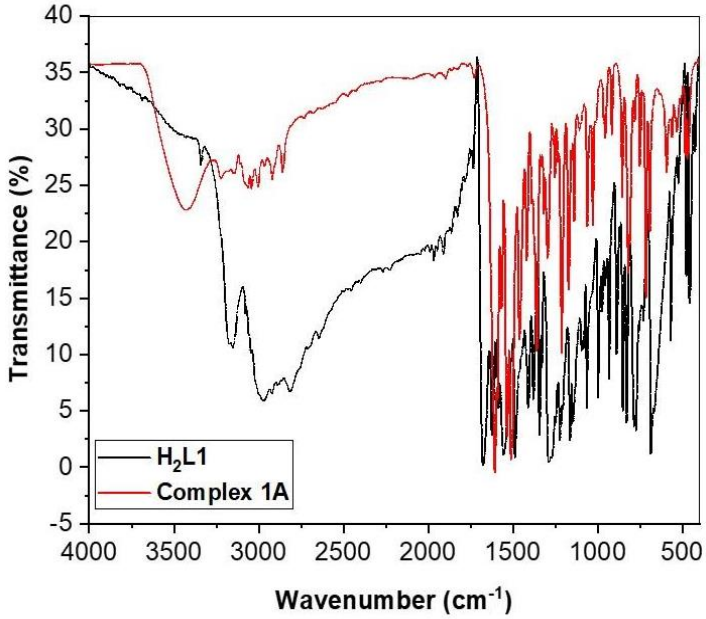

Figure 46. Overlapping of the mid-infrared spectra of **H_2L1** and **1A** in KBr, at room temperature.

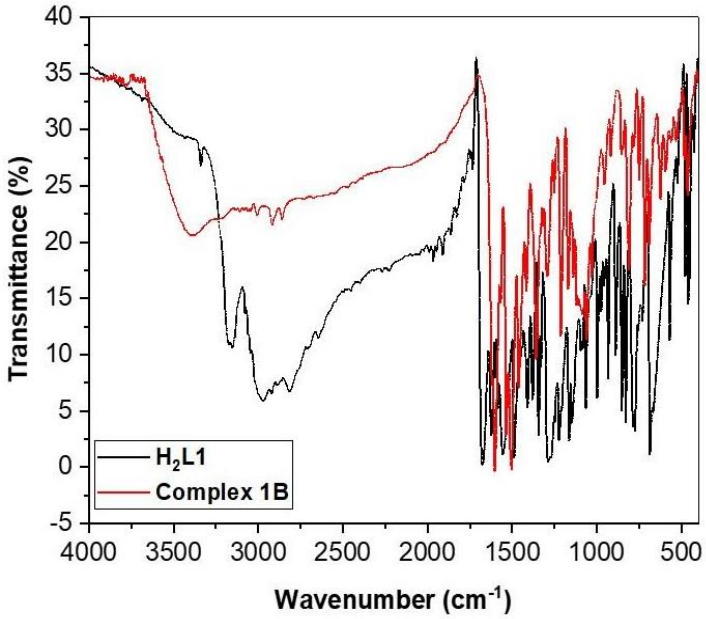

Figure 47. Overlapping of the mid-infrared spectra of **H_2L1** and **1B** in KBr, at room temperature.

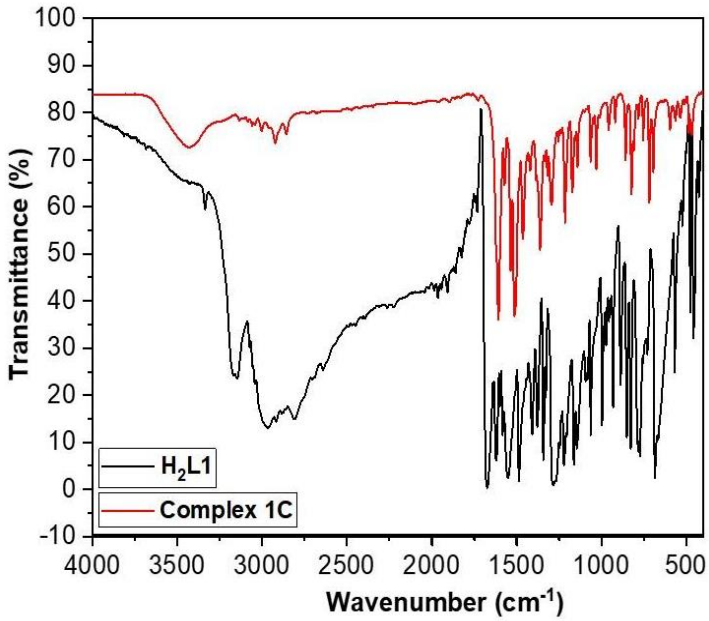

Figure 48. Overlapping of the mid-infrared spectra of **H_2L1** and **1C** in KBr, at room temperature.

Table 12. Selected vibrational absorptions (cm^{-1}) for **H_2L1** and their copper(II) complexes.

Assingment	H_2L1	Complex 1A	Complex 1B	Complex 1C
υN−H	3175	-----	3212	3244
$\upsilon O-H_{phenol}$	3339	-----	-----	-----
$\upsilon O-H_{water}$	-----	3390	3384	3424
υC=O	1670	1514	1603	1607
υC=N	1623	1605	1603	1609
δC=N−H	1546	1566	1538	1537
$\delta C-O-H_{phenol}$	1485	-----	-----	-----
$\upsilon(NO_2)_{ass}$	-----	-----	-----	1370
$\upsilon C=C_{arom}$	1370	1366	1359	1356
$\delta O-H_{phenol}$	1377	-----	-----	-----
$\upsilon C-O_{phenol}$	1340	1300	1311	1317
$\upsilon(NO_2)_{sym}$	-----	-----	-----	1213
$\delta C=C-H_{phenol}$	1290	1218	1282	1283
υN−N	1160	1165	1160	1068
υNO	-----	-----	-----	1022
$\upsilon(ClO_4)_{ass}$	-----	-----	1105	-----
υClO_4	-----	-----	1028	-----
$\upsilon(ClO_4)_{sym}$	-----	-----	623	-----
υCu−O	-----	591	589	591
υCu−N	-----	529	529	553
δO−Cu−N	-----	472	465	460

When comparing the spectra of the ligand and its respective complexes, a shift of bands to lower energy values associated with common groups is observed. This pattern suggests coordination, and is accompanied by the disappearance of other bands, such as the O−H stretching of phenol, absent in the spectra of all the complexes, thus confirming deprotonation of the hydroxyl group.

Complexes **1B** and **1C** exhibit anions (perchlorate and nitrate) coordinated to the metal ion. Thus, it is expected that the N-H group of the hydrazone present in the ligand remains protonated in the complex, a fact confirmed by the ν(N−H) bands present in the complexes at 3212 and 3244 cm^{-1}, respectively (Pavia *et al.*,

2015; Silverstein, 2000). For complex **1B**, bands related to the $\upsilon(ClO_4)_{ass}$ stretching vibration at 1105 cm^{-1}, υClO_4 at 1028 cm^{-1}, and $\upsilon(ClO_4)_{sym}$ at 623 cm^{-1} are observed, which are consistent with the monodentate binding of perchlorate to copper (Nakamoto, 1978; Rey, 2019). For complex **1C**, absorptions related to the $\upsilon(NO_2)_{ass}$ stretching, $\upsilon(NO_2)_{sym}$ stretching, and υNO stretching vibrations indicate that coordination of the nitrate ion occurs in a monodentate manner. Literature reports that if bands related to the nitrate ion are observed at around 1400-1300 cm^{-1}, the ion acts as a monodentate ligand in the complex (Jaafar *et al.*, 2024; Nakamoto, 1978).

The stretching vibration ν(C=N) of the azomethine group is observed at 1623 cm^{-1} in the free ligand. In complexes **1A**, **1B**, and **1C**, this band is shifted to 1605, 1603, and 1609 cm^{-1}, respectively, suggesting coordination *via* this group. Additionally, the band related to the ν(C=O) stretching vibration overlaps, in **1C**, with the ν(C=N) stretching, possibly due to coordination involving this group, placing it very close to the ν(C=N) stretching (Nakamoto, 1978; Pavia *et al.*, 2015; Silverstein, 2000).

In addition to these ligand-related bands, some metal-ligand vibrations were identified in the spectra of complexes. These include absorptions at around 590 cm^{-1} associated to the ν(Cu–O1) stretching vibration, bands at approximately 530-550 cm^{-1} related to the ν(Cu–O2) stretching vibration, and an absorption at around 460-470 cm^{-1} related to the δ(O−Cu−N) bending (Moura *et al.*, 2023; Nakamoto, 1978).

5.2.2.3 Electronic Spectroscopy in UV-Vis

The synthesized complexes could not be studied in solution due to their low solubility in common solvents. In contrast, ligand **H_2L1** was characterized by UV-Vis electronic spectroscopy in DMF at different concentrations.

Figure 49 illustrates the electronic spectra of **H_2L1** and its precursors. This *N*-acylhydrazone exhibits four main absorptions in the range of 250 to 500 nm, comprising two bands and two shoulders. Upon comparing the spectrum of the ligand with its precursors, it is observed that two of the absorptions are present in the precursors, corresponding to transitions of the phenol and/or pyridine rings. Among the four main absorptions, an intense band centered at 292.5 nm [molar

absorptivity (ε) equal to 19,441 ± 203 L mol^{-1} cm^{-1}] and a shoulder at ~304 nm (17,213 ± 190 L mol^{-1} cm^{-1}) are strictly related to *N*-acylhydrazone processes, as they are absent in the spectra of precursors. The broad band observed at 341.5 nm (15,343 ± 138 L mol^{-1} cm^{-1}) exists in the spectrum of 5-methylsalicylaldehyde, and undergoes a bathochromic shift in the hydrazone.

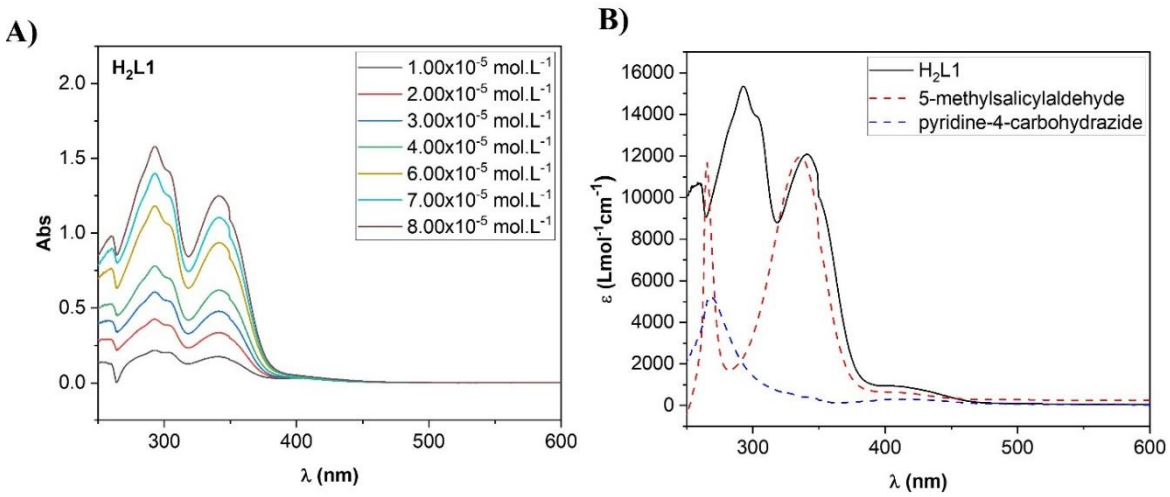

Figure 49. A) UV-Vis electronic spectrum of **H_2L1** at different concentrations in DMF solution. **B)** UV-Vis electronic spectra of **H_2L1** and its precursors (5.0×10^{-5} mol L^{-1}) in DMF solution.

5.2.2.4 Diffuse Reflectance

The diffuse reflectance technique was chosen due to the low solubility shown by the complexes synthesized from **H_2L1**. Throughout this work, much will be discussed regarding the spectroscopy of the copper(II) ion because the electronic properties of these complexes are highly influenced by stereochemistry.

The free copper(II) ion has a d^9 electronic configuration, with 9 electrons distributed over five degenerate *d* orbitals. In the presence of a ligand field, these *d* orbitals lose their degeneracy and split into different energy levels according to the symmetries presented by these orbitals (Figure 50). This splitting allows for electronic transitions between the orbitals, known as *d-d* transitions. The energy difference between these split orbitals is strongly influenced by the nature of the ligands (according to the spectrochemical series) and the geometry of the metal center (Huheey, 1972; Miessler & Tarr, 2004).

Copper(II) complexes in octahedral environments are highly distorted (due to the Jahn-Teller effect), with tetragonally elongation along the *z*-axis being the most common distortion (Hathaway & Billing, 1970). Generally, these complexes exhibit three absorption bands, although they may not always be well resolved, sometimes appearing as a single broad band around 600-700 nm (Lever, 1984).

On the other hand, copper(II) complexes with a coordination number 5 can typically be found in two stereochemical limits: trigonal bipyramidal and square pyramidal. However, intermediates between these two boundaries are often found (Lever, 1984). The electronic spectra of trigonal bipyramidal complexes usually exhibit a less intense band at higher energies and a more intense band at lower energies. In contrast, electronic spectra of square pyramidal complexes often show a more intense absorption band in the higher energy region and a less intense one at lower energy. The less intense bands may sometimes be obscured or appear as shoulders (Lever, 1984; Manonmani *et al.*, 2000; Vaidyanathan *et al.*, 1998).

Tetracoordinate copper(II) complexes can be found at the stereochemical limits of tetrahedral and square planar geometries, being the latter more common. Tetrahedral copper(II) complexes are invariably distorted, typically showing four absorptions, three of which are related to *d-d* transitions and the fourth absorption band attributed to distortions (Lever, 1984). Tetrahedral copper(II) complexes are favored by weak field or bulky ligands, whereas the ligands reported in this study are strong field ligands; consequently, for a tetracoordinate complex, the favored stereochemistry would be square planar. Many square-planar copper(II) complexes are reddish and exhibit weak absorption bands around 440-560 nm. The literature reports that square planar copper(II) complexes containing Schiff bases show absorption bands across a broad wavelength range: 500 to 769 nm (Lever, 1984). In summary, the electronic spectra of copper(II) coordination compounds provide valuable information about coordination sphere and molecular geometry.

Figure 50 recapitulates the orbital splitting patterns that *d* orbitals of the metal can undergo in different symmetries.

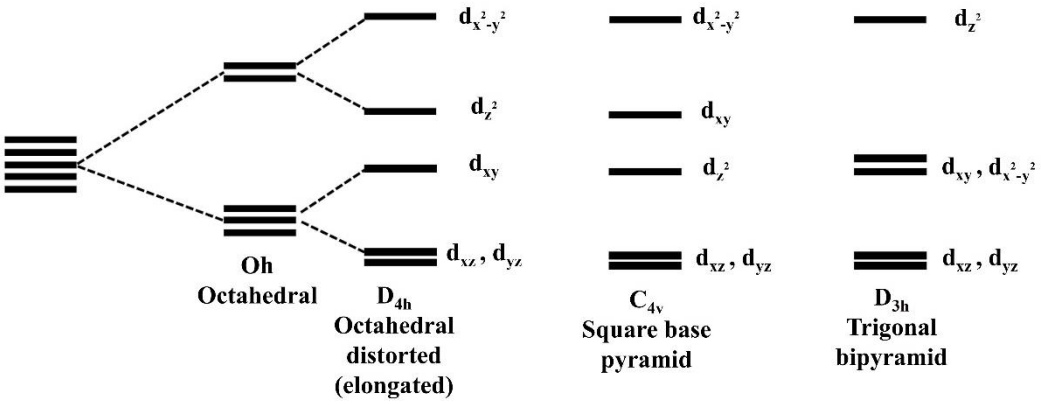

Figure 50. Diagram of the splitting of energy levels of *d* orbitals in different symmetries.

Figure 51 presents the diffuse reflectance electronic spectrum of complex **1A** diluted in barium sulfate, along with the deconvoluted bands. Five absorption bands were obtained between 250 nm and 800 nm using an absorption fitting. The component at 284.5 nm in complex **1A** may be related to the aromatic rings. The hydrazone-associated absorptions observed at 292.5 and 304 nm, as well as the phenol-centered band at 341.5 nm in the ligand are bathocromically shifted in **1A** (as already reported by us for similar systems (Rada *et al.*, 2019)), being assigned to the components at ~342 hydrazone-associated absorptions and ~442 nm the phenol-centered band. The latter has, in fact, two contributing constituents, being the second one probably related to a LMCT transition from the phenolate ion to copper(II). Finally, an extended band centered at around 647.5 nm is connected to *d-d* transitions. This value is within the common range for copper(II) complexes, as previously mentioned (Hathaway & Billing, 1970; Lever, 1984). Indeed, the work by Rodríguez *et al.* (2021) describes *d-d* components at 637 and 715 nm for a hydrazone-derived copper(II) complex with the same coordination sphere (in terms of the donor atoms set) proposed by us for compound **1A**.

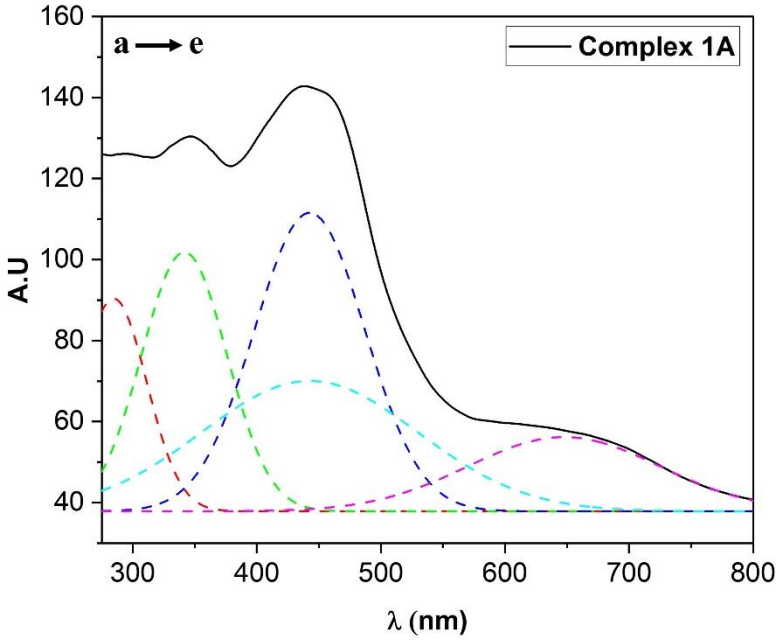

Figure 51. Electronic diffuse reflectance spectrum of **1A,** in black. Main components obtained by band fitting: a) 284.5 nm, b) 341.5 nm, c) 442.5 nm, d) 443 nm and e) 647.5 nm.

The diffuse reflectance electronic spectrum of complex **1B** is shown in Figure 52, along with the main absorption bands obtained by the band deconvolution method. The spectrum was deconvoluted into six absorption bands were obtained between 250 nm and 800 nm using an absorption fitting. The component at 271.7 nm in complex **1B** may be related to the aromatic rings. The ligand's band at 341.5 nm appears in the spectrum of complex **1B** at 347 nm and is also present in the precursors, related to transitions of the phenol and pyridine rings and the hydrazone-associated absorptions observed at 292.5 and 304 nm, as well as the phenol-centered band at 341.5 nm in the ligand are bathocromically shifted in **1B** being assigned to the components at ~342 and ~442 nm. Three bands are observed in the 400 nm region: 416 nm, 461 nm, and 461.5 nm. As discussed for complex **1A**, the band at 416 nm is possibly related the hydrazone-associated absorptions and the charge transfer from the phenolate ion to the Cu^{2+} ion, while the bands at 461 nm and 461.5 nm are related to *d-d* transitions in a square planar system, as suggested for these **H_2L1** systems. The absorption band at 680 nm is essentially related to the *d-d* transition in copper(II) complexes (Lever, 1984; Vaidyanathan *et al.*, 1998).

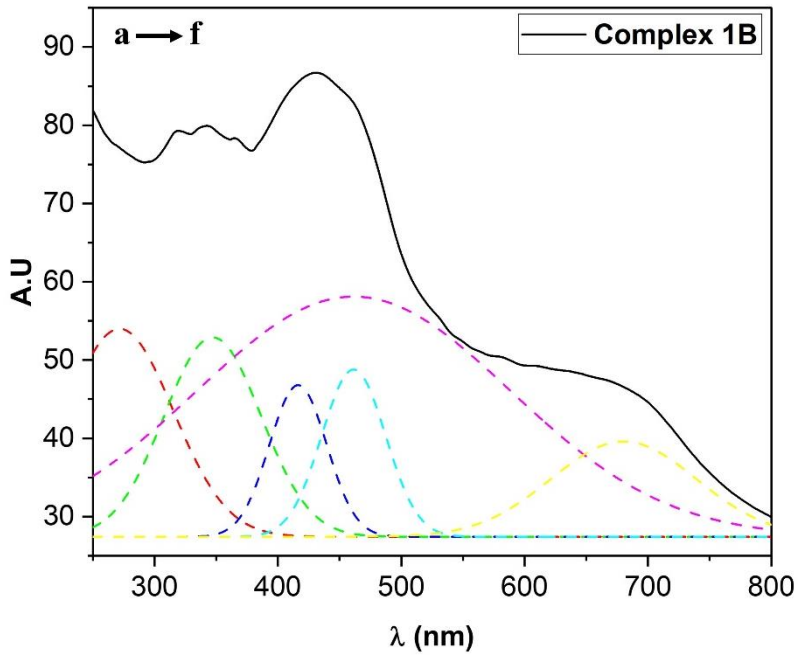

Figure 52. Electronic diffuse reflectance spectrum of **1B,** in black. Main components obtained by band fitting: a) 271.7 nm, b) 347 nm, c) 416 nm, d) 461 nm, e) 461.5 nm and f) 680 nm.

Complex **1C** exhibits (Figure 53) bands similar to those observed in the other complexes. The band around 270 nm shows a hypsochromic shift compared to the other complexes in the **H_2L1** series and the free ligand (which occurs around 291.5 nm) and is attributed to the aromatic rings. The hydrazone-associated absorptions observed at 292.5 and 304 nm, as well as the phenol-centered band at 341.5 nm in the ligand are bathocromically shifted in **1C** being assigned to the components at ~342 and ~442 nm (which occurs around 347 nm, 416 nm and 461 nm). The band at 630.7 nm is related to a *d-d* transition, and for complex **1C**, this band has a shorter wavelength, indicating higher energy in the electronic transition, suggesting that this complex may be more distorted than complexes **1A** and **1B**, which would justify greater splitting between its orbitals (Hathaway & Billing, 1970; Lever, 1984; Vaidyanathan *et al.*, 1998).

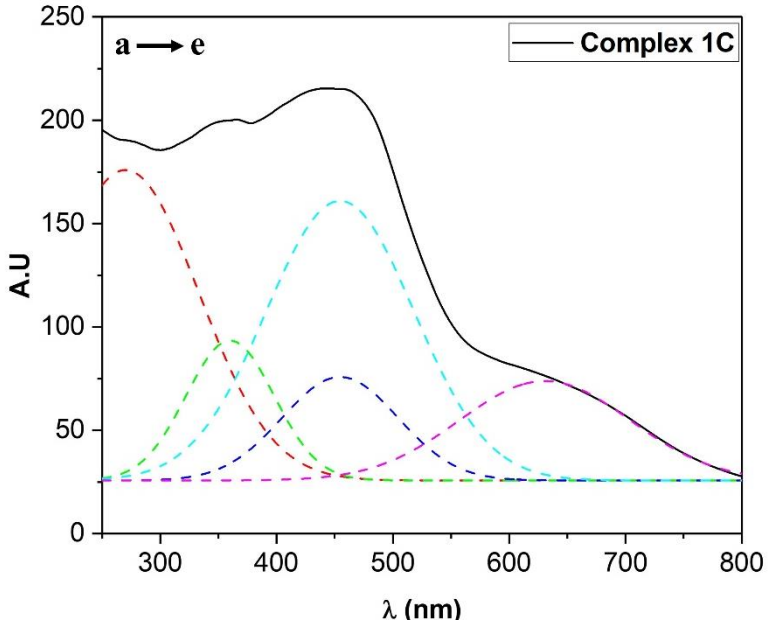

Figure 53. Electronic diffuse reflectance spectrum of **1C,** in black. Main components obtained by band fitting: a) 270 nm, b) 360 nm, c) 454 nm, d) 454.5 nm and e) 630.7 nm.

Although the complexes synthesized for the series of ligand **H_2L1** were not obtained in crystalline form, hindering a more detailed elucidation of their structures, the results obtained indicate a good correlation with the proposed structures. However, undoubtedly, further study with different techniques is necessary to better understand the structural nature and its influences on different properties of complexes **1A**, **1B**, and **1C**.

5.2.2.5 Electrochemical behavior - Cyclic Voltammetry

The electrochemical behavior of the complexes was evaluated by cyclic voltammetry using a three-electrode system under conditions analogous to those used for the respective ligand. Upon dissolution in a DMF solution containing $TBAPF_6$, the complexes precipitated. Therefore, the precipitate was filtered, and the remaining solution was evaluated. Complex **1C** exhibits much lower solubility in common solvents compared to **1A** and **1B**, rendering electrochemical studies impractical. The voltammograms of complexes **1A** and **1B** are shown in Figure 54 and were obtained at different scan rates.

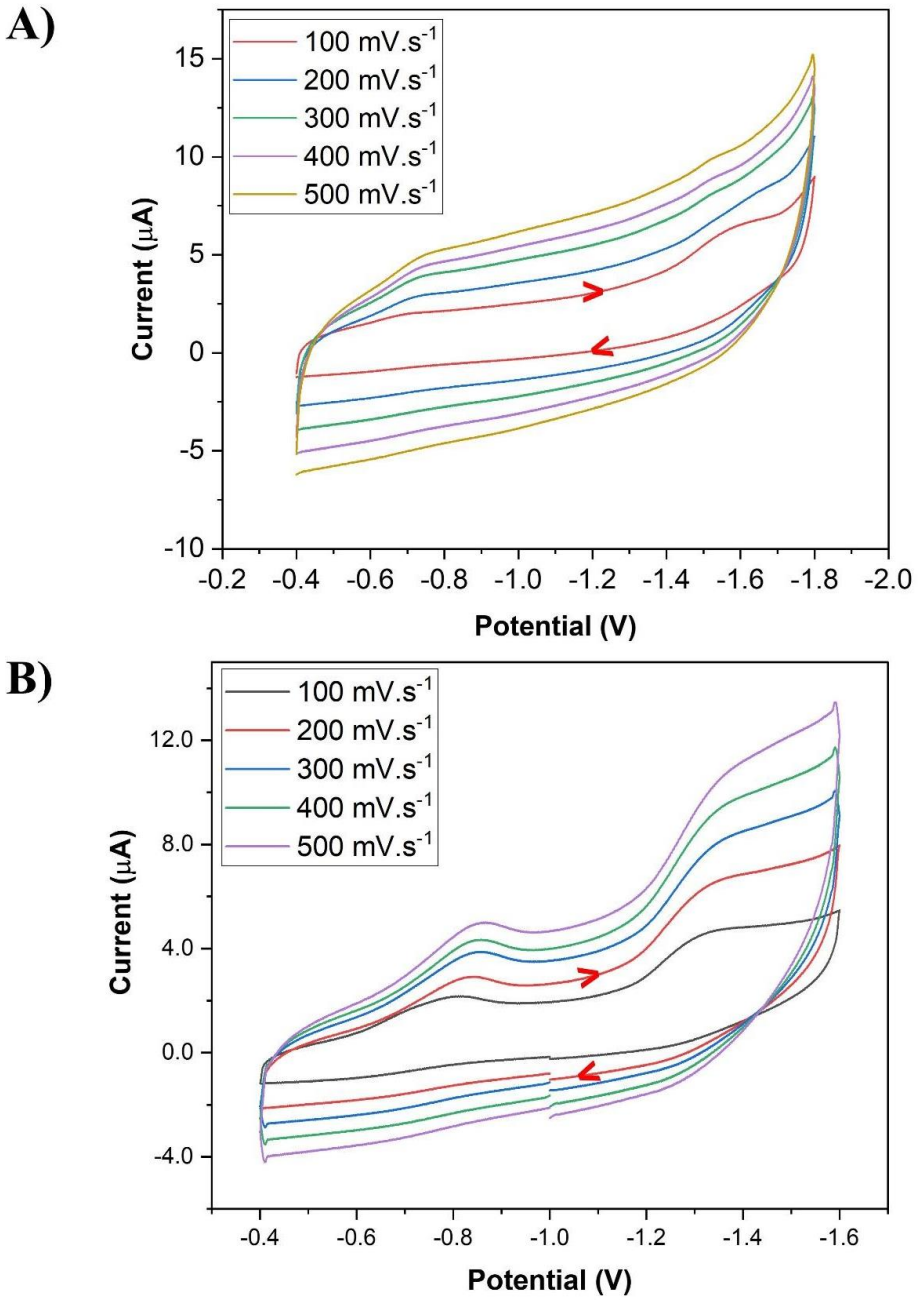

Figure 54. Representative cyclic voltammograms of complexes **(A) 1A** and **(B) 1B** at different scan rates, measured in DMF/0.1 mol L^{-1} $TBAPF_6$ (25 ºC), using a GCE as the working electrode.

Figure 54A shows the cyclic voltammogram of complex **1A**, which due to its low solubility appears with low resolution, which impacts the reliability of electrochemical calculations. Nevertheless, some considerations can still be made from the analysis of this voltammogram. As previously discussed, the free ligand **H_2L1** itself is electroactive, indicating that the cathodic peak at around –1.57 V *vs*. Ag/AgCl is related to a reduction process inherent to the ligand. Conversely, the cathodic peak at –0.72 V *vs*. Ag/AgCl is possibly associated with the Cu^{2+}/Cu^{+} redox couple, consistent with values in literature for similar complexes (Lawrence

et al., 2019; Moura *et al.*, 2023; Sangeetha *et al.*, 1999; Torelli *et al.*, 2000).

The voltammogram of complex **1B** (Figure 54B) exhibits better resolution, likely due to its higher solubility. In this voltammogram, two cathodic peaks can be clearly observed: the peak at –1.35 V *vs*. Ag/AgCl corresponds to the reduction of the C=N group in the ligand, while the peak around –0.81 V *vs*. Ag/AgCl was assigned to the Cu^{2+}/Cu^{+} redox couple (Lawrence *et al.*, 2019; Moura *et al.*, 2023; Sangeetha *et al.*, 1999; Torelli *et al.*, 2000).

From the voltammograms of the complexes, and doing some correlations, it is possible to obtain electrochemical parameters that can indicate the number of electrons involved (n), the redox mechanism, the transport process and even the transfer coefficient (α) (Abbar & Nandibewoor, 2012). The table 13 exhibit the electrochemical parameters obtained to **H_2L1** series.

The relationship between the square root of the scan rate and the peak current provides insights into the type of transport process in cyclic voltammetry (Abbar & Nandibewoor, 2012). Analyzing this relationship for **1A** and **1B** reveals a linear correlation, indicating that the system is diffusion-controlled (Abbar & Nandibewoor, 2012; Gosser, 1993), which is further confirmed by the linearity of the association between the logarithms of the potential and of the scan rate, with slopes less than or approximately equal to 0.5 (Laviron *et al.*, 1980).

Table 13. Estimated electrochemical parameters for the studied complexes.

Complex	**1A**	**1B**
E_{pc1} **(V *vs* Ag/AgCl)**	–0.72	–0.81
$E_{pc1½}$ **(V *vs* Ag/AgCl)**	–0.53	–0.65
α_{c1}	0.37	0.38
n_{c1}	0.68	0.75
E_{pc2} **(V *vs* Ag/AgCl)**	---	–1.35
$E_{pc2½}$ **(V *vs* Ag/AgCl)**	---	–1.22
α_{c2}	---	0.27
n_{c2}	---	1.36

The structural differences between complexes **1A** and **1B** result in slightly shifted cathodic potential values, although they are still close. Furthermore, the cathodic potentials obtained for the complexes below 1.0 V *vs*. Ag/AgCl suggest the involvement of one electron in the process, likely associated with the Cu^{2+}/Cu^{+} redox couple, which is consistent with its mononuclear nature (Moura *et al.*, 2023; Sangeetha *et al.*, 1999; Torelli *et al.*, 2000).

5.3 H_2L2 Series

5.3.1 Synthesis of the Compounds belonging to the H_2L2 Series

Crystals of **H_2L2** were obtained with good yields from the condensation between 5-methylsalicylaldehyde and furan-2-carboxyhydrazide. All its copper(II) complexes were obtained in crystalline form as well, and with an appreciable yield. Figure 55 shows the synthesis scheme of the ligand and its complexes.

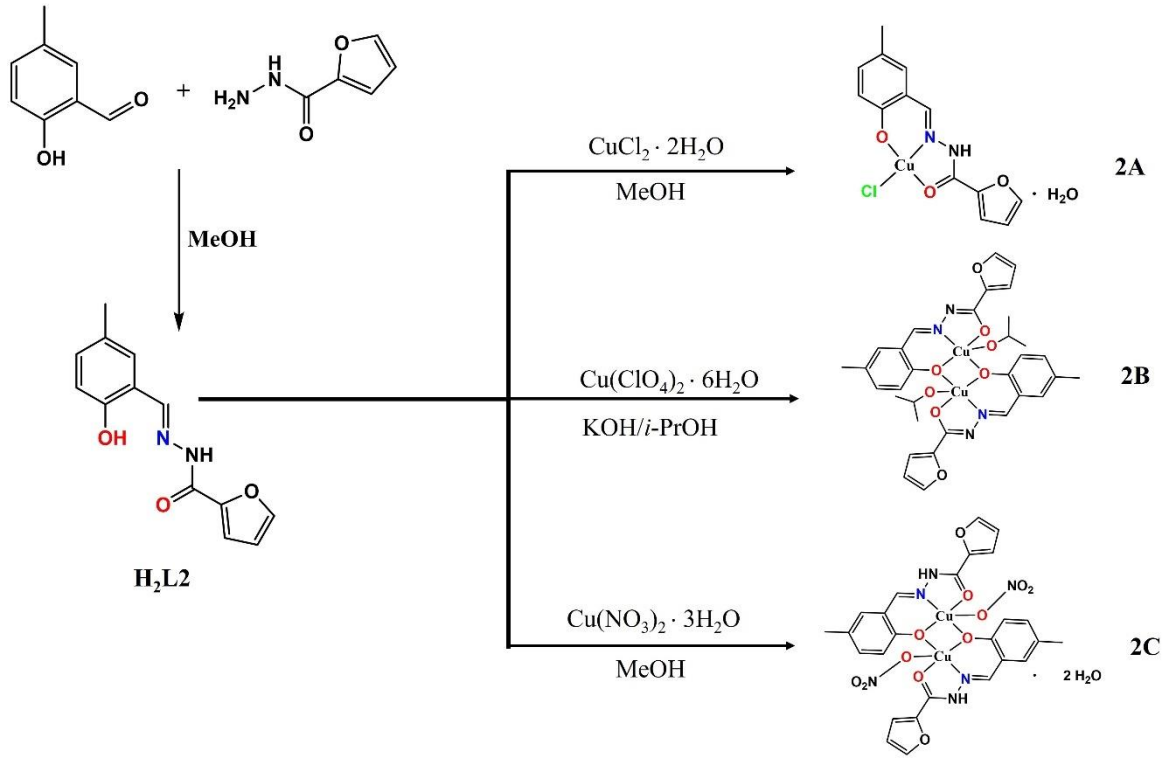

Figure 55. General scheme of the synthesis of the **H_2L2** ligand and complexes **2A, 2B** and **2C.**

In the TGA analysis for the **H_2L2** ligand (Figure 56), it is possible to observe two thermal events in the region of 100-150 ºC, corresponding to a mass loss of approximately 6.7%, suggesting the loss of a hydration water molecule.

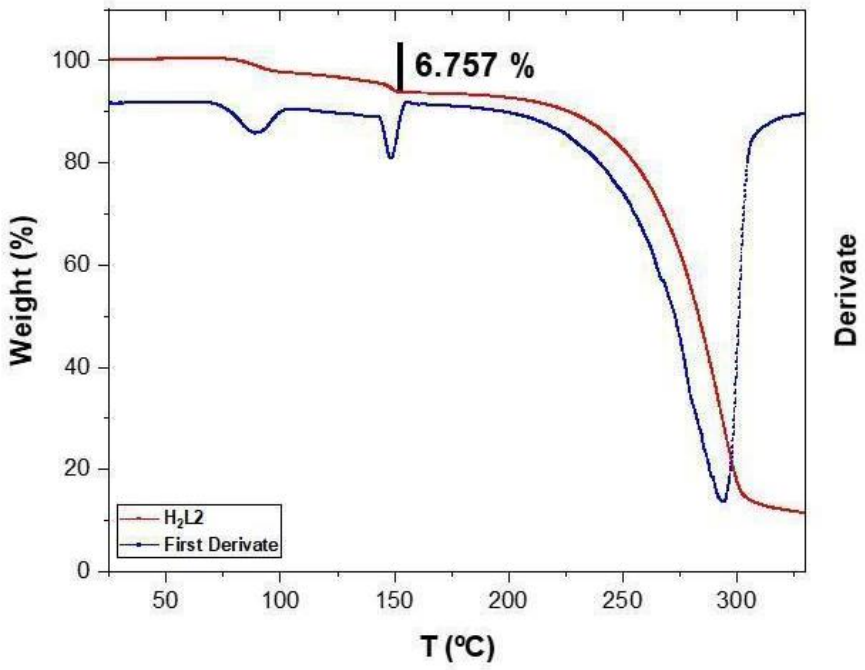

Figure 56. Thermogravimetric curve for the ligand **H_2L2.**

In the TGA analysis for complex **2A** (Figure 57), it is possible to observe a mass loss of approximately 4.2% at around 100-120 ºC, corresponding to the removal of a hydration molecule. Between 260-300 ºC another thermal event is observed with a mass loss of 15.4%, corresponding to the loss of the chloride ion in the form of HCl. The presence of the chloride ion could also be confirmed by AgCl precipitation, adding a few drops of 0.1 mol. L^{-1} aqueous solution of silver nitrate to a $1x10^{-3}$ mol. L^{-1} methanolic solution of complex **2A**. The remaining solid residue corresponds to 22.3%, considering that it is CuO, we will have 17.8% of the copper(II) ion in the complex **2A** sample.

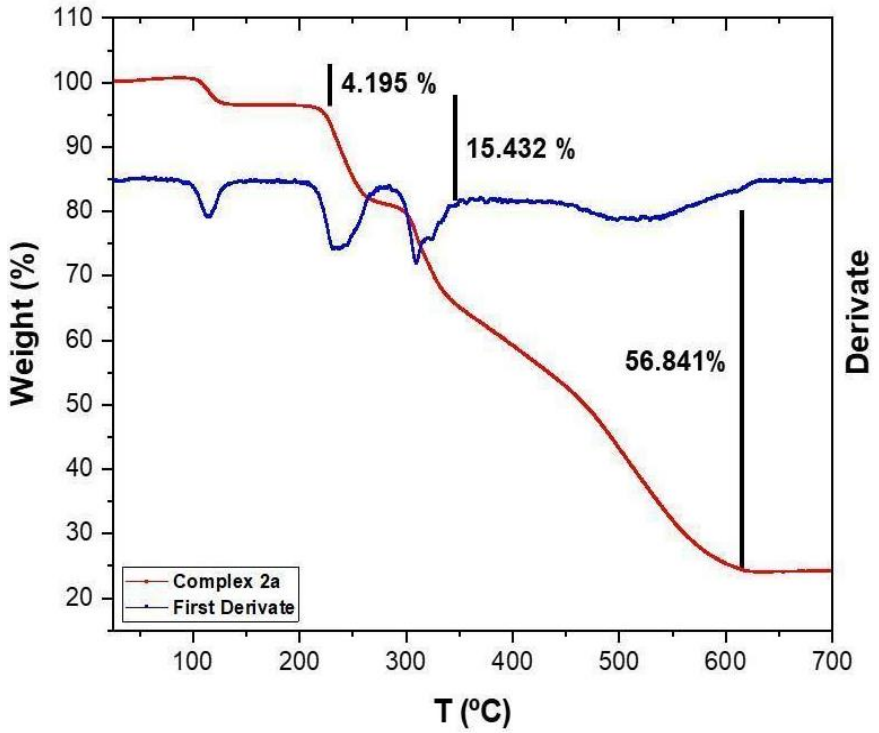

Figure 57. Thermogravimetric curve for complex **2A.**

In the TGA analysis for complex **2B** (Figure 58), it is possible to observe a mass loss of approximately 13% at around 90-140 ºC, corresponding to the loss of two isopropanol molecules. The solid residue obtained corresponds to 22.4%, considering that this residue is CuO, it is calculated that 17.9% of the copper(II) in the complex sample.

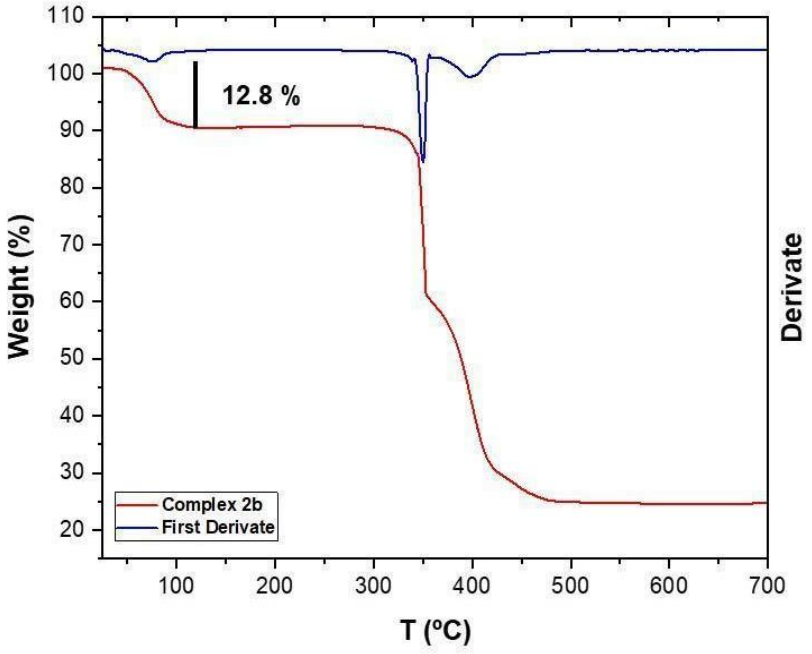

Figure 58. Thermogravimetric curve for complex **2B.**

In the TGA analysis for complex **2C** (Figure 59), it was possible to observe three thermal events before the decomposition of the organic fraction of complex **2C**. In the region 100-160 ºC, a loss of 5.79% of mass is noted, suggesting that in this range the complex loses 3/2 molecules of water and half a molecule of O_2 resulting from the decomposition of the nitrate ion. The sum of the losses from the two thermal events between 180-420 ºC corresponds to 12.12% of mass, this loss may be related to the nitrogenous inorganic fraction in the form of two NO_2 molecules (calculated 11.9%) (Fei et al., 2019). O The solid residue obtained corresponds to 20.8%, considering that this residue is CuO, it is calculated 16.6% of the copper(II) in the complex sample.

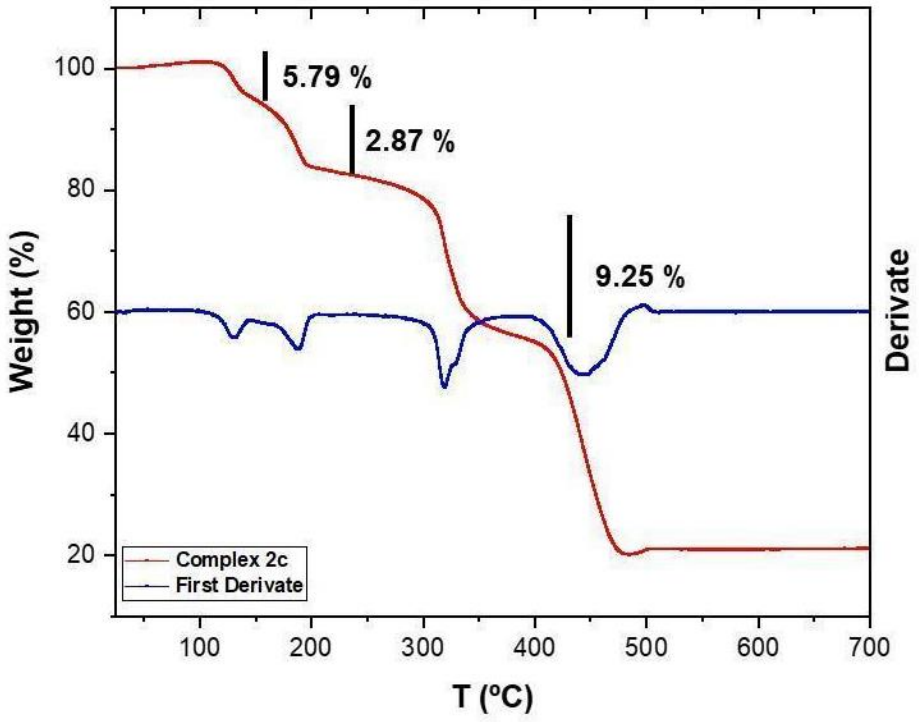

Figure 59. Thermogravimetric curve for complex **2C.**

5.3.2 Characterization the Compounds belonging to the H_2L2 Series

5.3.2.1 Elementar Analysis (CHNS) and Copper content (ICP-OES)

The elemental analysis tests were carried out with the samples in their crystalline form, the results obtained are listed in Table 14:

Table 14. Calculated and experimental elemental analyses of the complexes **2A, 2B** and **2C.**

Complexes	**%C**		**%H**		**%N**		**%Cu**	
	calculated	found	calculated	found	calculated	found	calculated	found
2A	43.3	43.6	3.6	3.7	7.8	7.8	17.6	17.9
2B	52.5	52.4	5.0	4.8	7.7	7.8	17.4	18.2
2C	40.4	39.9	3.4	3.0	10.9	10.6	16.4	16.2

5.3.2.2 Molar conductivity studies

Conductivity is a physical property with broad applications in physicochemical processes. Comparing the conductivity of different solutions can be challenging due to its dependence on concentration. Conversely, molar conductivity is a characteristic property of chemical substances that remains independent of their concentrations (Ali *et al.*, 2013). The molar conductivity of the compounds was measured in DMF at concentrations of 1×10^{-3} mol $L^{-1.}$ The obtained molar conductivity values for the studied complexes are consistent with similar complexes reported in the literature (Ali *et al.*, 2013; Geary, 1971; Santiago *et al.*, 2020).

Similar to other physicochemical methods, molar conductance has been utilized for the structural elucidation of newly synthesized metal complexes. Metal complexes exhibit varying molar conductance values that are characteristic features of their structures. These values often differ for the same complexes when studied in different solvents (Ali *et al.*, 2013; Geary, 1971).

Table 15 lists the obtained molar conductivity values for complexes **2A**, **2B**, and **2C**, along with various types of possible electrolytes in DMF, correlated with data obtained by Geary (1971).

Table 15. Relationship between the molar conductivity data obtained with the electrolyte system.

Complexes	**2A**	**2B**	**2C**
Molar conductance ($\Omega^{-1}cm^2mol^{-1}$)	25.9	2.68	160.4
Electrolyte	1:1	Non-electrolyte	1:2

Complex **2B** exhibits very low molar conductivity, indicating it behaves as a non-electrolyte species. This suggests that in solution, the complex remains in a dimeric form with only solvent exchange occurring at the axial coordination position. On the other hand, complex **2A** displays higher molar conductivity than complex **2B**, confirming its slightly electrolytic nature. Alternatively, it can be considered that some chloride ions may exchange with solvent molecules, allowing for an equilibrium between chloride-coordinated and solvent-coordinated forms. This justifies the higher molar conductivity of complex **2A** compared to complex **2B**, although it remains low when compared to other 1:1 electrolyte under the same conditions (Ali *et al.*, 2013; Geary, 1971).

Complex **2C** exhibits higher molar conductivity compared to complexes **2A** and **2B**, indicating it behaves as a 1:2 type electrolyte. The rationale behind this electrolytic behavior lies in the presence of nitrate ions in the structure, which dissociate upon dissolution in solution. The reaction below illustrates the dissociation process that occurs with complex **2C** in DMF solution:

$$[Cu_2(HL)_2(NO_3)_2]\cdot 2H_2O \rightarrow [Cu_2(HL)_2]^{2+} + 2\ NO_3^- + 2\ H_2O$$

5.3.2.3 Crystal Structure of Complexes by Single Crystal XRD

The complexes **2A**, **2B**, and **2C** were analyzed by single-crystal X-ray diffraction. Table 16 presents the obtained crystallographic parameters.

Table 16. Experimental crystallographic details for complexes **2A, 2B** and **2C.**

Crystal	**Complex 2A**	**Complex 2B**	**Complex 2C**
Chemical formula	$C_{13}H_{13}O_4N_2ClCu$	$C_{32}H_{36}O_8N_4Cu_2$	$C_{13}H_{13}N_3O_7Cu$ (monomer)
*M*r (g mol^{-1})	360.24	731.73	386.80
Crystal system, space group	Monoclinic, $P2_1/c$	Monoclinic, $P2_1/c$	Triclinic, P_{-1}
Temperature (K)	293	296	298
a, *b*, *c* (Å)	12.6740(4), 6.9206(2), 16.1553(5)	6.2379(5), 14.5843(10), 17.5885(11)	7.1609(1) 10.7439(2) 11.0077(3)
β (°)	91.109(3)	94.394(2)	84.989(2)
V (Å^3)	1416.74(7)	1595.39(2)	1774.5(2)
Z	4	2	2
Radiation type	Mo *K*α	Mo *K*α	Cu Kα
μ (mm^{-1})	1.746	1.390	2.516
Crystal size (mm)	0.20 × 0.05 × 0.04	0.07 × 0.08 × 0.35	0.03 × 0.07 × 0.19

Complex **2A** crystallized in the monoclinic system, space group P21/*c*, with four molecules of the complex per unit cell. In the solid state, the complex contains one hydration water molecule per complex unit (Figure 60A).

In coordination chemistry and crystallography, the structural parameter (τ) is used to describe the geometry of coordination complexes. For complexes with a coordination number of 5, the Addison parameter (τ_5) is employed (Addison *et al.*, 1984). For complexes with a coordination number of 4, the parameter τ_4 is used (Yang *et al.*, 2007), which allows estimation of the geometry around the central atom. Copper(II) complexes with a coordination number of 4 can predominantly adopt either a square planar or tetrahedral geometry (Huheey, 1972). Ligand constraints often play a significant role and can induce unusual geometries in copper(I) and copper(II) centers (Yang *et al.*, 2007).

According to Addison *et al.* (1984), τ_5 can be obtained from the expression:

$$\tau_5 = \frac{\beta - \alpha}{60^\circ}$$

Where α and β are the two largest angles around the metal center. If the τ_5 value is closer to 1, the metal center will be closer to a trigonal bipyramidal geometry and D_3h symmetry. Conversely, if τ_5 is closer to 0, the metal center will be nearer to a square pyramidal geometry and C_4v symmetry (Addison *et al.*, 1984).

According to Yang *et al.* (2007) the parameter (τ_4) for complexes with a coordination number of 4 can be estimated using the following equation:

$$\tau_4 = \frac{360^\circ - (\alpha + \beta)}{141^\circ}$$

Where α and β are the two largest angles around the metal center. If the τ_4 value is closer to 1, the metal center is nearer to a tetrahedral geometry and Td symmetry. Conversely, if τ_4 is closer to 0, the metal center is nearer to a square planar geometry and D_4h symmetry (Yang *et al.*, 2007).

The τ_4 value obtained for complex **2A** was 0.13, indicating that the geometry around the copper atom is nearly perfectly square planar, with a mean deviation from the plane of 0.075 Å. The copper(II) ion is coordinated by three donor atoms from the hydrazone ligand and one chloride. The ligand H_2L_2 is deprotonated at the phenolic oxygen O1, i.e., it is present in the HL^- form (Moura *et al.*, 2023).

Complex **2B** is the dimeric form of complex **2A** (Figure 60B), where chloride ions from a pair of mononuclear units are lost, and phenoxo bridges replace them, thus connecting the metal centers and resulting in a single species. This complex crystallizes in the monoclinic system, space group $P2_1/c$, with two dinuclear molecules per unit cell. The resulting dimer is essentially planar with an intermediate distance of 3.0153 Å. Unlike complex **2A**, the ligand is fully deprotonated, coordinated in its iminolated form B_2^{2-}. The average Cu-donor distance in the equatorial plane is 1.940 Å, and a molecule of isopropanol, derived from the recrystallization solvent, occupies a fifth coordination site in the axial position.

Due to the Jahn-Teller effect, the Cu−O4 distance is 2.416 Å. Thus, each copper center is pentacoordinate, exhibiting a distorted square pyramidal geometry with τ_5 = 0.22 (Addison *et al.*, 1984; Moura *et al.*, 2023). The axial ligands on each metal ion point in opposite directions relative to the plane of the dimer. Sangeetha *et al.* (1999) and Gordon *et al.* (2008), reported crystal structures of double-bridged phenoxo dimers of copper(II) complexes containing fully deprotonated ONO *N*-acylhydrazone donor atoms. In these cases, two molecules occupy the axial positions similar to the isopropanol observed in complex **2B**. The intermediate distance found in these examples was 3.041 Å, which is very close to the distance observed for complex **2B**.

Complex **2C** crystallizes in the triclinic system, space group P_{-1} (Figure 60C), with two asymmetric units consisting of a partially deprotonated *N*-acylhydrazone ligand HL^-, a nitrate ion, a copper(II) center, and one water molecule per unit cell. The asymmetric units are organized into a dimeric structure.

Each metal site in the dimer is pentacoordinate, with each copper center exhibiting a slightly distorted square pyramidal geometry with τ_5 = 0.045 (Addison *et al.*, 1984; Moura *et al.*, 2023). In the equatorial plane, the *N*-acylhydrazone ligand acts as a tridentate ligand, with the oxygen of the phenolate ion O3 bridging between the two copper(II) centers. Unlike complex **2B**, the Cu···Cu distance is shorter, with a value of 2.9846 Å. The average Cu-equatorial donor distance is 1.954 Å. An oxygen atom O5 from a nitrate ion occupies the fifth coordination site, bonded axially to each metal site, pointing in opposite directions relative to the dimer plane. The Cu−O5 distance is 2.314 Å, due to the Jahn-Teller effect.

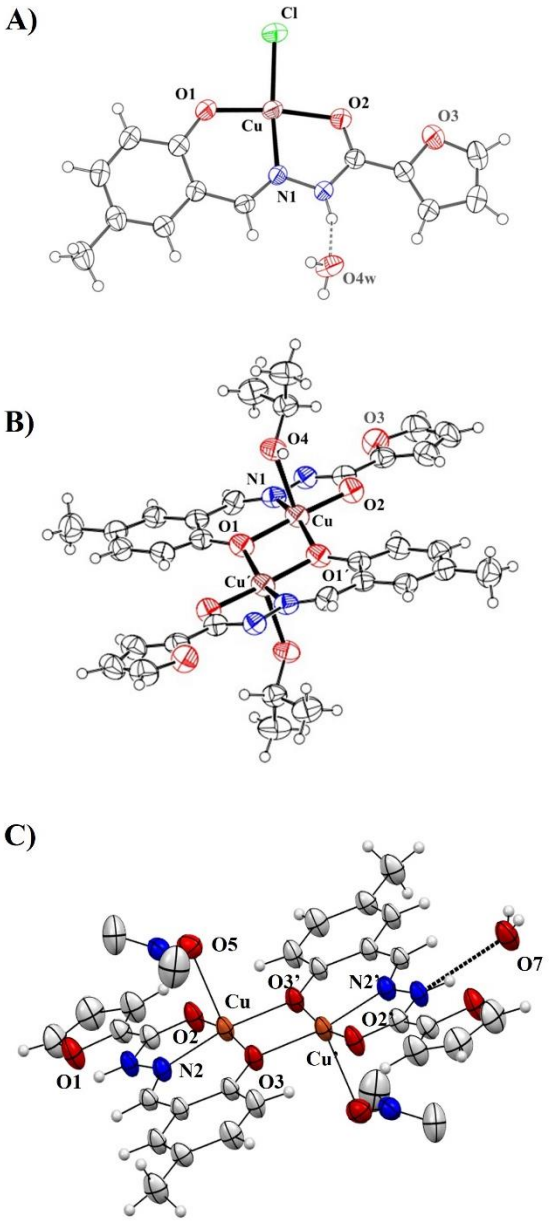

Figure 60. Crystal structure representation of **(A)** the mononuclear complex **2A, (B)** the dimeric form complex **2B** and **C)** the dimeric form complex **2C.** Only the main atoms are labeled. Ellipsoids drawn at the 50% probability level.

Table 17. Select bond distances for **H_2L2** series complexes.

Complex	**2A**	**2B**	**2C**
Bonds	Bond distances / Å		
Cu–Cl	2.2078(6)	–	–
Cu–O1	1.8943(15)	1.944(3)	–
Cu–O1´	–	1.967(3)	–
Cu–O2	1.9694(14)	1.932(3)	1.976(5)
Cu–O4	–	2.416(4)	–
Cu–O3	–	–	1.941(4)
Cu–O3'	–	–	1.960(4)
Cu–O5	–	–	2.314(6)
Cu–N1	1.9359(17)	1.919(4)	–
Cu–N2	–	–	1.939(5)

Table 18. Select bond angles for **H_2L2** series complexes.

Complex	**2A**	**2B**	**2C**	**Complex**	**2A**	**2B**	**2C**
Angles	Bond angles / º			Angles	Bond angles / º		
O1–Cu–Cl	92.63(4)	–	–	O2–Cu–O3	–	–	167.0(2)
O2–Cu–Cl	94.59(5)	–	–	O2–Cu–O3'	–	–	105.44(19)
N1–Cu–Cl	169.63(5)	–	–	O2–Cu–O5	–	–	87.0(2)
O1–Cu–O2	172.21(6)	172.89(14)	–	O2–Cu–N2	–	–	81.0(2)
O1–Cu–O4	–	89.58(13)	–	O3–Cu–O3'	–	–	80.20(19)
O1–Cu–N1	92.61(6)	93.42(15)	–	O3–Cu–O5	–	–	87.0(2)
O2–Cu–O4	–	95.86(13)	–	O3–Cu–N2	–	–	91.9(2)
O2–Cu–N1	80.73(7)	81.56(15)	–	O5–Cu– O3'	–	–	94.1(2)
O1–Cu–O1´	–	79.11(15)	–	O5–Cu–N2	–	–	94.3(2)
O2–Cu–O1´	–	103.96(13)	–	N2–Cu–O3^{i}	–	–	169.7(2)
N1–Cu–O1´	–	159.88(15)	–	Cu–O3–Cu'	–	–	99.80(19)
N1–Cu–O4	–	95.12(14)	–				
O1´–Cu–O4	–	103.41(13)	–				

5.3.2.4 Infrared Vibrational Spectroscopy

Analyzing the infrared spectra obtained for the compounds, it is noted that most of the absorptions observed in the spectrum of the **H_2L2** ligand are still present in their respective complexes. However, some shifts and disappearances of bands, as well as the emergence of new absorptions, in the spectra of complexes **2A**, **2B** and **2C** suggest coordination (Figures 61-63).

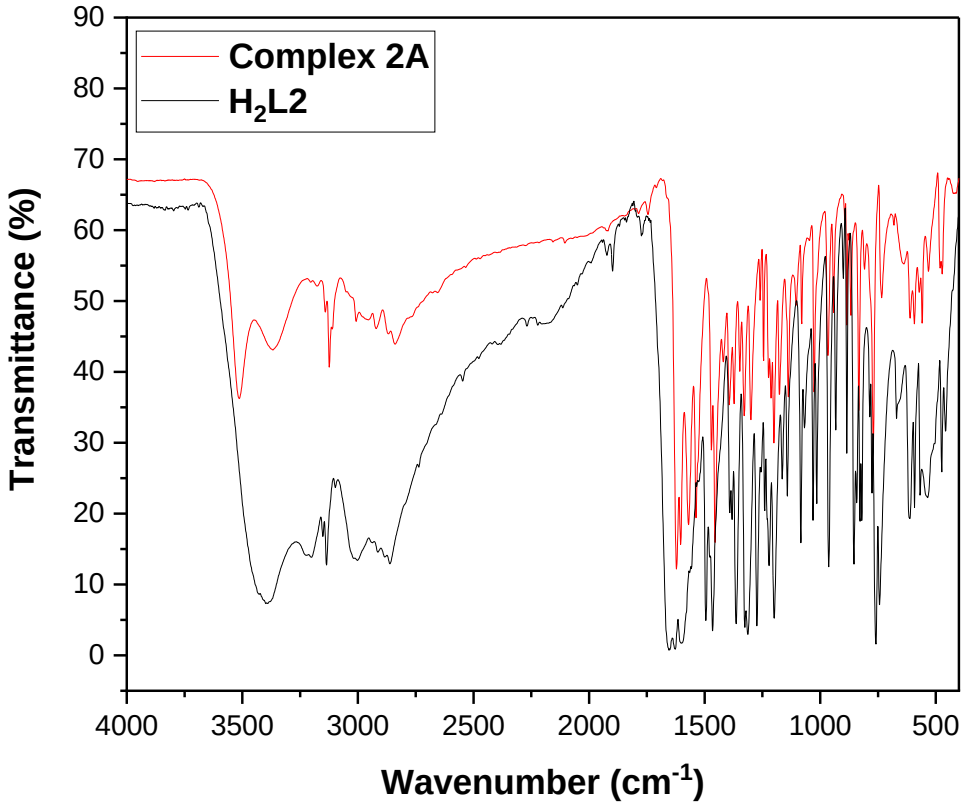

Figure 61. Overlapping of the mid-infrared spectra of **H_2L2** and complex **2A** in KBr, at room temperature.

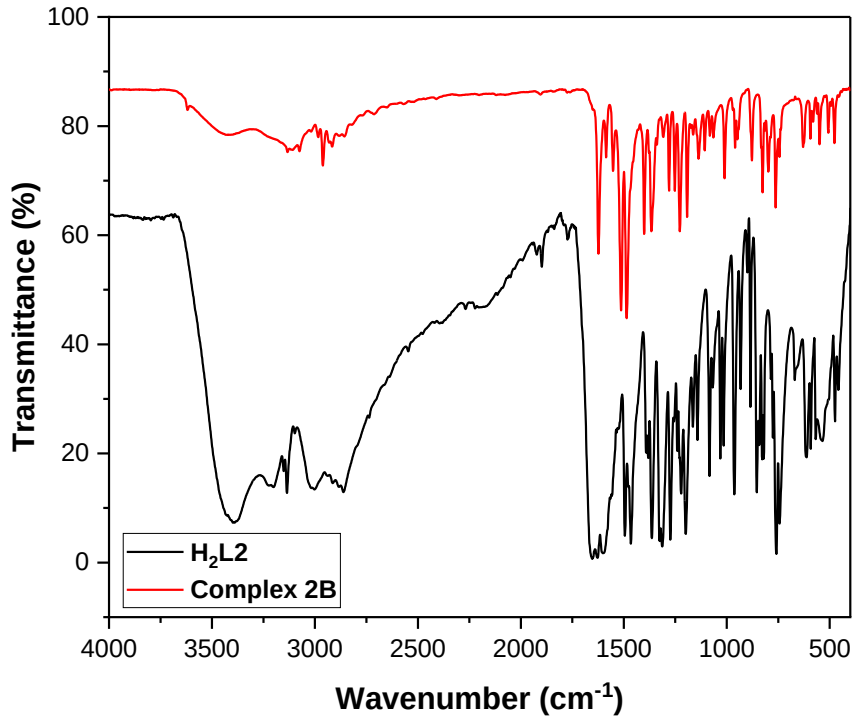

Figure 62. Overlapping of the mid-infrared spectra of **H_2L2** and complex **2B** in KBr, at room temperature.

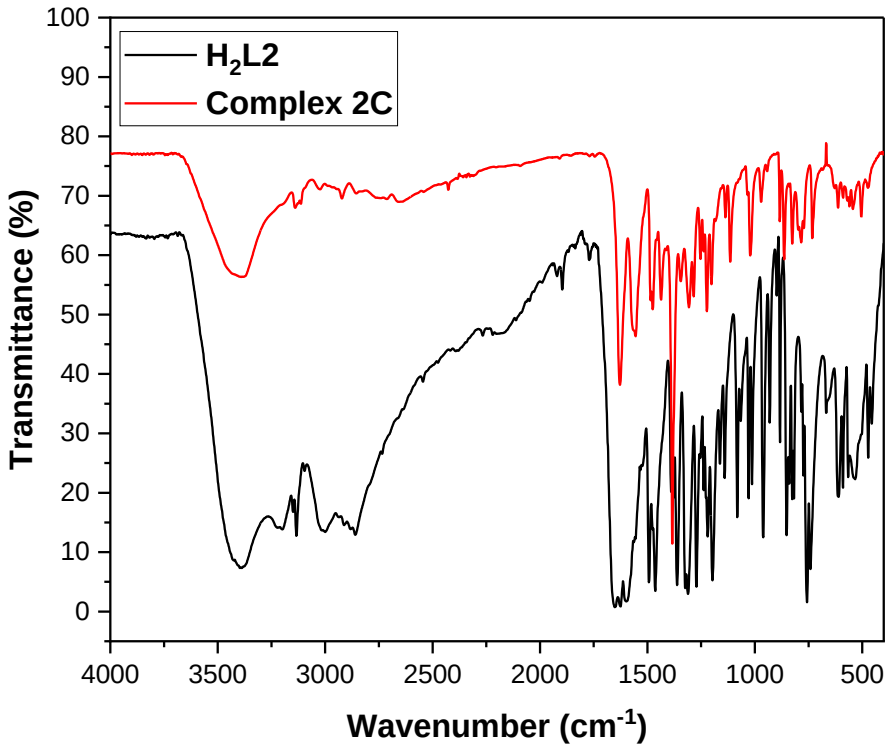

Figure 63. Overlapping of the mid-infrared spectra of **H_2L2** and complex **2C** in KBr, at room temperature.

Table 19. Selected vibrational absorptions (cm^{-1}) for **H_2L2** and their complexes.

Assingment	H_2L2	Complex 2A	Complex 2B	Complex 2C
υN−H	3225	3514	-----	3404
$\upsilon O-H_{phenol}$	3202	-----	-----	-----
υC=O	1653	1622	1513	1630
υC=N	1628	1604	1623	1610
δC=N−H	1495	1394	-----	1568
$\delta C-O-H_{phenol}$	1465	-----	-----	-----
$\upsilon(NO_2)_{ass}$	-----	-----	-----	1383
$\upsilon C=C_{arom}$	1364	1245	1250	1349
$\upsilon C-O_{phenol}$	1326	1373	1228	1345
$\upsilon(NO_2)_{sym}$	-----	-----	-----	1305
$\delta C=C-H_{phenol}$	1313	1300	1228	1281
υN−N	1164	1138	1065	1118
υNO	-----	-----	-----	1020
υCu−O	-----	533	594	540
υCu−N	-----	593	-----	608
δO−Cu−N	-----	473	-----	505

In general, a shift to lower energy bands related to common groups of the ligand with those of the complexes can be observed. This shift suggests coordination, as the ligand's rigidity decreases upon coordination, weakening its bonds and justifying the shift to lower energy values.

Complexes **2A** and **2C** feature ionic species (chloride and nitrate) coordinated to the metal ion. Therefore, it is expected that the N−H group of the hydrazone present in the ligand remains protonated in the complex as a counterion, confirmed by the bands υN−H observed in the complexes at 3514 and 3404 cm^{-1}, respectively. For complex **2B**, the hydrazone band is not observed due to deprotonation.

The carbonyl absorption ν(C=O) shifts from 1653 cm^{-1} in the ligand to 1622 cm^{-1} in complex 2A, 1513 cm^{-1} in complex **2B**, and 1630 cm^{-1} in complex **2C**. The band related to ν(C=O) in complex **2B** is typical of hydrazone coordination in the iminolato form. In addition to these ligand-based bands, some

metal-ligand vibrations were also identified in the spectra of the complexes. Among these, absorptions at 533 cm^{-1} [ν(Cu–O)], 594 cm^{-1} [ν(Cu–O2)], and 540 cm^{-1} were noted for the respective complexes (Moura *et al.*, 2023; Paiva *et al.*, 2024; Silverstein, 2000).

For complex **2C**, bands related to $\upsilon(NO_2)_{ass}$, $\upsilon(NO_2)_{sym}$, and υNO associated with the nitrate ion coordination can be observed. The literature reports that if bands related to the nitrate ion are around 1400-1300 cm^{-1}, the ion is coordinated monodentate in the complex (Nakamoto, 1978). This fact is confirmed by X-ray structure analysis, allowing correlation with the obtained data.

5.3.2.5 Electronic Spectroscopy in UV-Vis

The ligand and the obtained complexes were analyzed by UV-Vis electronic spectroscopy at various concentrations using DMF as the solvent. The UV-Vis spectrum of ligand **H_2L2** (Figure 64) exhibits five main absorptions in the range of 250 to 500 nm, comprising four bands and one shoulder. Upon comparison with its precursors, three of these absorptions are observed in the precursors, associated with transitions of the phenol and/or furan rings. The intense absorptions observed at 292 nm (248.50 ± 150 L mol^{-1} cm^{-1}) and 304 nm (25,700 ± 150 L mol^{-1} cm^{-1}) are potentially related to processes strictly associated with *N*-acylhydrazone, as they are absent in the precursor spectra. On the other hand, the broad band observed at 336 nm (16,500 ± 100 L mol^{-1} cm^{-1}), although also present in the spectrum of 5-methylsalicylaldehyde, exhibits higher molar absorptivity in the ligand, suggesting it also involves contribution from the hydrazone bridge between the rings.

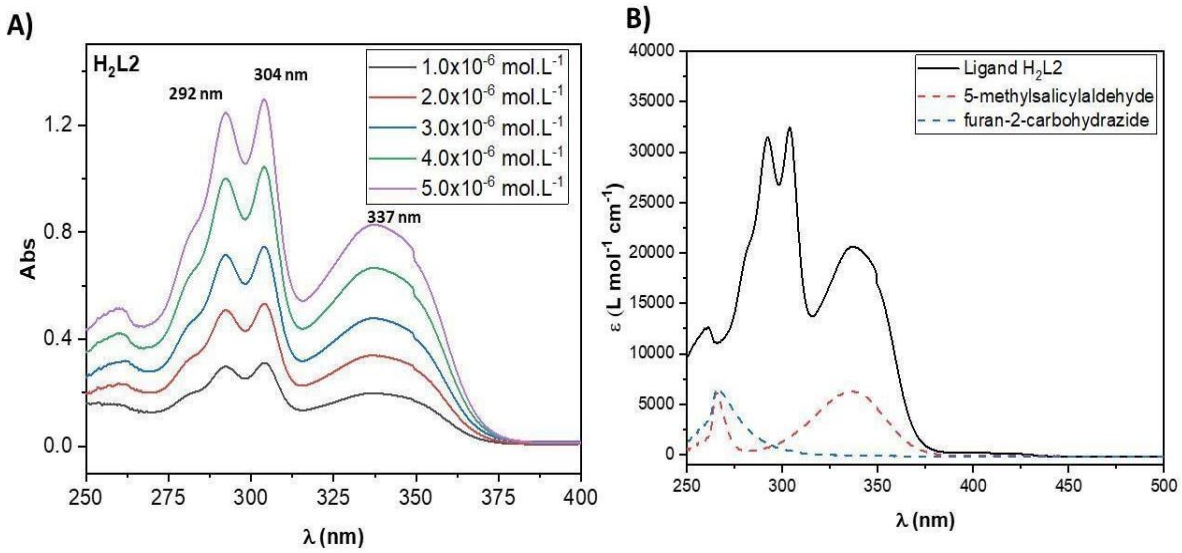

Figure 64. A) Electronic spectrum of the **H_2L2** ligand in solution with DMF, at different concentrations. **B)** Electronic spectra of the ligand in solution with DMF 5×10^{-5} mol L^{-1} and its precursors under the same conditions.

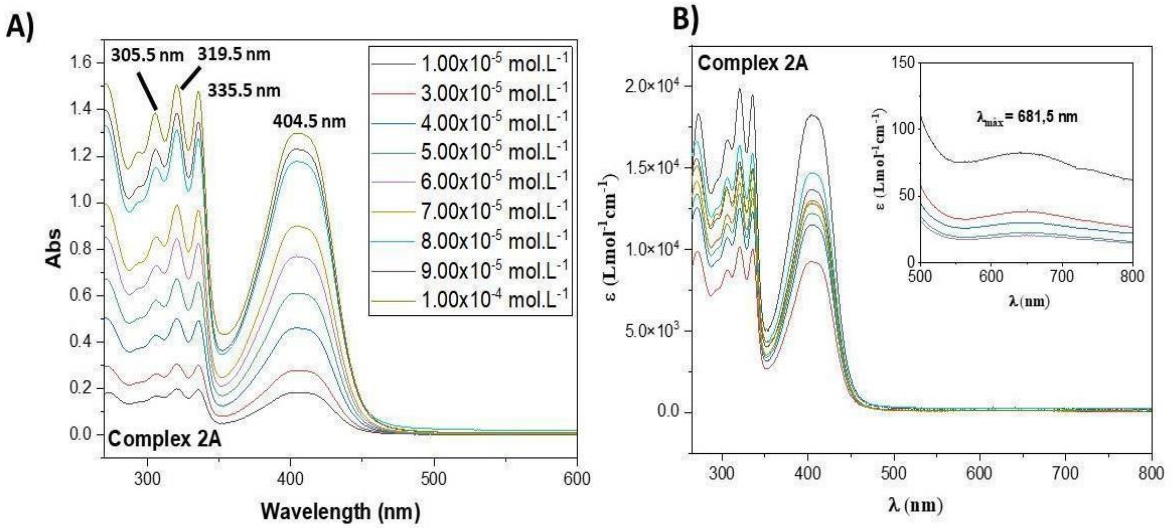

Figure 65. A) Electronic spectrum of complex **2A** in solution with DMF, at different concentrations. **B)** Electronic spectra of complex **2A** in solution with DMF as a function of molar absorptivity in the range of 300-800 nm.

Complex **2A** displays six main absorptions in the range of 250 to 500 nm, consisting of five bands and one shoulder (Figure 65). Upon comparison of the complex spectrum with the ligand, it is evident that five of these absorptions are present in the ligand and three in its precursors, as discussed previously. The intense bands around 250, 305.5 (14,045 ± 788 L mol^{-1} cm^{-1}) nm, and 319.5 (15,355 ± 632 L mol^{-1} cm^{-1}), akin to those in the ligand, are likely associated with processes strictly related to *N*-acylhydrazone, as they are absent in the precursor spectra. The broad band observed at 335.5 (15,126 ± 606 L mol^{-1} cm^{-1}) nm,

although also present in the spectrum of 5-methylsalicylaldehyde, exhibits higher molar absorptivity in both the ligand and complex **2A**, suggesting involvement of the hydrazone bridge between the rings, similar to complexes **2B** and **2C**.

In contrast to the ligand spectrum, the complex **2A** (Figure 65) spectrum shows a broad and intense band around 404.5 (13,413 ± 522 L mol^{-1} cm^{-1}) nm. (Figure 66). This band is attributed to charge transfer from the phenolate ion to the Cu^{2+} metal center. Such a band is present in all copper(II) complexes evaluated in this study and may indicate coordination, as the Cu^{2+} ion can deprotonate the ligand. The band at 681.5 (85.94 ± 1.92 L mol^{-1} cm^{-1}) nm corresponds to a *d-d* transition; its low molar absorptivity can be justified by the Laporte selection rule, which prohibits such electronic transitions, but they can occur due to vibrational states distorting the molecular geometry (vibronic coupling), thereby altering the system's symmetry and allowing the transition to proceed.

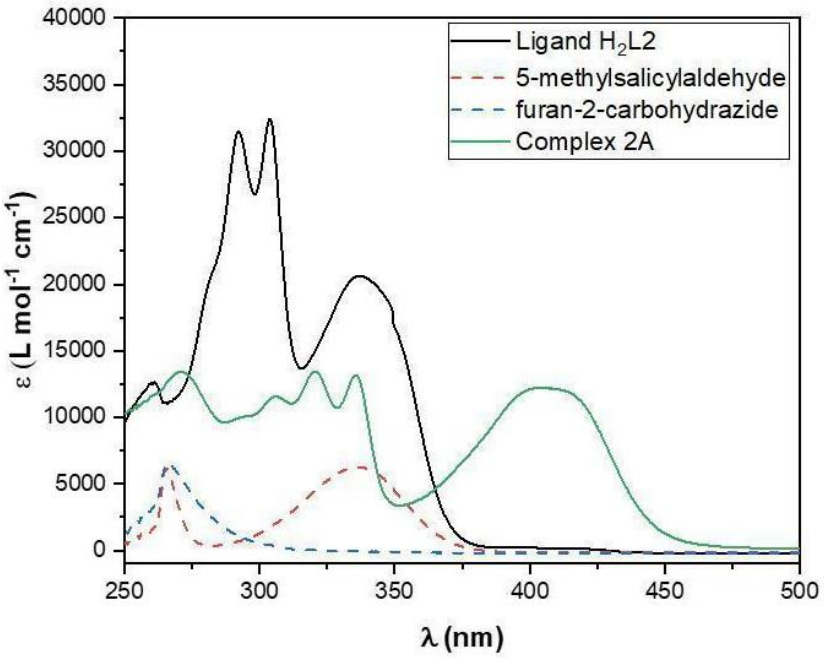

Figure 66. Electronic spectra of **2A**, **H_2L2** and precursors in solution with DMF 5 × 10^{-5} mol L^{-1}.

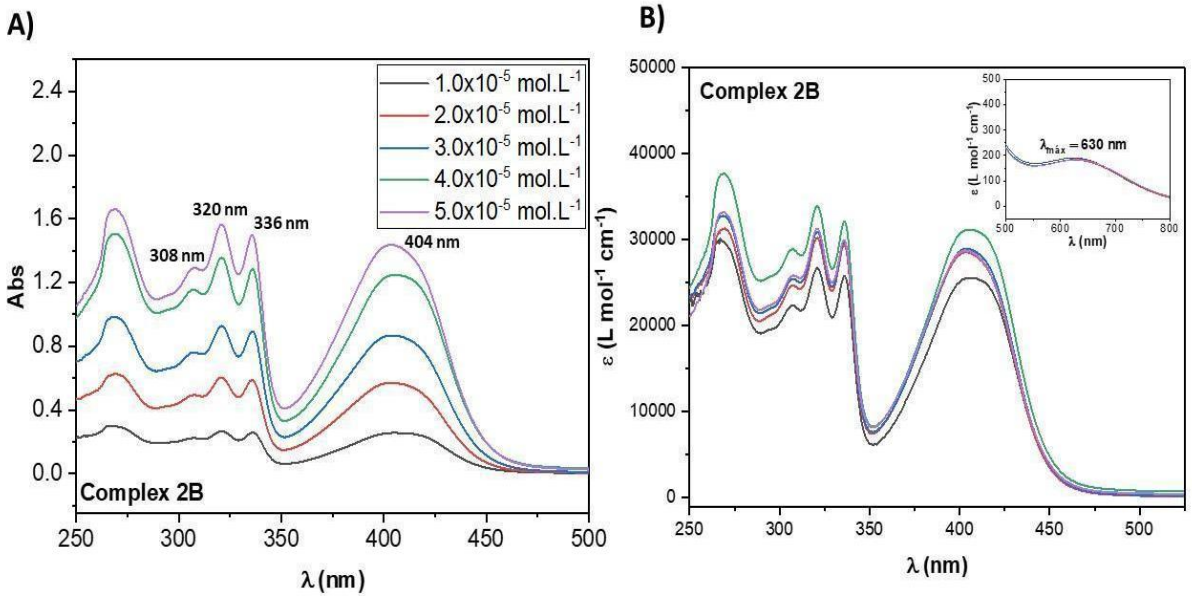

Figure 67. A) Electronic spectrum of complex **2B** in solution with DMF, at different concentrations. **B)** Electronic spectra of complex **2B** in solution with DMF as a function of molar absorptivity in the range of 250-800 nm.

Complex **2B**, like other derivatives derived from the ligand **H_2L2**, exhibits six main absorptions in the range of 250 to 500 nm, comprising five bands and one shoulder (Figure 67). The spectral profile of complex **2B** is similar to that of complex **2A**, given that complex **2B** is the dimeric form of complex **2A**. The intense bands around 270, 308 (27,195 ± 1,358 L mol^{-1} cm^{-1}), and 320 (32,445 ± 1,215 L mol^{-1} cm^{-1}) nm are likely associated with processes strictly related to *N*-acylhydrazone, as these bands are absent in the precursor spectra. The broad band observed at 336 (31,081 ± 1,015 L mol^{-1} cm^{-1}) nm, also seen in the spectrum of 5-methylsalicylaldehyde, exhibits higher molar absorptivity in both the ligand and complex **2B**, suggesting involvement of the hydrazone bridge between the rings, a feature observed in other complexes of this series.

In addition to the aforementioned bands, there is a broad and intense band around 404 (29,870 ± 1,033 L mol^{-1} cm^{-1}) nm, unlike what is observed in the ligand spectrum (Figure 68). This band is attributed to charge transfer from the phenolate ion to the Cu^{2+} metal center. The band at 630 (183 ± 0.91 L mol^{-1} cm^{-1}) nm is related to a *d-d* transition.

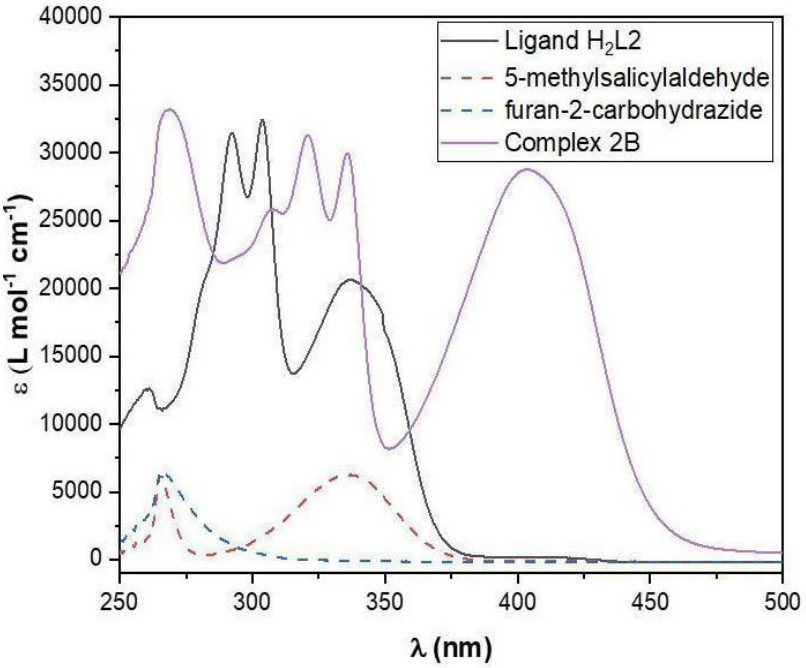

Figure 68. Electronic spectra of **2B**, **H_2L2** and precursors in solution with DMF 5×10^{-5} mol L^{-1}.

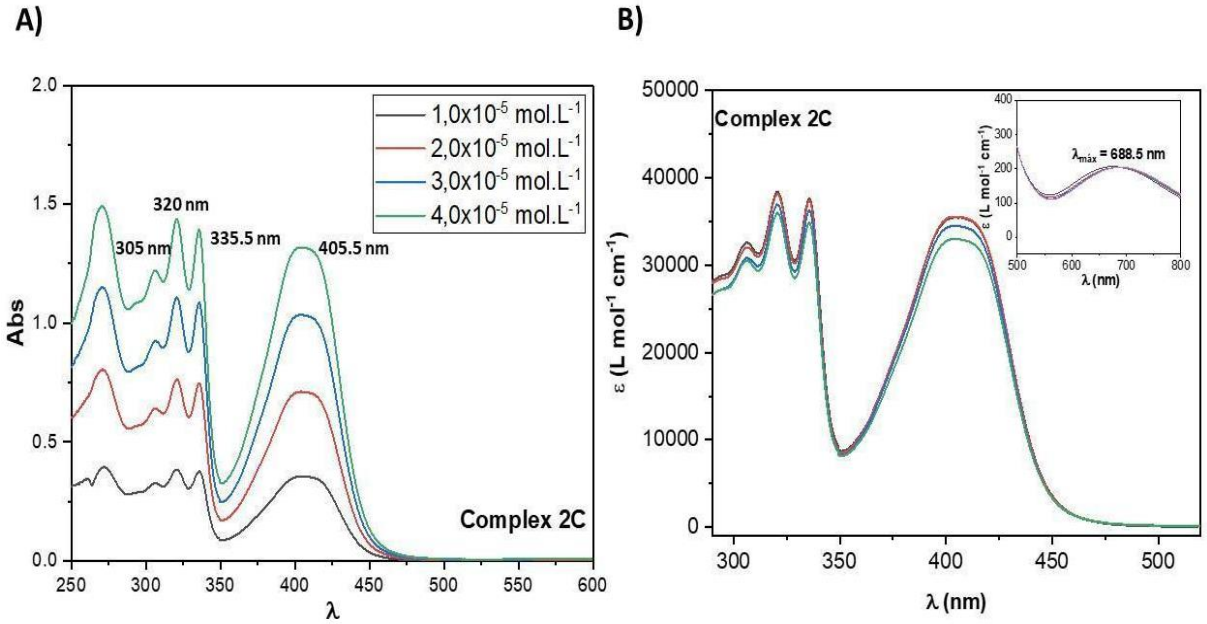

Figure 69. A) Electronic spectrum of **2C** in solution with DMF, at different concentrations. **B)** Electronic spectra of **2C** in solution with DMF as a function of molar absorptivity in the range of 250-800 nm.

The electronic spectrum of the complex **2C** (Figure 69) exhibits six main absorptions in the range of 250 to 500 nm, comprising five bands and one shoulder. The spectral profile of complex **2C** is similar to that of other complexes in the **H_2L2** series. The intense bands around 270, 305 (20,114 ± 461 L mol^{-1} cm^{-1}), and 320 (35,905 ± 698 L mol^{-1} cm^{-1}), as discussed earlier, are likely associated with specific processes related to *N*-acylhydrazone, as they are absent in the precursors of the **H_2L2** ligand. The broad band observed at 335.5 (34,985 ± 848 L mol^{-1} cm^{-1}) nm, also seen in the spectrum of 5-methylsalicylaldehyde, exhibits higher molar absorptivity in both the ligand and complex **2C**, suggesting involvement of the hydrazone bridge between the rings, consistent with other complexes in the series.

In addition to the aforementioned bands, there is a broad and intense band around 405.5 (33,162 ± 878 L mol^{-1} cm^{-1}) nm, unlike what is observed in the ligand spectrum (Figure 70). This band is attributed to charge transfer from the phenolate ion to the Cu^{2+} metal center. The band at 688.5 (204.45 ± 0.53 L mol^{-1} cm^{-1}) nm is related to a *d-d* transition.

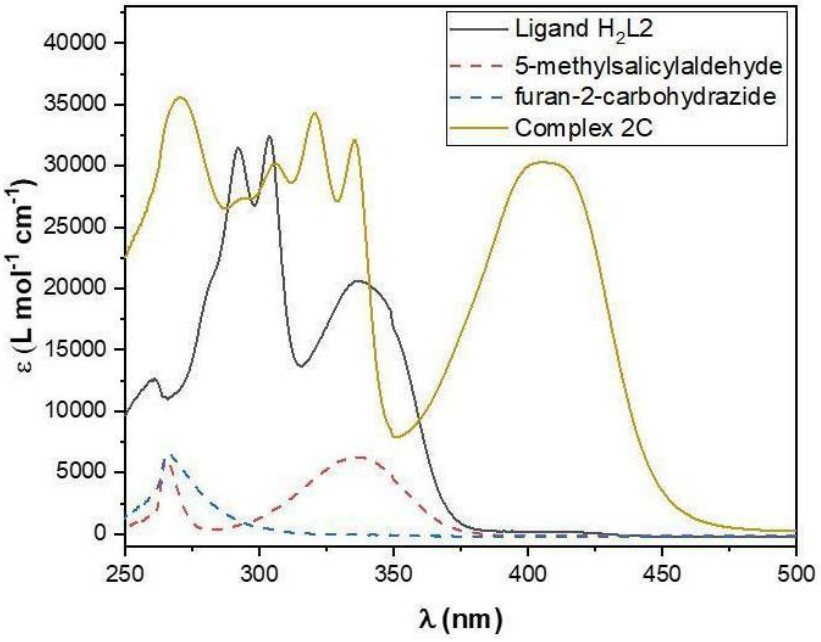

Figure 70. Electronic spectra of **2C**, **H_2L2** and precursors in solution with DMF 5 × 10^{-5} mol L^{-1}.

Figure 71 displays the UV-Vis electronic spectra of the ligand and its respective complexes in the range of 250-500 nm. The spectra profiles of the complexes are quite similar in this region, differing in their molar absorptivity values, given that complexes **2B** and **2C** are dimers and, supposedly in solution, can dissociate into mononuclear forms similar to complex **2A**. Thus, the presence of the iminolate tautomeric form in the ligand **H_2L2** and in complex **2B**, and especially as dimers in complexes **2B** and **2C**, where the number of absorptive groups is doubled compared to complex **2A**, may explain the observed changes in molar absorptivity values. Bands related to ligand transitions undergo a bathochromic shift upon coordination.

The bands associated with *d-d* transitions are consistent with the presence of a square planar copper center in the mononuclear complex **2A** and two in the binuclear complexes **2B** and **2C**, indicating that the isopropanol ligands are likely lost upon dissolution of dimer **2B** in DMF, as well as the nitrate ligands in the dimer of complex **2C**. Differences in energy between complexes **2A**, **2B**, and **2C** are perceptible in this region due to the unequal coordination spheres of these complexes.

Literature reports indicate that the electronic spectrum in the solid state (Nujol-mull transmission) of mononuclear species $[Cu(Hsa)Cl(OH_2)]\cdot H_2O$ shows a maximum d-d absorption at 680 nm (Chan *et al.*, 1995). On the other hand, the electronic spectrum of the methanolic solution of the dimer $[Cu(bhsNO_2)OH_2]_2$ exhibits a weak band at 640 nm, which can be compared with complexes **2B** and **2C** (Sangeetha *et al.*, 1999). Additionally, the solid-state spectrum of the dinuclear complex $[Cu(sb)]_2$ has its maximum *d-d* absorption at 615 nm (Ainscough *et al.*, 1998). Data obtained from the literature for analogous complexes suggest that mononuclear square planar complexes have a maximum *d-d* absorption transition around 680 nm, whereas dinuclear square planar complexes have a maximum d-d absorption transition around 615-640 nm.

Analyzing the electronic spectra in the 500-800 nm range for the complexes, it is observed that complex **2A** exhibits a maximum *d-d* absorption at 681.5 nm, suggesting that even in solution, the complex maintains its square planar structure, where the chloride ligand can be substituted by a solvent molecule. Complex **2B** shows *d-d* absorption at 630 nm, indicating that the complex maintains its dimeric square planar structure. In contrast, complex **2C**,

which is a dimer in the solid state, shows *d-d* absorption at 688.5 nm, suggesting that the complex dissociates in solution, forming two mononuclear square planar species analogous to complex **2A**.

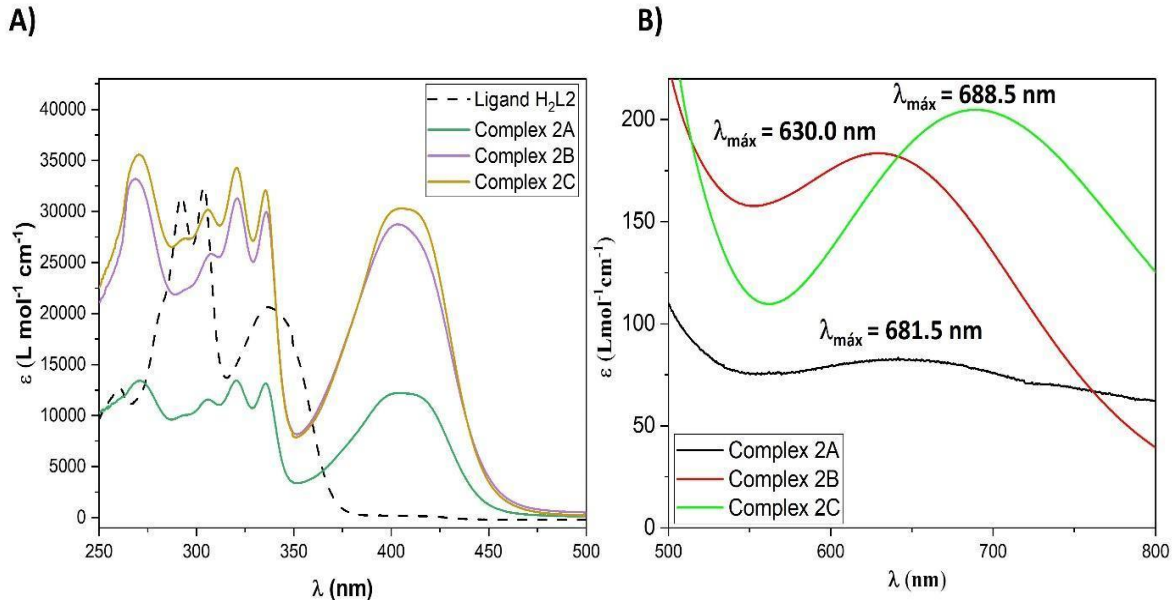

Figure 71. A) Electronic spectra of the ligand and its complexes in DMF solution 5×10^{-5} mol L^{-1} in the range 250-500 nm relating to molar absorptivity. **B)** Electronic spectra of complexes **2A**, **2B** and **2C** in DMF solution 5×10^{-3} mol L^{-1} in the range 500-600 nm relating to molar absorption.

5.3.2.6 Diffuse Reflectance

The data obtained through diffuse reflectance for the **H_2L2** series complexes enable the exploration of the structural modifications that these complexes may or may not undergo in solution. The complexes were diluted in barium sulfate.

Figure 72 presents the electronic spectrum obtained via diffuse reflectance of the **2A** complex. The spectrum reveals four absorption bands identified through band deconvolution. The band at 258 nm can be correlated with the band around 270 nm observed in the ligand and its precursors, potentially associated with conjugated bonds in the aromatic rings. The band at 319.5 nm is attributed to the *N*-acylhydrazone, as it is not observable in the electronic spectra of the precursors and ligand in solution, suggesting a charge transfer from the hydrazone to the Cu^{2+} metal ion. The characteristic charge transfer band from the phenolate ion to Cu^{2+} is observed at 397 nm, while the band related to the *d-d* transition is found at 716 nm.

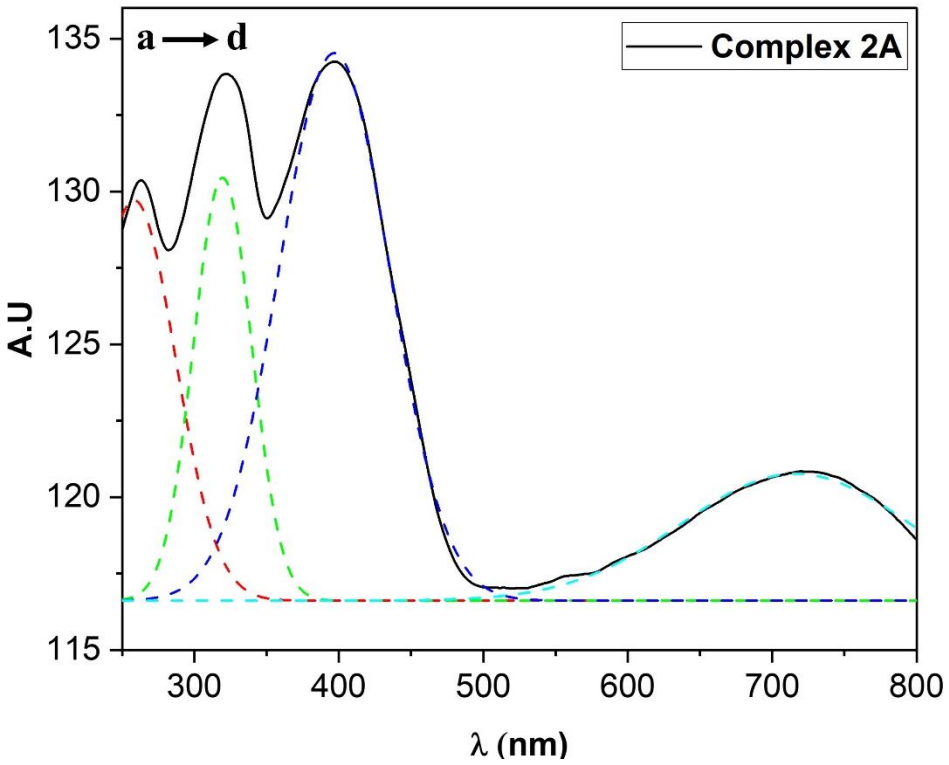

Figure 72. Electronic diffuse reflectance spectrum of **2A,** in black. Main components obtained by band fitting: a) 258 nm, b) 319.5 nm, c) 397 nm and d) 716 nm.

The electronic spectrum obtained via diffuse reflectance for the **2B** complex is shown in Figure 73, where five bands are observed through band deconvolution. Notably, the band at 255 nm can be correlated with the band at 270 nm observed for the ligand and its precursors. This band is likely associated with the conjugated double bonds present in the aromatic rings of phenol and furan. The bands at 312 and 332 nm are related solely to the hydrazone moiety. The band at 388 nm can be attributed to charge transfer from the phenolate ion to Cu^{2+}, while the band at 688 nm corresponds to the characteristic *d-d* transition.

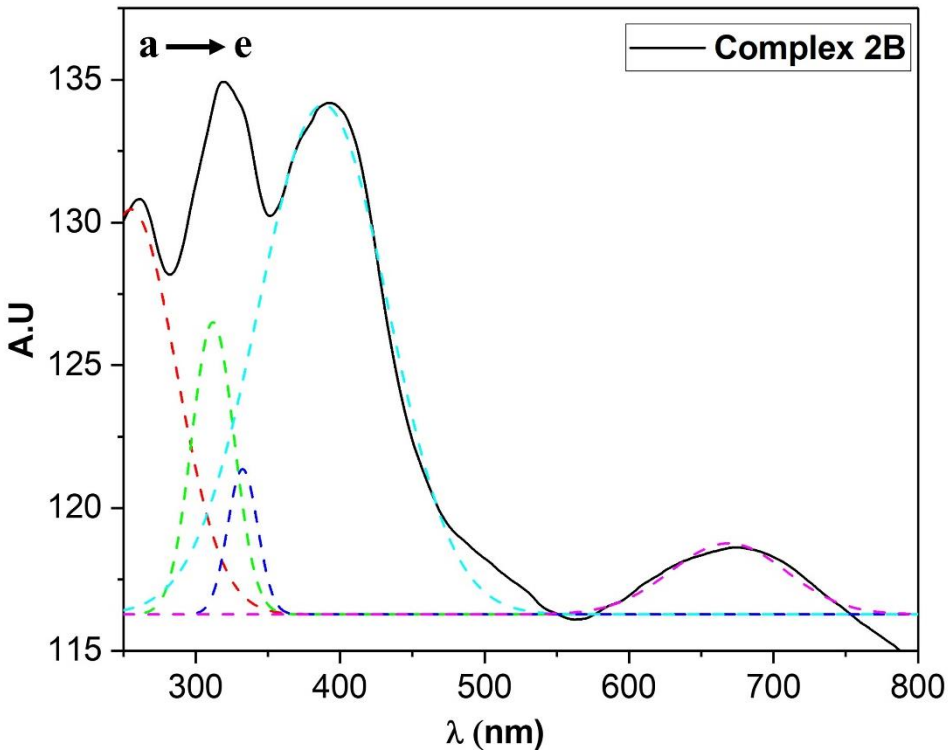

Figure 73. Electronic diffuse reflectance spectrum of **2B,** in black. Main components obtained by band fitting: a) 255 nm, b) 312 nm, c) 332.5 nm, d) 388 nm and e) 688 nm.

The electronic spectrum of the **2C** complex, obtained via diffuse reflectance and shown in Figure 74, reveals six bands identified through band deconvolution. Some of these bands are analogous to those previously discussed for the **2A** and **2B** complexes, such as the bands at 251, 311, and 398 nm, which are related to aromatic conjugated double bonds, the hydrazone bridge, and charge transfer from the phenolate ion to the Cu(II) metal ion, respectively. The bands observed at 507, 636, and 715 nm are associated with *d-d* transitions in the Cu(II) ion and are typically observed as a broad band in the range of 600-700 nm, rather than as distinct peaks.

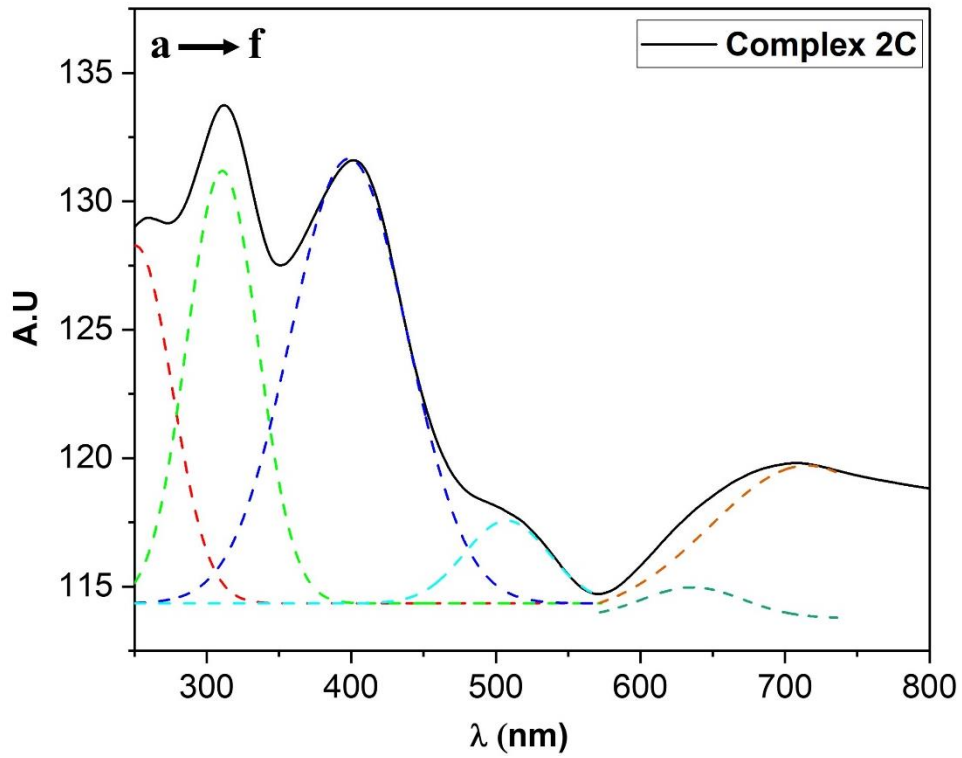

Figure 74. Electronic diffuse reflectance spectrum of **2C,** in black. Main components obtained by band fitting: a) 251 nm, b) 311 nm, c) 398 nm, d) 507 nm, e) 636 nm and f) 715 nm.

Table 20. Comparison of electronic spectra by diffuse reflectance with those obtained in solution for complexes of the **H_2L2** series.

Complexes	**Transitions**							
	precursors-related		*N*-acylhydrazone		Phenolate → Cu^{2+}		*d-d* transition	
	DRIFTS (nm)	UV-Vis (nm)	DRIFTS (nm)	UV-Vis (nm)	DRIFTS (nm)	UV-Vis (nm)	DRIFTS (nm)	UV-Vis (nm)
2A	258	250	319.5	319.5	397	404.5	716	681.5
2B	255	270	311	308	388	404.5	688	630
2C	251	270	312	305	398	405.5	715	688.5

The spectroscopic data presented in Table 20 correlate the λ_{max} values obtained from electronic spectra in solution and in the solid state via diffuse reflectance for the **H_2L2** series complexes. Analysis of the data reveals that some common bands exhibit significant shifts, particularly those associated with ligand-to-metal charge transfer and *d-d* transitions. These observations are consistent with similar complexes reported in the literature (Billing & Underhill, 1968; Calinescu *et al.*, 2008; Moura *et al.*, 2023; Sadhukhan *et al.*, 2019).

Bands related to double bonds in the aromatic ring (ILCT) show shifts; specifically, complex **2A** exhibits a bathochromic shift, whereas complexes **2B** and **2C** display hypsochromic shifts. Bands associated with the hydrazone bridge show a bathochromic shift, but no shift is observed in complex **2A**, suggesting that in solution, the energy of this band is the same as in the solid state. The characteristic charge transfer band from the phenolate ion to Cu(II) shows a considerable hypsochromic shift, indicating that charge transfer in solution occurs at lower energy.

The *d-d* transitions also exhibit shifts when comparing their diffuse reflectance spectra to those obtained in solution, suggesting a significant change in the coordination sphere of the Cu(II) ion, with complex **2B** showing the greatest variation. For complexes **2A** and **2C**, the values are close, confirming that complex **2C** does not maintain its dimeric integrity in solution, instead forming a monomeric species analogous to complex **2A** (Moura *et al.*, 2023).

5.3.2.7 EPR Spectroscopy

Electron Paramagnetic Resonance (EPR) is a branch of spectroscopy in the microwave region that allows the study of electromagnetic radiation absorption by materials containing atoms or molecules with an unpaired electron in the presence of external static magnetic fields. In this context, the total electronic spin angular momentum of the atoms or molecules is $S > 0$, and the material exhibits paramagnetic behavior. Energy absorption from the electromagnetic field occurs resonantly, inducing transitions between the Zeeman sublevels of the unpaired electrons. EPR does not occur in materials where all electrons are paired due to the Pauli Exclusion Principle. Therefore, substances active in EPR include free organic radicals, transition metal ions, metals, crystals with defects, and so on. Consequently, EPR provides insights into the structures of synthesized complexes: mononuclear complexes will be paramagnetic, while binuclear complexes will be diamagnetic and silent in EPR. Additionally, the technique offers information about the coordination sphere of complexes, aiding in the elucidation of the geometry around the metal ion (Bray, 1969; Eaton & Eaton, 1995; Pake, 1962).

The complexes were evaluated both in the solid state and in DMF solution (77K). In the solid state, complex **2B** (Figure 75A). is silent due to its dimeric nature, while complex **2A** is paramagnetic in both the solid state and in solution, exhibiting a characteristic axial spectrum with additional features of an unknown paramagnetic impurity (Figure 75B). This impedes the observation of hyperfine splitting under these conditions. Complex **2C** is virtually silent in the solid state (Figure 77); however, in DMF solution, it displays an axial spectrum with hyperfine splitting patterns related to copper, indicating that the dimer obtained in the solid state dissociates into its respective monomers upon dissolution in DMF. The EPR data are summarized in Table 21.

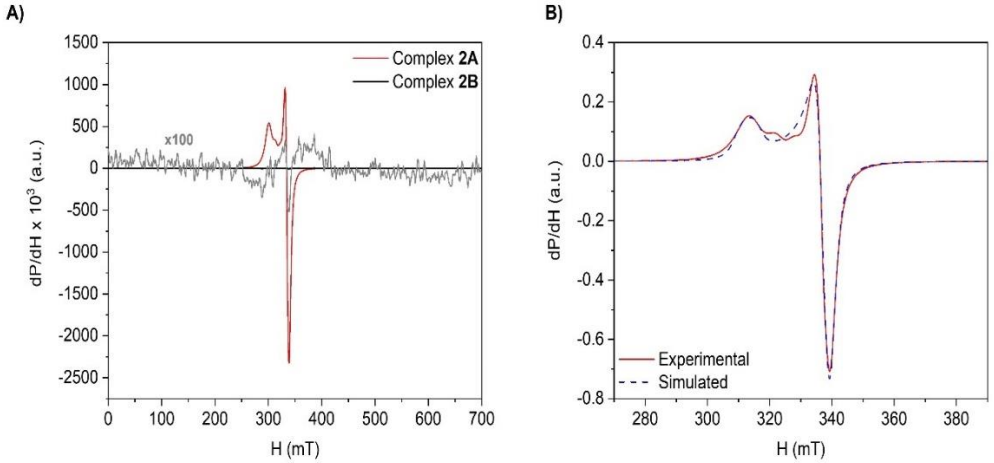

Figure 75. X-band EPR spectra in the solid state, at room temperature, of **(A)** complexes **2A** and **2B** (a 100x amplification of the spectrum of **2B** is included as a light gray curve for the sake of comparison) and **(B)** compound **2A** in a more detailed measurement, along with the simulated profile for the main set of peaks.

Table 21. EPR parameters for complexes **2A, 2B** and **2C** in the solid state (r.t.) and in frozen (77 K) DMF solution.

Complexes	**Component(s) A (copper-containing)**			
	$g_{//}$	$g_{\perp}$	$A_{//}$ (10^{-4} cm^{-1})	$A_{\perp}$ (10^{-4} cm^{-1})
	Solid (r.t. – 300 K)			
2A	2.22	2.07	–	–
	DMF solution (77 K)			
2A	2.21	2.06	182	12.0
2B	2.24	2.05	178	1.0
2C	2.26	2.05	165	11.7

EPR data can provide information on the ground states of the d_{x2-y2} and d_{z2} orbitals based on g-values. The g-value is a primary empirical parameter that characterizes the response of a paramagnetic species, providing a quantitative measure of the analyte's magnetic moment and being sensitive to electronic changes in the compound's structure.

The fact that g// > g⊥ > 2.0023 indicates unpaired electron localization in the d_{x2-y2} orbital of copper, suggesting tetragonal symmetry around the metal center, consistent with the crystal structure of complex **2A** (Anacona *et al.*, 2015; Garribba & Micera, 2006). Conversely, when complex **2A** is dissolved in a frozen DMF solution, it exhibits an axial spectrum with the characteristic four-line pattern of copper. However, a more detailed analysis reveals at least two sets of peaks, suggesting the coexistence of a pair of species in the medium. Based on conductometric experiments, these peaks can be attributed to the original complex **2A** and to the solvent-exchanged complex $[Cu(HL)DMF]^+$. The Sakaguchi ratio (Sakaguchi & Addison, 1979) g // / A // was calculated to be 121 cm^{-1}, indicating that the square planar geometry is maintained after dissolution of complex **2A**. Moreover, the derivative obtained in DMF solution, $[Cu(HL)DMF]^+$, shows a higher g// value, suggesting an NO_3-type coordination.

The EPR spectrum of complex **2B** in DMF solution (Figure 76B) exhibits a profile very similar to that of complex **2A** (Figure 76A), albeit with lower intensity. This suggests that under these conditions, a fraction of the dimer is dissociated, yielding the EPR-active mononuclear species [Cu(L)DMF], for which g// and g⊥ values of 2.24 and 2.05 were determined. A Sakaguchi ratio of 126 cm^{-1} was calculated, again indicating a square planar geometry. Conversely, it is likely that most of the EPR-silent dimer remains in equilibrium in solution.

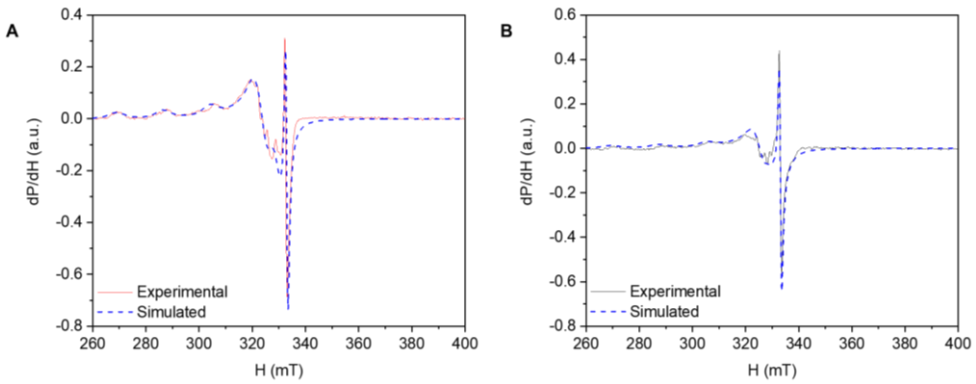

Figure 76. X-band EPR spectra in frozen DMF (77 K) of **(A)** complex **2A** and **(B)** complex **2B**. Simulated profiles are given as dashed blue lines.

For the EPR spectrum of complex **2C**, the observed g// > g⊥ > 2.0023 suggests the localization of unpaired electrons in the d_{x2-y2} orbital of copper, indicating a strongly distorted tetragonal symmetry around the metal ion center, as the obtained Sakaguchi ratio is 137 cm^{-1}. The data suggest that in DMF solution, complex **2C** dissociates into its monomer $[Cu(HL)DMF]^+$, which is isostructural with the species formed when complex **2A** is in DMF solution.

The covalency parameter (α^2) was estimated for the obtained complexes using the equation proposed by Kivelson and Neiman (Kivelson & Neiman, 1961).

$$\alpha^2 = \left(\frac{A_\parallel}{0.036}\right) + (g_\parallel - 2.0023) + \frac{3}{7}(g_\perp - 2.0023) + 0.04$$

If the value of α^2 is 0.5, it suggests complete covalent bonding, whereas a value of 1.0 indicates entirely ionic bonding. For complexes **2A**, **2B**, and **2C**, the following α^2 values were obtained: 0.77, 0.79, and 0.78, respectively, indicating that the metal-donor bonds in these complexes exhibit an intermediate covalent character.

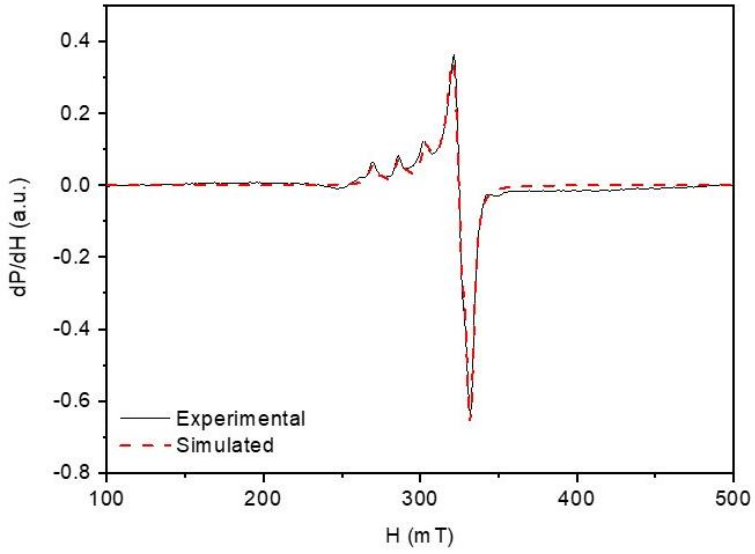

Figure 77. X-band EPR spectra of complex **2C** in frozen (77 K) solution of DMF.

5.3.2.8 Electrochemical behavior - Cyclic Voltammetry

The electrochemical behavior of the **H_2L2** system was evaluated by cyclic voltammetry, in a three-electrode system, in a DMF solution containing 0.1 mol/L of $TBAPF_6$ as supporting electrolyte in N_2 at room temperature. The voltammograms of the complexes and the **H_2L2** ligand are shown below and were

obtained at different scan rate.

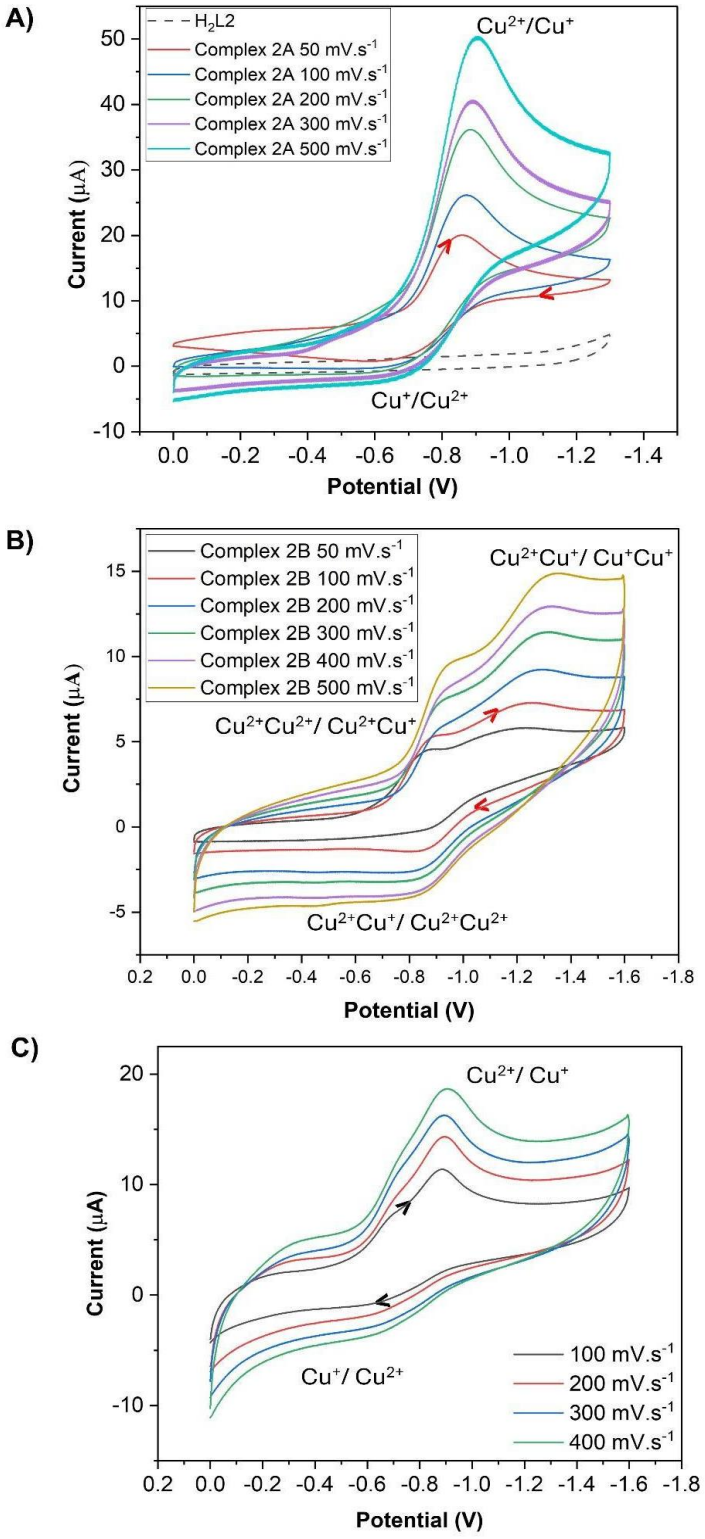

Figure 78. (A) Representative cyclic voltammograms of complex **2A**, at different scan rates, measured in DMF/0.1 mol L^{-1} $TBAPF_6$ (25 °C), using a GCE as the working electrode. The cyclic voltammogram of ligand **H_2L2** was included for the sake of comparison (black dashed curve). (B) Series of representative cyclic voltammograms of complex **2B**, at different scan rates, under the same conditions. (C) Series of representative cyclic voltammograms of complex **2C**, at different scan rates, under the same conditions.

From the voltammograms of the complexes obtained and some correlations, it is possible to obtain electrochemical parameters that can indicate the number of electrons involved (n), the redox mechanism involved, the transport process and even the transfer coefficient (α) (Abbar & Nandibewoor, 2012).

The relationship between the square root of the scan rate and the peak current provides insights into the type of transport process in cyclic voltammetry (Abbar & Nandibewoor, 2012). Analyzing this relationship for the studied ligands reveals a linear correlation, indicating that the system is diffusion-controlled (Abbar & Nandibewoor, 2012; Gosser, 1993). This is further confirmed by the linear relationship between the logarithm of the potential and the logarithm of the scan rate, where the slope coefficient value being less than or approximately equal to 0.5 suggests diffusion control (Laviron *et al.*, 1980).

Table 22. Estimated electrochemical parameters for the studied complexes.

Complex	**2A**	**2B**	**2C**
E_{pa} **(V *vs* Ag/AgCl)**	–0.60	–0.84	–0.61
$E_{pa½}$ **(V *vs* Ag/AgCl)**	---	–0.91	–0.66
α_a	---	0.66	1.19
n_a	---	1.33	0.80
E_{pc1} **(V *vs* Ag/AgCl)**	–0.87	–0.89	–0.70
$E_{pc1½}$ **(V *vs* Ag/AgCl)**	–0.73	–0.75	---
α_{c1}	0.52	0.19	---
n_{c1}	0.65	1.89	---
E_{pc2} **(V *vs* Ag/AgCl)**	---	–1.25	–0.88
$E_{pc2½}$ **(V *vs* Ag/AgCl)**	---	–0.80	–0.64
α_{c2}	---	0.19	0.62
n_{c2}	---	0.62	0.68

Analyzing graph, figure 78A, it is observed that the ligand is not electroactive within the evaluated potential range. Comparing the data obtained from Table 22 and Figure 78, a cathodic peak at –0.87 V vs Ag/AgCl and a poorly defined shoulder related to the anodic process around –0.60 V vs Ag/AgCl are observed, suggesting an irreversible process. The cathodic potential was analyzed, suggesting the involvement of one electron in the process, possibly related to the

Cu^{2+}/Cu^{+} redox pair, consistent with its mononuclear nature.

In the voltammograms of complexes **2B** and **2C** in Figures 78B and 78C, multiple redox processes are observed. In complex **2B**, two cathodic peaks are evident at -0.89 and –1.25 V vs Ag/AgCl. By comparing electrochemical parameters, it can be suggested that the first cathodic peak involves two electrons in the process. One of these electrons is likely associated with the reduction of the azomethine group, which may occur at a potential close to when the ligand is coordinated, while the other electron is involved in the redox process related to the Cu^{2+}/Cu^{+} couple. For the second cathodic process, occurring around –1.25 V, one electron is estimated to be involved, possibly related to the redox couple Cu^{2+}/Cu^{+} and Cu^{+}/Cu^{+}. The second cathodic process, occurring around –1.25 V, involves one electron, likely related to the Cu^{2+}/Cu^{+} redox pair. This process is completely irreversible, suggesting rapid decomposition of the fully reduced form of the complex, as reported by Torelli *et al.* (2000) for a similar dicopper compound (Torelli *et al.*, 2000). This provides clear evidence that complex **2B** largely preserves its dimeric nature after dissolution in DMF. Sangeetha *et al.* (1999) reported, for the dimer $[Cu(bhsNO_2)OH_2]_2$, a pair of consecutive reduction responses at –0.63 and –1.25 V vs Ag/AgCl attributed to the processes $Cu^{2+}Cu^{2+}/Cu^{2+}Cu^{+}$ and $Cu^{2+}Cu^{+}$ /$Cu^{+}Cu^{+}$ (Sangeetha *et al.*, 1999). In the anodic part, only an electrochemical signal with an anodic peak around –0.85 V vs Ag/AgCl can be observed, possibly related to the $Cu^{+}Cu^{+}/Cu^{2+}Cu^{2+}$ redox couple. Obtaining only one anodic peak agrees with analogous complexes synthesized in the literature (Sangeetha *et al.*, 1999; Torelli *et al.*, 2000).

Complex **2C** also exhibits two cathodic peaks similar to those of complex **2B**. However, the cathodic peak around –0.70 V vs Ag/AgCl is poorly defined, unlike complex **2B**. Thus, the reliability of this peak is low, precluding Tofel plot analysis. Nonetheless, its presence may indicate that complex **2C** does not remain in its dimeric form in DMF solution, potentially dissociating into two parts akin to complex **2A**. The second cathodic peak, well-defined at around –0.88 V vs Ag/AgCl, involves one electron in the redox process, possibly related to the Cu^{2+}/Cu^{+} pair, assuming the complex does not maintain its dimeric integrity.

Comparing the obtained data reveals that both complexes **2A** and **2B**, as well as **2C**, exhibit a redox event around −0.85 V related to the Cu^{2+}/Cu^{+} redox pair. Figure 78A shows a poorly defined shoulder related to anodic process around −0.61 V vs Ag/AgCl, suggesting an irreversible process like that observed for complex **2A**. The reduction and oxidation potentials for complexes **2A** and **2C** are very close, indicating that the dimeric nature of complex **2C** is lost due to dissociation in DMF solution. Due to similarities in their coordination spheres, the studied complexes undergo the first reduction step at nearly the same potential (Abbar & Nandibewoor, 2012; Sangeetha *et al.*, 1999; Torelli *et al.*, 2000).

5.3.2.9 Complexation Studies

The complexation study for the **H_2L2** series complexes was conducted to replicate conditions closely resembling their synthesis. Thus, analyses were carried out in methanol, with the addition of drops of a sodium hydroxide solution equimolar to that of the ligand for complex **2B**.

Solutions of the ligand at a concentration of 4×10^{-5} mol L^{-1} were prepared, as well as solutions of starting salts (copper(II) chloride dihydrate, copper(II) perchlorate hexahydrate, and copper(II) nitrate trihydrate) at 3×10^{-4} mol L^{-1}. The ligand solutions for copper(II) chloride dihydrate and copper(II) nitrate trihydrate salts were diluted to 2×10^{-5} mol L^{-1}, while for copper(II) perchlorate hexahydrate salt, the solution was diluted by adding an equal volume of a sodium hydroxide solution at 4×10^{-5} mol.L^{-1}. Successive additions of 0.05 equivalent of the starting salt solution were then made to the ligand solution.

By adding equivalent amounts of the starting salts to the ligand solution, changes were monitored using UV-Vis electronic spectroscopy. The band around 400 nm, associated with the phenol functional group, was closely monitored as a reliable indicator of complexation. With successive additions of the starting salt equivalents, an increase in absorbance of this band was observed, indicating the transfer of charge from the phenolate ion to the central copper(II) ion. In addition to the increased absorbance of the band around 400 nm, the formation of different isosbestic points was also observed, indicating the presence of at least two species in equilibrium in solution.

Figure 79 depicts the increase in absorbance of the band around 400 nm with successive additions of copper(II) chloride to the **H_2L2** ligand solution. The study was conducted in triplicate, and thus, the values were averaged with respect to the added equivalent of Cu^{2+}. The curve shows a saturation trend near 1 equivalent of copper(II) ion, suggesting that the stoichiometry of the mononuclear complex formed in solution is 1:1, consistent with the structure of the obtained complex.

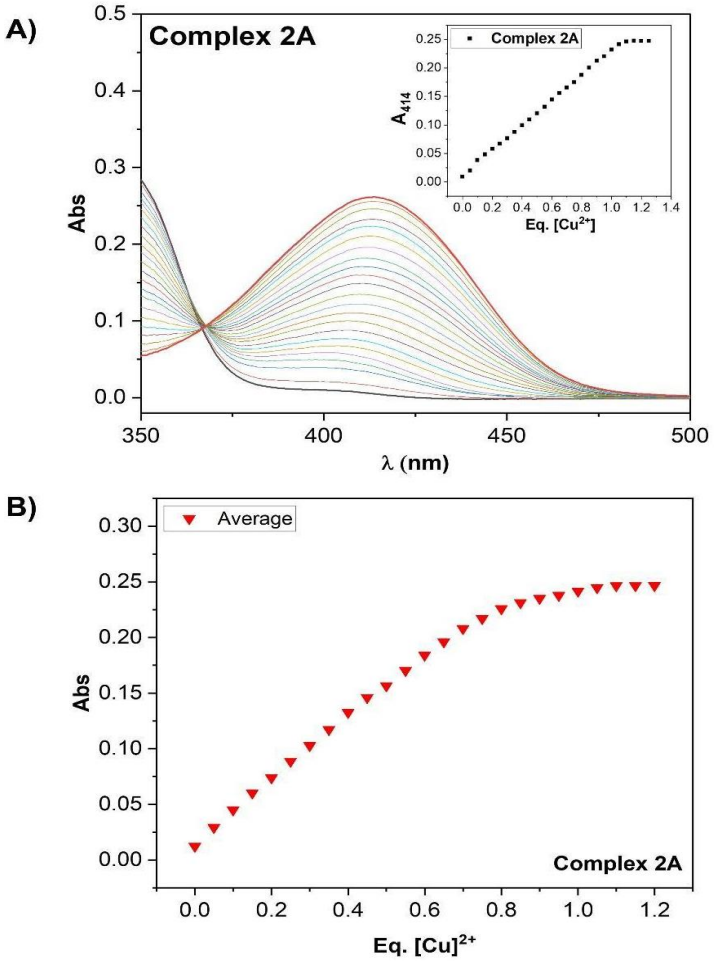

Figure 79. A) Study of complexation of complex **2A** and the relationship between absorbance and the number of Cu^{2+} equivalents. **B)** Result of the average of triplicates of the complexation study of complex **2A.**

Similar to what was observed for complex **2A**, Figure 80 demonstrates that the addition of equivalents of Cu^{2+} from copper(II) perchlorate hexahydrate to the **H_2L2** ligand solution leads to an increase in absorbance of the band around 400 nm. The study was conducted in triplicate, and thus, values were averaged with respect to the added equivalent of Cu^{2+} to the methanolic solution equilibrated

with sodium hydroxide. The curve shows a saturation trend near 1 equivalent of copper(II) ion, suggesting that the stoichiometry of the complex formed in solution is 1:1. Despite the complex being dinuclear in the solid state, the stoichiometry in solution is 1:1.

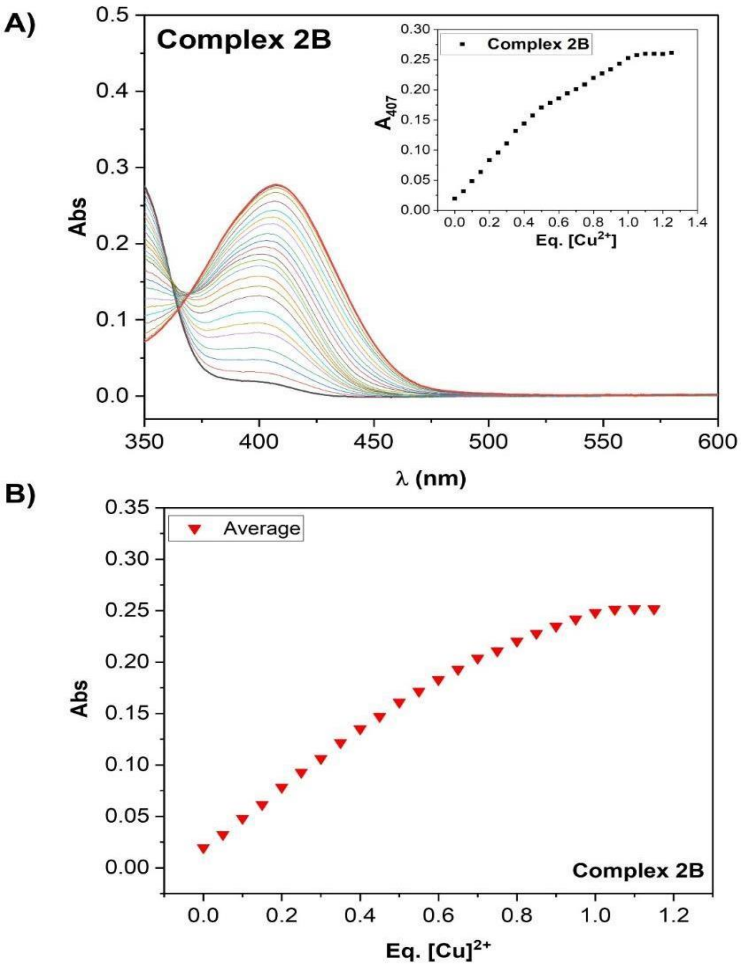

Figure 80. A) Study of complexation of complex **2B** and the relationship between absorbance and the number of Cu^{2+} equivalents. **B)** Result of the average of triplicates of the complexation study of complex **2B.**

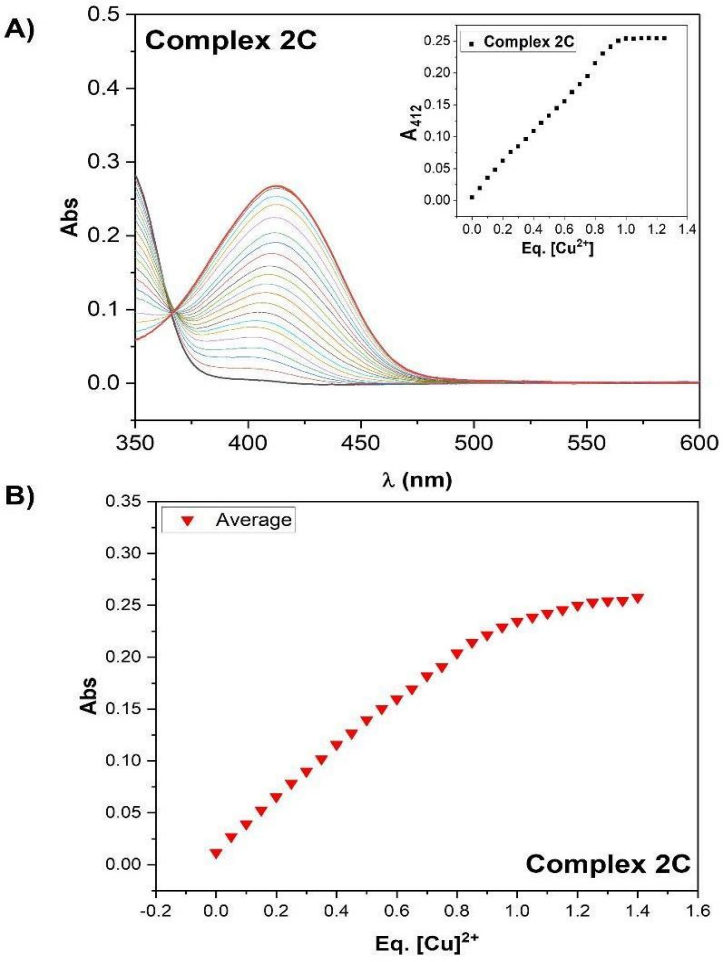

Figure 81. A) Study of complexation of complex **2C** and the relationship between absorbance and the number of Cu^{2+} equivalents. **B)** Result of the average of triplicates of the complexation study of complex **2C.**

Similarly to what was observed for the other complexes, the addition of equivalents of copper(II) nitrate trihydrate increases the absorbance of the analyzed band around 400 nm (Figure 81). The study was conducted in triplicate, allowing for the averaging of values with respect to the added equivalent of Cu^{2+} to the methanolic solution. The curve shows a saturation trend near 1 equivalent of copper(II) ion, suggesting that the stoichiometry of the complex formed in solution is 1:1. Similar to complex **2B**, the stoichiometry of the binuclear complex **2C** is also 1:1.

For complexes derived from the studied **H_2L2** ligand, the complexation study neither refutes nor confirms the number of metal centers present in the complexes in methanolic solution, but indicates the favored stoichiometry type in

solution under conditions similar to those used in their synthesis (Padnya *et al.*, 2021).

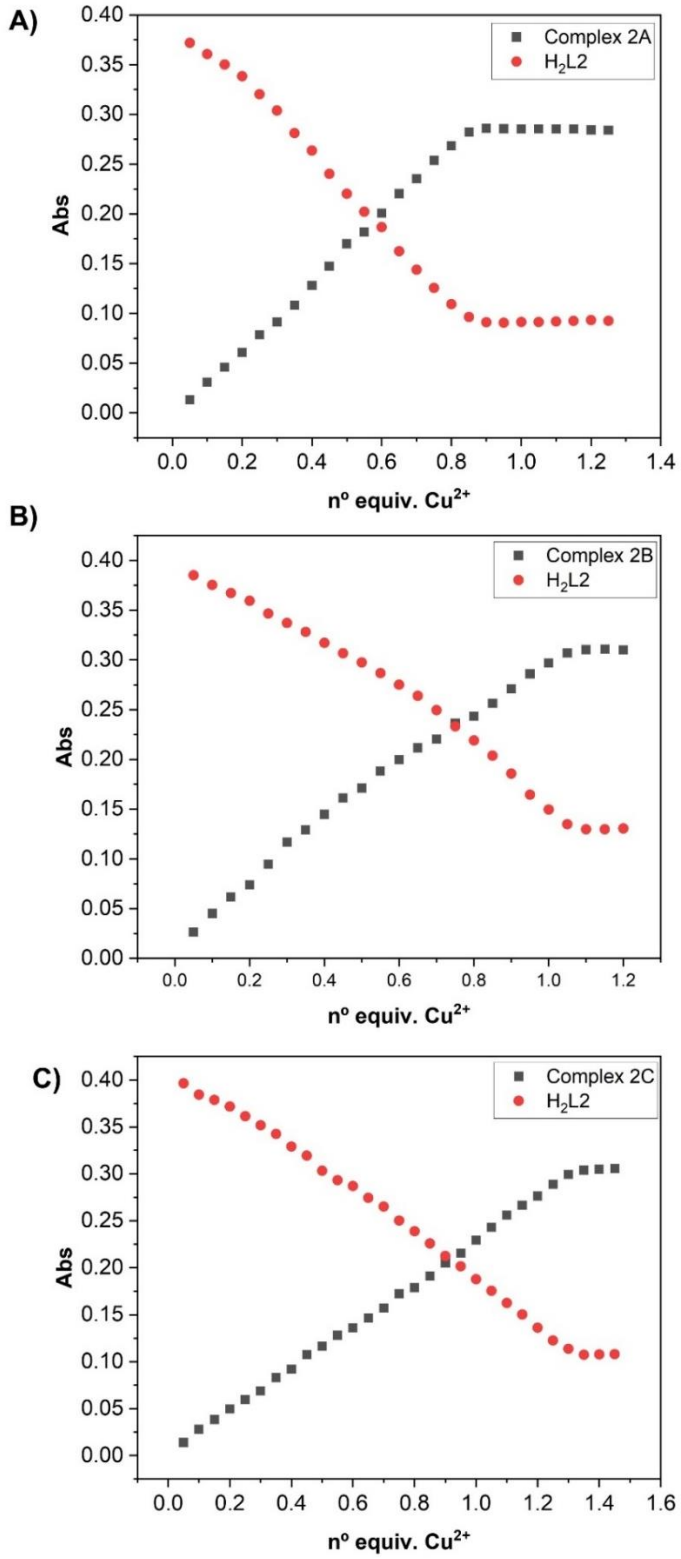

Figure 82. Qualitative graph that illustrates the variation of ligand species and their respective complexes based on the absorbance and number of equivalents of the salts used. A) **2A**, B) **2B** and C) **2C**.

Figure 82 enables an indirect analysis of species concentration variation through changes in absorbance of the ligand bands (around 330 nm) and the obtained complexes (around 400 nm). Comparing the graphs in figure 82, it is observed that when the equivalent reaches 1, the absorbance becomes constant, indicating a potential equilibrium between the free ligand and the formed complex. (Abdelrahman *et al.*, 2021).

5.3.2.10 Interaction studies with HSA and molecular docking

Molecular docking studies were conducted for the complexes **2A** and **2B**, as well as for the ligand **H_2L2**. The data obtained are part of the work published in the journal Dalton Transictions in 2023 (Moura *et al.*, 2023). The molecular docking studies were initially focused on three drug interaction sites (DS), located in regions IIA (DS1), IIIA (DS2), and IB (DS3). Additionally, the studies were extended to include the FA6 region, a site associated with fatty acids.

The crystallographic structures selected for this study are analogous to those under experimental conditions, specifically HSA devoid of fatty acids. All selections were sourced from the Protein Data Bank (PDB). The PDB entry 2bxe features the structure of diflunisal (a nonsteroidal anti-inflammatory drug) bound to sites DS1, DS2, and FA6, with a resolution of 2.95 Å. The second structure chosen for this study was PDB 2bxe, which includes the nonsteroidal anti-inflammatory drug azapropazone bound to sites DS1 and DS3, with a resolution of 2.70 Å. The third selected structure was PDB 2vue, which presents a bilirubin molecule at site DS3 and has a resolution of 2.42 Å.

Under more physiological conditions (i.e., 1 or 2% MeOH/PBS, pH 7.4), which were employed in the interaction studies with HSA, the spectral profiles of the compounds exhibit some modifications. Electronic transitions were theoretically calculated using a continuous solvation model to simulate the spectra of **H_2L2** and its complexes (**2A** and **2B**) in aqueous solution, thereby simplifying the assignment of bands used to monitor these interactions. Figure 83 illustrates the involved molecular orbitals displays the absorption profile of the ligand in 1% MeOH/PBS, with the spectrum in DMF (at the same concentration) included as a reference. The primary difference between them is related to the relative intensities of the bands. The calculated wavelength for the HOMO-LUMO transition, 337 nm, matches the experimental value precisely.

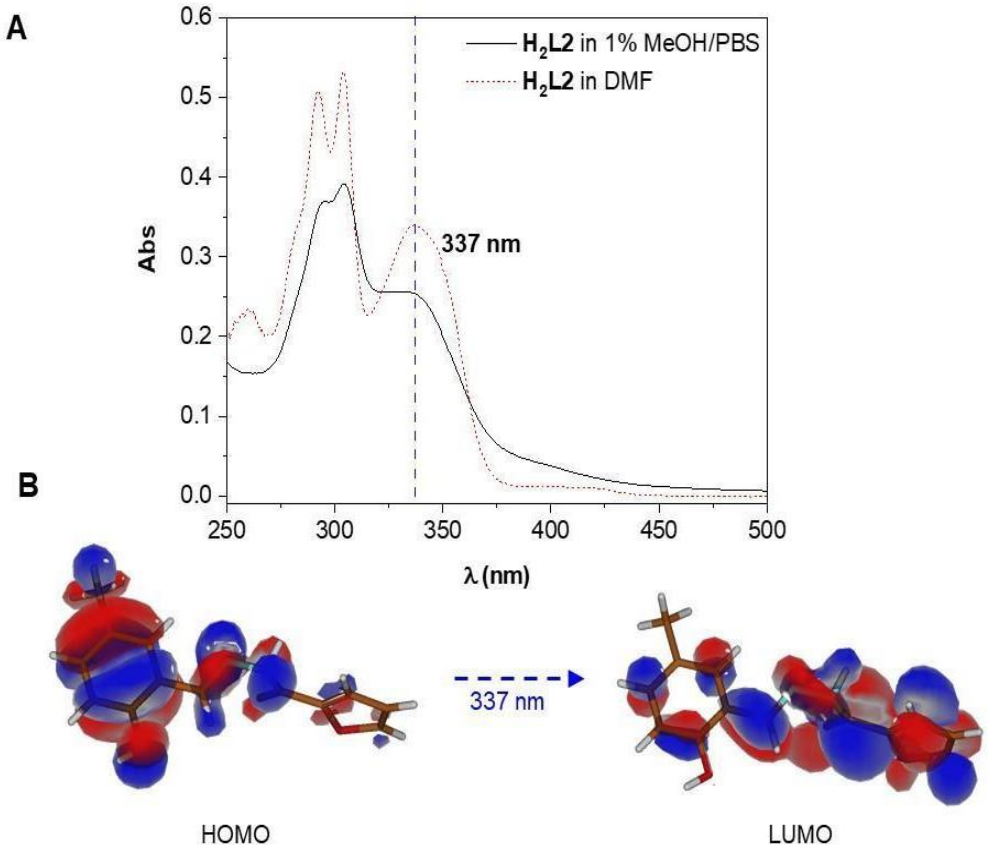

Figure 83. (A) UV-Vis spectra of ligand **H_2L2** (2.0×10^{-5} mol L^{-1}) in 1% MeOH / PBS, pH 7.4 (black solid curve) and in DMF (red dotted curve), at r.t. Position of the HOMO-LUMO calculated transition is given as a dashed blue line **(B)** Frontier orbitals that take part in the process.

Figure 84 (A) displays the UV-Vis spectra of complex **2A** in 1% MeOH/PBS (left) and complex 2 in 2% MeOH/PBS (right). For comparison purposes, the corresponding spectra in DMF (at the same concentration) are also shown. A clear hypsochromic shift is observed in both systems when transitioning from DMF to an aqueous-rich medium.

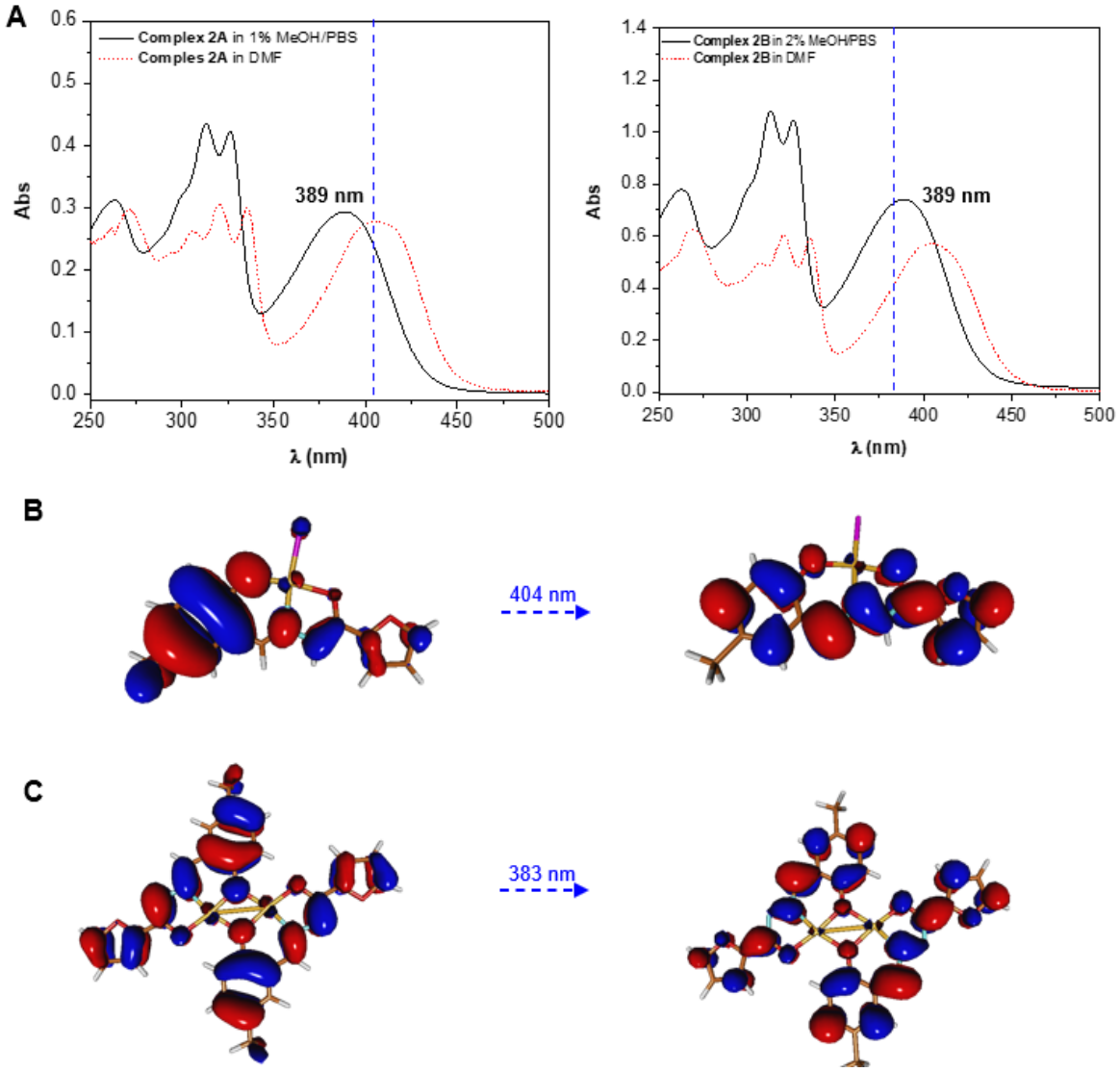

Figure 84. (A) Left: UV-Vis spectra of complex **2A** (2.0 × 10-5 mol L-1) in 1% MeOH / PBS, pH 7.4 (black solid curve) and in DMF (red dotted curve), at r.t. Right: UV-Vis spectra of complex **2B** (2.0 × 10-5 mol L-1) in 2% MeOH / PBS, pH 7.4 (black solid curve) and in DMF (red dotted curve), at r.t. Positions of the calculed transitions are given in both cases as blue dashed lines. **(B)** Orbitals of complex **2A** involved in the process at 389 nm. **(C**) Orbitals of complex **2B** involved in the process at 389 nm.

The calculated electronic transitions align well with those observed experimentally, particularly for complex **2B**. The ~20 nm discrepancy between the empirical and predicted wavelength values for the 389 nm band in the spectrum of complex **2A** is likely attributed to the partial replacement of chloride by a water molecule in the copper coordination sphere. Balsa, L. M. *et al.* (2023) reported an absorption centered at 387 nm for the $[Cu(HL)OH_2]^+$ cation, involving the 3-methoxysalicylaldehyde 2-thienylhydrazone ligand in PBS (Balsa, L. M. *et al.*, 2023; Balsa, M. L. *et al.*, 2023). Figure 84(B) illustrates the molecular orbitals

involved in this absorption, calculated at 404 nm. Conversely, Figure 84(C) depicts the molecular orbitals involved in the equivalent transition for complex **2B**, estimated at 383 nm (experimental: 389 nm). As shown, in both cases, orbitals distributed across the entire molecules participate in these transitions.

No theoretical molecular docking study was performed for complex **2C**; however, the results obtained for complexes **2A** and **2B** are consistent with those for complex **2C**. When comparing the electronic spectrum of complex **2C** in DMF with that under physiological conditions, a hypsochromic shift similar to that observed for the spectra of complexes **2A** and **2B** is noted. Furthermore, the electronic transition observed at 389 nm for complexes **2A** and **2B** is also present in the electronic spectrum of complex **2C** in 2% MeOH/PBS, suggesting that this may be the same electronic transition involving similar orbitals. This observation implies that complex **2C** may not maintain its dimeric integrity in solution, undergoing dissociation to form complex **2A**.

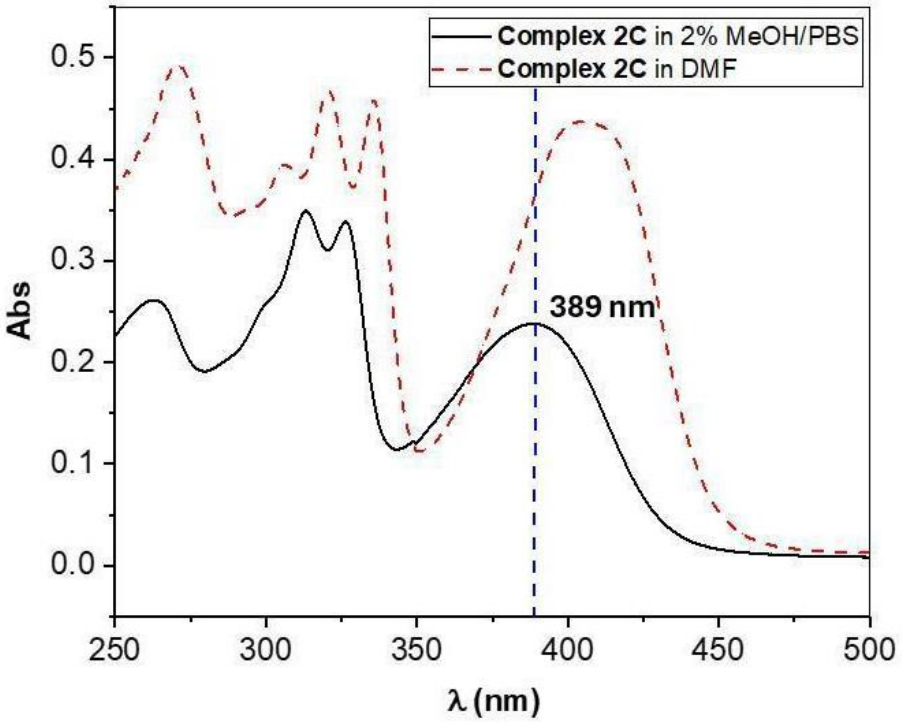

Figure 85. UV-Vis spectra of complex **2C** (2.0×10^{-5} mol L^{-1}) in 2% MeOH / PBS, pH 7.4 (black solid curve) and in DMF (red dotted curve), at r.t.

Human serum albumin (HSA) is a 66.35 kDa globular protein synthesized by the liver. Globular proteins are characterized by their intermediate solubility in aqueous solutions, forming colloidal solutions, which distinguishes them from fibrous proteins (the other principal type), which are virtually insoluble. HSA is composed of 585 amino acids along a single chain, features a high cysteine content, a significant proportion of negatively charged amino acids, and is typically non-glycosylated. As the most abundant protein in plasma, HSA exhibits an extraordinary capacity for binding both endogenous and exogenous ligands. It serves as the primary carrier of fatty acids, influences the pharmacokinetics of many drugs, facilitates the metabolic modification of certain substances, and neutralizes potential toxins (Fanali *et al.*, 2012). For these reasons, studying the interactions between this protein and the **H_2L2** compounds and their complexes is of intrinsic interest.

Figure 86 (A) illustrates the spectral changes in the 300-500 nm range resulting from the successive addition of HSA to a solution of **H_2L2** at 2×10^{-5} mol L^{-1}. The absorbance at 400 nm increases while the absorbance around 340 nm decreases as the titration progresses. An isosbestic point is clearly identified at 350 nm, indicating the presence of only two absorbing species in equilibrium: free **H_2L2** and bound **H_2L2**. Plotting the absorbance at 400 nm against the equivalents of HSA (Figure 86 (A), *inset*) produces a sigmoid curve that stabilizes when [HSA]/[**H_2L2**] = 0.50, suggesting that HSA can accommodate up to two molecules of ligand. The detection of an isosbestic point, along with the sigmoid shape rather than hyperbolic of the curve in the *inset*, suggests that a cooperative process is occurring. Monitoring the absorption band at 337 nm was strategic, as it corresponds to the complete HOMO-LUMO transition of the molecule (Figure 84 (B)), where the electron density in an orbital centered on the phenol ring is excited to an empty orbital located over the furan. Therefore, any interaction between **H_2L2** and HSA would be detected.

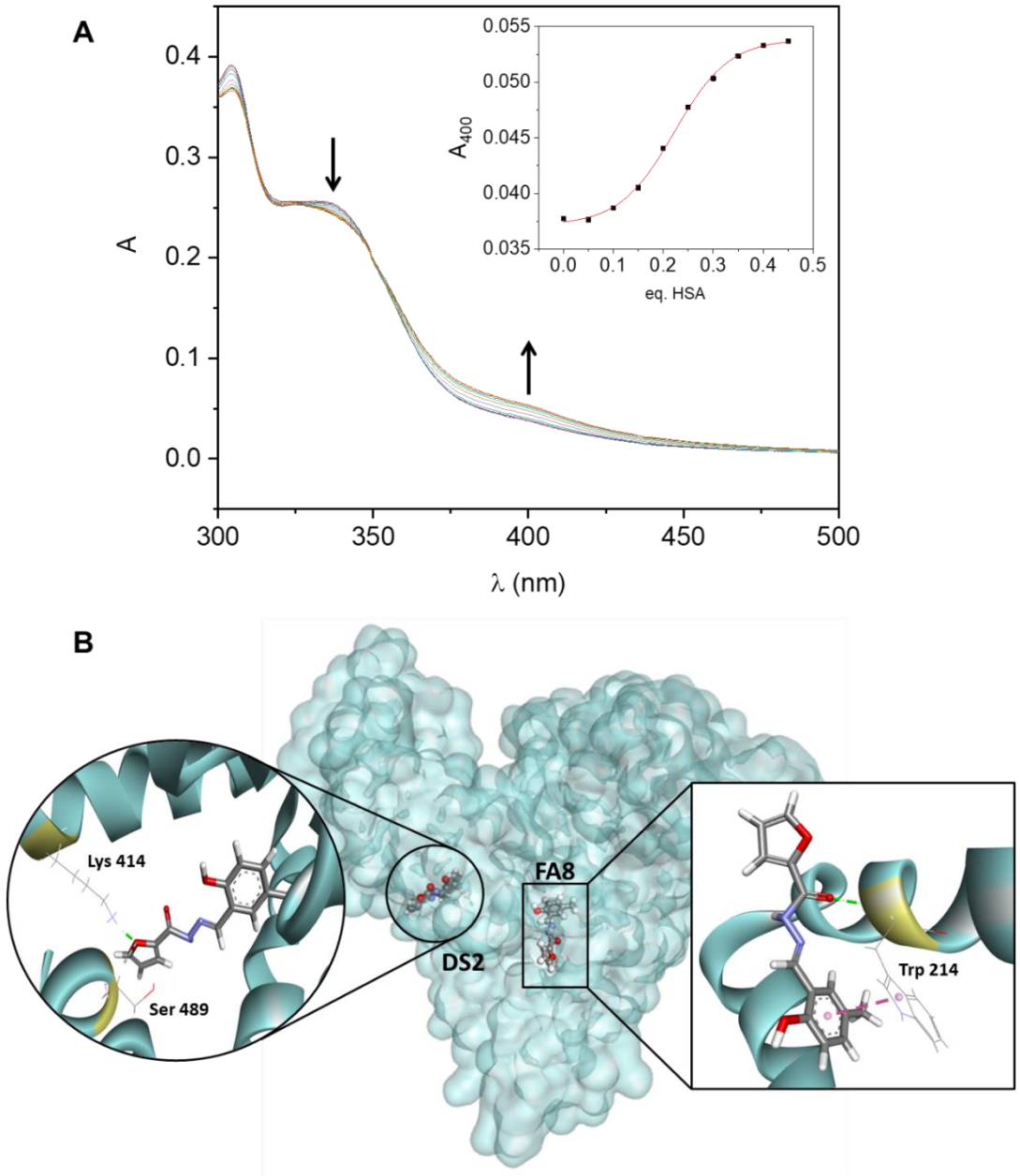

Figure 86. (A) UV-Vis titration of a 2 × 10^{-5} mol L^{-1} **H_2L2** solution (1% MeOH / PBS, pH 7.4) with HSA at 25 ºC. *Inset*: absorbance at 400 nm as a function of HSA equivalents; data were fitted using a sigmoidal function. **(B) H_2L2** conformers obtained through molecular docking for DS2 and FA8 sites and representation of the possible interactions with amino acids presents in each site.

Molecular docking simulations were conducted to identify different binding sites on HSA concerning its interactions and potential affinity for **H_2L2**. HSA comprises three homologous domains (I, II, and III), each divided into subdomains A and B, with common structural motifs (Fanali *et al.*, 2012; Merlot *et al.*, 2014). The studies initially focused on the three drug interaction sites (DS), located in regions IIA (DS1), IIIA (DS2), and IB (DS3), and were subsequently

extended to the FA6 region. Optimal interactions were observed around the DS2 site (with a study radius of 10 Å) and the FA6 site (9 Å). However, an unusual behavior was noted at the FA6 site, where the ligand shifted from the studied region to a nearby region known as FA8. The energy values obtained were −48.05 kcal mol^{-1} (DS2) and −48.66 kcal mol^{-1} (FA8). Figure 86 (B) illustrates the position and sites where **H_2L2** was most effectively located, thereby supporting the experimental ligand-protein stoichiometry of 2:1.

When a solution of complex **2A** (2×10^{-5} mol L^{-1}) is titrated with HSA, a different behavior is observed (Figure 87 (A)): the absorption originally present at 388 nm is bathochromically shifted to 394 nm as the protein concentration increases. Isosbestic points can be easily identified around 330, 345, and 404 nm during the initial additions of HSA, indicating once again that only two absorbing species (free and bound forms of the complex) are initially in equilibrium. Subsequently, a stabilization appears to occur, although the isosbestic points are not as well-defined as at the beginning of the titration. Plotting the absorbance at 430 nm as a function of HSA equivalents (Figure 87(A), *inset*) yields a sigmoid curve that stabilizes around [HSA]/[**2A**] = 0.25, suggesting that HSA can accommodate up to four units of the mononuclear complex. Cooperative binding likely occurs again in this study (Yoguim *et al.*, 2022).

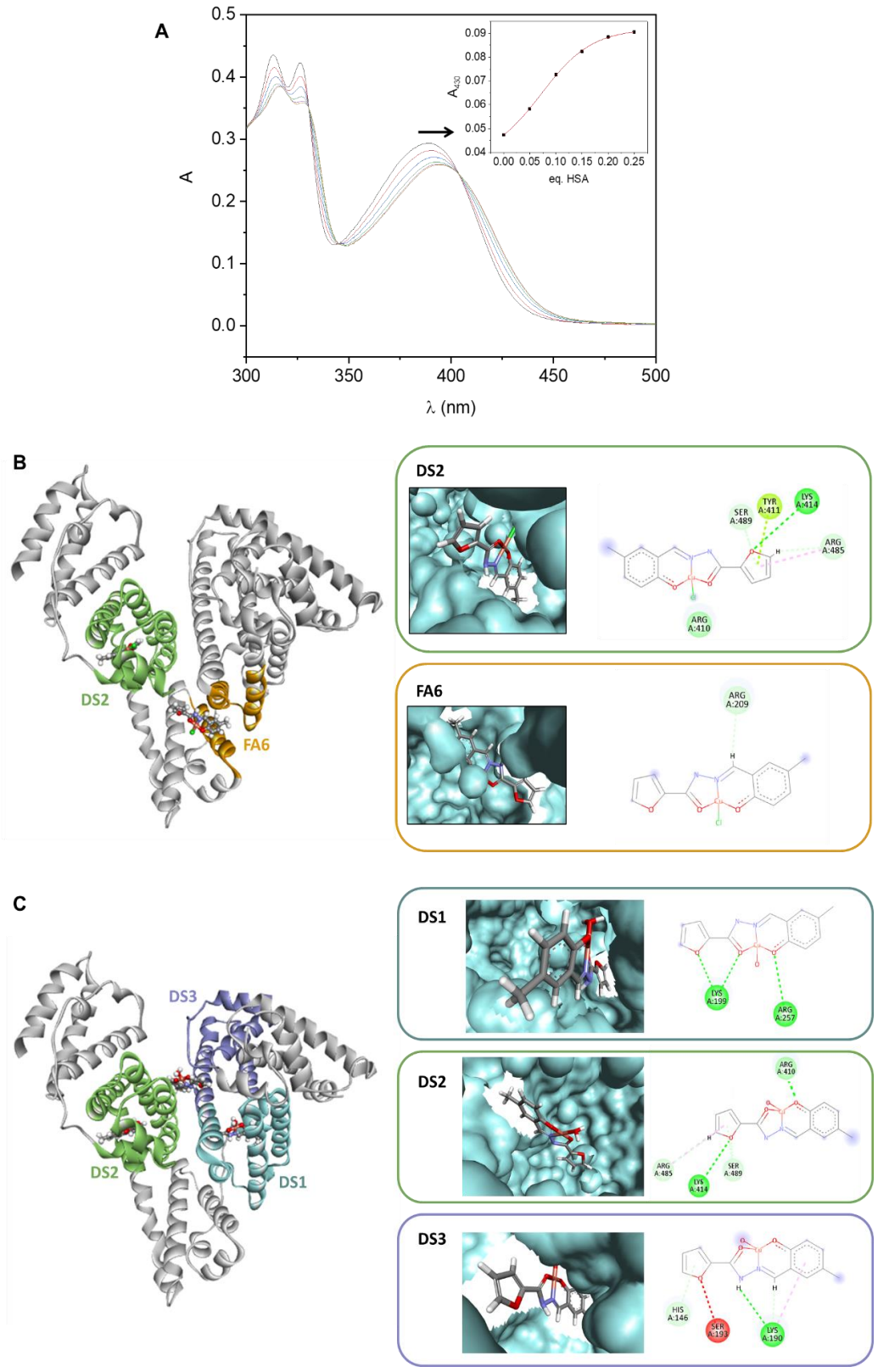

Figure 87. (A) UV-Vis titration of a 2 × 10^{-5} mol L^{-1} complex 2A solution (1% MeOH / PBS, pH 7.4) with HSA at 25 ºC. *Inset*: absorbance at 430 nm as a function of HSA equivalents; data fitted with a sigmoidal function. **(B)** Molecular docking results with indication of the pose and most probable interactions of **2A** at DS2 and FA6 sites and **(C)** Its aquated derivate **2A**$^{+}$ at DS1, DS2 and DS3 sites.

During the docking simulation phase, it was important to consider the likely replacement of water, at least to some extent, by the chloride ligand following the dissolution of complex **2A** in PBS, generating the cationic species $[Cu(C_{13}H_{11}O_3N_2)OH_2]^+$ (complex **2A**$^+$). This can be inferred, for example, from the conductivity measurements discussed earlier. Consequently, interactions with HSA were evaluated for both the neutral complex **2A** and its cationic derivative **2A**$^+$. The calculations suggest that the unmodified compound has an affinity for the DS2 and FA6 sites, while its cationic derivative **2A**$^+$ interacts well with the DS1, DS2, and DS3 sites. Given that the solution of complex **2A** consists of a mixture of unmodified and modified complexes in water, it is anticipated that four sites on HSA might be involved in the interaction: DS1 (**2A**$^+$), DS2 (**2A** and **2A**$^+$), DS3 (**2A**$^+$), and FA6 (**2A**). This helps to elucidate the apparent 4:1 stoichiometry of the complex to the protein observed. Figures 87 B and C present the results obtained from molecular docking studies for complexes **2A** and **2A**$^+$. The parameters used for complex **2A** were: DS2 - radius 9 Å and flexibility of asparagine-391; FA6 - radius 6 Å with no amino acid substitution required. For complex **2A**$^+$, the parameters were: DS1 - radius 8 Å and flexibility of arginine-222; DS2 - radius 9 Å and flexibility of asparagine-391; DS3 - radius 11 Å and protonation of histidine-146. The energetic results for **2A** are −58.05 kcal mol^{-1} for DS2 and −43.82 kcal mol^{-1} for FA6, indicating that the DS2 site has a lower energy value, suggesting a possible preferential region. For complex **2A**$^+$, the energetic values were quite similar for DS1 (−57.63 kcal mol^{-1}) and DS2 (−57.49 kcal mol^{-1}), whereas for DS3, the value was −41.07 kcal mol^{-1}. Analysis of the docking results for this derivative does not propose a preferential region.

On the other hand, titration of a 2×10^{-5} mol L^{-1} solution of complex **2B** with HSA results in the spectral changes presented in Figure 88(A). Overall, the observed profile is quite similar to that described for complex **2A**, with a bathochromic shift of the band originally centered at 388 nm to 398 nm as the protein concentration increases. However, the saturation profile is markedly different: plotting the absorbance at 430 nm against the equivalents of HSA yields an irregular pattern, apparently involving multiple stages, which only stabilizes around [HSA]/[**2B**] = 1.00 (Figure 88 (A)). This is likely related to the partial breakdown of the dimer into [Cu(L2)DMF] monomers, as previously discussed. Due to this peculiarity, no specific function was fitted to the experimental curve

obtained.

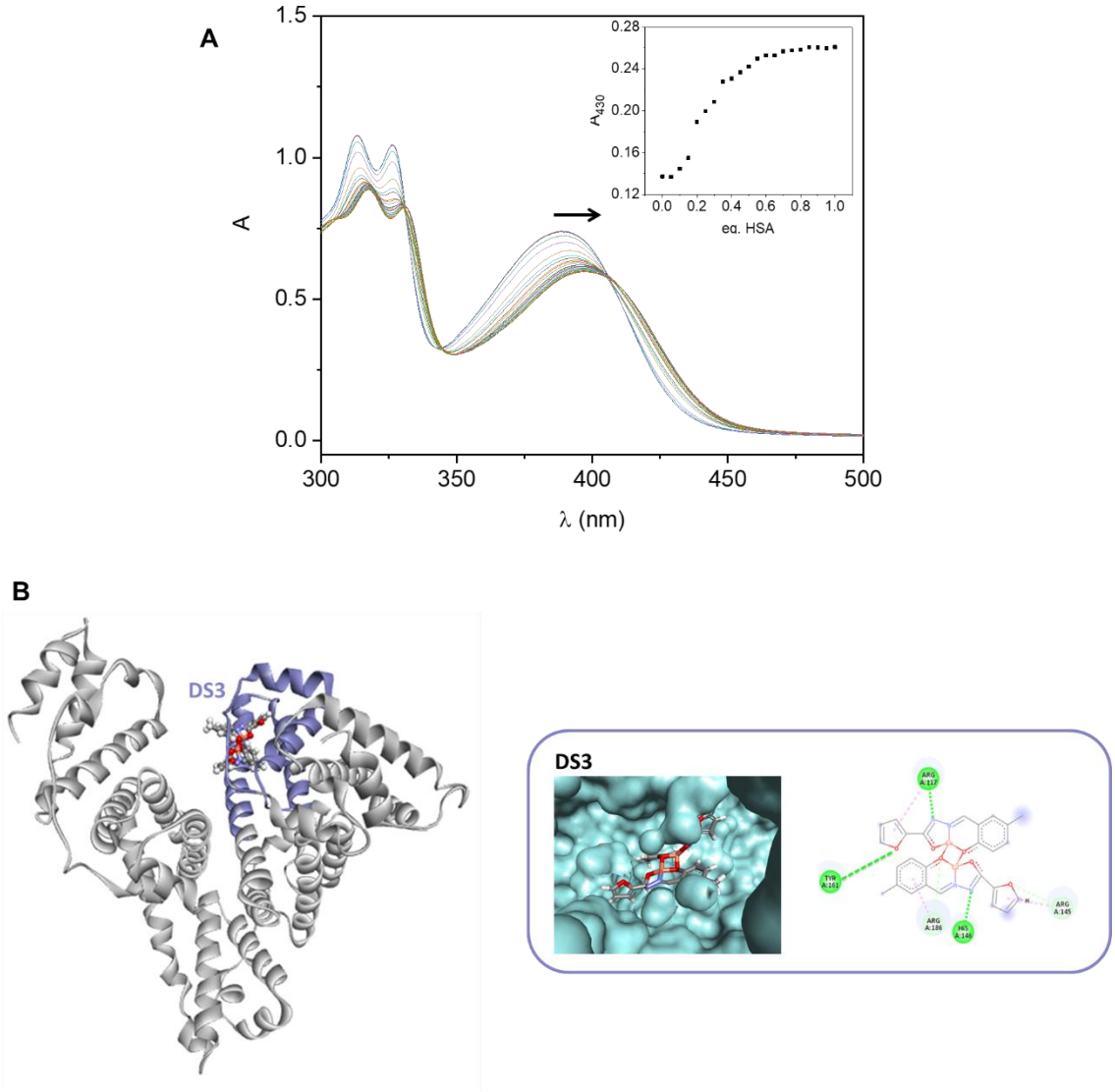

Figure 88. (A) UV-Vis titration of a 2 × 10^{-5} mol L^{-1} solution of **2B** (2% MeOH / PBS, pH 7.4) with HSA at 25 ºC. *Inset:* absorbance at 430 nm as a function of HSA equivalents. **(B)** Molecular docking results with indication of pose and most probable interactions of the neutral, dimeric complex **2B** at the DS3 site.

Due to the dimensions of the dimeric species, molecular docking simulations were conducted only for the DS3 site, as it features a large entry aperture and there are no literature reports of structures containing species of this size interacting with DS1, DS2, and FA6. The optimal condition was achieved using a radius of 9 Å with the protonation of histidine-146 (Figure 88 (B)). An interaction energy value of −73.15 kcal mol^{-1} was calculated. Stabilization at the site involves both unconventional and conventional hydrogen bonds with residues Arg, His, and Tyr.

Although the saturation profile around 430 nm indicates an irregular pattern, complicating a specific fit to the experimental curve, it is evident that saturation occurs at [HSA]/[**2B**] = 1.00, indicating that the stoichiometry of the protein-complex **2B** interaction is 1:1. This stoichiometry is consistent when considering the size of complex **2B**, which is significantly larger than the ligand **H_2L2** and complex **2A**, making it difficult for one protein unit to interact with more than one unit of complex **2B**.

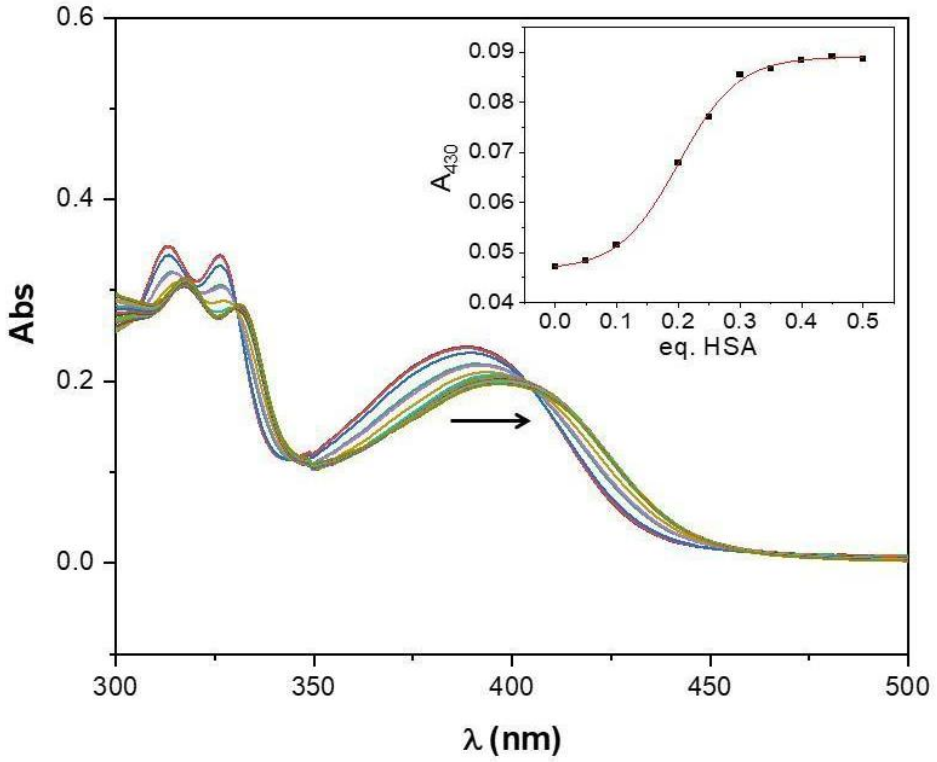

Figure 89. UV-Vis titration of a 2 × 10^{-5} mol L^{-1} solution of complex **2C** (2% MeOH / PBS, pH 7.4) with HSA at 25 ºC. *Inset:* absorbance at 430 nm as a function of HSA equivalents.

Molecular docking simulations were not performed for complex **2C**, but its interaction with HSA was evaluated. A titration of a 2 × 10^{-5} mol L^{-1} solution of complex **2C** with HSA was conducted, resulting in the spectral modifications presented in Figure 89. Generally, the observed profile is quite similar to that described for complexes **2A** and **2B**, with a bathochromic shift of the band originally centered around 388 nm to 404 nm as the protein concentration increases. Isosbestic points can be easily identified around 330, 345, and 404 nm during the initial additions of HSA, indicating once again that only two absorbing species (free and bound forms of the complex) are initially in equilibrium. Notably, the isosbestic points observed for complex **2C** are identical to those for complex **2A**, reinforcing the possibility that complex **2C** in solution does not

maintain its dimeric integrity and converts to the mononuclear complex **2A**. Subsequently, a stabilization appears to occur, although the isosbestic points are not as well defined as at the beginning of the titration. Plotting the absorbance at 430 nm versus the equivalents of HSA (Figure 89 *inset*) yields a sigmoidal curve that stabilizes around [HSA]/[**2C**] = 0.50, indicating that HSA can accommodate up to two molecules of the complex. Cooperative binding likely occurs again in this study.

Comparing the HSA interaction results for complex **2A** and complex **2C** reveals that, although the profiles are identical, the stabilization differs. In complex **2A**, one protein molecule can accommodate four molecules of complex **2A** in both its neutral and charged forms. In contrast, in complex **2C**, one protein molecule can accommodate two molecules of the complex. This result is consistent with the fact that each **2C** molecule can generate two **2A** molecules, as the calculation of equivalents is performed for the complex in its dimeric form.

5.3.2.11 Cytotoxicity and antiproliferative activity studies

Cytotoxicity studies were conducted for **H_2L2** and its complexes **2A**, **2B**, and **2C**; the parameter was assessed using the MTT assay in MDA-MB-231 cells (triple-negative breast adenocarcinoma). The clinical agent cisplatin (CDDP) was employed as an inorganic reference of antiproliferative activity, in addition to the clinical (organic) drug doxorubicin.

Table 23. IC_{50} [μM] values of the N-acylhydrazonic ligand **H_2L2,** its copper(II) complexes **2A, 2B** and **2C, CDDP and DOX** clinical references on MDA-MB-231 cells after 24 h of incubation.

Compound	IC_{50} [μM]
H_2L2	>50
$Cu(NO_3)_2 \cdot 3H_2O$	>50
Complex 2A	2.0 ± 0.1
Complex 2B	1.3 ± 0.1
Complex 2C	1.2 ± 0.1
CDDP	131 ± 18 Balsa *et al.* (2021)
DOX	1.3 Ayoub *et al.* (2017)

The results presented in Table 23 indicate that all complexes were capable of reducing cell viability in the sub micromolar concentration range (0.5-2.5 μM), with similar IC_{50} values for both dimers (complexes **2B** and **2C**, approximately 1.25 μM) and a slightly higher value of 2.0 μM for complex **2A**. Although **2C** is ionic in nature, this does not prevent it from entering the cell, suggesting that some transporter may be involved in the process. Additionally, the fact that the antiproliferative activity of this compound, considering the standard deviation involved, is twice that observed for complex **2A** reinforces the possibility that complex **2C** undergoes dissociation in solution. The antiproliferative activity of the studied complexes is greater than that of cisplatin (CDDP), which has an IC_{50} value of 131 μM in MDA-MB-231 cells. Furthermore, the IC_{50} values obtained for the **H_2L2** series of complexes against MDA-MB-231 cells are comparable to those of the clinical reference drug doxorubicin (DOX) (Ayoub *et al.*, 2017).

In contrast, the IC_{50} values for **H_2L2** itself and free Cu^{2+} (metal cation) exceed 50 μM in the MDA-MB-231 cell line, highlighting the critical role of coordination in modulating the anticancer activity of copper complexes containing hydrazonic ligands. This effect has been reported for other copper(II) complexes (Balsa *et al.*, 2021; Balsa, L. M. *et al.*, 2023; Balsa, M. L. *et al.*, 2023; Rada *et al.*, 2019; Rada *et al.*, 2020).

5.4. H_2L3 Series

5.4.1 Synthesis of the Compounds belonging to the H_2L3 Series

The ligand was synthesized *via* condensation reaction, using the precursors 5-methylsalicylaldehyde and 5-phenylisoxazole-3-carbohydrazide. Suitable yields were obtained. Reacting **H_2L3** with copper(II) chloride dihydrate or copper(II) nitrate trihydrate afforded the same product, **3A**, which was obtained as a powder with satisfactory yields. Figure 90 illustrates the synthesis of the ligand and **3A**.

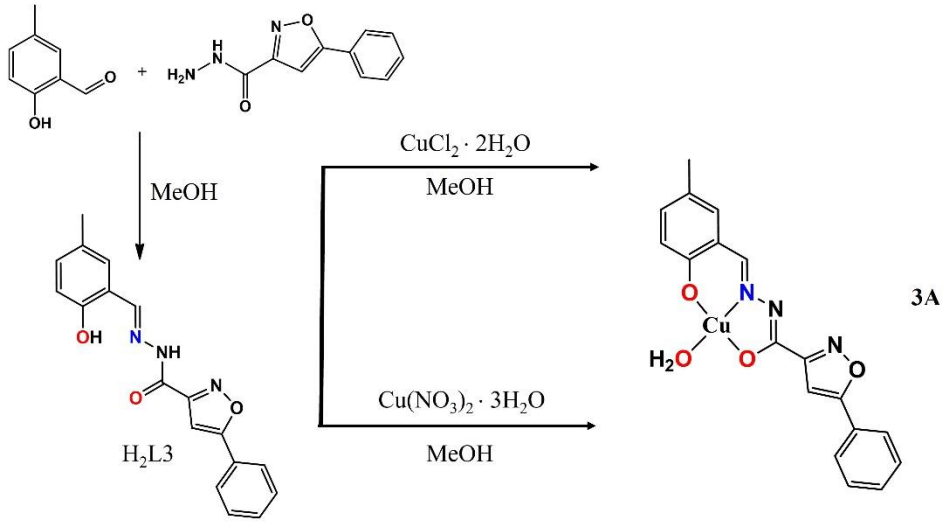

Figure 90. General scheme of the synthesis of the **H_2L3** ligand and complex **3A.**

The absence of chloride ions in the coordination sphere was confirmed using a 0.1 mol L^{-1} silver nitrate solution. Successive additions of silver nitrate to the complex solution demonstrated that no chloride ions were present in the coordination sphere, nor were they present as counterions, as evidenced by the absence of silver chloride precipitation.

The thermogravimetric analysis of complex **3A** (Figure 91), on the other hand, shows a thermal event at around 270 ºC, corresponding to a weight loss of 3.2%, suggesting that it is associated with the coordinated water molecule (calc. 4.5%). Above 300 ºC, significant mass losses are observed, which are attributed to the organic fraction present in the ligand. Complex **3A** exhibited a residual mass of 20.62%, likely corresponding to copper(II) oxide, indicating 16.6% of copper in the sample. This is consistent with the percentage obtained from ICP-OES (16.1%), suggesting that the proposed structure for this complex is coherent.

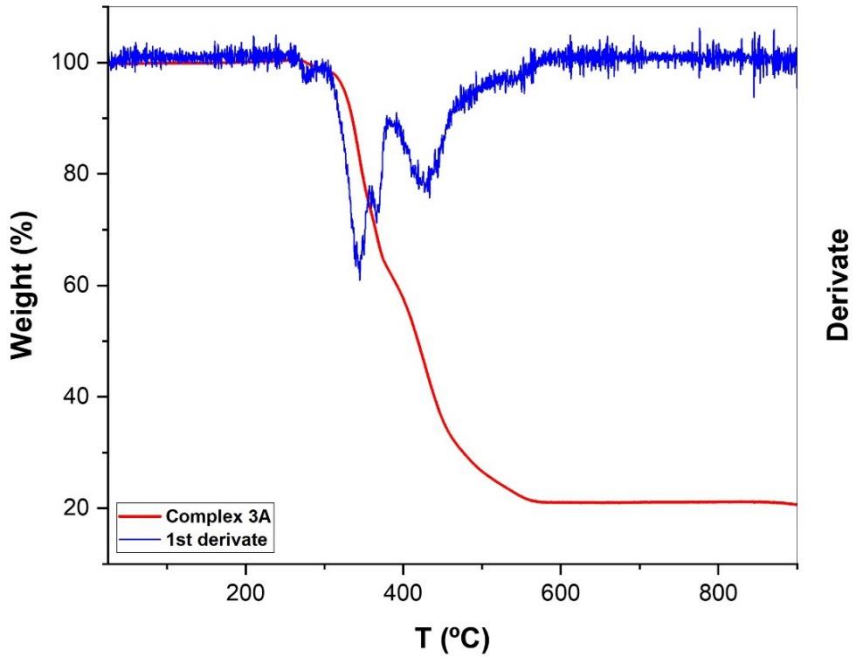

Figure 91. Thermogravimetric curve for complex **3A.**

Although soluble in pure organic solvents, the aqueous solution assays for interaction studies with HSA were not feasible. Both the complex and the ligand were highly insoluble in PBS buffer mixtures with many tested solvents, including methanol, ethanol, isopropanol, acetone, acetonitrile, DMF, and DMSO.

5.4.2 Characterization of ligand H_2L3 and its complex 3A

5.4.2.1 Copper content (ICP-OES)

Cu analysis was performed on a complex sample following purification by recrystallization in methanol. The obtained result is in Table 24:

Table 24. Relationship between the percentage of copper calculated and that found.

Complex	**%Cu**	
	calculated	found
3A	15.8	16.1

5.4.2.2 Molar conductivity studies

Table 25 correlates the obtained molar conductivity value for **3A** with the type of electrolyte in DMF, compared with the data reported by Geary (1971).

Table 25. Relationship between the molar conductivity data obtained with the electrolyte system.

Complex	**3A**
Molar conductance ($\Omega^{-1}cm^2mol^{-1}$)	3.20
Electrolyte	Non-electrolyte

Complex **3A** behaves as a non-electrolyte in DMF solution, suggesting that the proposed structure is consistent. Under this condition, the water molecule may be replaced by DMF molecules without altering the non-electrolytic nature of the complex. Additionally, DMF molecules can occupy axial positions, binding in a weaker way to the metal ion due to the Jahn-Teller effect.

5.4.2.3 Infrared Vibrational Spectroscopy

Analysis of the infrared vibrational spectrum of complex **3A** and ligand **H_2L3** (Figure 92) reveals shifts in certain bands associated with the stretching of characteristic functional groups, as well as the appearance and disappearance of specific bands. These factors can indicate coordination.

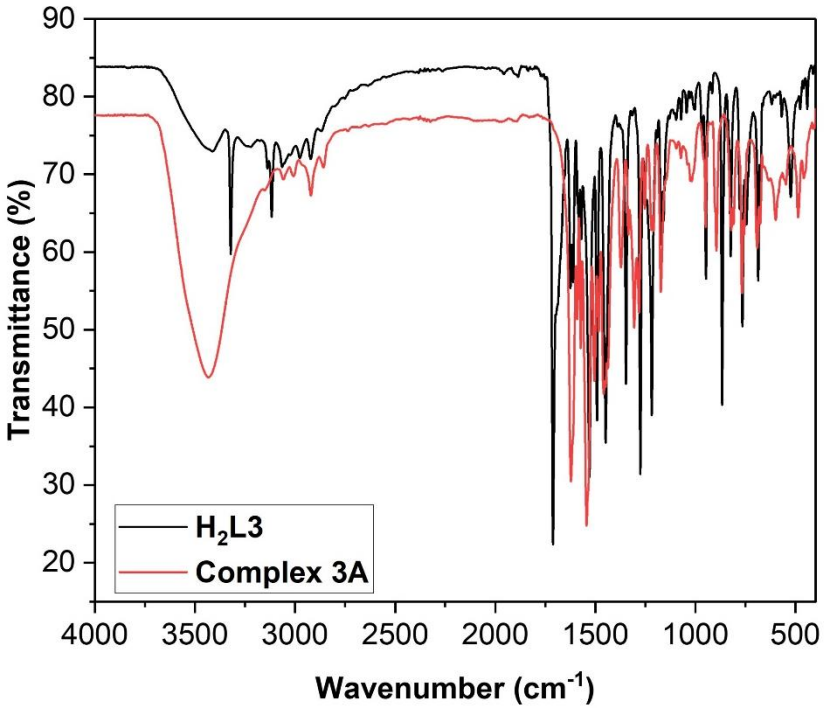

Figure 92. Overlapping of the mid-infrared spectra of **H_2L3** and complex **3A** in KBr, at room temperature.

Table 26. Selected vibrational absorptions (cm^{-1}) for **H_2L3** and complex **3A.**

Assingment	H_2L3	Complex 3A
υN−H	3150	-----
υO−H_{phenol}	3315	-----
υO−H_{water}	----	3435
υC=O	1672	1570
υC=N	1623	1618
δC−O−H_{phenol}	1479	-----
υC=C_{arom}	1345	1307
υC−O_{phenol}	1273	1281
δC=C−H_{phenol}	1217	1207
υN−N	1170	1170
υCu−O	-----	544
υCu−N	-----	600
δO−Cu−N	-----	485

The infrared vibrational spectrum of the complex exhibited several characteristic bands also observed in the ligand spectrum, albeit shifted, suggesting the coordination of the ligand to the copper(II) ion. The absence of the N−H stretching vibration in the complex supports the proposed structure and the obtained molar conductivity, indicating that the coordinated ligand is in the iminolato form, as observed in complex **2B**. The stretching bands of C=O and C=N were shifted to lower wavenumbers compared to those of the free ligand, suggesting coordination of the metal ion by the donor atoms of these functional groups. The C=O stretching band is significantly shifted, a characteristic of the iminolato form, where electronic delocalization with the hydrazone portion decreases the bond's vibrational frequency, justifying the shift to lower energy values (Moura *et al.*, 2023; Rada *et al.*, 2019). The absence of the O−H stretching band in the complex confirms the formation of the phenolate ion in the coordination, as evidenced by the νC−O band of the phenol. Additionally, some metal-ligand vibrations were identified in the complex spectrum, including absorptions at 544 cm^{-1} [ν(Cu–O)] and 600 cm^{-1} [ν(Cu–N)] for complex **3A** (Moura *et al.*, 2023).

Figure 93 shows the vibrational spectra of ligand **H_2L3** and **3A** obtained from different copper salts: copper(II) chloride dihydrate and copper(II) nitrate trihydrate. The results clearly demonstrate the overlapping bands of complex **3A** obtained via different routes, suggesting that the compound can be synthesized from different starting salts and, thus, that counter-ions are not present.

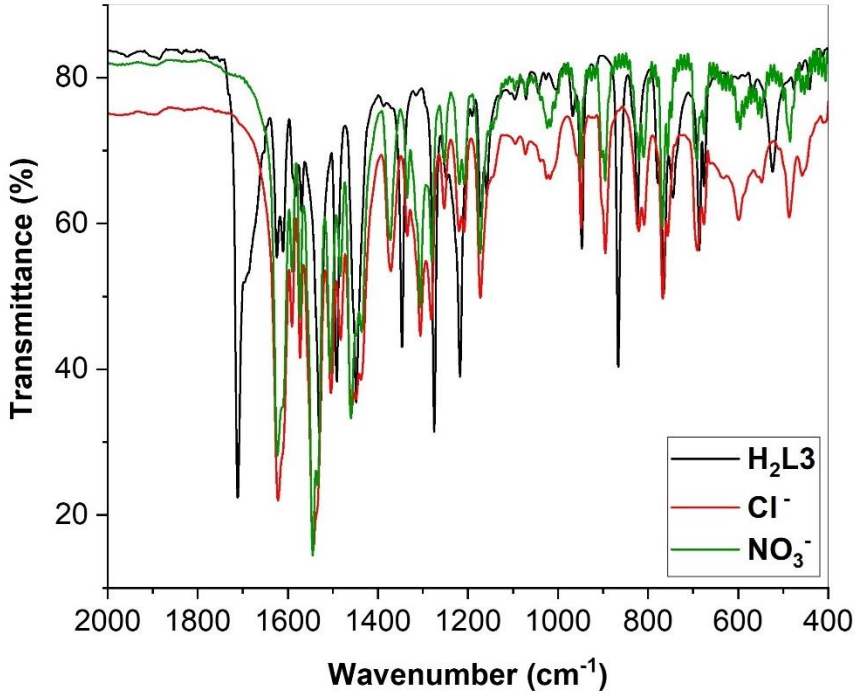

Figure 93. Comparison of infrared vibrational spectra of the ligand **H_2L3** and complex **3A** obtained by different starting salts.

5.4.2.4 Electronic Spectroscopy in UV-Vis and Diffuse Reflectance

The ligand and the obtained complex were analyzed by UV-Vis electronic spectroscopy at various concentrations using DMF as the solvent. The spectrum of **H_2L3** displays five main absorptions in the range 250-500 nm, comprising three bands and two shoulders (at around 270 and 300 nm), according to Figure 94A. Comparison of the spectrum with those of its precursors (Figure 94B) reveals that two of these absorptions come from them, being related to transitions within the phenol and phenylisoxazole rings. The intense bands observed at 281 nm (29,139 ± 671 L mol^{-1} cm^{-1}) and 289.5 nm (30,120 ± 684 L mol^{-1} cm^{-1}), along with the shoulder at around 300 nm, are likely associated with *N*-acylhydrazone-derived processes, as these are absent in precursors' spectra. Conversely, the broad band centered at 338.5 nm (13,524 ± 161 L mol^{-1} cm^{-1}), although also present in the spectrum of the precursor 5-methylsalicylaldehyde, may additionally reflect the contribution of the *N*-acylhydrazonic bridge between the rings, as it exhibits a bathochromic shift compared to the precursor.

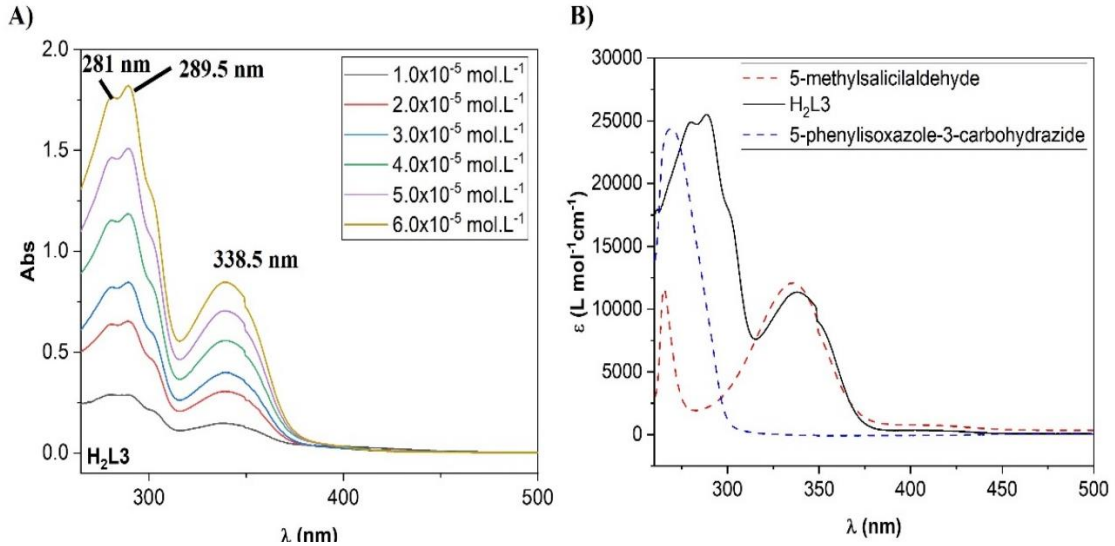

Figure 94. A) Electronic spectrum of **H_2L3** in DMF solution, at different concentrations. **B)** Electronic spectra of the ligand and precursors in DMF solution (5×10^{-5} mol L^{-1}).

Complex **3A** exhibits four main absorptions in the range of 250 to 600 nm (Figure 95). Comparison of this spectrum with that of the ligand reveals that three of the absorptions are present in it, as previously discussed. The intense bands around 303.5 nm (12,941 ± 61 L mol^{-1} cm^{-1}) and 319.5 nm (13,409 ± 77 L mol^{-1} cm^{-1}) can be observed in the ligand at 281 and 289.5 nm, but with a bathochromic shift, indicating that coordination lowers the transition energy of these bands. This supports the hypothesis that these bands are likely related to processes involving the *N*-acylhydrazone, given that they are absent in the spectra of the precursors and that coordination affects their energy. Additionally, the electronic transitions observed in this region are related to the conjugated bonds within the aromatic fraction of the ligand (Eid *et al.*, 2021; Rada *et al.*, 2019; Rada *et al.*, 2020).

The broad band observed at 335.5 nm (11,127 ± 68 L mol^{-1} cm^{-1}) is present in the spectrum of 5-methylsalicylaldehyde, suggesting that this band also has a contribution from the hydrazone bridge between the rings, as seen in the **H_2L2** series complexes. Unlike the ligand spectrum, the spectrum of complex **3A** displays an intense and broad band at around 406 nm (11,119 ± 78 L mol^{-1} cm^{-1}). This absorption is attributed to the charge transfer from the phenolate ion to the Cu^{2+} metal center. This band is absent in the spectra of the free ligands evaluated in this study and may indicate coordination, as the presence of the Cu^{2+} ion may lead to ligand deprotonation. The band at 633 nm (97.71 ± 1.57 L mol^{-1} cm^{-1}) is associated with *d-d* transitions, with low molar absorptivity justifiable by the fact that such electronic transitions are Laporte-forbidden, as previously discussed.

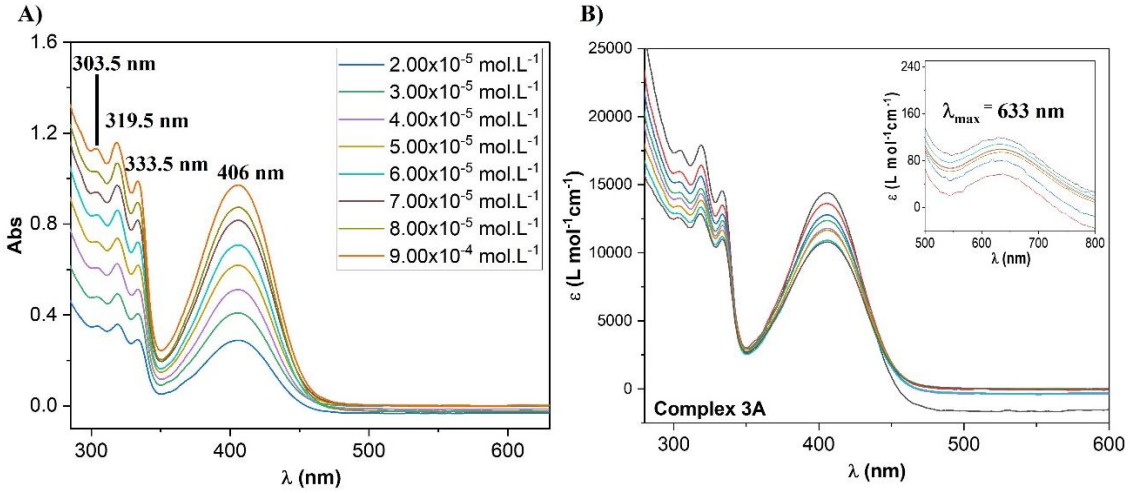

Figure 95. A) Electronic spectra of **3A** in DMF solution, at different concentrations. **B)** The same spectra as a function of molar absorptivity.

Figure 96 displays the diffuse reflectance electronic spectrum of complex **3A**, along with the main components obtained through band deconvolution. The spectrum was deconvoluted into four absorptions. One of them, at around 257 nm, corresponds to the shifted band present in the ligand at approximately 281 nm, associated with the conjugated bonds in the aromatic portion of **H_2L3**. The band observed at 322 nm in the diffuse reflectance spectrum correlates with the one appearing at 333.5 nm in the solution spectrum and may be related to transitions involving the *N*-acylhydrazone moiety. On the other hand, the LM charge transfer band from phenolate to copper(II) is observed at 421 nm. The *d-d* transition was centered at 691 nm, which means a bathochromic shift of around 60 nm in relation to the corresponding band in DMF solution.

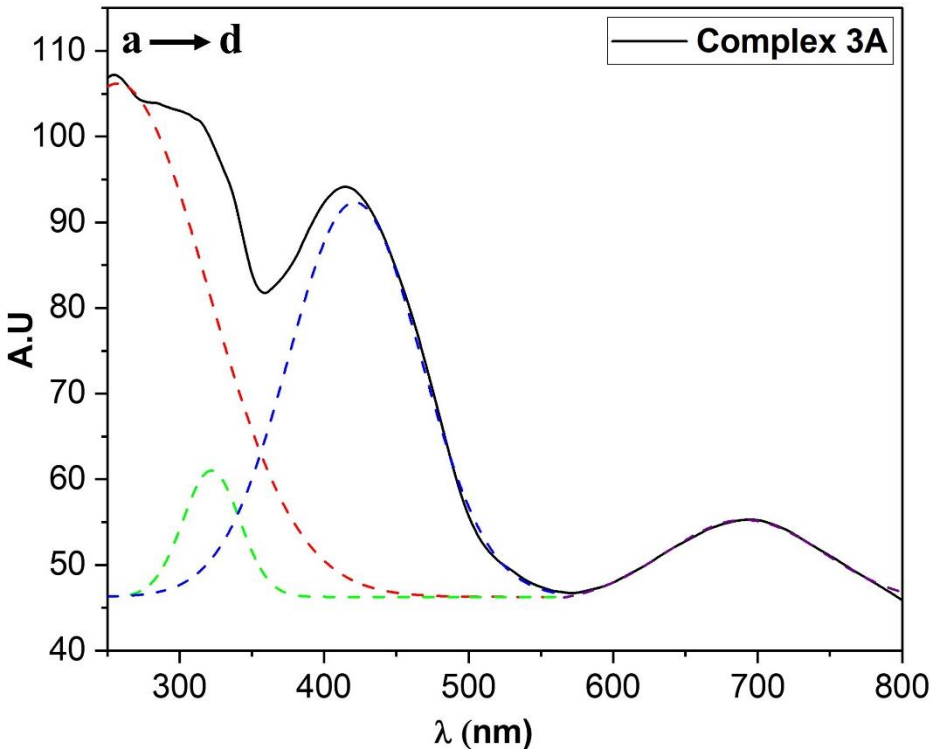

Figure 96. Electronic diffuse reflectance spectrum of **3A**, in black. Main components obtained by band fitting: a) 257 nm, b) 322 nm, c) 421 nm and d) 691 nm.

Table 27 correlates the obtained λ_{max} values for the electronic spectra of complex **3A** in DMF solution and in the solid state (diffuse reflectance). Analysis of the results reveals similar bands, albeit with shifts. The bands centered at 257 and 322 nm are associated with electronic transitions in the ligand portion, while the band at 421 nm is related to LMCT transitions from the phenolate ion to the copper(II) center, but exhibits a significant bathochromic shift. This shift suggests that in solution, the coordination sphere of the metal may undergo modifications, influencing the energy of this band. A similar observation can be made for the band at 691 nm, related to the *d-d* transition. The bathochromic shift in this band compared to the electronic spectrum in DMF solution indicates a change in the stereochemistry of the complex once it is dissolved. In solution, solvent molecules may axially coordinate to the copper(II) ion, causing tetragonal distortion due to the Jahn-Teller effect, which accounts for the energy shift of the *d-d* transitions (Hathaway & Billing, 1970; Lever, 1984; Moura *et al.*, 2023).

Table 27. Comparison of electronic spectra by diffuse reflectance with those obtained in solution for complex **3A.**

Complex	**Transitions**							
	precursors-related		*N*-acylhydrazone		Phenolate → Cu^{2+}		*d-d* transition	
	DRIFTS (nm)	UV-Vis (nm)	DRIFTS (nm)	UV-Vis (nm)	DRIFTS (nm)	UV-Vis (nm)	DRIFTS (nm)	UV-Vis (nm)
3A	257	281	322	333.5	421	406	691	633

Table 27 correlates the obtained λ_{max} values for the electronic spectrum of complex **3A** in DMF solution and by diffuse reflectance diluted with barium sulfate. Analysis of the results reveals similar bands, albeit with shifts. The bands at 257 and 322 nm are associated with electronic transitions in the ligand portion, while the band at 421 nm is related to charge transfer from the phenolate ion to the copper(II) ion but exhibits a significant bathochromic shift. This shift suggests that in solution, the coordination sphere of the metal ion may undergo modifications, influencing the energy of this band. A similar observation can be made for the band at 691 nm, related to the *d-d* transition. The bathochromic shift in this band compared to the electronic spectrum in solution indicates a change in the stereochemistry of the complex in solution. In solution, solvent molecules may axially coordinate to the copper(II) ion, causing tetragonal distortion due to the Jahn-Teller effect, which accounts for the energy shift of the d-d transition due to the different distortions experienced by the d orbitals when the metal ion is coordinated with axial solvent molecules (Hathaway & Billing, 1970; Lever, 1984; Moura *et al.*, 2023).

5.4.2.5 Electrochemical Behavior - Cyclic Voltammetry

The electrochemical behavior of **3A** was evaluated by cyclic voltammetry using a three-electrode system, under conditions analogous to those used for its ligand. The complexes obtained from chloride and nitrate salts were dissolved in a DMF solution with $TBAPF_6$ as the supporting electrolyte, under N_2 atmosphere, without prior control of the analyte concentrations. From the voltammograms of the complexes (Figure 98), electrochemical parameters were obtained (Table 28).

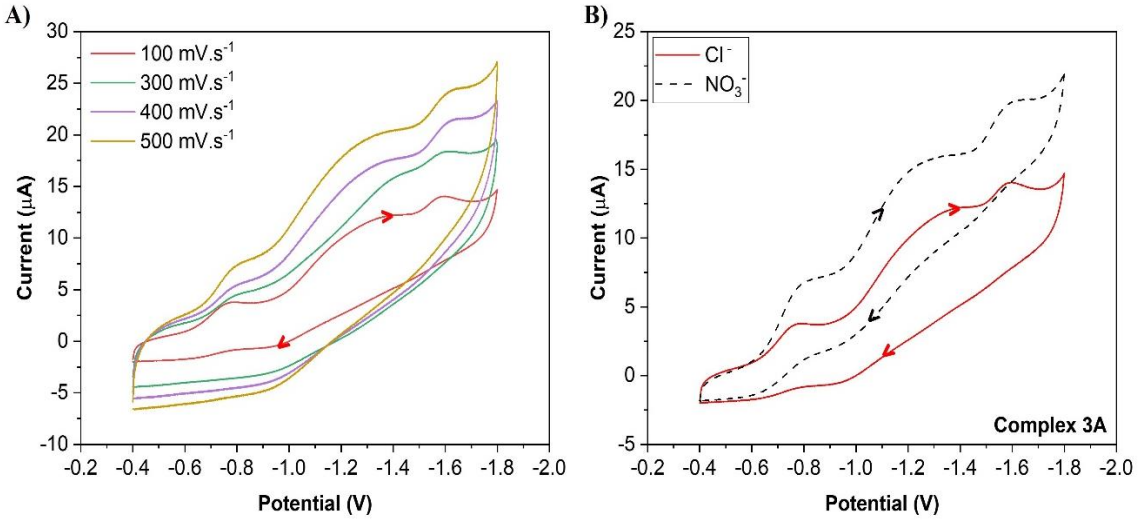

Figure 97. (A) Representative cyclic voltammograms of **3A**, at different scan rates, measured in DMF/0.1 mol L-1 TBAPF6 (25 ºC), using a GCE as the working electrode. **(B)** Comparison of cyclic voltammograms for complex **3A** samples obtained from different starting salts, with a scan rate of 100 mV s^{-1} and under the same experimental conditions.

Figure 97A shows cyclic voltammograms of complex **3A**, indicating no evidence of anodic (oxidation) processes, which along with potential dependence on scan rate can confirm the irreversible nature of redox processes (Compton & Banks, 2007; Jayamani *et al.*, 2014; Jayamani *et al.*, 2015; Laviron *et al.*, 1980). Two well-resolved cathodic peaks and a broad cathodic wave, which lowers the reliability regarding the number of electrons involved, can be observed. The peak at –0.76 V *vs*. Ag/AgCl corresponds to the $Cu^{2+/}Cu^{+}$ redox couple, consistent with the potential range of other synthesized complexes involving this redox pair. The cathodic peak around –1.38 V *vs*. Ag/AgCl is less defined, probably indicating the involvement of multiple species in equilibrium. The peak at –0.76 V *vs*. Ag/AgCl likely relates to a species coordinated with water molecules, given its potential aligns with other complexes possibly coordinated similarly. Conversely, the broad cathodic peak at around –1.38 V *vs*. Ag/AgCl may involve species of the complex coordinated with DMF solvent molecules, which suggests a different coordination environment from water-coordinated species. The ligand **H_2L3** is electroactive, showing a cathodic peak at the potential of –1.71 V *vs*. Ag/AgCl. For this reason, the peak detected at –1.60 V *vs*. Ag/AgCl was assigned to the coordinated ligand's reduction process. The shift of the cathodic potential towards less negative values suggests that the positive charge of the metal ion facilitates the reduction of the azomethine group. Other reduced species such as copper(I) and phenoxyl radicals

are not expected in this potential range (Manzur *et al.*, 2009).

Figure 97B compares the cyclic voltammograms of complex **3A** obtained from different copper(II) salts. Observed current intensities differ due to variations in solution concentrations, influencing the observed current values. However, the electrochemical behavior of the compounds is remarkably similar, with almost the same cathodic potential values. This reaffirms the concept that complex **3A** can be obtained *via* different synthetic routes starting from different precursor salts.

Table 28. Estimated electrochemical parameters for the studied complexes.

Complex	**3A**		
E_{pc1} **(V *vs* Ag/AgCl)**	–0.76	E_{pc3} **(V *vs* Ag/AgCl)**	–1.60
$E_{pc1½}$ **(V *vs* Ag/AgCl)**	–0.59	$E_{pc3½}$**(V *vs* Ag/AgCl)**	–1.28
α_{c1}	0.24	α_{c3}	0.20
n_{c1}	1.16	n_{c3}	0.75

The relationship between the square root of scan rate and peak current provides information about the type of transport process in cyclic voltammetry (Abbar & Nandibewoor, 2012). Analyzing this relationship for the studied ligands reveals a linear correlation, indicating a diffusion-controlled behavior (Abbar & Nandibewoor, 2012; Gosser, 1993), a hypothesis further supported by the linear relationship between the logarithms of the potential and of scan rate, with slope less than or nearly equal to 0.5 (Compton & Banks, 2007; Laviron *et al.*, 1980). Both processes seem to involve only one electron each.

5.4.2.6 Complexation Studies

The complexation study for the **H_2L3**-derived series of complexes was conducted in order to closely replicate the synthetic conditions. Therefore, the analyses were carried out in methanol. Solutions of the ligand were prepared at a concentration of 4×10^{-5} mol L^{-1}, while both solutions containing the starting salts [copper(II) chloride dihydrate and copper(II) nitrate trihydrate] at 3×10^{-4} mol L^{-1}.

Upon adding equivalents of the starting salt to the ligand solution, changes were monitored using UV-Vis electronic spectroscopy. The band around 405 nm, associated with the LMCT transition from the phenolate ion to the cupric center, was tracked as an indicator of complexation. Successive additions of the starting salts led to an increase in the absorbance of this band. In addition, some isosbestic

points were observed, suggesting the presence of only two absorbing species in the solution equilibrium, i.e., free and coordinated ligand.

Figure 98A illustrates the spectral profile observed during the titration of **H_2L3** with copper(II) chloride solution. The study was performed in triplicate, and the average absorbance values were plotted against the equivalents of Cu^{2+} added (Figure 98B). The curve shows a saturation trend near 1 equivalent of copper, suggesting that the stoichiometry of the complex formed in solution is 1:1, which is consistent with the structure proposed for the complex isolated in the synthesis.

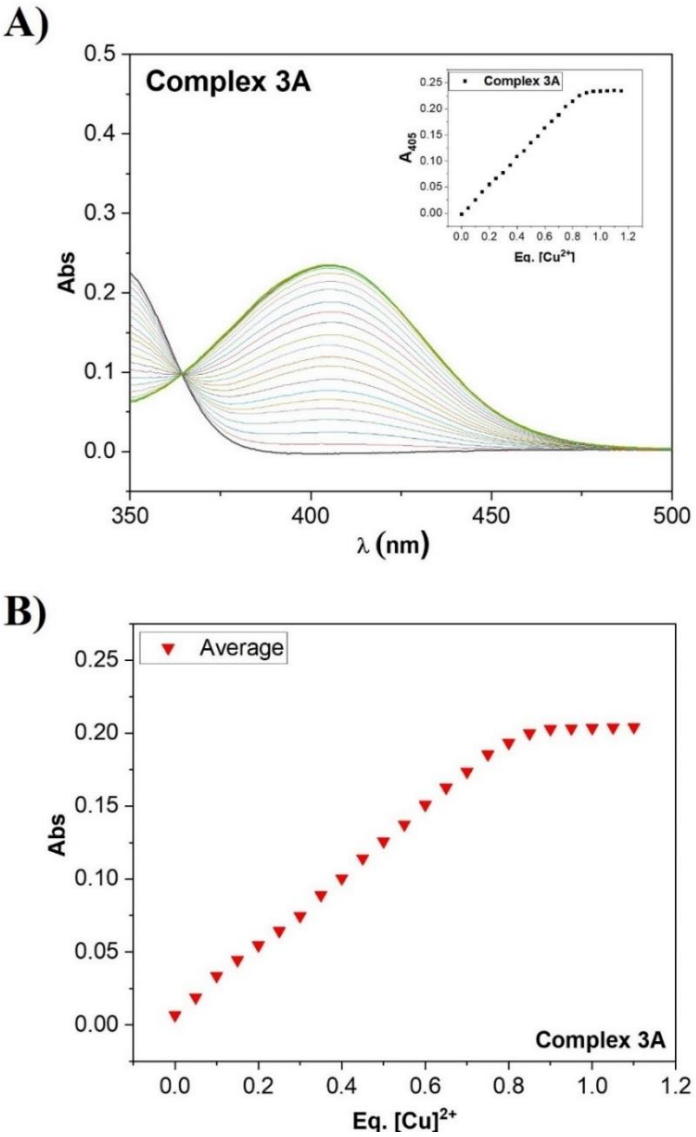

Figure 98. A) Study of complexation of **3A** and the relationship between absorbance and the number of Cu^{2+} equivalents. **B)** Result of the average of triplicates of the complexation study of **3A.**

Figure 99 presents a comparison of the electronic spectral profiles for the

H_2L3-derived complexes formed from different starting copper(II) salts (chloride and nitrate). A comparison of the electronic spectra for the copper(II) complexes obtained from different starting salts suggests that the species formed in solution are virtually the same. So we can conclude that the complex **3A** obtained from copper(II) chloride is identical to that obtained from copper(II) nitrate, in solution and in the solid state, as also observed in the infrared spectrum analysis. It is possible that the bulky phenylisoxazole substituent present in **H_2L3** may limit the structural variability of the complexes derived from this ligand.

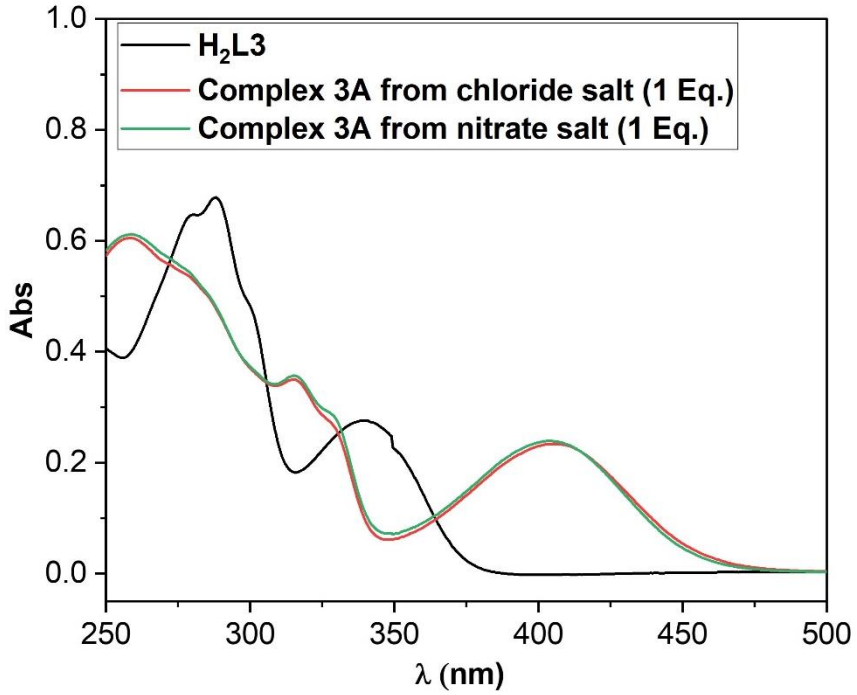

Figure 99. Comparison of the electronic spectra, in MeOH, of the free ligand **H_2L3** (4×10^{-5} mol L^{-1}) and the copper(II) complex formed by the addition of 1 eq the respective chloride and nitrate salts.

Figure 100, on the other hand, enables an indirect analysis of the species (free ligand and complex) concentration changes along titration by simultaneously monitoring the absorbance of a ligand (at 339 nm) and a complex (405 nm) band. Once again, absorbance stabilizes at around 1 equivalent of copper, suggesting an equilibrium condition between the free ligand and **3A**.

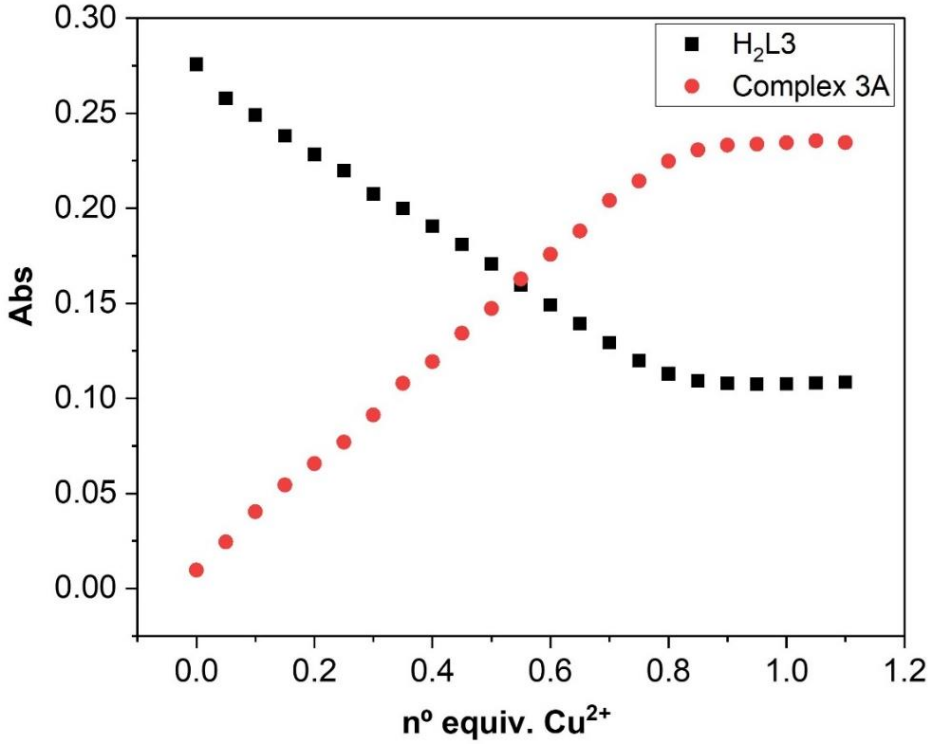

Figure 100. Qualitative graph that illustrates the variation of ligand species and their respective **3A** based on the absorption and number of equivalents of the salts used.

5.5 H_2L4 Series

5.5.1 Synthesis of the Compounds belonging to the H_2L4 Series

The ligand **H_2L4** was synthesized via a condensation reaction between 5-methylsalicylaldehyde and 1-methyl-imidazole-2-carbohydrazide, the latter being prepared from the respective ester by our collaborators Hélcio Marcondes and Prof. Claudio Donnici (UFMG), with a good yield. The complexes were obtained as powders under the same conditions and with appreciable yields. Figure 101 illustrates the whole synthesis scheme within this series.

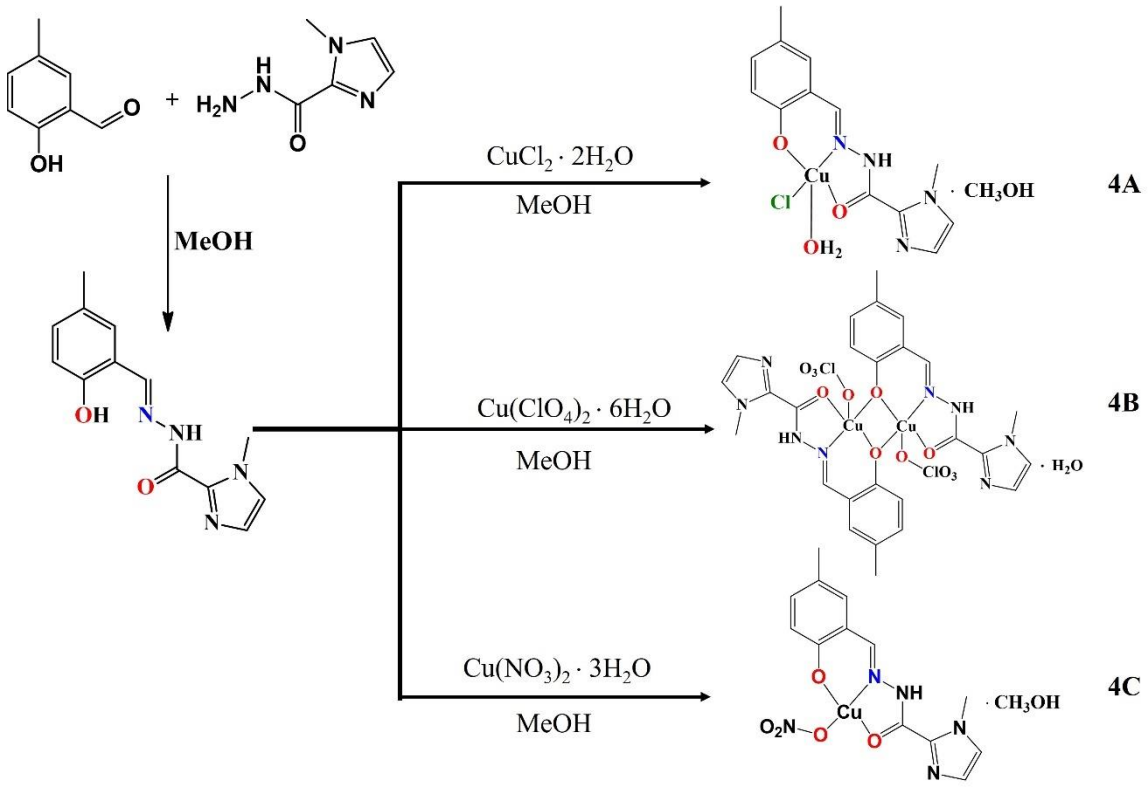

Figure 101. General scheme of the synthesis of the **H_2L4** and complexes **4A**, **4B** and **4C**.

The thermogravimetric analysis of complex **4A** (Figure 102) reveals two thermal events between 30-250 ºC. The first event, starting at around 40 ºC with a mass loss of 6.42%, is indicative of the removal of a component that is not part of the coordination sphere, such as moisture or a residual solvent from the synthesis; in this case, methanol. The second mass loss, starting at around 200 ºC, is likely related to the removal of a coordinated water molecule and hydration methanol, with a loss of 10.55% (calculated: 10.1%). Finally, the residual mass is 16.2%,

and given that the analysis was conducted in an argon atmosphere, it is probable that this residue is in the form of metallic copper. This is in agreement with the 16.6% found by ICP-OES. Since the copper percentage for the suggested structure is calculated to be 15.6%, this supports the consistency of the proposed structure with the results obtained from both the thermogravimetric and copper elemental analyses. Complex **4B**, which contains a coordinated perchlorate ion, could not be analyzed by thermogravimetry due to its potential explosive nature.

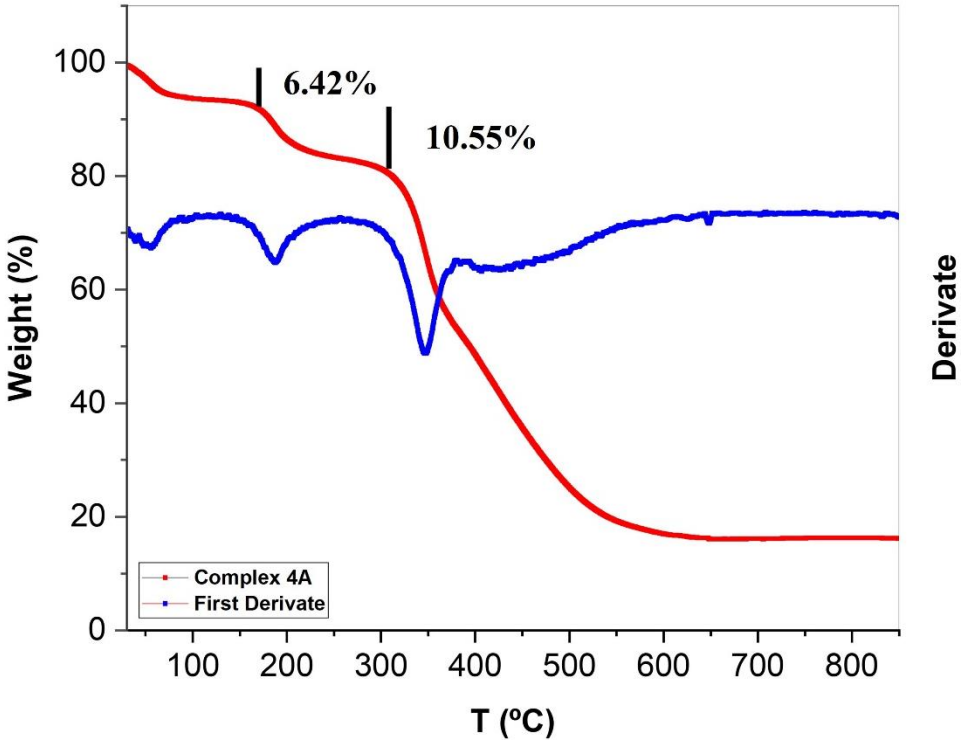

Figure 102. Thermogravimetric curve for complex **4A.**

The thermogravimetric curve for complex **4C** (Figure 103) displays three thermal events between 30-400 ºC. The first event, starting at around 30 ºC, shows a mass loss of 7.40%, which is likely related to the loss of moisture and residual solvent molecules (methanol), as observed for compound **4A**. Another mass loss of 8.35% occurs at around 170 ºC, possibly associated with the loss of a molecule of O_2 from the thermal decomposition of the nitrate ion (calculated: 7.70%) (Fei *et al.*, 2019). A thermal event at 310 ºC shows a mass loss of 28.8%, suggesting that this loss is related to the inorganic residual fraction of the nitrate ion in the form of NO_x and the organic fraction relative to the ligand.

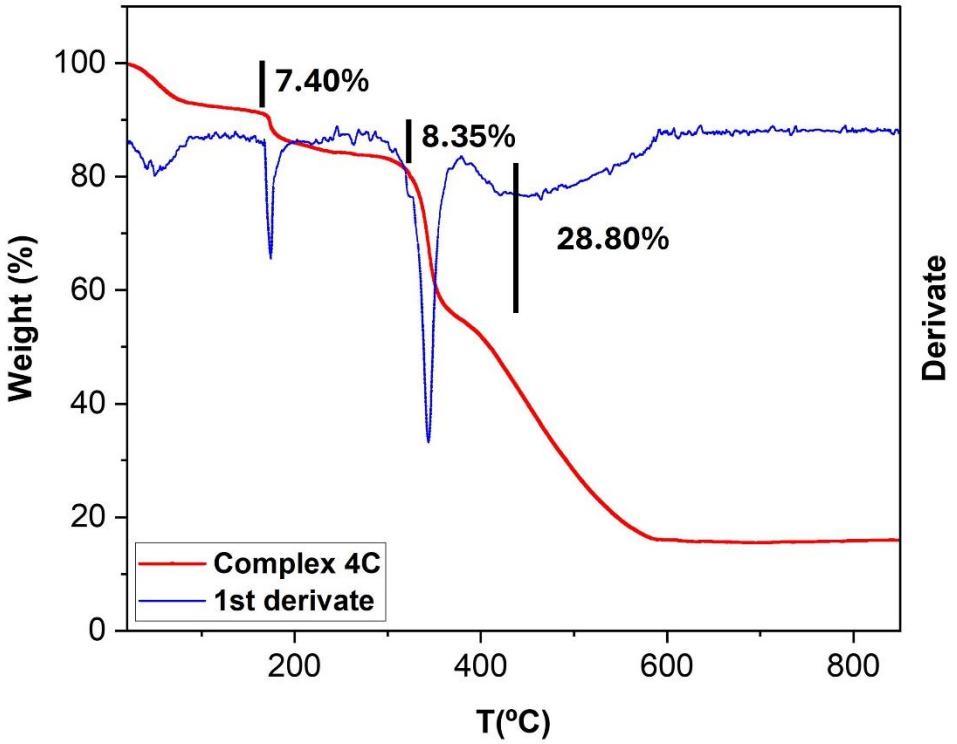

Figure 103. Thermogravimetric curve for complex **4C.**

5.5.2 Characterization of ligand H_2L4 and their complexes

5.5.2.1 Elementar Analysis (CHN) and Copper content (ICP-OES)

Elemental analysis tests were conducted on the samples following purification by recrystallization in methanol. The obtained results are listed in Table 29.

Table 29. Calculated and experimental elemental analyses of the complexes **4A, 4B** and **4C.**

Complexes	**%C**		**%H**		**%N**		**%Cu**	
	calculated	found	calculated	found	calculated	found	calculated	found
4A	41.4	---	4.7	---	13.8	---	15.6	16.4
4B	36.4	36.6	3.3	3.1	13.0	12.6	14.8	14.7
4C	40.5	40.6	4.1	3.5	16.9	16.7	15.3	15.8

5.5.2.2 Molar conductivity studies

Table 30 lists the molar conductivity values obtained for complexes **4A**, **4B**, and **4C**, along with the different possible types of electrolytes using DMF as solvent, correlated with data provided by Geary (1971).

Table 30. Relationship between the molar conductivity data obtained with the electrolyte system.

Complexes	**4A**	**4B**	**4C**
Molar conductance ($\Omega^{-1}cm^2mol^{-1}$)	65.26	144.8	55.22
Electrolyte	1:1	1:2	1:1

Complex **4A** exhibits molar conductivity within the range typical for 1:1 electrolytes in DMF solution, which is consistent with the proposed structure. The departure of the chloride ion facilitates the entry of a solvent molecule into the coordination sphere, similar to what was proposed for complex **2A**. In **4A**, it is believed that the equilibrium favors the departure of the chloride ion more than in complex **2A**, as the former demonstrates a higher molar conductivity.

Complex **4B** shows the highest molar conductivity among the **H_2L4** series. This value falls within the range for 1:2 electrolytes in DMF solution, which is in line with the proposed structure (Geary, 1971). It is suggested that the perchlorate ions in complex **4B** are axially coordinated. The axial coordination is weaker due to the tetragonal distortion common to Cu^{2+} complexes, indicating that removal of coordinated perchlorate ions in solution is a facilitated process:

$$\mathbf{[Cu_2(HL)_2(ClO_4)_2]\cdot H_2O \rightarrow [Cu_2(HL)_2]^{2+} + 2\ ClO_4^- + H_2O}$$

Complex **4C**, instead, exhibits a much lower molar conductivity compared to complex **4B**. However, considering the proposed structures for complexes **4A** and **4C**, similarities in their coordination spheres can be observed, which justifies their comparable molar conductivities. Consequently, complex **4C** falls within the typical range for 1:1 electrolytes. As with complexes **2A** and **4A**, there exists an equilibrium between the dissociated and non-dissociated forms, which accounts for the molar conductivity value obtained.

5.5.2.3 Infrared Vibrational Spectroscopy

Analyzing the infrared vibrational spectra obtained for the compounds, a behavior analogous to that observed in other series can be noted. However, certain shifts and disappearances of bands, as well as the emergence of new absorptions in the spectra of complexes, suggest the occurrence of coordination (as can be seen in Figures 104-106 and in the data summarized in Table 31).

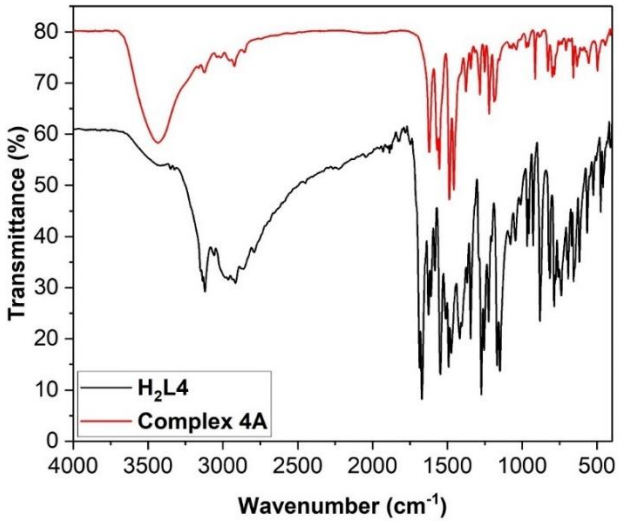

Figure 104. Overlapping of the mid-infrared spectra of **H_2L4** and **4A** in KBr, at room temperature.

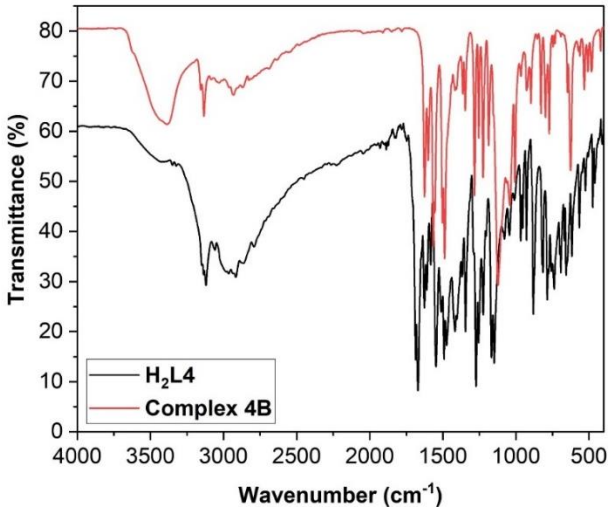

Figure 105. Overlapping of the mid-infrared spectra of **H_2L4** and **4B** in KBr, at room temperature.

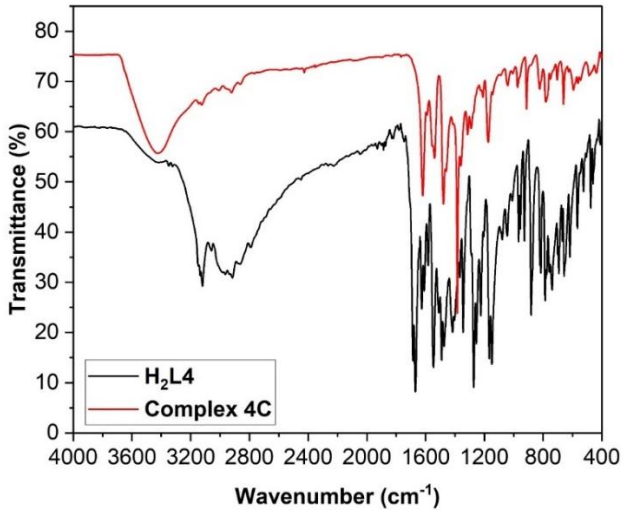

Figure 106. Overlapping of the mid-infrared spectra of **H_2L4** and **4C** in KBr, at room temperature.

Table 31. Selected vibrational absorptions (cm^{-1}) for **H_2L4** and their complexes.

Assingment	H_2L4	Complex 4A	Complex 4B	Complex 4C
υN−H	3119	3118	3128	3124
υO−H_{phenol}	3425	-----	-----	-----
υO−H_{water}	-----	3430	3390	3425
υC=O	1672	1570	1564	1555
υC=N	1626	1621	1621	1619
δC=N−H	1547	1485	1487	1477
δC−O−H_{phenol}	1491	-----	-----	-----
υ(NO_2)$_{ass}$	-----	-----	-----	1381
υC=C_{arom}	1343	1553	1553	1540
υC−O_{phenol}	1271	1283	1279	1288
υ(NO_2)$_{sym}$	-----	-----	-----	1317
δC=C−H_{phenol}	1222	1220	1220	1211
υN−N	1147	1170	1186	1173
υ(ClO_4)$_{ass}$	-----	-----	1122	-----
υ(ClO_4)	-----	-----	1041	-----
υNO	-----	-----	-----	1046
υ(ClO_4)$_{sym}$	-----	-----	626	-----
υCu−O	-----	554	533	543
υCu−N	-----	621	563	595
δO−Cu−N	-----	494	483	487

Upon comparing the ligand-related bands with those of their respective complexes, it is observed that most of the bands shift to lower energy values. As previously discussed, this shift indicates coordination.

The studied complexes exhibit ionic species, such as chloride, perchlorate, and nitrate coordinated to the metal ion. Consequently, it is expected that the N−H group of the hydrazone in the ligand remains protonated in all the complexes, which is confirmed by the νN−H bands observed in **4A**, **4B**, and **4C** at 3118, 3128, and 3124 cm^{-1}, respectively (Pavia *et al.*, 2015; Silverstein, 2000).

The ν(C=N) stretching of the azomethine group is at 1626 cm^{-1} for **H_2L4**. In complexes **4A**, **4B** and **4C**, this band appears somewhat shifted to 1621, 1621, and 1619 cm^{-1}, respectively, indicating coordination by this group. Indeed, our previous experience shows that this absorption is not so sensible to complexation

(Nakamoto, 1978; Pavia *et al.*, 2015; Silverstein, 2000).

The carbonyl absorption ν(C=O) shifts from 1672 cm^{-1} in the ligand to 1570 cm^{-1} in complex **4A**, 1564 cm^{-1} in **4B**, and 1555 cm^{-1} in **4C**. This shift occurs because the C=O bond becomes weakened upon coordination and vibrates at a lower frequency, in addition to the electronic delocalization favored in the hydrazone portion, which explains the band shift observed when comparing the ligand to the complexes. In addition to the ligand-based bands, some metal-ligand vibrations were also identified in the spectra of the complexes. These include the Cu−O stretching absorptions at 554 (**4A**), 533 (**4B**), and 543 cm^{-1} (**4C**) (Nakamoto, 1978; Pavia *et al.*, 2015; Silverstein, 2000).

For complex **4B**, bands related to the vibrational modes of the perchlorate ion are observed, supporting the proposed structure for the complex. Similar to what was discussed for complex **1B**, the bands for $\upsilon(ClO_4)_{ass}$ at 1122 cm^{-1}, υClO_4 at 1041 cm^{-1}, and $\upsilon(ClO_4)_{sym}$ at 626 cm^{-1} are consistent with the monodentate coordination mode of perchlorate to the metal ion (Nakamoto, 1978; Rey, 2019).

For complex **4C**, on the other hand, absorptions for $\upsilon(NO_2)_{ass}$ at 1381 cm^{-1}, $\upsilon(NO_2)_{sym}$ at 1317 cm^{-1}, and υNO at 1046 cm^{-1} are observed and correspond to the monodentate coordination of the nitrate ion (Nakamoto, 1978).

In addition to the bands related to the stretching of the main functional groups, correlations can be made with some bands obtained for the binuclear complexes in the form of dimers from this study. Literature data allow for the elucidation of dinuclear complex structures containing the phenolate bridge group of the type O−Cu−O, suggesting two main vibrational modes in angular systems, one around 770 cm^{-1} and the other around 500 cm^{-1} (Hewkin & Griffith, 1966). In hydrazone-containing systems, the O−Cu−O motif exhibits intense bands around 770 and 730 cm^{-1} (Mohan *et al.*, 1992). Since monocrystals could not be obtained for elucidating the suggested dimeric structure for complex **4B**, some correlations regarding spectroscopic properties become more relevant. Thus, a comparison of the infrared vibrational spectra of the dimeric complexes **2B** and **2C**, for which X-ray structures have been elucidated, with that of **4B** was performed (Figure 107).

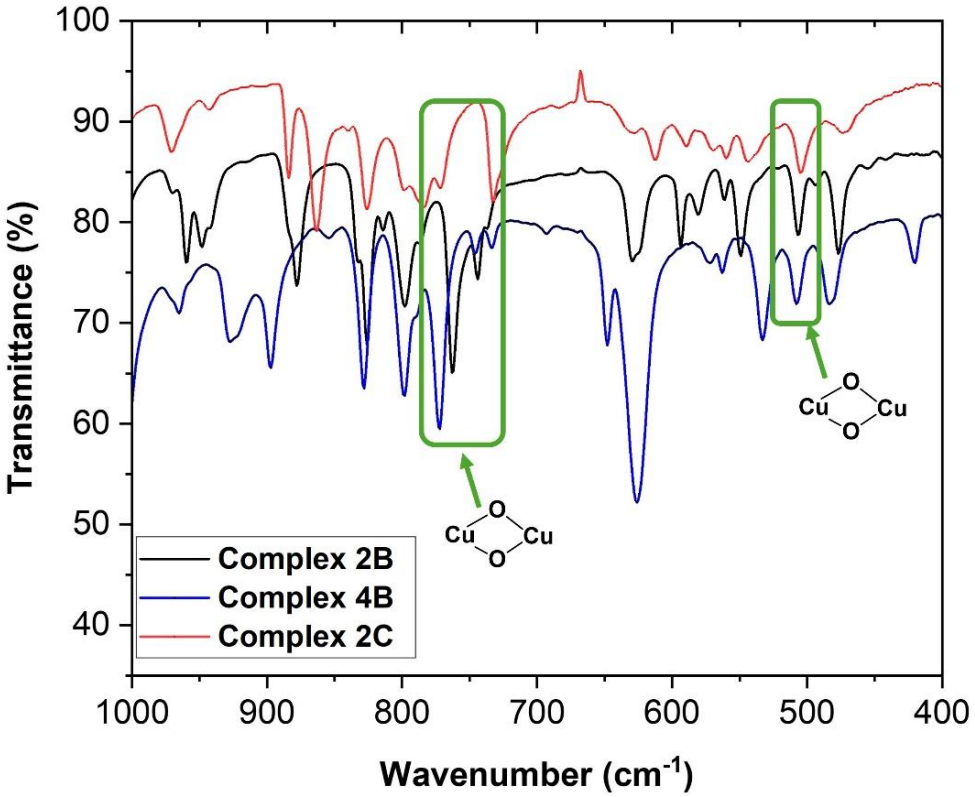

Figure 107. Comparative overlay of mid-infrared spectra of complexes **2B**, **2C** and **4B** in KBr, at room temperature. Some common features are highlighted.

Upon comparing the overlaid spectra, it is observed that the band in the region of 770 cm^{-1} appears in the dimeric species **2B** and **2C** at 761 and 732 cm^{-1}, respectively, as well as in complex **4B,** at 771 cm^{-1}. The fact that **4B** exhibits the O−Cu−O stretching band at a higher wavenumber may indicate a larger opening angle in the phenolate-copper(II) cycle. Additionally, another stretch related to the O−Cu−O group is observed consistently around 500 cm^{-1}: at 506 cm^{-1} for complex **2B**, 505 cm^{-1} for **2C**, and 508 cm^{-1} for **4B**. These data provide further insight into the proposed structure (Hewkin & Griffith, 1966; Mohan *et al.*, 1992).

5.5.2.4 Electronic Spectroscopy in UV-Vis

The ligand **H_2L4** and the obtained complexes were analyzed by UV-Vis electronic spectroscopy under similar conditions to those used throughout this study. The spectrum of **H_2L4**, shown in Figure 108, exhibits five main absorption features in the range of 250 to 500 nm, comprising four distinct bands and a shoulder. A slight discontinuity is observed around 350 nm in the spectrum, which is attributed to the transition between light sources going from Vis to UV regions.

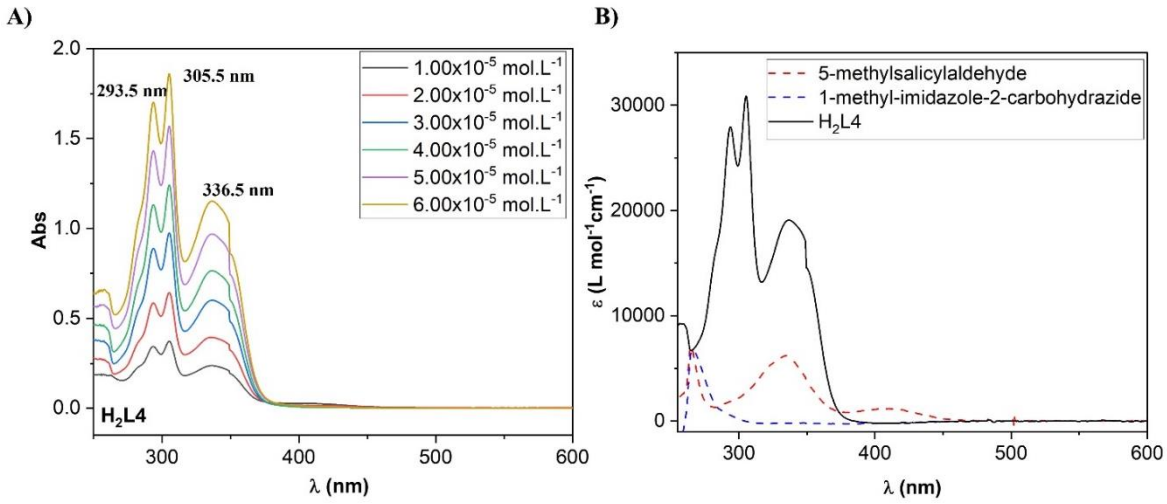

Figure 108. A) UV-Vis electronic spectrum of **H_2L4** at different concentrations in DMF solution. **B)** UV-Vis spectra of the ligand and its precursors (5.0×10^{-5} mol L^{-1}) in DMF solution.

When comparing the spectrum of the ligand with its precursors (Figure 108B), it is evident that two of the absorptions are present in the precursors, which are associated with transitions of the phenol and/or imidazole rings. The electronic behavior of the **H_2L4** ligand is similar to that of the other ligands discussed, as the intense bands observed at 293.5 nm (27,958 ± 444 L mol^{-1} cm^{-1}) and 305.5 nm (30,583 ± 474 L mol^{-1} cm^{-1}) are likely related to processes specifically involving the *N*-acylhydrazone moiety, since these bands are absent in the spectra of the precursors. The broad band observed at 336.5 nm (18,883 ± 328 L mol^{-1} cm^{-1}), although also present in the spectrum of 5-methylsalicylaldehyde, exhibits higher molar absorptivity in the ligand, suggesting a significant contribution from the hydrazone bridge between the rings.

The UV-Vis electronic spectrum of the complex **4A** (Figure 109), exhibits six absorptions between 250 and 500 nm, of which four are well-defined bands and two are less well-defined. Comparing the ligand spectrum with that of **4A**, it is evident that four bands are present in **H_2L4** and, among them, three bands in the ligand's precursors. The absorptions at 270 nm (18,521 ± 257 L mol^{-1} cm^{-1}) and 336.5 nm (13,063 ± 202 L mol^{-1} cm^{-1}) are related with the conjugated π-bonding systems of the phenol and/or imidazole rings, as they are observed in the spectra of **4A**, **H_2L4**, and its precursors. Additionally, the band centered at 417.5 nm (14,300 ± 207 L mol^{-1} cm^{-1}) in the spectrum of **4A** is associated to one present in the spectrum of the precursor 5-methylsalicylaldehyde, since it is related to the phenolate ion. Notably, this band increases in intensity in the complex because the

metal ion coordinates with the phenolate oxygen. This LMCT band, which is not observed in the spectrum of the free ligand, is a strong indicator of coordination.

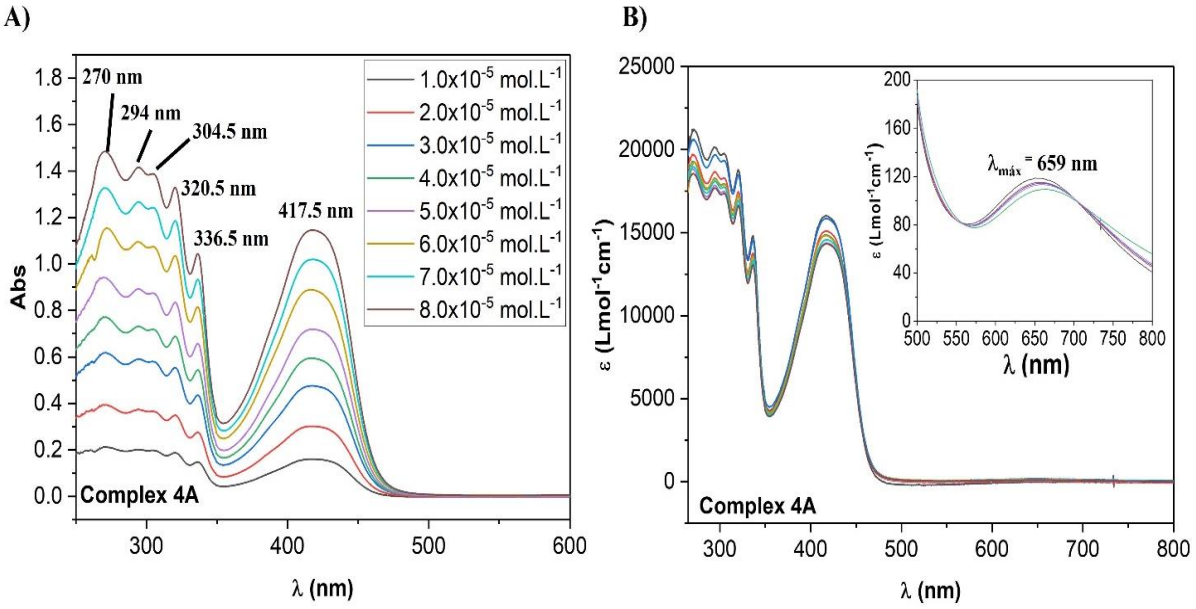

Figure 109. A) Electronic spectrum of complex **4A** in DMF solution, at different concentrations. **B)** Electronic spectra of complex **4A** in DMF solution as a function of molar absorptivity.

The bands at 294 nm (17,675 ± 258 L mol^{-1} cm^{-1}) and 304.5 nm (17,330 ± 257 L mol^{-1} cm^{-1}) are present only in the spectra of the ligand and the complex, suggesting that these bands are related to processes specific to the hydrazone system (Figure 110). In contrast, the band at 320.5 nm (18,521 ± 257 L mol^{-1} cm^{-1}) appears solely in the spectrum of the complex, possibly indicating an interaction between the metal ion and the hydrazone portion, as this region is dominated by electronic transitions associated with *N*-acylhydrazone (Figure 110).

The literature reports that some copper(II) complexes with similar ligands can exhibit bands around 294-304.5 nm. These bands are associated with n→π* and π→π* transitions related to the azomethine and carbonyl groups, respectively (Cohen *et al.*, 1967; Firmino *et al.*, 2016; Gegiou *et al.*, 1996; Sorrell, 1989).

The bands listed in Table 32 are associated with the hydrazonic portion common to both the ligand and the complex, with no significant shift observed in these bands. This suggests that the ligand in the complex is in its amide form rather than iminol, consistent with the proposed structure for the complex (Chew *et al.*, 2014). If the ligand were in the iminol form in complex **4A**, a shift in the

bands related to the hydrazonic portion would be expected, as the energy of the transitions would differ considerably (Chew *et al.*, 2014). Given that the ligand is present in the amide form in **4A**, a counterion is necessary.

The low molar absorptivity band at 659 nm (110.20 ± 2.73 L mol^{-1} cm^{-1}) is attributed to the *d-d* transition (Figure 109B), being consistent with other copper(II) complexes derived from *N*-acylhydrazone ligands (Rada *et al.*, 2019; Rada *et al.*, 2021; Rada *et al.*, 2020). As discussed in this work, a broad band in the 600-700 nm region may indicate that the Cu^{2+} ion exhibits stereochemistry similar to that found in complexes of the **H_2L2** series. The obtained value for the *d-d* transition aligns with those observed for copper(II) complexes with similar structures (Chew *et al.*, 2014; Kala *et al.*, 2007; Lever, 1984).

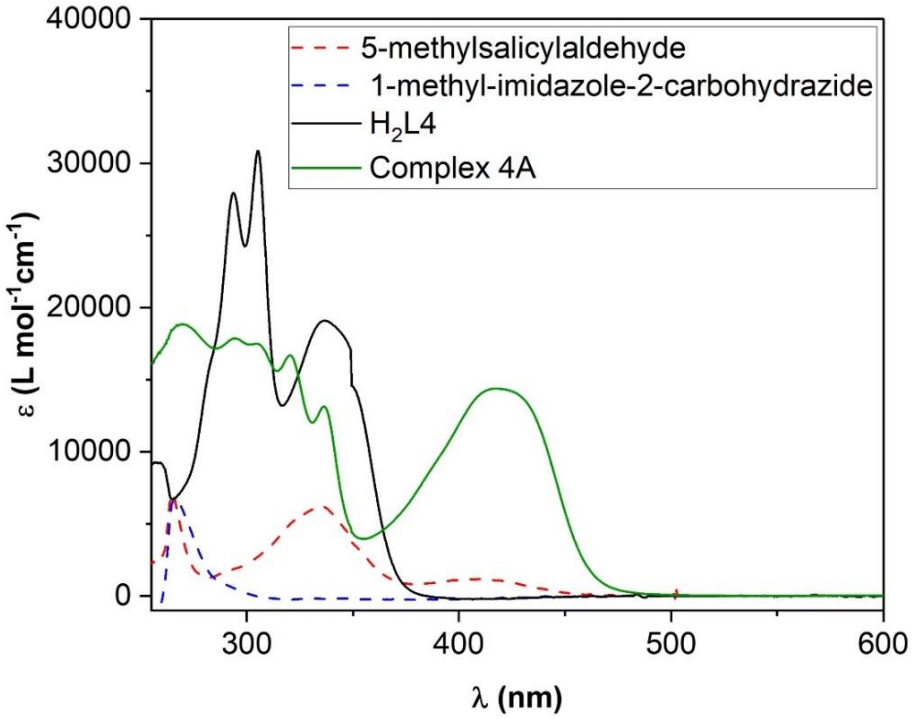

Figure 110. Electronic spectra of **4A, H_2L4** and its precursors in DMF solution (5×10^{-5} mol L^{-1}).

The electronic spectrum of complex **4B** (Figure 111) displays six absorption bands in the 250-500 nm range, similar to those observed for complex **4A**. The absorption bands at 268 nm (36,210 ± 1186 L mol^{-1} cm^{-1}) and 336.5 nm (24,094 ± 843 L mol^{-1} cm^{-1}) are associated with conjugated systems in the phenolic and imidazole aromatic rings. On the other hand, the bands at 293.5 nm (31,913 ± 1064 L mol^{-1} cm^{-1}) and 305 nm (31,447 ± 1065 L mol^{-1} cm^{-1}) are observed only in the spectrum of the ligand and its complexes, suggesting they are

related to the hydrazonic portion.

The bands listed in Table 32 are associated with the hydrazonic portion common to both the ligand and the complex (Figure 111). As previously mentioned, no significant shift in these bands is observed, indicating that the ligand in the complex is in its amide form rather than iminol, consistent with the proposed structure for the complex (Chew *et al.*, 2014).

The band at 418 nm (28,471 ± 976 L mol^{-1} cm^{-1}) is present in the electronic spectrum of the precursor 5-methylsalicylaldehyde (Figure 112); however, this band is more intense in the complex, suggesting that it can be attributed to a charge transfer from the phenolate ion to the metal. The band around 400 nm is observed in all the complexes evaluated in this study, serving as a key transition to suggest the coordination of the metal to the *N*-acylhydrazone ligand. The band at 320.5 nm (31,428 ± 1075 L mol^{-1} cm^{-1}) is only observed in the complexes, indicating it may be related to a charge transfer from the hydrazonic portion to the metal ion.

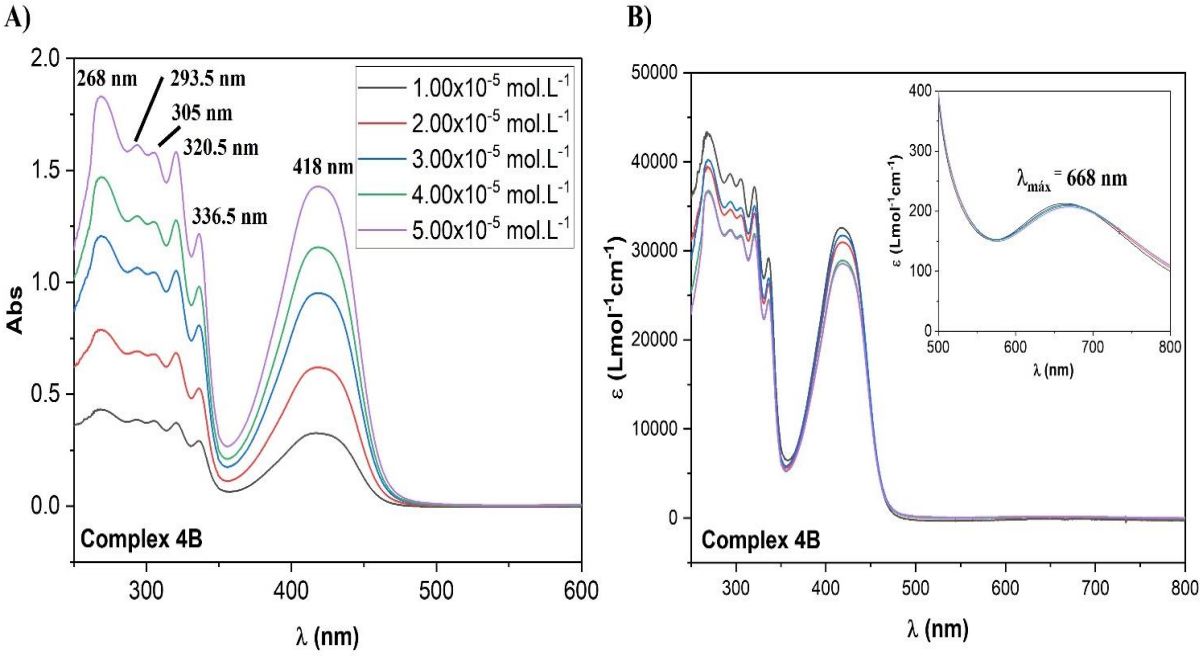

Figure 111. A) Electronic spectrum of **4B** in DMF solution, at different concentrations. **B)** Electronic spectra of complex **4B** in DMF solution as a function of molar absorptivity.

The low molar absorptivity band at 668 nm (207.3 ± 1.35 L mol^{-1} cm^{-1}) is associated with the *d-d* transition (Figure 111B), consistent with copper(II) complexes derived from *N*-acylhydrazone ligands. Analogous to what was discussed for complex **4A**, the presence of a broad band in the 600-700 nm region

may suggest that the Cu^{2+} ion exhibits a similar stereochemistry to the complexes in the **H_2L2** series (Moura *et al.*, 2023). Although the obtained value for the *d-d* transition aligns with pentacoordinated copper(II) complexes in solution, the differing *d-d* transition value might indicate a distinct coordination sphere for complexes **4A** and **4B** (Chew *et al.*, 2014; Kala *et al.*, 2007; Lever, 1984). This discrepancy may arise from the lability of the counter-ion position; since complex **4B** contains the perchlorate ion as a counter-ion, possibly in the axial position, its departure from the coordination sphere is more facile compared to the chloride ion. This allows a greater fraction of species in complex **4B** to have the axial coordination site available for substitution by water or solvent molecules.

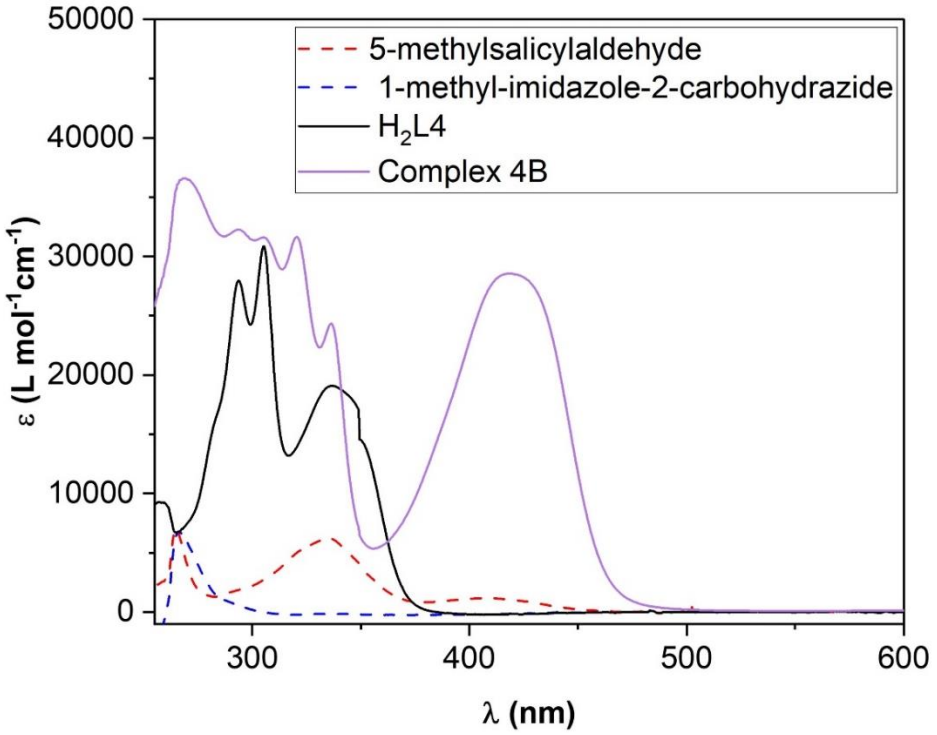

Figure 112. Electronic spectra of **4B, H_2L4** and its precursors in DMF solution (5×10^{-5} mol L^{-1}).

The electronic spectrum of complex **4C** is similar to that of the other complexes in the **H_2L4** series, displaying six absorption bands in the 200-500 nm range (Figure 113). The bands at 268 nm (18,149 ± 400 L mol^{-1} cm^{-1}) and 336.5 nm (12,345 ± 294 L mol^{-1} cm^{-1}) are associated with the conjugated bonds in the phenolic and imidazolic aromatic rings (Moura *et al.*, 2023).

Table 32 compares the bands uniquely associated with the hydrazonic moiety observed in the ligand and its complexes at 293.5 nm (16,190 ± 354 L mol^{-1} cm^{-1}) and 305.5 nm (15,931 ± 356 L mol^{-1} cm^{-1}). No significant shift in these bands is observed when compared with those of the ligand, suggesting that

the ligand in the complex is in its amide form rather than the iminol form, consistent with the proposed structure for the complex (Chew *et al.*, 2014).

The bands at 417 nm (14,390 ± 361 L mol^{-1} cm^{-1}) and 320.5 nm (16,038 ± 364 L mol^{-1} cm^{-1}) are related to charge transfer transitions, as they are observed exclusively in the electronic spectra of the **H_2L4** series complexes. The 417 nm band is attributed to charge transfer from the phenolate ion to the metal ion (MLCT), while the 320.5 nm band is possibly associated with the hydrazonic moiety (Figure 114A) (Rada *et al.*, 2019; Rada *et al.*, 2021; Rada *et al.*, 2020).

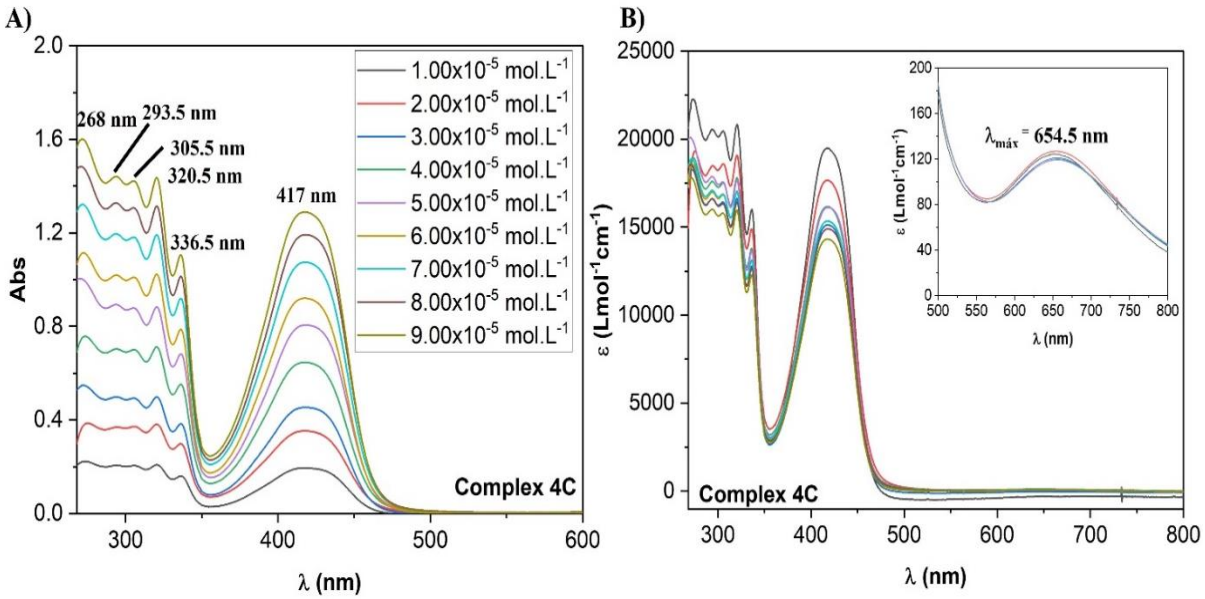

Figure 113. A) Electronic spectrum of **4C** in solution with DMF, at different concentrations. **B)** Electronic spectra of **4C** in solution with DMF as a function of molar absorptivity in the range of 250-800 nm.

The band at 654.5 nm (117.2 ± 1.72 L mol^{-1} cm^{-1}) is associated to *d-d* transitions (Figure 113B), consistent with copper(II) complexes of *N*-acylhydrazones. Analogous to the discussion for the other complexes, the presence of a broad band in the 600-700 nm region may indicate that the Cu^{2+} ion exhibits stereochemistry similar to that in the **H_2L2** series complexes (Moura *et al.*, 2023).

As observed in Figure 114B, the value obtained for the *d-d* transition in complex **4C** differs from that observed for complex **4B** but is quite similar to that observed for complex **4A**. This suggests that the species in solution for complex **4C** are more similar to those in complex **4A**, which is consistent with the molar

conductivity data indicating proximity between these two complexes. This implies that complexes **4A** and **4C** may be in equilibrium between their dissociated and non-dissociated forms. The structure observed in **2A** shows that the chloride ligand occupies the molecular plane, resulting in more intense interactions that hinder its departure during dissociation and facilitate the equilibrium between dissociated and non-dissociated species. The proposed structures for complexes **4A** and **4C** are analogous to those observed in complex **2A**, thus allowing for a similar equilibrium. In contrast, this equilibrium is less favored in complex **4B**, where, according to the proposed structure, the perchlorate ions occupy axial positions. In this position, due to the Jahn-Teller effect, the ligands bind weaklier, facilitating dissociation and accounting for the differences in *d-d* transitions among these complexes.

Beyond the potential for dissociation to form different species in equilibrium, another relevant factor is that, based on the obtained data, it can be suggested that complex **4B** is in its dimeric form. As a binuclear complex in dimeric form, its electronic transitions involving d orbitals will be particularly distinct from those observed in the mononuclear complexes **4A** and **4C**, as previously noted in (Ainscough *et al.*, 1998; Moura *et al.*, 2023); Sangeetha *et al.* (1999). Table 32 lists the bands common to both the ligand and its complexes.

Table 32. Relationship between the different electronic transitions in **H_2L4** ligand and its complexes.

Compounds	**n→π***	**π→π***
H_2L4	293.5 nm	305.5 nm
Complex 4A	294 nm	304.5 nm
Complex 4B	293.5 nm	305 nm
Complex 4C	293.5 nm	305.5 nm

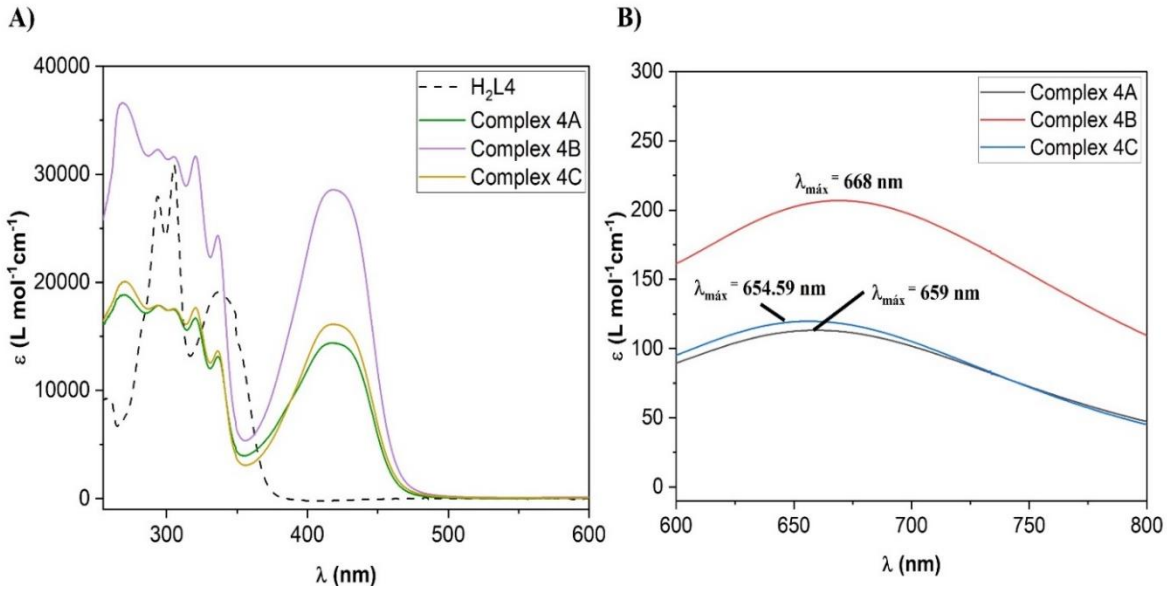

Figure 114. A) Electronic spectra of the **H_2L4** and its complexes in DMF solution 5×10^{-5} mol L^{-1} in the range 250-500 nm relating to molar absorptivity. **B)** Electronic spectra of complexes **4A**, **4B** and **4C** in DMF solution 5×10^{-3} mol L^{-1} in the range 600-800 nm relating to molar absorptivity.

5.5.2.5 Diffuse Reflectance

This technique enables the identification of bands that can be attributed to the presence of coordinated metals within molecules and, when compared with UV-Vis spectroscopy in solution, can provide insights into possible interactions with the solvent (Billing & Underhill, 1968). Furthermore, diffuse reflectance spectroscopy can reveal whether a complex will undergo significant structural changes in solution, given that the spectra obtained in UV-Vis solution versus solid state may differ.

The complexes **4A**, **4B**, and **4C** were analyzed using diffuse reflectance spectroscopy, diluted in a solid mixture of barium sulfate.

Figure 115 displays the electronic spectrum obtained via diffuse reflectance for complex **4A**, along with the main bands identified through band deconvolution. The spectrum was deconvoluted into four absorption bands. One of these bands, around 251 nm, corresponds to the shifted band observed in the precursors and ligand around 270 nm, associated with conjugated linkages in the aromatic ring. The broadened band at 324.5 nm is related to charge transfer from the hydrazone moiety to the metal ion, which appears at 320.5 nm in the UV-Vis spectrum in solution. The charge transfer band from the phenolate ion to the metal ion is observed at 425 nm, along with the *d-d* transition observed at 676 nm.

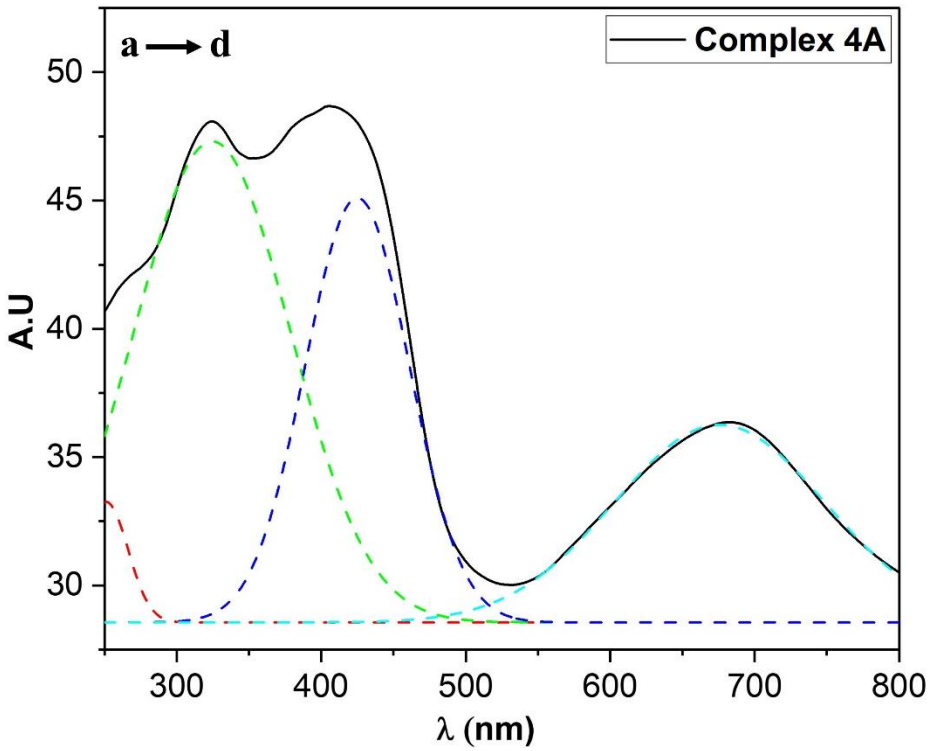

Figure 115. Electronic diffuse reflectance spectrum of **4A**, in black. Main components obtained by band fitting: a) 251 nm, b) 324.5 nm, c) 425 nm and d) 676 nm.

Figure 116 presents the electronic diffuse reflectance spectrum for **4B**, along with the main bands identified through band deconvolution. The spectrum was deconvoluted into five absorption bands, with two of them being very close to each other around 415 nm, associated with charge transfer from the phenolate ion to the Cu(II) metal center. An absorption band around 252.6 nm was observed, corresponding to the shifted band found in the precursors and the ligand around 270 nm, related to conjugated linkages in the aromatic ring. The band at 319 nm is associated with hydrazonic portion, appearing at 320.5 nm in the UV-Vis solution spectrum. The band related to the *d-d* transition can be observed at 672 nm.

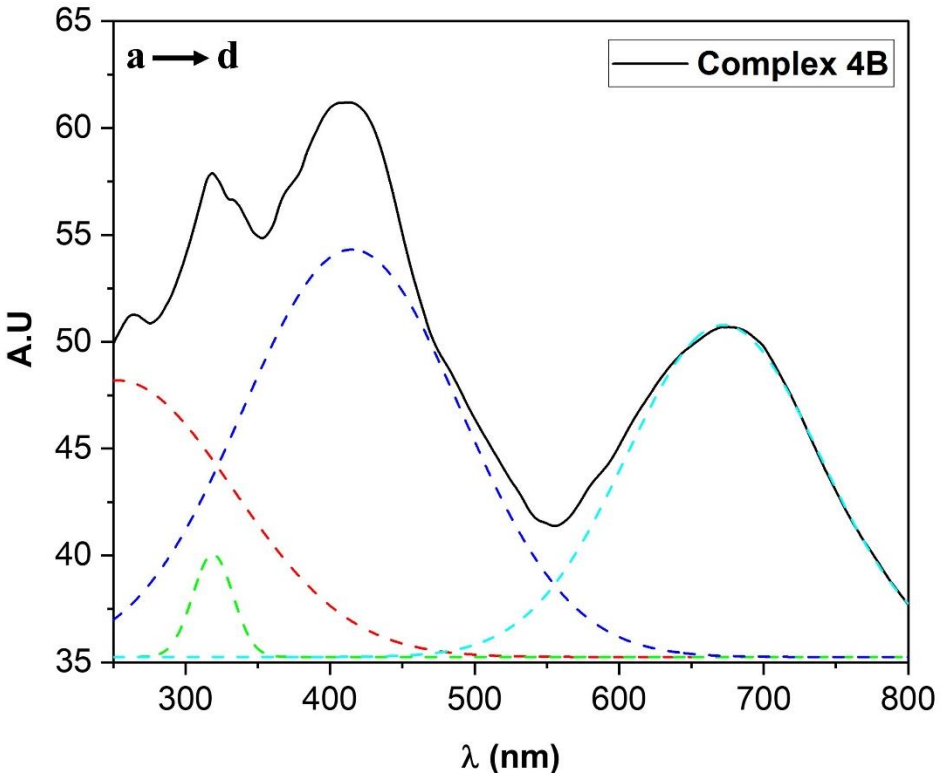

Figure 116. Electronic diffuse reflectance spectrum of **4B**, in black. Main components obtained by band fitting: a) 252.6 nm, b) 319 nm, c) 415 nm and d) 672 nm.

The electronic spectrum by diffuse reflectance for complex **4C** is shown in Figure 117, along with the main bands identified through band deconvolution. The spectrum was deconvoluted into five absorption bands, with one band around 259 nm attributed to a shifted band present in the precursors and the ligand around 270 nm, associated with conjugated linkages in the aromatic ring. The band at 320.7 nm is related to hydrazonic portion, which appears at 320.5 nm in the UV-Vis spectrum in solution. A low absorbance band at 368.7 nm was also obtained through deconvolution, potentially related to conjugated double bonds in the aromatic ring, which appears around 336 nm in the ligand and the complexes in solution. The charge transfer band from the phenolate ion to the metal center is observed at 413 nm, while the *d-d* transition band can be seen at 662 nm.

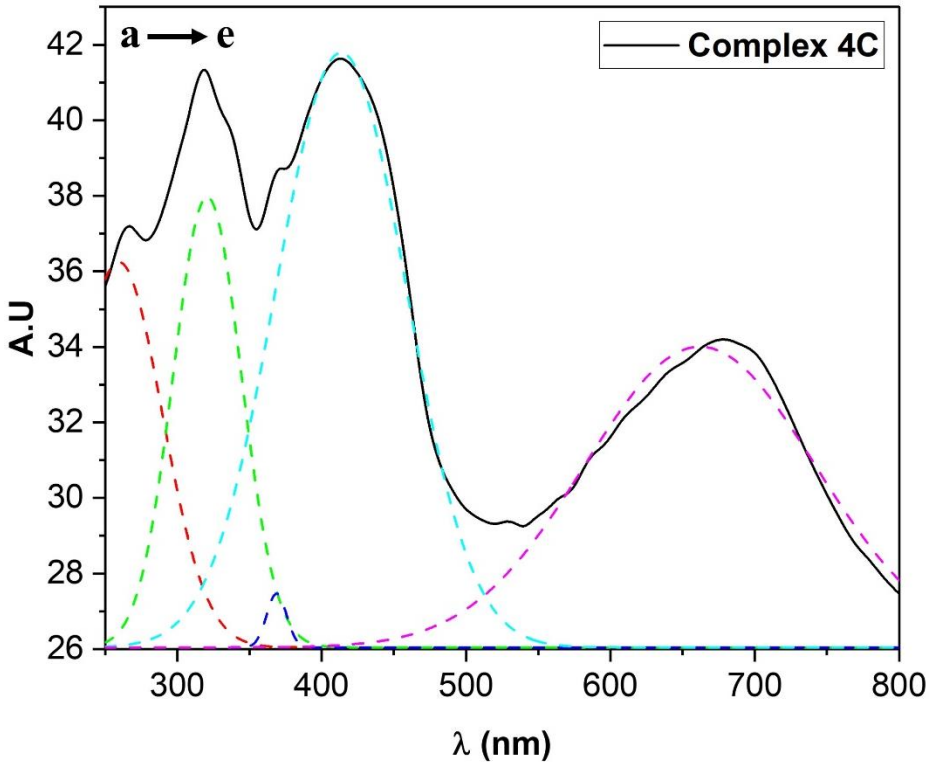

Figure 117. Electronic diffuse reflectance spectrum of **4C**, in black. Main components obtained by band fitting: a) 259 nm, b) 320.7 nm, c) 368.7 nm, d) 413 nm and e) 662 nm.

Table 33. Comparison of electronic spectra by diffuse reflectance with those obtained in solution for complexes of the **H_2L4** series.

Complexes	**Transitions**							
	precursors-related		*N*-acylhydrazone		Phenolate → Cu^{2+}		*d-d* transition	
	DRIFTS (nm)	UV-Vis (nm)	DRIFTS (nm)	UV-Vis (nm)	DRIFTS (nm)	UV-Vis (nm)	DRIFTS (nm)	UV-Vis (nm)
4A	251	270	324.5	320.5	425	417.5	676	659
4B	252.6	268	319	320.5	415	418	672	668
4C	259	268	320.7	320.5	413	417	662	654.5

The spectroscopic data presented in Table 33 correlate the λ_{max} values obtained from electronic spectra in solution and in the solid state via diffuse reflectance. Analysis of the obtained data reveals the absence of certain bands that are distinctly observed in the electronic spectra in solution, suggesting that some electronic transitions are facilitated when the species are in solution. Conversely, some common bands do not undergo significant shifts, particularly those related to charge transfer from the ligand to the metal ion. However, transitions associated with conjugated bonds exhibit hypsochromic shifts in the solid state.

Bands associated with *d-d* transitions exhibit bathochromic shifts in the solid state, indicating that these transitions have higher energy in solution, likely due to the increased degrees of freedom of the species in solution as well as solvent effects. Complex **4B** shows minimal variation in its *d-d* transition band, suggesting that this complex, although it may be dissociated, does not undergo significant structural changes in solution. In contrast, complexes **4A** and **4C** exhibit notable variations when comparing electronic spectra obtained by different techniques, suggesting that the coordination sphere of these complexes may undergo modifications in solution, impacting the λ_{max} values obtained (Calinescu *et al.*, 2008; Repich *et al.*, 2017). The λ_{max} values obtained by diffuse reflectance for the studied complexes are consistent with literature data for complexes with similar structures, suggesting that the proposed structure for these complexes is supported by the obtained results (Repich *et al.*, 2017).

5.5.2.6 Electrochemical behavior - Cyclic Voltammetry

The electrochemical behavior of the **H_2L4** system was assessed employing cyclic voltammetry in a three-electrode setup under nitrogen at room temperature; DMF containing 0.1 mol L^{-1} of $TBAPF_6$ as the supporting electrolyte was used as solvent. The voltammograms of the complexes, obtained at different scan rates, are presented below (Figure 118).

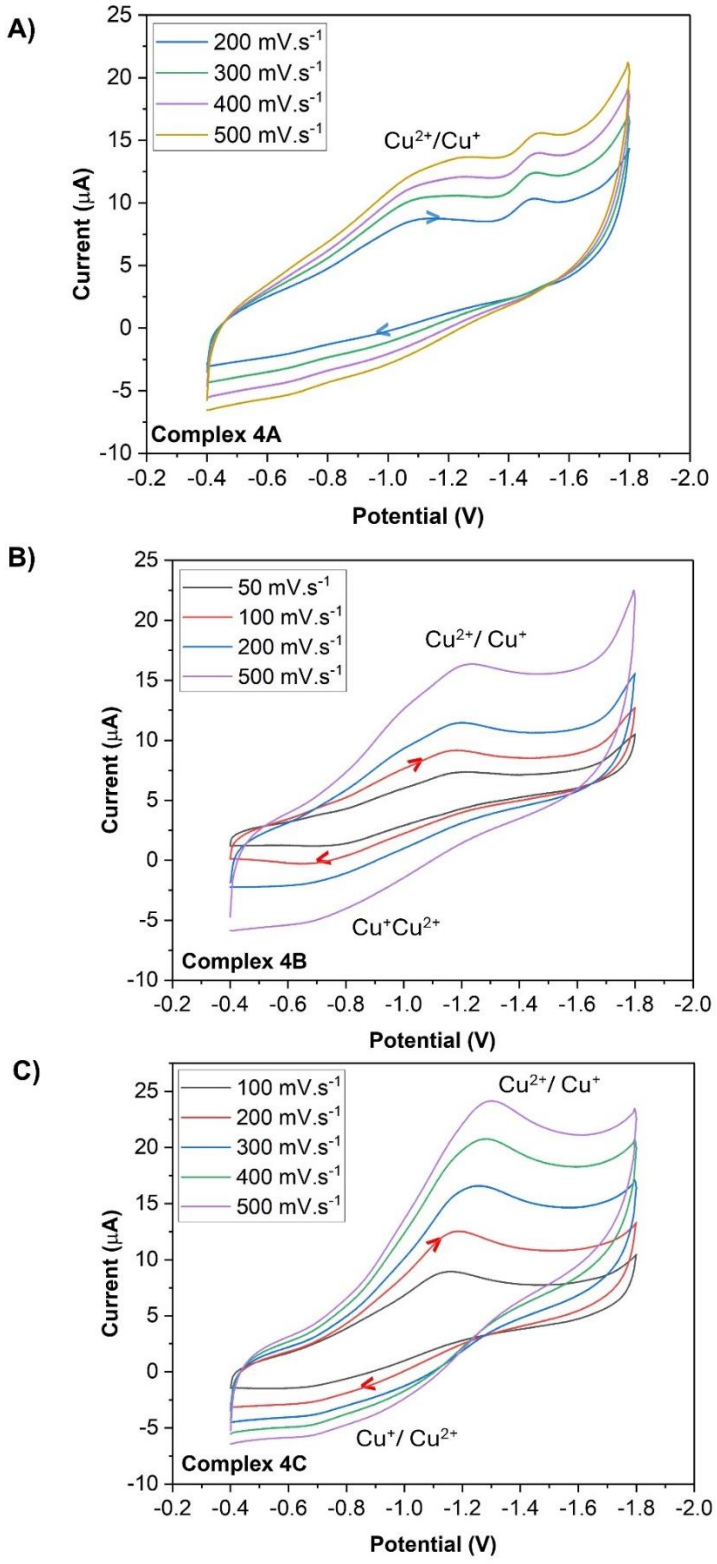

Figure 118. (A) Representative cyclic voltammograms of complex **4A**, at different scan rates, measured in DMF/0.1 mol L^{-1} $TBAPF_6$ (25 °C), using a GCE as the working electrode. **(B)** Series of representative cyclic voltammograms of complex **4B**, at different scan rates, under the same conditions. **(C)** Series of representative cyclic voltammograms of complex **4C**, at different scan rates, under the same conditions.

From the voltammograms of the complexes and some correlations, it is possible to derive electrochemical parameters that can indicate the number of electrons involved (n), the redox mechanism, the transport process, and even the transfer coefficient (α) (Abbar & Nandibewoor, 2012).

Table 34. Estimated electrochemical parameters for the complexes studied.

Complex	4A	4B	4C
E_{pc1} (V *vs* Ag/AgCl)	–1.10	–1.17	–1.13
$E_{pc1½}$ (V *vs* Ag/AgCl)	–0.44	–0.74	–0.83
α_{c1}	0.072	0.24	0.14
n_{c1}	1.01	1.23	1.10
E_{pc2} (V *vs* Ag/AgCl)	–1.48	---	---
$E_{pc2½}$ (V *vs* Ag/AgCl)	–1.63	---	---
α_{c2}	0.50	---	---
n_{c2}	0.64	---	---

The relationship between the square root of the scan rate and the peak current provides information about the type of transport process in cyclic voltammetry (Abbar & Nandibewoor, 2012). Analyzing this relationship for the studied ligands reveals a linear correlation, indicating that the system is diffusion-controlled (Abbar & Nandibewoor, 2012; Gosser, 1993; Laviron *et al.*, 1980), as confirmed by the linear relationship between the logarithm of the potential and the logarithm of the scan rate. The obtained slope value, being less than or close to 0.5, suggests diffusion control (Laviron *et al.*, 1980).

Oxidation processes could not be observed with high clarity in the cyclic voltammograms of the complexes. Similarly, the dependence of the potential on the scan rate may confirm the irreversible nature of the redox processes (Compton & Banks, 2007; Jayamani *et al.*, 2015; Laviron *et al.*, 1980).

Figure 118 (A) illustrates the cyclic voltammogram of complex **4A**, which shows two cathodic peaks. As previously discussed, the free **H_2L4** ligand is electroactive, suggesting that the cathodic peak around –1.48 V vs Ag/AgCl corresponds to the reduction process associated with the ligand. Conversely, the cathodic peak at –1.10 V vs Ag/AgCl is likely related to the Cu^{2+}/Cu^{+} redox couple, which aligns with values reported in the literature for similar complexes (Lawrence *et al.*, 2019; Moura *et al.*, 2023; Sangeetha *et al.*, 1999; Torelli *et al.*,

2000). The free ligand exhibits a cathodic peak near −1.45 V vs Ag/AgCl, but upon coordination with the metal ion, this peak shifts to −1.48 V vs Ag/AgCl. This shift suggests that coordination hinders the reduction process of the ligand, as the metal ion, being positively charged, takes precedence in the reduction process over the ligand (Jayamani *et al.*, 2015).

Graph B in Figure 118 displays the cyclic voltammogram of **4B**, revealing a well-defined cathodic peak at −1.17 V vs Ag/AgCl. Electrochemical parameters suggest that the reduction process involves a single electron, corresponding to the Cu^{2+}/Cu^{+} redox couple. Based on the electrochemical parameters, complex **4B** undergoes a one-electron reduction process, indicating that its dimeric integrity may not be preserved in solution, unlike in complex **2C**. Therefore, the dissociation of the dimer into its respective monomers results in the formation of mononuclear species, justifying the observation of a single cathodic potential, as reported by Iqbal *et al.* (2013), Jayamani *et al.* (2014) e (Naskar *et al.*, 2011). The electronic spectra in solution and those obtained by diffuse reflectance for complex **4B** show minimal variation in the λ_{max} values associated with the *d-d* transition, suggesting that the symmetry of the coordination sphere of **4B** remains relatively unchanged, consistent with the proposed structure and the obtained electrochemical results.

The voltammogram of complex **4C** shown in panel C of Figure 118 displays a single cathodic peak at −1.13 V vs Ag/AgCl, which, according to the estimated electrochemical parameters, is associated with the Cu^{2+}/Cu^{+} redox couple. The cathodic potentials obtained for the complexes in the **H_2L4** series are very similar, reinforcing the possibility that the predominant species in solution have highly similar structures.

The voltammogram of complex **4C** shown in panel C of Figure 118 displays a single cathodic peak at −1.13 V vs Ag/AgCl, which, according to the estimated electrochemical parameters, is associated with the Cu^{2+}/Cu^{+} redox couple. The cathodic potentials obtained for the complexes in the **H_2L4** series are very similar, reinforcing the possibility that the predominant species in solution have highly similar structures. The voltammograms of complexes **4B** and **4C** (panels A and B in Figure 118) do not exhibit the cathodic peak associated with the **H_2L4** ligand, as seen in complex **4A.**

5.5.2.7 Complexation Studies

The study of complexation for the **H_2L4** series complexes was conducted to replicate synthesis conditions. Therefore, analyses were performed in methanol, with incremental additions of an equimolar solution of the ligand.

Solutions of **H_2L4** at 2×10^{-5} mol L^{-1} were prepared, along with solutions of starting salts (copper(II) chloride dihydrate, copper(II) perchlorate hexahydrate, and copper(II) nitrate trihydrate) at 3×10^{-4} mol L^{-1}. Successive additions of 0.05 equivalent of the starting salt solution were then made to the ligand solution.

Similar to observations in the complexation study of the **H_2L2** series complexes, monitoring changes via UV-Vis electronic spectroscopy revealed that upon adding successive equivalents of the starting salts to the ligand solution, changes were observed. The band around 410 nm, associated with the phenol functional group, was monitored as a reliable indicator of complexation. With each successive addition of starting salt equivalents, an increase in absorbance of this band indicated the transfer of charge from the phenolate ion to the center of the copper(II) metal ion. In addition to the increase in absorbance around 410 nm, the formation of distinct isobestics points was observed, suggesting the presence of at least two species in equilibrium in solution.

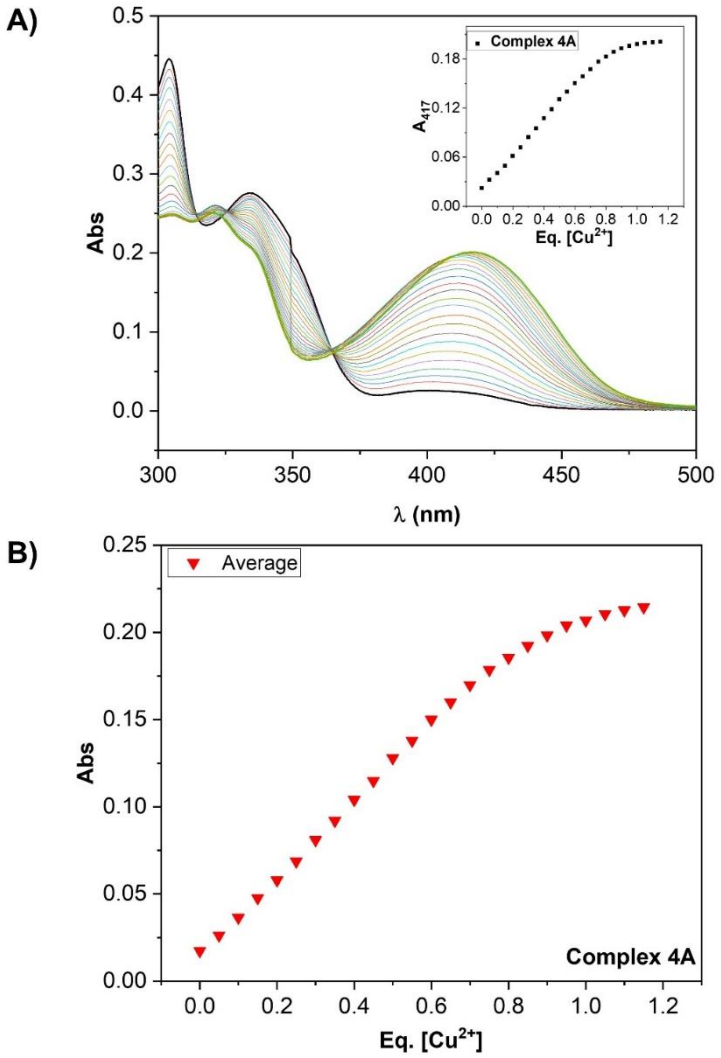

Figure 119. A) Study of complexation of complex **4A** and the relationship between absorbance and the number of Cu^{2+} equivalents. **B)** Result of the average of triplicates of the complexation study of complex **4A.**

Figure 119 (A) depicts the increase in absorbance of the band around 417 nm with successive additions of copper(II) chloride to the **H_2L4** ligand solution. The study was conducted in triplicate (Figure 119 (B)), and thus, an average of the values was taken in relation to the added Cu^{2+} equivalents. The curve shows a saturation trend near 1 equivalent of copper(II), suggesting that the stoichiometry of the mononuclear complex formed in solution is 1:1, consistent with the structure of the obtained complex.

As successive equivalents of Cu^{2+} ions from copper(II) chloride are added to the ligand solution, an increase in the intensity of the band around 417 nm and a bathochromic shift of this band can be observed. In addition to the formation of the 417 nm band, the appearance of isobestic points indicative of equilibrium

species formation is also observed. The formation of the 417 nm band, its bathochromic shift, and the presence of isobestic points collectively indicate the coordination of the ligand to the Cu^{2+} metal center.

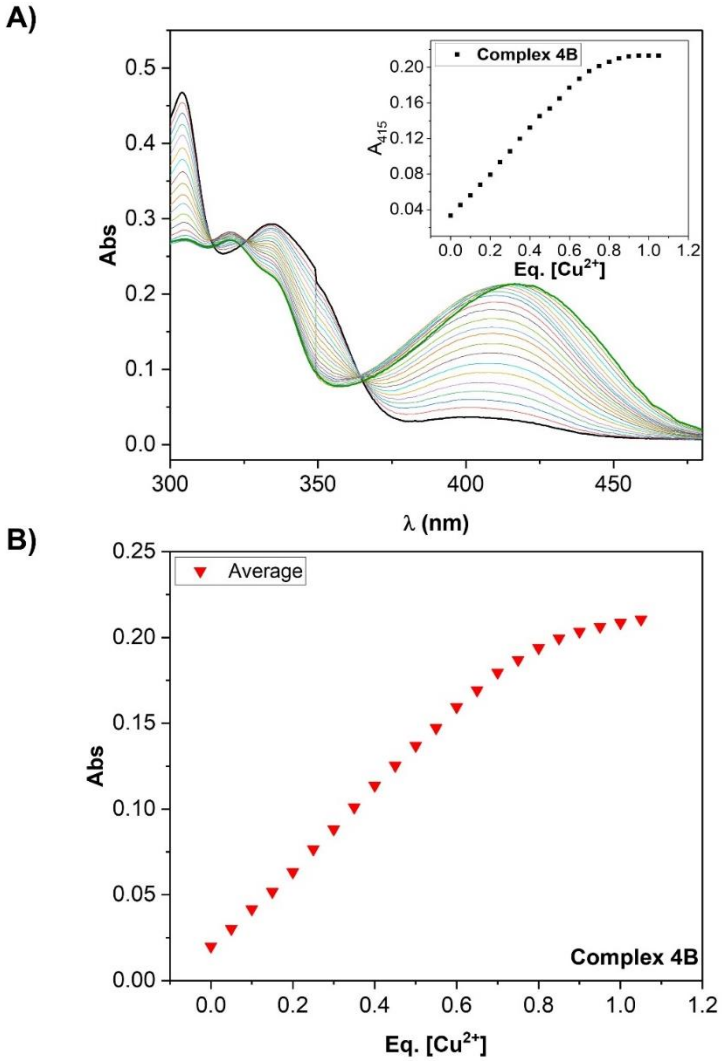

Figure 120. A) Study of complexation of complex **4B** and the relationship between absorbance and the number of Cu^{2+} equivalents. **B)** Result of the average of triplicates of the complexation study of complex **4B.**

Figure 120 (A) illustrates the increase in absorbance of the band around 415 nm with successive additions of copper(II) perchlorate hexahydrate to the **H_2L4** ligand solution. The study was conducted in triplicate, and thus, an average of the values was taken in relation to the added Cu^{2+} equivalents (Figure 120 (B)). The curve demonstrates a saturation trend near 1 equivalent of copper(II), suggesting that the stoichiometry of the dinuclear complex formed in solution is 1:1, consistent with the structure of the obtained complex.

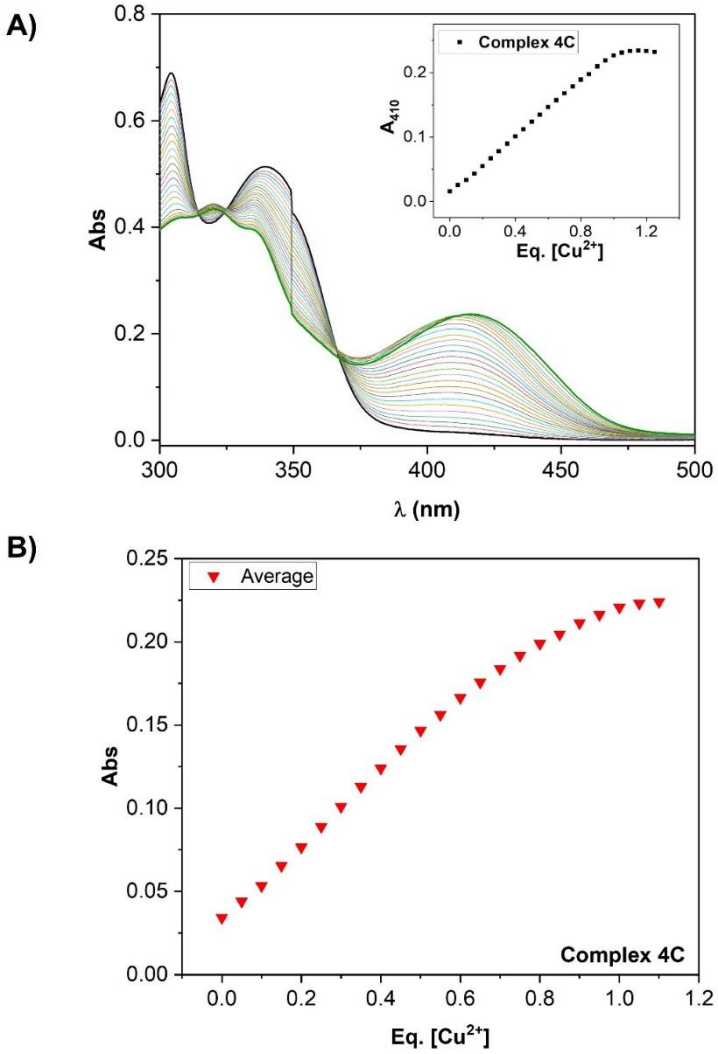

Figure 121. A) Study of complexation of complex **4C** and the relationship between absorbance and the number of Cu^{2+} equivalents. **B)** Result of the average of triplicates of the complexation study of complex **4C.**

Figure 121A depicts the increase in absorbance of the band around 410 nm with successive additions of copper(II) nitrate trihydrate to a **H_2L4** solution. The study was conducted in triplicate, and thus, an average of the values was taken in relation to Cu^{2+} equivalents added (Figure 121B). The curve shows a saturation trend near 1 equivalent of copper(II), suggesting that the stoichiometry of the mononuclear complex formed in solution is 1:1, consistent with the structure of the obtained complex.

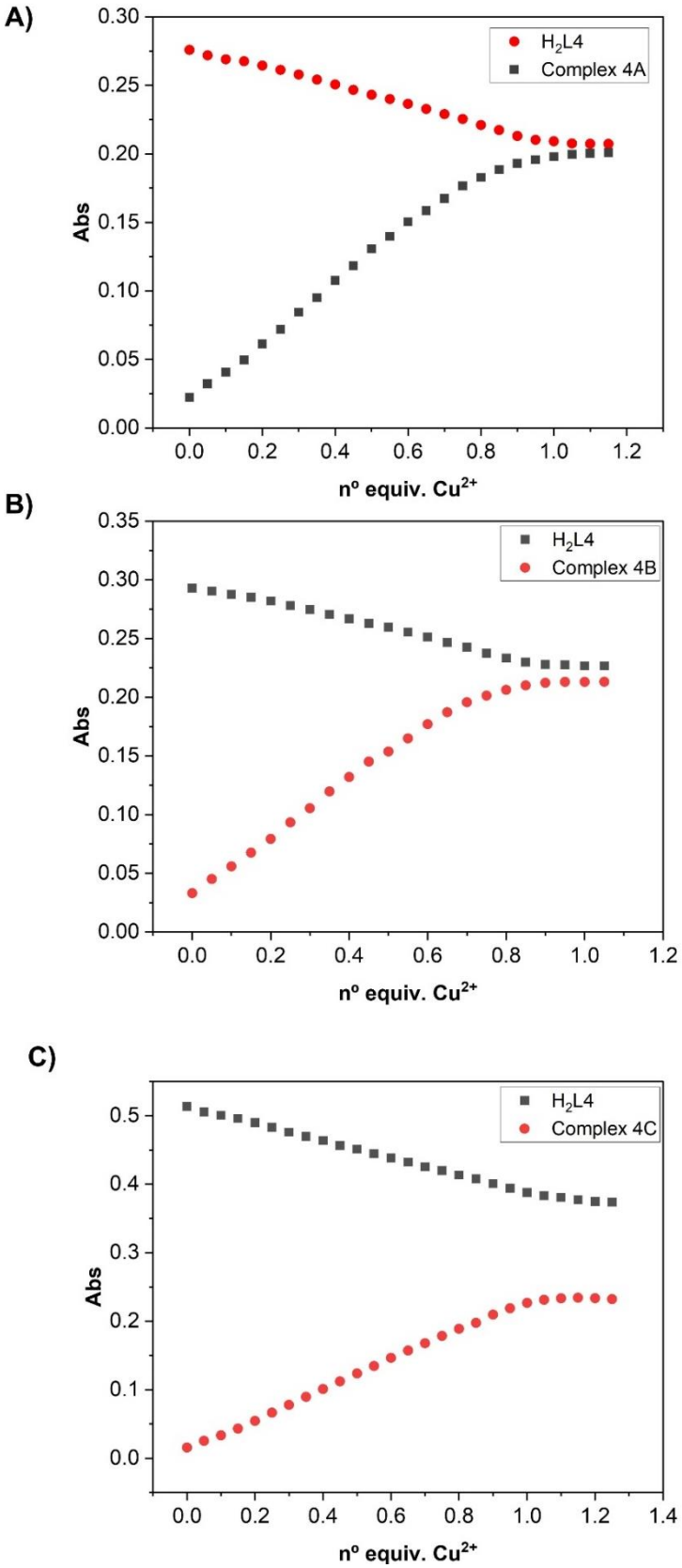

Figure 122. Qualitative graph that illustrates the variation of ligand species and their respective complexes based on the absorption and number of equivalents of the salts used.

Figure 122 enables an indirect analysis of species concentration variation by monitoring changes in absorbance of the ligand bands (around 333 nm) and the obtained complexes (around 410 nm). Comparing the graphs in Figure 122 reveals that at 1 equivalent, the absorbance stabilizes, suggesting a potential equilibrium between free ligand and formed complex. Unlike observations in the **H_2L2** series complexes, no intersection of the graphs is observed, indicating that absorbances do not equalize at any point.

5.5.2.8 Interaction studies with HSA

Under more physiological conditions (i.e., 5% *i*-PrOH/PBS, pH 7.4), which were employed in the studies of interaction with HSA, the spectral profiles of **H_2L4** undergo only minimal modification. Figure 123 illustrates the absorption pattern of the ligand in 5% *i*-PrOH/PBS, with the spectrum in DMF (at the same concentration) included as a reference.

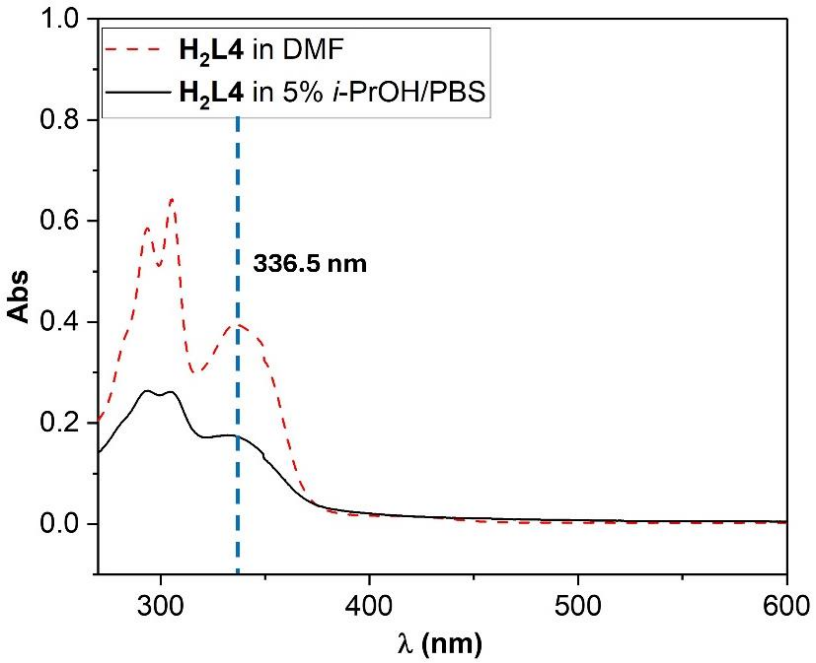

Figure 123. UV-Vis spectra of **H_2L4** (2.0×10^{-5} mol L^{-1}) in 5% i-PrOH / PBS, pH 7.4 (black solid curve) and in DMF (red dotted curve). Position of the transition is given as a dashed blue line.

Comparing the spectra obtained in physiological medium (pH 7.4) and in DMF solution from Figure 123 reveals minimal changes, except for the difference in absorbance, suggesting that the electronic transition nature observed in the ligand remains largely unaffected even under different conditions in aqueous media (Moura *et al.*, 2023). Figure 124 depicts the spectral changes in the 250-600 nm region resulting from successive additions of HSA to a solution of **H_2L4**

at 2 × 10^{-5} mol L^{-1}. An increase in absorbance across all absorption bands is observed during HSA addition, indicating that the observed enhancement stems from electronic transitions within the HSA molecule itself. This observation suggests that **H_2L4** does not interact with HSA, a conclusion supported by the absence of isosbestic points, indicating no equilibrium of species in solution.

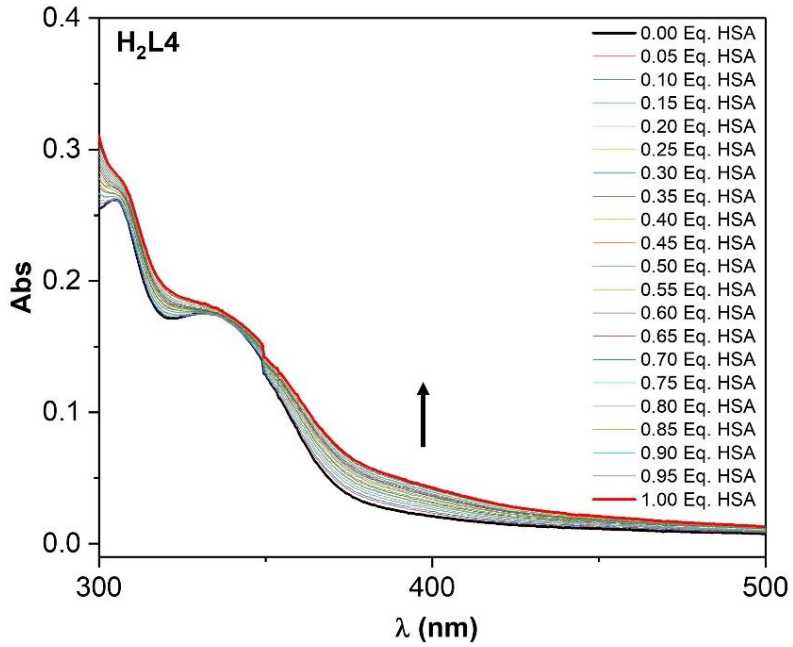

Figure 124. UV-Vis titration of a 2 × 10^{-5} mol L^{-1} **H_2L4** solution (5% i-PrOH / PBS, pH 7.4) with HAS at room temperature.

Similar to what was done for the **H_2L4** ligand, its complexes **4A**, **4B**, and **4C** were studied under more physiological conditions (10% *i*-PrOH/PBS, pH 7.4), which were employed in the studies of interaction with HSA. Different from the ligand, spectral profiles of these compounds undergo some modifications. Figure 125 presents the absorption patterns of **4A**, **4B**, and **4C** in 10% *i*-PrOH/PBS, with the spectrum in DMF (at the same concentration) included as a reference.

The absorption bands in the 200-350 nm (UV) region are more defined in DMF than in physiological conditions, and in the 400 nm region, a band around 415 nm appears in DMF solution while buffered solution shows two absorption bands around 417 nm and 440 nm. This suggests that a water-rich environment may favor different charge transfers, as indicated by molar conductivity data suggesting dissociation of the obtained complexes in solution, leaving more free sites for different interactions. This can explain the appearance of this new band, which is certainly related to interactions of the metal ion with the ligand, as observed in other literature works (Patra *et al.*, 2018; Ribeiro & Correia, 2024).

.

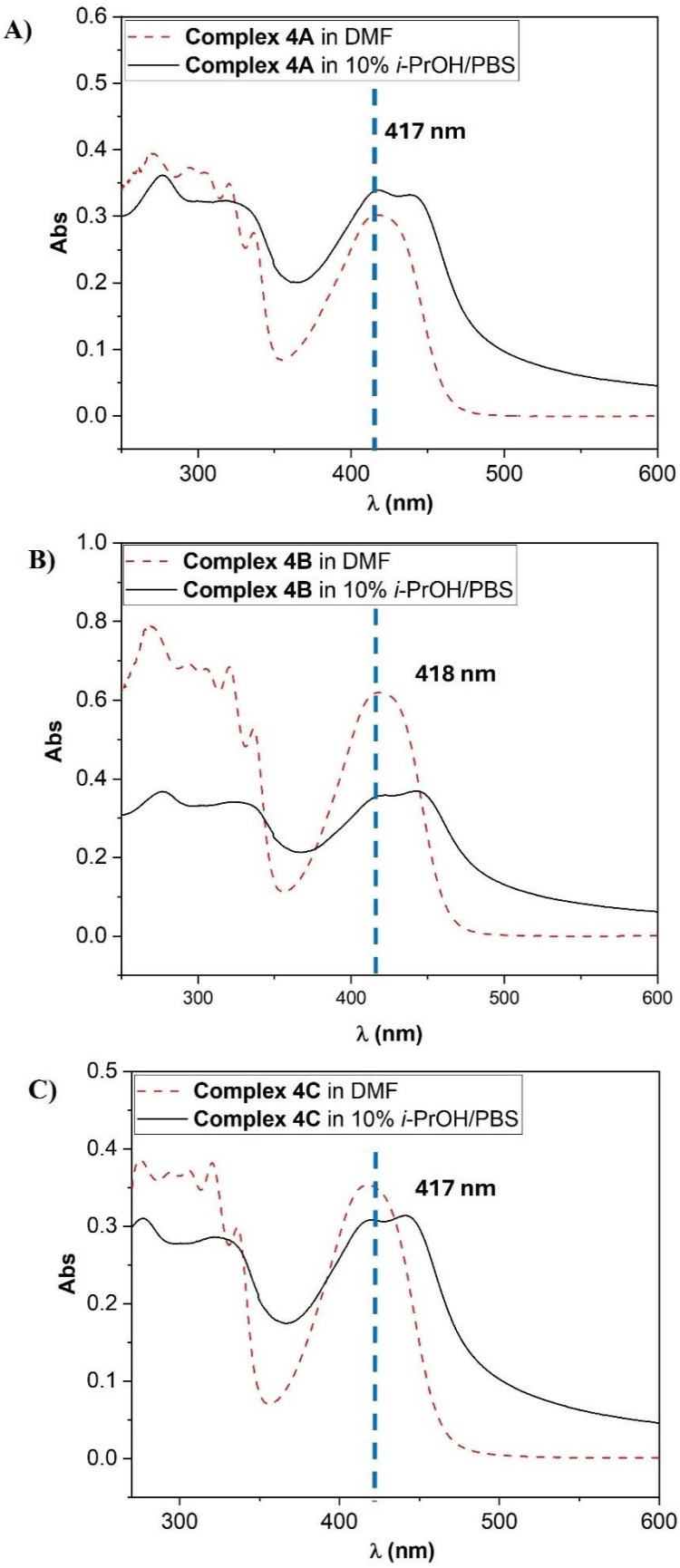

Figure 125. UV-Vis spectra of **A) 4A, B) 4B** and **C) 4C** (2.0×10^{-5} mol L^{-1}) in 10 % *i*-PrOH / PBS, pH 7.4 (black solid curve) and in DMF (red dotted curve), at r.t.

The interaction activity with HSA for the complexes exhibited a different behavior compared to the complexes in the **H_2L2** series. When a solution of complex **4A** (2×10^{-5} mol L^{-1}) is titrated with HSA, the absorption originally present at 417 nm undergoes a hypsochromic shift to 410 nm as the protein concentration increases, accompanied by a decrease in absorbance throughout the additions of HSA. Conversely, the absorption at around 336 nm shows increased absorbance with the addition of HSA. Isosbestic points can be identified around 375 nm and 465 nm during the initial HSA additions, indicating once again that only two absorbing species (free and bound forms of the complex) are initially in equilibrium. Subsequently, stabilization appears to occur.

Plotting absorbance at 417 nm against equivalents of HSA (Figure 126, *inset*) yields a sigmoidal curve with a correlation coefficient of 0.99, stabilizing around [HSA]/[**4A**] = 0.5. This suggests that HSA can host up to two units of the mononuclear complex, indicating possible binding cooperativity in this study, akin to the complexes in the **H_2L2** series.

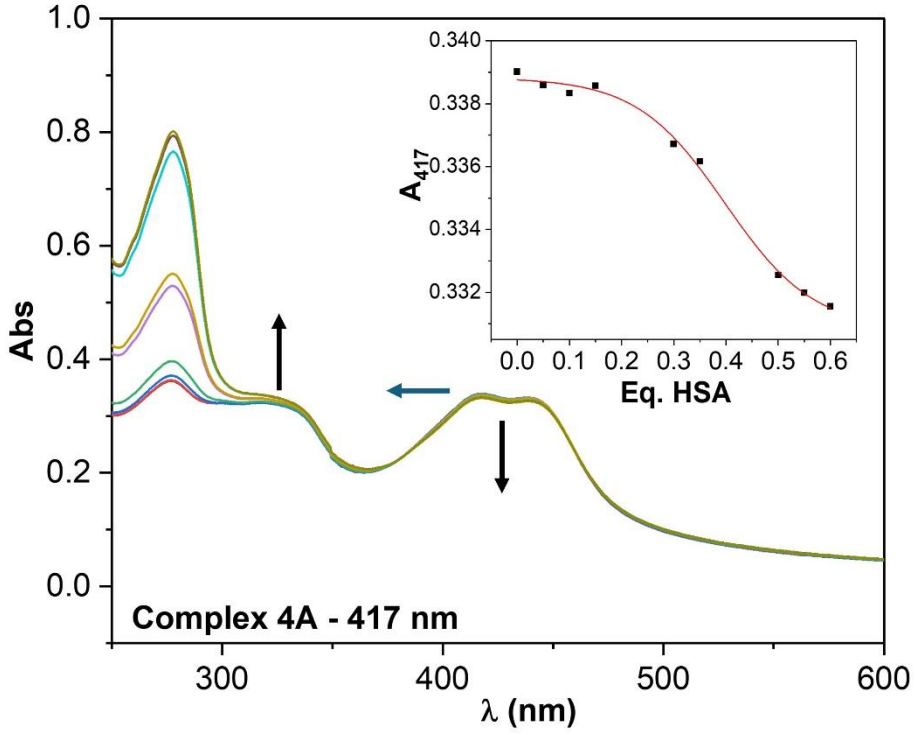

Figure 126. UV-Vis titration of a 2×10^{-5} mol L^{-1} **4A** solution (10 % *i*-PrOH / PBS, pH 7.4) with HSA at 25 ºC. *Inset:* absorbance at 417 nm as a function of HSA equivalents; data were fitted using a sigmoidal function.

When a solution of complex **4B** (2×10^{-5} mol L^{-1}) is titrated with HSA, spectral changes similar to those observed for **4A** are observed. The absorption originally present at 421 nm undergoes a hypsochromic shift to 412 nm as the protein concentration increases, accompanied by a decrease in absorbance throughout the additions of HSA. Additionally, the absorption band at 336 nm shows increased absorbance with the addition of HSA. Isobestic points can be identified around 370 nm and 475 nm during the initial HSA additions, indicating that only two absorbing species (i.e., free and bound forms of the complex) are in equilibrium. Plotting absorbance at 421 nm vs equivalents of HSA (Figure 127, *inset*) yields a sigmoidal curve with correlation coefficient of 0.99, stabilizing at around [HSA]/[**4B**] = 0.5. This suggests that HSA can host up to two units of the complex, indicating possible binding cooperativity in this study once again.

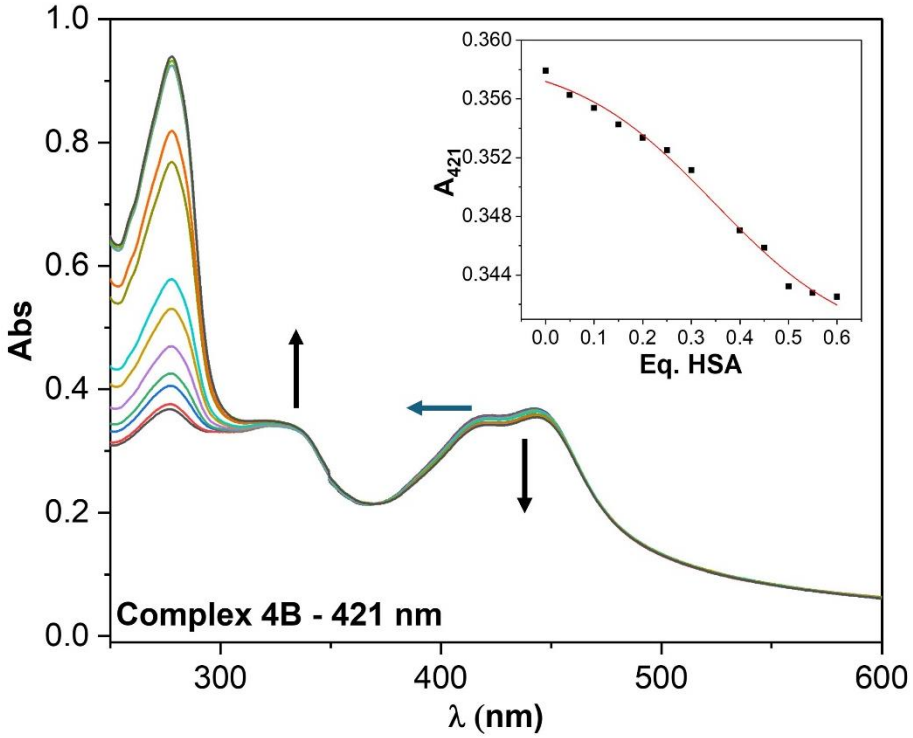

Figure 127. UV-Vis titration of a 2×10^{-5} mol L^{-1} **4B** solution (10 % *i*-PrOH / PBS, pH 7.4) with HSA at 25 ºC. *Inset:* absorbance at 421 nm as a function of HSA equivalents; data were fitted using a sigmoidal function.

When a solution of complex **4C** (2×10^{-5} mol L^{-1}) is titrated with HSA, spectral changes similar to those observed for other complexes in the **H_2L4** series are noted. The absorption originally present at 419 nm undergoes a hypsochromic shift to 415 nm as the protein concentration increases, accompanied by a decrease in absorbance throughout the additions of HSA. Additionally, the absorption band

around 336 nm shows increased absorbance with the addition of HSA. Isosbestic points can be identified around 378 nm and 465 nm during the initial HSA additions, indicating that only two absorbing species (free and bound forms of the complex) are in equilibrium. Plotting absorbance at 419 nm against equivalents of HSA (Figure 128, *inset*) yields a sigmoidal curve with a correlation coefficient of 0.99, stabilizing around [HSA]/[**4C**] = 0.5, suggesting that HSA can accommodate up to two units of the complex, and, once again, indicating a possible binding cooperativity for the interaction between **4C** and HSA.

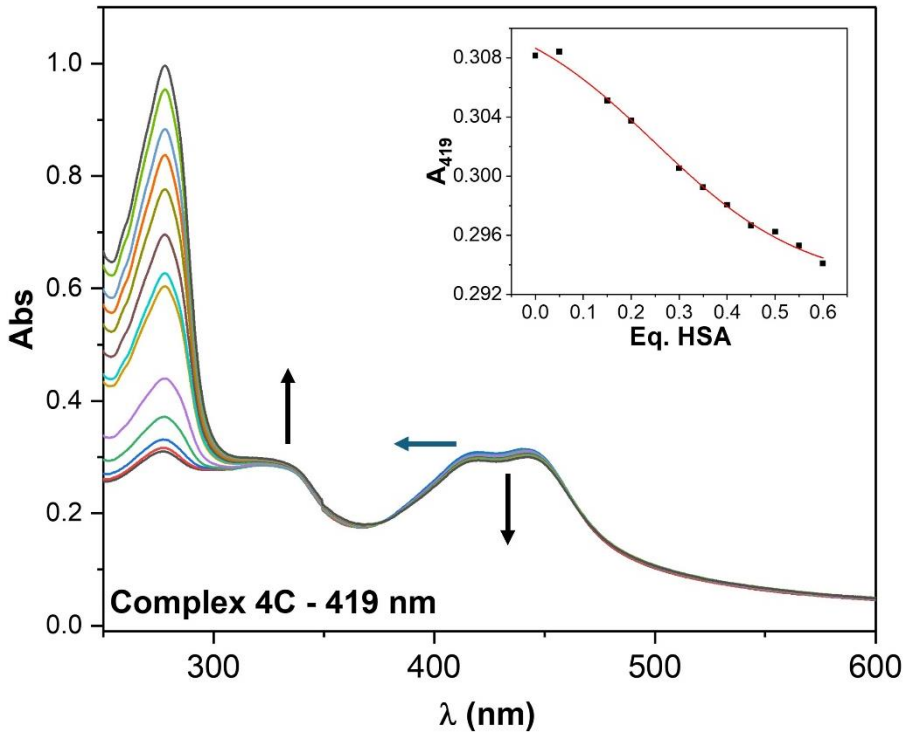

Figure 128. UV-Vis titration of a 2 × 10^{-5} mol L^{-1} **4C** solution (10 % *i*-PrOH / PBS, pH 7.4) with HSA at 25 ºC. *Inset:* absorbance at 419 nm as a function of HSA equivalents; data were fitted using a sigmoidal function.

The data obtained from HSA interaction studies with the ligand and complexes of the **H_2L4** series indicate that the free ligand does not interact with HSA, which does not imply a lack of pharmacological functionality as it may be transported by other carrier proteins (Kratz & Elsadek, 2012; Wanat, 2020).

Conductometric assays suggest that the obtained complexes undergo dissociation in solution, forming cationic species neutralized by chloride, perchlorate, and nitrate ions respectively. This suggests that most of the complexes in solution may be replaced by solvent molecules after dissociation. Although molecular docking tests were not conducted for these species with

HSA, it is plausible that the species in solution are very similar, allowing them to interact at the same binding sites on the protein, explaining the consistent 2:1 ratio at which all complexes interact with HSA.

Assays conducted for complexes **2A** and **2B** indicate that the DS3 site is common in the protein interaction with these complexes, suggesting that this site is involved in the interaction with **H_2L4** series complexes. Furthermore, the DS2 site for complex **2A** is favored considering its substituted and non-substituted water structures. Therefore, the DS2 site may be the second site involved in HSA protein interaction with complexes **4A**, **4B**, and **4C**. However, further studies are still necessary, as the decrease in absorbance at 417 nm and its hypsochromic shift may suggest that the interactions these complexes engage in with HSA are of a distinct nature.

6. Conclusions

Four *N*-acylhydrazones derived from precursor 5-methylsalicylaldehyde, three of which new, and their new copper(II) complexes prepared from chloride, perchlorate, and nitrate starting salts (a total of 10 complexes) were synthesized and fully characterized using analytical and spectroscopic techniques. The single-crystal structures of all the four ligands and three complexes were determined by X-ray diffraction analyses. The absorption bands in the spectra of the ligands and complexes were successfully assigned.

The systems related to the ligands **H_2L2** (hydrazide substituent: furan) and **H_2L4** (*N*-methylimidazole) are the most interesting and promising in the context of the development of anticancer drugs, due to their better solubility prospects.

Complexes derived from **H_2L2** and **H_2L4** were isolated as mononuclear or dinuclear (dimeric) species, depending on the starting salt and the experimental conditions used during the syntheses.

Under a more biological point of view, the furan-containing ligand **H_2L2** demonstrated good interaction with the blood protein HSA, with each protein unit being able to accommodate up to two molecules of the ligand. **H_2L4**, on the other hand, was unable to interact with HSA under the evaluated conditions. The reasons behind this difference are still not clear.

Complexes **2A**, **2B**, **2C**, **4A**, **4B**, and **4C**, belonging to these systems, were able to interact with HSA. In all the studies conducted, one protein unit was able to bind more than one unit of the complex, whether it was a dimer or not. Docking calculations helped to identify potential interaction sites for the ligand **H_2L2** and complexes **2A** and **2B** within the carrier protein HSA.

Studies revealed that the complexes **2A**, **2B** and **2C**, and, to a lesser extent, the ligand **H_2L2**, exhibit a potent antiproliferative activity against human breast cancer cells, with activity superior to that of cisplatin, in the concentration range of 10^{-6} mol L^{-1}. The findings demonstrated that the free ligand and free copper(II) ions exhibited low antiproliferative activity, thus highlighting the significant role of ligand coordination to the metal ion for antitumor activity.

In conclusion, the present work reinforces the idea that *N*-acylhydrazones and, specially, their copper(II) complexes may represent a promising structural motif for the development of highly active potential antitumor agents, which can be used in the future as substituents of the widely used platinum drugs.

7. Bibliography

ABBAR, J.; NANDIBEWOOR, S. Voltammetric Behavior of Chlorzoxazone and Its Electroanalytical Determination in Pharmaceutical Dosage Form and Urine at Gold Electrode. **Critical Reviews in Analytical Chemistry**, 42, n. 3, p. 272-281, 2012/07/01 2012.

ABBAS, Z.; REHMAN, S. An overview of cancer treatment modalities. **Neoplasm**, 1, p. 139-157, 2018.

ABDELRAHMAN, S.; ALGHRABLY, M.; CAMPAGNA, M.; HAUSER, C. A. E. *et al.* Metal Complex Formation and Anticancer Activity of Cu(I) and Cu(II) Complexes with Metformin. **Molecules**, 26, n. 16, p. 4730, 2021.

ADDISON, A. W.; RAO, T. N.; REEDIJK, J.; VAN RIJN, J. *et al.* Synthesis, structure, and spectroscopic properties of copper(II) compounds containing nitrogen–sulphur donor ligands; the crystal and molecular structure of aqua[1,7-bis(N-methylbenzimidazol-2′-yl)-2,6-dithiaheptane]copper(II) perchlorate. **Journal of the Chemical Society, Dalton Transactions**, n. 7, p. 1349-1356, 1984. 10.1039/DT9840001349.

AGUILAR-JIMÉNEZ, Z.; ESPINOZA-GUILLÉN, A.; RESENDIZ-ACEVEDO, K.; FUENTES-NORIEGA, I. *et al.* The importance of being Casiopeina as polypharmacologycal profile (mixed chelate–copper (II) complexes and their in vitro and in vivo activities). **Inorganics**, 11, n. 10, p. 394, 2023.

AINSCOUGH, E. W.; BRODIE, A. M.; DOBBS, A. J.; RANFORD, J. D. *et al.* Antitumour copper(II) salicylaldehyde benzoylhydrazone (H2sb) complexes: physicochemical properties and the single-crystal X-ray structures of [{Cu(H2sb)(CCl3CO2)2}2] and [{Cu(Hsb) (ClO4) (C2H5OH)}2] and the related salicylaldehyde acetylhydrazone (H2sa) complex, [Cu(Hsa)Cl(H2O)]·h2O. **Inorganica Chimica Acta**, 267, n. 1, p. 27-38, 1998/01/03/ 1998.

ALI, I.; WANI, W. A.; SALEEM, K. Empirical Formulae to Molecular Structures of Metal Complexes by Molar Conductance. **Synthesis and Reactivity in Inorganic, Metal-Organic, and Nano-Metal Chemistry**, 43, n. 9, p. 1162-1170, 2013/10/21 2013.

ALIZADEH, M.; BARATI, M.; SALEH-GHADIMI, S.; ROSHANRAVAN, N. *et al.* Industrial furan and its biological effects on the body systems. **Journal of Food Biochemistry**, 42, n. 5, p. e12597, 2018.

ALMEIDA, V. L. d.; LEITÃO, A.; REINA, L. d. C. B.; MONTANARI, C. A. *et al.* Câncer e agentes antineoplásicos ciclo-celular específicos e ciclo-celular não específicos que interagem com o DNA: uma introdução. **Química nova**, 28, p. 118-129, 2005.

ANACONA, J.; NORIEGA, N.; CAMUS, J. Synthesis, characterization and antibacterial activity of a tridentate Schiff base derived from cephalothin and sulfadiazine, and its transition metal complexes. **Spectrochimica Acta Part A: Molecular and Biomolecular Spectroscopy**, 137, p. 16-22, 2015.

ARRUEBO, M.; VILABOA, N.; SÁEZ-GUTIERREZ, B.; LAMBEA, J. *et al.* Assessment of the evolution of cancer treatment therapies. **Cancers**, 3, n. 3, p. 3279-3330, 2011.

AYOUB, N. M.; AL-SHAMI, K. M.; ALQUDAH, M. A.; MHAIDAT, N. M. Crizotinib, a MET inhibitor, inhibits growth, migration, and invasion of breast cancer cells in vitro and synergizes with chemotherapeutic agents. **OncoTargets and therapy**, p. 4869-4883, 2017.

BAKIR, M.; BROWN, O. Spectroscopic and electrochemical properties of di-2-pyridyl ketone

thiosemicarbazone [dpktsc] in non-aqueous media. **Journal of Molecular Structure**, 1006, n. 1, p. 402-408, 2011/12/14/ 2011.

BAKIR, M.; LAWRENCE, M. A.; NELSON, P. N.; CONRY, R. R. Spectroscopic and electrochemical properties of di-2-thienyl ketone thiosemicarbazone (dtktsc): electrochemical reactions with electrophiles (H+ and CO2). **Electrochimica Acta**, 212, p. 1010-1020, 2016.

BAKIR, M.; LAWRENCE, M. A. W.; FERHAT, M.; CONRY, R. R. Spectroscopic, electrochemical and X-ray crystallographic properties of a novel palladium(II) complex of thioamide deprotonated di-2-pyridyl ketone thiosemicarbazone (dpktsc-H)−. **Journal of Coordination Chemistry**, 70, n. 17, p. 3048-3064, 2017/09/02 2017.

BAKIR, M.; LAWRENCE, M. A. W.; MCBEAN, S. Spectroscopic and electrochemical properties of group 12 acetates of di-2-pyridylketone thiophene-2-carboxylic acid hydrazone (dpktch-H) complexes. The structure of [Cd(η3-N,N,O-dpktch-H)2]. **Spectrochimica Acta Part A: Molecular and Biomolecular Spectroscopy**, 146, p. 323-330, 2015/07/05/ 2015.

BALSA, L. M.; FERRARESI-CUROTTO, V.; LAVECCHIA, M. J.; ECHEVERRÍA, G. A. *et al.* Anticancer activity of a new copper (ii) complex with a hydrazone ligand. Structural and spectroscopic characterization, computational simulations and cell mechanistic studies on 2D and 3D breast cancer cell models. **Dalton Transactions**, 50, n. 28, p. 9812-9826, 2021.

BALSA, L. M.; RODRIGUEZ, M. R.; FERRARESI-CUROTTO, V.; PARAJÓN-COSTA, B. S. *et al.* Finding New Molecular Targets of Two Copper(II)-Hydrazone Complexes on Triple-Negative Breast Cancer Cells Using Mass-Spectrometry-Based Quantitative Proteomics. **International Journal of Molecular Sciences**, 24, n. 8, p. 7531, 2023.

BALSA, L. M.; RUIZ, M. C.; SANTA MARIA DE LA PARRA, L.; BARAN, E. J. *et al.* Anticancer and antimetastatic activity of copper(II)-tropolone complex against human breast cancer cells, breast multicellular spheroids and mammospheres. **Journal of Inorganic Biochemistry**, 204, p. 110975, 2020/03/01/ 2020.

BALSA, M. L.; BARAN, J. E.; LEÓN, E. I. Copper Complexes as Antitumor Agents: In vitro and In vivo Evidence. **Current Medicinal Chemistry**, 30, n. 5, p. 510-557, 2023.

BERN, M.; SAND, K. M. K.; NILSEN, J.; SANDLIE, I. *et al.* The role of albumin receptors in regulation of albumin homeostasis: Implications for drug delivery. **Journal of Controlled Release**, 211, p. 144-162, 2015.

BEVERS, L. E.; HAGEDOORN, P.-L.; HAGEN, W. R. The bioinorganic chemistry of tungsten. **Coordination Chemistry Reviews**, 253, n. 3-4, p. 269-290, 2009.

BILLING, D.; UNDERHILL, A. Diffuse reflectance and far-infra-red (450-190 cm− 1) spectra of some tetragonally distorted copper (II) halide complexes with n-heterocyclic ligands. **Journal of Inorganic and Nuclear Chemistry**, 30, n. 8, p. 2147-2154, 1968.

BRAY, R. Electron paramagnetic resonance in biochemistry. **FEBS letters**, 5, n. 1, p. 1-6, 1969.

BROUSSY, S.; COPPEL, Y.; NGUYEN, M.; BERNADOU, J. *et al.* 1H and 13C NMR Characterization of Hemiamidal Isoniazid-NAD(H) Adducts as Possible Inhibitors Of InhA Reductase of Mycobacterium tuberculosis. **Chemistry – A European Journal**, 9, n. 9, p. 2034-2038, 2003.

BRUKER. **SAINT Integration Software**. Versão v8.34A. Madison, Wisconsin, USA: Bruker AXS Inc., 1999.

BURGOS-LOPEZ, Y.; DEL PLÁ, J.; BALSA, L. M.; LEÓN, I. E. *et al.* Synthesis, crystal structure and cytotoxicity assays of a copper(II) nitrate complex with a tridentate ONO acylhydrazone ligand. Spectroscopic and theoretical studies of the complex and its ligand. **Inorganica Chimica Acta**, 487, p. 31-40, 2019/03/01/ 2019.

CALINESCU, M.; ION, E.; GEORGESCU, R.; NEGREANUPRJOL, T. Synthesis and spectroscopic, antibacterial and antifungal studies on copper (II) complexes with 2-benzothiazolyl hydrazones. **Rev Roum Chim**, 53, n. 10, p. 911-919, 2008.

CHAN, S. C.; KOH, L. L.; LEUNG, P. H.; RANFORD, J. D. *et al.* Copper(II) complexes of the antitumour-related ligand salicylaldehyde acetylhydrazone (H2L) and the single-crystal X-ray structures of [{Cu(HL)H2O}2] · 2(NO3) and [{Cu(HL) (pyridine) (NO3)}2]. **Inorganica Chimica Acta**, 236, n. 1, p. 101-108, 1995/08/01/ 1995.

CHARMSAZ, S.; COLLINS, D. M.; PERRY, A. S.; PRENCIPE, M. Novel strategies for cancer treatment: highlights from the 55th IACR annual conference. : MDPI 2019.

CHEN, D.; MILACIC, V.; FREZZA, M.; DOU, Q. P. Metal complexes, their cellular targets and potential for cancer therapy. **Current pharmaceutical design**, 15, n. 7, p. 777-791, 2009.

CHEW, S. T.; LO, K. M.; LEE, S. K.; HENG, M. P. *et al.* Copper complexes with phosphonium containing hydrazone ligand: Topoisomerase inhibition and cytotoxicity study. **European journal of medicinal chemistry**, 76, p. 397-407, 2014.

CHHIKARA, B. S.; PARANG, K. Global Cancer Statistics 2022: the trends projection analysis. **Chemical Biology Letters**, 10, n. 1, p. 451-451, 2023.

CITRI, A.; YARDEN, Y. EGF–ERBB signalling: towards the systems level. **Nature reviews Molecular cell biology**, 7, n. 7, p. 505-516, 2006.

COHEN, M.; FLAVIAN, S.; LEISEROWITZ, L. Topochemistry. Part XXVI. The absorption spectra of some thermochromic N-salicylideneanilines and hydroxynaphthylideneanilines in the crystal. **Journal of the Chemical Society B: Physical Organic**, p. 329-334, 1967.

COMPTON, R. G.; BANKS, C. E. **Understanding Voltammetry**. World Scientific Publishing Company, 2007. 9789813106949.

CRYSALISPRO. Rigaku Oxford Diffraction. CrysAlisPro. **Rigaku Corporation, Tokyo, Japan.**, 2015.

CUKIERMAN, D. Physico-chemical optimization and Structure–Activity Relationship studies of aldehyde-derived N-acylhydrazones: towards the improvement of moderate metal chelators as a strategy against metal-enhanced aggregopathies. **Rio de Janeiro, Brazil: Pontifical Catholic University of Rio de Janeiro**, 2021.

CUKIERMAN, D. S.; ACCARDO, E.; GOMES, R. G.; DE FALCO, A. *et al.* Aroylhydrazones constitute a promising class of 'metal-protein attenuating compounds' for the treatment of Alzheimer's disease: a proof-of-concept based on the study of the interactions between zinc (II) and pyridine-2-carboxaldehyde isonicotinoyl hydrazone. **JBIC Journal of Biological Inorganic Chemistry**, 23, p. 1227-1241, 2018.

CUKIERMAN, D. S.; LÁZARO, D. F.; SACCO, P.; FERREIRA, P. R. *et al.* X1INH, an improved next-generation affinity-optimized hydrazonic ligand, attenuates abnormal copper (I)/copper (II)-α-Syn interactions and affects protein aggregation in a cellular model of synucleinopathy. **Dalton Transactions**, 49, n. 45, p. 16252-16267, 2020.

CUKIERMAN, D. S.; LIGIERO, C. B.; DE AVILLEZ, R. R.; REY, N. A. Crystal Structure and Hirshfeld Analysis of a Poorly Water Soluble Bis (ligand) copper (II) Complex Containing the Metallophore Pyridine-2-Carboxaldehyde 2-Furoyl Hydrazone. **Journal of Chemical Crystallography**, 53, n. 1, p. 8-15, 2023.

CUKIERMAN, D. S.; PINHEIRO, A. B.; CASTIÑEIRAS-FILHO, S. L.; DA SILVA, A. S. P. *et al.* A moderate metal-binding hydrazone meets the criteria for a bioinorganic approach towards Parkinson's disease: Therapeutic potential, blood-brain barrier crossing evaluation and preliminary toxicological studies. **Journal of inorganic biochemistry**, 170, p. 160-168, 2017.

D ÖZEL, A.; DURMUŞ, Z.; YıLMAZ, İ.; ÇUKUROVALı, A. *et al.* Electroreduction of some substituted hydrazones on platinum electrode in dimethylformamide. 2009.

DE OLIVEIRA SANTOS, M.; DE LIMA, F. C. d. S.; MARTINS, L. F. L.; OLIVEIRA, J. F. P. *et al.* Estimativa de incidência de câncer no Brasil, 2023-2025. **Revista Brasileira de Cancerologia**, 69, n. 1, 2023.

DEBELA, D. T.; MUZAZU, S. G.; HERARO, K. D.; NDALAMA, M. T. *et al.* New approaches and procedures for cancer treatment: Current perspectives. **SAGE open medicine**, 9, p. 20503121211034366, 2021.

DENNINGTON, R.; KEITH, T.; MILLAM, J.; GAUSSVIEW, V. **GaussView, Version 6.1.1**. Shawnee Mission, KS: Semichem Inc., 2019.

DOLOMANOV; V., O.; BOURHIS, L. J.; GILDEA, R. J. *et al.* OLEX2: A Complete Structure Solution, Refinement and Analysis Program. ***Journal of Applied Crystallography***, 42, n. 2, p. 339-341, 2009.

E VIGILÂNCIA, C. d. P. Instituto Nacional de Cancer José Alencar Gomes da Silva. Estimativa 2018: Incidência de Cancer no Brasil. Coordenação de Prevenção e Vigilância. Rio de Janeiro. 2018.

EATON, G. R.; EATON, S. S. Introduction to EPR imaging using magnetic-field gradients. **Concepts in Magnetic Resonance**, 7, n. 1, p. 49-67, 1995.

EID, A. M.; HAWASH, M.; AMER, J.; JARRAR, A. *et al.* Synthesis and Biological Evaluation of Novel Isoxazole-Amide Analogues as Anticancer and Antioxidant Agents. **BioMed Research International**, 2021, n. 1, p. 6633297, 2021.

ENDERS, D.; WORTMANN, L.; PETERS, R. Recovery of carbonyl compounds from N, N-dialkylhydrazones. **Accounts of chemical research**, 33, n. 3, p. 157-169, 2000.

FANALI, G.; DI MASI, A.; TREZZA, V.; MARINO, M. *et al.* Human serum albumin: From bench to bedside. **Molecular Aspects of Medicine**, 33, n. 3, p. 209-290, 2012/06/01/ 2012.

FARRUGIA, L. J. WinGX and ORTEP for Windows: an update. **J Appl Crystallogr**, 45, n. 4, p. 849-854, 2020/05/11 2012.

FEI, Z.; ZHANG, Y.; GE, M.; WANG, Y. *et al.* Probing thermal decomposition mechanism of molten nitrite/nitrates salt by time of flight mass spectrometry. **Solar Energy**, 183, p. 823-828, 2019/05/01/ 2019.

FEKRI, R.; SALEHI, M.; ASADI, A.; KUBICKI, M. Synthesis, characterization, anticancer and antibacterial evaluation of Schiff base ligands derived from hydrazone and their transition metal complexes. **Inorganica Chimica Acta**, 484, p. 245-254, 2019.

FERREIRA, B. L.; BRANDÃO, P.; MEIRELES, M.; MARTEL, F. *et al.* Synthesis, structural characterization, cytotoxic properties and DNA binding of a dinuclear copper (II) complex. **Journal of Inorganic Biochemistry**, 161, p. 9-17, 2016.

FIRMINO, G. S.; DE SOUZA, M. V.; PESSOA, C.; LOURENCO, M. C. *et al.* Synthesis and evaluation of copper (II) complexes with isoniazid-derived hydrazones as anticancer and antitubercular agents. **BioMetals**, 29, p. 953-963, 2016.

FOSS, S.; GREVYS, A.; SAND, K. M. K.; BERN, M. *et al.* Enhanced FcRn-dependent transepithelial delivery of IgG by Fc-engineering and polymerization. **Journal of Controlled Release**, 223, p. 42-52, 2016.

FRANZ, K. J.; METZLER-NOLTE, N. Introduction: metals in medicine. : ACS Publications. 119**:** 727-729 p. 2019.

FRISCH, M.; CLEMENTE, F. MJ Frisch, GW Trucks, HB Schlegel, GE Scuseria, MA Robb, JR Cheeseman, G. **Scalmani, V. Barone, B. Mennucci, GA Petersson, H. Nakatsuji, M. Caricato, X. Li, HP Hratchian, AF Izmaylov, J. Bloino and G. Zhe, Gaussian**, 9.

GAMOV, G.; KISELEV, A.; ZAVALISHIN, M.; YARULLIN, D. Formation and hydrolysis of pyridoxal-5′-phosphate hydrazones and Schiff bases: prediction of equilibrium and rate constants. **Journal of Molecular Liquids**, 369, p. 120961, 2023.

GARRIBBA, E.; MICERA, G. The determination of the geometry of Cu (II) complexes: an EPR spectroscopy experiment. **Journal of chemical education**, 83, n. 8, p. 1229, 2006.

GEARY, W. J. The use of conductivity measurements in organic solvents for the characterisation of coordination compounds. **Coordination Chemistry Reviews**, 7, n. 1, p. 81-122, 1971/10/01/ 1971.

GEGIA, M.; WINTERS, N.; BENEDETTI, A.; VAN SOOLINGEN, D. *et al.* Treatment of isoniazid-resistant tuberculosis with first-line drugs: a systematic review and meta-analysis. **The Lancet Infectious Diseases**, 17, n. 2, p. 223-234, 2017.

GEGIOU, D.; LAMBI, E.; HADJOUDIS, E. Solvatochromism in N-(2-Hydroxybenzylidene) aniline, N-(2-Hydroxybenzylidene) benzylamine, and N-(2-Hydroxybenzylidene)-2-phenylethylamine. **The Journal of Physical Chemistry**, 100, n. 45, p. 17762-17765, 1996.

GHOSHAL, S.; RIGNEY, G.; CHENG, D.; BRUMIT, R. *et al.* Institutional surgical response and associated volume trends throughout the COVID-19 pandemic and postvaccination recovery period. **JAMA network Open**, 5, n. 8, p. e2227443-e2227443, 2022.

GHUMAN, J.; ZUNSZAIN, P. A.; PETITPAS, I.; BHATTACHARYA, A. A. *et al.* Structural basis of the drug-binding specificity of human serum albumin. **J Mol Biol**, 353, n. 1, p. 38-52, Oct 14 2005.

GIBSON, S.; MCGUIRE, R.; REES, D. C. Principal components describing biological activities and molecular diversity of heterocyclic aromatic ring fragments. **Journal of medicinal chemistry**, 39, n. 20, p. 4065-4072, 1996.

GORDON, R. J.; CAMPBELL, J.; HENDERSON, D. K.; HENRY, D. C. *et al.* Polyacidic multiloading metal extractants. **Chemical communications**, n. 39, p. 4801-4803, 2008.

GOSSER, D. K. **Cyclic Voltammetry: Simulation and Analysis of Reaction Mechanisms**. VCH, 1993. 9783527282265.

GUAY, D. R. An update on the role of nitrofurans in the management of urinary tract infections. **Drugs**, 61, p. 353-364, 2001.

HATHAWAY, B.; BILLING, D. The electronic properties and stereochemistry of mono-nuclear complexes of the copper (II) ion. **Coordination Chemistry Reviews**, 5, n. 2, p. 143-207, 1970.

HEWKIN, D.; GRIFFITH, W. Infrared spectra of binuclear complexes. **Journal of the Chemical Society A: Inorganic, Physical, Theoretical**, p. 472-475, 1966.

HILLE, R. Molybdenum and tungsten in biology. **Trends in Biochemical Sciences**, 27, n. 7, p. 360-367, 2002.

HOUSECROFT, C. E.; SHARPE, A. G. **Inorganic Chemistry**. Pearson Prentice Hall, 2005. 9780130399137.

HU, J.; LIAO, C.; GUO, Y.; YANG, F. *et al.* Copper (II) complexes inducing apoptosis in cancer cells, and demonstrating DNA and HSA interactions. **Polyhedron**, 132, p. 28-38, 2017.

HUANG, P.; FENG, L.; OLDHAM, E. A.; KEATING, M. J. *et al.* Superoxide dismutase as a target for the selective killing of cancer cells. **Nature**, 407, n. 6802, p. 390-395, 2000.

HUBSCHLE, C. B.; SHELDRICK, G. M.; DITTRICH, B. ShelXle: a Qt graphical user interface for SHELXL. **Journal of Applied Crystallography**, 44, n. 6, p. 1281-1284, 2011.

HUHEEY, J. E. **Inorganic Chemistry; Principles of Structure and Reactivity**. Harper & Row, 1972. 9780060429843.

IQBAL, M.; AHMAD, I.; ALI, S.; MUHAMMAD, N. *et al.* Dimeric "paddle-wheel" carboxylates of copper (II): synthesis, crystal structure and electrochemical studies. **Polyhedron**, 50, n. 1, p. 524-531, 2013.

JAAFAR, M. I.; AHMED, R. K.; AL-KARAWI, A. J. M.; OMARALI, A.-A. B. *et al.* Designing a new bio-active copper (II)-triazole ester type complex based on copper (II)-catalyzed reaction. **Polyhedron**, 256, p. 116991, 2024.

JAYAMANI, A.; SENGOTTUVELAN, N.; CHAKKARAVARTHI, G. Synthesis, structural, electrochemical, DNA interaction, antimicrobial and molecular docking studies on dimeric copper (II) complexes involving some potential bidentate ligands. **Polyhedron**, 81, p. 764-776, 2014.

JAYAMANI, A.; SENGOTTUVELAN, N.; KANG, S. K.; KIM, Y.-I. Mono-and binuclear copper (II) complexes of the bipyridine ligand: Structural, electrochemical and biological studies. **Polyhedron**, 98, p. 203-216, 2015.

JOHNSON, E. R.; KEINAN, S.; MORI-SÁNCHEZ, P.; CONTRERAS-GARCÍA, J. *et al.* Revealing noncovalent interactions. **J Am Chem Soc**, 132, n. 18, p. 6498-6506, May 12 2010.

KAJAL, A.; BALA, S.; SHARMA, N.; KAMBOJ, S. *et al.* Therapeutic Potential of Hydrazones as Anti-Inflammatory Agents. **International journal of medicinal chemistry**, 2014, n. 1, p. 761030, 2014.

KALA, U.; SUMA, S.; KURUP, M. P.; KRISHNAN, S. *et al.* Synthesis, spectral characterization and crystal structure of copper (II) complexes of 2-hydroxyacetophenone-N (4)-phenyl semicarbazone. **Polyhedron**, 26, n. 7, p. 1427-1435, 2007.

KARLIN, K. D.; TYEKLAR, Z. **Bioinorganic Chemistry of Copper**. Springer Netherlands,

2012. 9789401168755.

KIVELSON, D.; NEIMAN, R. ESR studies on the bonding in copper complexes. **The Journal of Chemical Physics**, 35, n. 1, p. 149-155, 1961.

KÖLMEL, D. K.; KOOL, E. T. Oximes and Hydrazones in Bioconjugation: Mechanism and Catalysis. **Chemical Reviews**, 117, n. 15, p. 10358-10376, 2017/08/09 2017.

KOZUCH, S.; MARTIN, J. M. Halogen Bonds: Benchmarks and Theoretical Analysis. **J Chem Theory Comput**, 9, n. 4, p. 1918-1931, Apr 09 2013.

KRATZ, F.; ELSADEK, B. Clinical impact of serum proteins on drug delivery. **Journal of Controlled Release**, 161, n. 2, p. 429-445, 2012.

KRAUSE, L.; HERBST-IRMER, R.; SHELDRICK, G. M.; STALKE, D. Comparison of silver and molybdenum microfocus X-ray sources for single-crystal structure determination. **J Appl Crystallogr**, 48, n. Pt 1, p. 3-10, Feb 01 2015.

KUMAR, K. A.; JAYAROOPA, P. Isoxazoles: molecules with potential medicinal properties. **Int J Pharm Chem Biol Sci**, 3, p. 294-304, 2013.

LARSEN, M. T.; KUHLMANN, M.; HVAM, M. L.; HOWARD, K. A. Albumin-based drug delivery: harnessing nature to cure disease. **Molecular and cellular therapies**, 4, p. 1-12, 2016.

LAVIRON, E.; ROULLIER, L.; DEGRAND, C. A multilayer model for the study of space distributed redox modified electrodes: Part II. Theory and application of linear potential sweep voltammetry for a simple reaction. **Journal of Electroanalytical Chemistry and Interfacial Electrochemistry**, 112, n. 1, p. 11-23, 1980.

LAWRENCE, M. A. W.; LORRAINE, S. C.; WILSON, K.-A.; WILSON, K. Review: Voltammetric properties and applications of hydrazones and azo moieties. **Polyhedron**, 173, p. 114111, 2019/11/15/ 2019.

LAZNY, R.; NODZEWSKA, A. N, N-dialkylhydrazones in organic synthesis. From simple N, N-dimethylhydrazones to supported chiral auxiliaries. **Chemical reviews**, 110, n. 3, p. 1386-1434, 2010.

LEBLANC, Y.; BERGER, M.; SEIFERT, A.; BIHOREAU, N. *et al.* Human serum albumin presents isoform variants with altered neonatal Fc receptor interactions. **Protein Science**, 28, n. 11, p. 1982-1992, 2019.

LEVER, A. B. P. **Inorganic Electronic Spectroscopy**. Elsevier, 1984. v. v. 33). 9780444416995.

LI, Y.; HERMANSON, D. L.; MORIARITY, B. S.; KAUFMAN, D. S. Human iPSC-derived natural killer cells engineered with chimeric antigen receptors enhance anti-tumor activity. **Cell stem cell**, 23, n. 2, p. 181-192. e185, 2018.

LIANG, F.; LI, S.; LINDSAY, S.; ZHANG, P. Synthesis, Physicochemical Properties, and Hydrogen Bonding of 4(5)-Substituted 1-H-Imidazole-2-carboxamide, a Potential Universal Reader for DNA Sequencing by Recognition Tunneling. **Chemistry – A European Journal**, 18, n. 19, p. 5998-6007, 2012.

LIPPARD, S. J.; BERG, J. M. **Principles of Bioinorganic Chemistry**. University Science Books, 1994. 9780935702729.

LIU, R.; CUI, J.; DING, T.; LIU, Y. *et al.* Research progress on the biological activities of metal

complexes bearing polycyclic aromatic hydrazones. **Molecules**, 27, n. 23, p. 8393, 2022.

LOBUE, P. A.; MOSER, K. S. Use of isoniazid for latent tuberculosis infection in a public health clinic. **American journal of respiratory and critical care medicine**, 168, n. 4, p. 443-447, 2003.

LUO, J.; ELLEDGE, S. J. Deconstructing oncogenesis. **Nature**, 453, n. 7198, p. 995-996, 2008.

MANONMANI, J.; THIRUMURUGAN, R.; KANDASWAMY, M.; KUPPAYEE, M. *et al.* Synthesis of mononuclear nickel(II) and copper(II) complexes using compartmental ligands: X-ray and electrochemical studies. **Polyhedron**, 19, n. 18, p. 2011-2018, 2000/09/30/ 2000.

MANZUR, J.; MORA, H.; VEGA, A.; VENEGAS-YAZIGI, D. *et al.* Mononuclear and polynuclear copper (II) complexes derived from pyridylalkylaminomethylphenol polypodal ligands. **Inorganic chemistry**, 48, n. 18, p. 8845-8855, 2009.

MCMURRAY, H. R.; SAMPSON, E. R.; COMPITELLO, G.; KINSEY, C. *et al.* Synergistic response to oncogenic mutations defines gene class critical to cancer phenotype. **Nature**, 453, n. 7198, p. 1112-1116, 2008.

MERLOT, A. M.; KALINOWSKI, D. S.; RICHARDSON, D. R. Unraveling the mysteries of serum albumin—more than just a serum protein. **Frontiers in Physiology**, 5, 2014-August-12 2014. Mini Review.

MIESSLER, G. L.; TARR, D. A. **Inorganic Chemistry**. Pearson Education, 2004. 9788131712900.

MOHAN, M.; GUPTA, N. K.; KUMAR, M.; JHA, N. K. *et al.* Synthesis, magnetic and electrochemical properties of binuclear copper (II) complexes of pyridoxal hydrazones. **Inorganica chimica acta**, 197, n. 1, p. 39-46, 1992.

MOLINARO, C.; MARTORIATI, A.; PELINSKI, L.; CAILLIAU, K. Copper complexes as anticancer agents targeting topoisomerases I and II. **Cancers**, 12, n. 10, p. 2863, 2020.

MONDAL, J.; PANIGRAHI, A.; KHUDA-BUKHSH, A. Conventional chemotherapy: problems and scope for combined therapies with certain herbal products and dietary supplements. **Austin J Mol Cell Biol**, 1, n. 1, p. 1-10, 2014.

MONTAGNER, D.; GANDIN, V.; MARZANO, C.; ERXLEBEN, A. DNA damage and induction of apoptosis in pancreatic cancer cells by a new dinuclear bis (triazacyclonane) copper complex. **Journal of Inorganic Biochemistry**, 145, p. 101-107, 2015.

MORRISON, C. N.; PROSSER, K. E.; STOKES, R. W.; CORDES, A. *et al.* Expanding medicinal chemistry into 3D space: Metallofragments as 3D scaffolds for fragment-based drug discovery. **Chemical science**, 11, n. 5, p. 1216-1225, 2020.

MORRISON, C. N.; PROSSER, K. E.; STOKES, R. W.; CORDES, A. *et al.* Correction: Expanding medicinal chemistry into 3D space: metallofragments as 3D scaffolds for fragment-based drug discovery. **Chemical Science**, 13, n. 32, p. 9450-9452, 2022.

MOSES, M. A.; BREM, H.; LANGER, R. Advancing the field of drug delivery: taking aim at cancer. **Cancer cell**, 4, n. 5, p. 337-341, 2003.

MOURA, F. d. S.; SOBRINHO, Y. S.; STELLET, C.; SERNA, J. D. P. *et al.* Copper(ii) complexes of a furan-containing aroylhydrazonic ligand: syntheses, structural studies, solution chemistry and interaction with HSA. **Dalton Transactions**, 52, n. 47, p. 17731-17746, 2023. 10.1039/D3DT02597G.

MUHAMMAD, H.; TAHIRI, I. A.; MUHAMMAD, M.; MASOOD, Z. *et al.* A comprehensive heterogeneous electron transfer rate constant evaluation of dissolved oxygen in DMSO at glassy carbon electrode measured by different electrochemical methods. **Journal of Electroanalytical Chemistry**, 775, p. 157-162, 2016/08/15/ 2016.

NAJI, A.; EITOKU, M.; FAVIER, B.; DESCHASEAUX, F. *et al.* Biological functions of mesenchymal stem cells and clinical implications. **Cellular and Molecular Life Sciences**, 76, p. 3323-3348, 2019.

NAKAMOTO, K. **Infrared and Raman Spectra of Inorganic and Coordination Compounds**. Wiley, 1978. 9780471629795.

NASKAR, J. P.; BISWAS, C.; GUHATHAKURTA, B.; ALIAGA-ALCALDE, N. *et al.* Oximato bridged copper (II) dimers: Synthesis, crystal structure, magnetic, thermal and electrochemical properties. **Polyhedron**, 30, n. 13, p. 2310-2319, 2011.

OBERLEY, L. W.; BUETTNER, G. R. Role of superoxide dismutase in cancer: a review. **Cancer research**, 39, n. 4, p. 1141-1149, 1979.

OBSERVATORY, G. C. **Global Cancer Observatory**. https://gco.iarc.fr/, 2024.

OUYANG, X.; TELLI, M. L.; WU, J. C. Induced pluripotent stem cell-based cancer vaccines. **Frontiers in Immunology**, 10, p. 1510, 2019.

PADNYA, P.; SHIBAEVA, K.; ARSENYEV, M.; BARYSHNIKOVA, S. *et al.* Catechol-Containing Schiff Bases on Thiacalixarene: Synthesis, Copper (II) Recognition, and Formation of Organic-Inorganic Copper-Based Materials. **Molecules**, 26, n. 8, p. 2334, 2021.

PAIVA, V. M.; DE OLIVEIRA, S. M.; DE ALMEIDA, C. M. d. S.; DE ARAUJO, J. R. *et al.* Pumpkin (Cucurbita maxima) seed-derived nitrogen, phosphorus, and sulfur carbon quantum dot as an inhibitor of corrosion for mild steel in HCl solution. **Journal of Materials Research and Technology**, 28, p. 2504-2515, 2024.

PAKE, G. E. Paramagnetic resonance: an introductory monograph. **(No Title)**, 1962.

PATRA, D.; PAUL, S.; SEPAY, N.; KUNDU, R. *et al.* Structure-activity relationship on DNA binding and anticancer activities of a family of mixed-ligand oxidovanadium (V) hydrazone complexes. **Journal of Biomolecular Structure and Dynamics**, 36, n. 16, p. 4143-4155, 2018.

PAVIA, D.; LAMPMAN, G.; KRIZ, G.; VYVYAN, J. **Introdução à espectroscopia**. Cengage Learning, 2015. 9788522123384.

PILLERON, S.; SOTO-PEREZ-DE-CELIS, E.; VIGNAT, J.; FERLAY, J. *et al.* Estimated global cancer incidence in the oldest adults in 2018 and projections to 2050. **International journal of cancer**, 148, n. 3, p. 601-608, 2021.

PINHEIRO, P. d. S. M.; RODRIGUES, D. A.; ALVES, M. A.; TINOCO, L. W. *et al.* Theoretical and experimental characterization of 1, 4-N··· S σ-hole intramolecular interactions in bioactive N-acylhydrazone derivatives. **New Journal of Chemistry**, 42, n. 1, p. 497-505, 2018.

PURANDARA, H.; RAGHAVENDRA, S.; FORO, S.; PATIL, P. *et al.* Synthesis, spectroscopic characterization, crystal structure, Hirshfeld surface analysis and third-order nonlinear optical properties of 2-(4-chlorophenoxy)-N'-[(1E)-1-(4-methylphenyl) ethylidene] acetohydrazide. **Journal of Molecular Structure**, 1185, p. 205-211, 2019/06/05/ 2019.

RADA, J. P.; BASTOS, B. S.; ANSELMINO, L.; FRANCO, C. H. *et al.* Binucleating hydrazonic ligands and their μ-hydroxodicopper (II) complexes as promising structural motifs for enhanced antitumor activity. **Inorganic Chemistry**, 58, n. 13, p. 8800-8819, 2019.

RADA, J. P.; FORTÉ, J.; GONTARD, G.; BACHELET, C.-M. *et al.* Novel luminescent benzopyranothiophene-and BODIPY-derived aroylhydrazonic ligands and their dicopper (II) complexes: syntheses, antiproliferative activity and cellular uptake studies. **JBIC Journal of Biological Inorganic Chemistry**, 26, n. 6, p. 675-688, 2021.

RADA, J. P.; FORTÉ, J.; GONTARD, G.; CORCÉ, V. *et al.* Isoxazole-Derived Aroylhydrazones and Their Dinuclear Copper (II) Complexes Show Antiproliferative Activity on Breast Cancer Cells with a Potentially Alternative Mechanism Of Action. **ChemBioChem**, 21, n. 17, p. 2474-2486, 2020.

REPICH, H.; ORYSYK, S.; ORYSYK, V.; ZBOROVSKII, Y. L. *et al.* Influence of synthesis conditions on complexation of Cu (II) with O, N, O tridentate hydrazone ligand. X-ray diffraction and spectroscopic investigations. **Journal of Molecular Structure**, 1146, p. 222-232, 2017.

REY, N. A. **Binucleating aroylhydrazonic ligands and their dicopper (II) complexes as new classes of potential anticancer agents: syntheses, chemical characterization and biological activity**. 2019. -, PUC-Rio.

RIBEIRO, N.; CORREIA, I. A review of hydrazide-hydrazone metal complexes' antitumor potential. **Frontiers in Chemical Biology**, 3, p. 1398873, 2024.

ROAT-MALONE, R. M. **Bioinorganic Chemistry: A Short Course**. Wiley, 2007. 9780471761136.

RODRÍGUEZ, M. R.; BALSA, L. M.; PIRO, O. E.; ETCHEVERRÍA, G. A. *et al.* Synthesis, crystal structure, spectroscopic characterization, DFT calculations and cytotoxicity assays of a new cu (II) complex with an acylhydrazone Ligand derived from thiophene. **Inorganics**, 9, n. 2, p. 9, 2021.

ROLLAS, S.; GÜNIZ KÜÇÜKGÜZEL, Ş. Biological activities of hydrazone derivatives. **Molecules**, 12, n. 8, p. 1910-1939, 2007.

ROSENBERG, B.; VAN CAMP, L.; GRIMLEY, E. B.; THOMSON, A. J. The inhibition of growth or cell division in Escherichia coli by different ionic species of platinum (IV) complexes. **Journal of Biological Chemistry**, 242, n. 6, p. 1347-1352, 1967.

ROSENBERG, B.; VAN CAMP, L.; KRIGAS, T. Inhibition of cell division in Escherichia coli by electrolysis products from a platinum electrode. **Nature**, 205, n. 4972, p. 698-699, 1965.

ROSSI, L. M.; NEVES, A.; BORTOLUZZI, A. J.; HÖRNER, R. *et al.* Synthesis, structure and properties of unsymmetrical μ-alkoxo-dicopper (II) complexes: biological relevance to phosphodiester and DNA cleavage and cytotoxic activity. **Inorganica chimica acta**, 358, n. 6, p. 1807-1822, 2005.

ROSSI, L. M.; NEVES, A.; HÖRNER, R.; TERENZI, H. *et al.* Hydrolytic activity of a dinuclear copper (II, II) complex in phosphate diester and DNA cleavage. **Inorganica Chimica Acta**, 337, p. 366-370, 2002.

RUIZ-AZUARA, L.; BASTIAN, G.; BRAVO-GÓMEZ, M. E.; CAÑAS, R. C. *et al.* Abstract CT408: Phase I study of one mixed chelates copper (II) compound, Casiopeína CasIIIia with antitumor activity and its mechanism of action. **Cancer Research**, 74, n. 19_Supplement, p. CT408-CT408, 2014.

SADHUKHAN, D.; MAITI, M.; BAUZÁ, A.; FRONTERA, A. *et al.* Synthesis, structure, physicochemical characterization and theoretical evaluation of non-covalent interaction energy of a polymeric copper (II)-hydrazone complex. **Inorganica Chimica Acta**, 484, p. 95-103, 2019.

SAHU, G.; SAHU, K.; PATRA, S. A.; MOHAPATRA, D. *et al.* Hydrolytically stable TiIV–Hydrazone-Based metallodrugs: protein interaction and anticancer potential. **ACS Applied Bio Materials**, 6, n. 12, p. 5360-5371, 2023.

SAKAGUCHI, U.; ADDISON, A. W. Spectroscopic and redox studies of some copper (II) complexes with biomimetic donor atoms: implications for protein copper centres. **Journal of the Chemical Society, Dalton Transactions**, n. 4, p. 600-608, 1979.

SALONI DATTANI, F. S., Hannah Ritchie and Max Roser. **"Causes of Death"** https://ourworldindata.org/causes-of-death, 2023. Disponível em: https://ourworldindata.org/causes-of-death#article-citation. Acesso em: 07-28.

SAND, K. M. K.; BERN, M.; NILSEN, J.; NOORDZIJ, H. T. *et al.* Unraveling the interaction between FcRn and albumin: opportunities for design of albumin-based therapeutics. **Frontiers in immunology**, 5, p. 682, 2015.

SANGEETHA, N. R.; BARADI, K.; GUPTA, R.; PAL, C. K. *et al.* Synthesis, structure and properties of a dicopper(II) complex. **Polyhedron**, 18, n. 10, p. 1425-1429, 1999/03/26/ 1999.

SANTIAGO, P. H. O.; SANTIAGO, M. B.; MARTINS, C. H. G.; GATTO, C. C. Copper(II) and zinc(II) complexes with Hydrazone: Synthesis, crystal structure, Hirshfeld surface and antibacterial activity. **Inorganica Chimica Acta**, 508, p. 119632, 2020/08/01/ 2020.

SANTINI, C.; PELLEI, M.; GANDIN, V.; PORCHIA, M. *et al.* Advances in copper complexes as anticancer agents. **Chemical reviews**, 114, n. 1, p. 815-862, 2014.

SELVAM, P.; SATHIYAKUMAR, S.; SRINIVASAN, K.; PREMKUMAR, T. A Copper(II) complex of a new hydrazone: A solid-state single source precursor for the preparation of both Cu and CuO nanoparticles. **Journal of Molecular Structure**, 1177, p. 469-475, 2019/02/05/ 2019.

SHAPIRA, A.; LIVNEY, Y. D.; BROXTERMAN, H. J.; ASSARAF, Y. G. Nanomedicine for targeted cancer therapy: towards the overcoming of drug resistance. **Drug resistance updates**, 14, n. 3, p. 150-163, 2011.

SHELDRICK, G. M. A short history of SHELX. **Acta Crystallogr A**, 64, n. Pt 1, p. 112-122, Jan 2008.

SHELDRICK, G. M. Crystal structure refinement with SHELXL. **Acta Crystallogr C Struct Chem**, 71, n. Pt 1, p. 3-8, Jan 2015.

SIEGEL, R. L.; MILLER, K. D.; WAGLE, N. S.; JEMAL, A. Cancer statistics, 2023. **CA: a cancer journal for clinicians**, 73, n. 1, 2023.

SILVERSTEIN, R. M. **Identificação espectrométrica de compostos orgânicos**. Livros Técnicos e Científicos, 2000. 9788521612308.

SOCEA, L.-I.; BARBUCEANU, S.-F.; PAHONTU, E. M.; DUMITRU, A.-C. *et al.* Acylhydrazones and Their Biological Activity: A Review. **Molecules**, 27, n. 24, p. 8719, 2022.

SORRELL, T. N. Synthetic models for binuclear copper proteins. **Tetrahedron**, 45, n. 1, p. 3-68, 1989.

SPEK, A. Structure validation in chemical crystallography. **Acta Crystallographica Section D**, 65, n. 2, p. 148-155, 2009.

SREENIVASULU, R.; REDDY, K. T.; SUJITHA, P.; KUMAR, C. G. *et al.* Synthesis, antiproliferative and apoptosis induction potential activities of novel bis (indolyl) hydrazide-hydrazone derivatives. **Bioorganic & medicinal chemistry**, 27, n. 6, p. 1043-1055, 2019.

SUN, L.-C.; H COY, D. Somatostatin receptor-targeted anti-cancer therapy. **Current drug delivery**, 8, n. 1, p. 2-10, 2011.

SUN, L.-C.; MACKEY, L. V.; LUO, J.; FUSELIER, J. A. *et al.* Targeted chemotherapy using a cytotoxic somatostatin conjugate to inhibit tumor growth and metastasis in nude mice. **Clinical medicine. Oncology**, 2, p. CMO. S970, 2008.

SWINNEY, D. C.; ANTHONY, J. How were new medicines discovered? **Nature reviews Drug discovery**, 10, n. 7, p. 507-519, 2011.

SYSTÈMES, B. D. Discovery
Studio Visualizer. San Diego Dassault Systèmes 2021.

TAKAHASHI, K.; YAMANAKA, S. Induction of pluripotent stem cells from mouse embryonic and adult fibroblast cultures by defined factors. **cell**, 126, n. 4, p. 663-676, 2006.

TAN, C.-P.; LU, Y.-Y.; JI, L.-N.; MAO, Z.-W. Metallomics insights into the programmed cell death induced by metal-based anticancer compounds. **Metallomics**, 6, n. 5, p. 978-995, 2014.

THOTA, S.; RODRIGUES, D. A.; PINHEIRO, P. d. S. M.; LIMA, L. M. *et al.* N-Acylhydrazones as drugs. **Bioorganic & medicinal chemistry letters**, 28, n. 17, p. 2797-2806, 2018.

TORELLI, S.; BELLE, C.; GAUTIER-LUNEAU, I.; PIERRE, J. L. *et al.* pH-Controlled Change of the Metal Coordination in a Dicopper(II) Complex of the Ligand H−BPMP: Crystal Structures, Magnetic Properties, and Catecholase Activity. **Inorganic Chemistry**, 39, n. 16, p. 3526-3536, 2000/08/01 2000.

TROPOL'SKAYA, T.; MUNIN, E.; KITAEV, Y. P. Hydrazones 61. Electrochemical reduction of the aryl-and acylhydrazones in nonaqueous solution. **Bulletin of the Academy of Sciences of the USSR. Division of Chemical Sciences**, 28, n. 5, p. 919-925, 1979.

TROST, B. M.; FLEMING, I. **Comprehensive Organic Synthesis: Selectivity, Strategy, and Efficiency in Modern Organic Chemistry**. Pergamon Press, 1991. 9780080359298.

UPPAL, G.; BALA, S.; KAMBOJ, S.; SAINI, M. Therapeutic review exploring antimicrobial potential of hydrazones as promising lead. **Der Pharma Chemica**, 3, n. 1, p. 250-268, 2011.

VAIDYANATHAN, M.; VISWANATHAN, R.; PALANIANDAVAR, M.; BALASUBRAMANIAN, T. *et al.* Copper (II) complexes with unusual axial phenolate coordination as structural models for the active site in galactose oxidase: X-ray crystal structures and spectral and redox properties of [Cu (bpnp) X] complexes. **Inorganic chemistry**, 37, n. 25, p. 6418-6427, 1998.

VALTER, K.; CHEN, L.; KRUSPIG, B.; MAXIMCHIK, P. *et al.* Contrasting effects of glutamine deprivation on apoptosis induced by conventionally used anticancer drugs. **Biochimica et Biophysica Acta (BBA)-Molecular Cell Research**, 1864, n. 3, p. 498-506, 2017.

VAN DER HEIJDEN, O.; PARK, S.; VOS, R. E.; EGGEBEEN, J. J. J. *et al.* Tafel Slope Plot as a

Tool to Analyze Electrocatalytic Reactions. **ACS Energy Letters**, 9, n. 4, p. 1871-1879, 2024/04/12 2024.

VERMA, G.; MARELLA, A.; SHAQUIQUZZAMAN, M.; AKHTAR, M. *et al.* A review exploring biological activities of hydrazones. **Journal of Pharmacy and Bioallied Sciences**, 6, n. 2, p. 69-80, 2014.

VITÓRIO, F.; PEREIRA, T. M.; CASTRO, R. N.; GUEDES, G. P. *et al.* Synthesis and mechanism of novel fluorescent coumarin–dihydropyrimidinone dyads obtained by the Biginelli multicomponent reaction. **New Journal of Chemistry**, 39, n. 3, p. 2323-2332, 2015. 10.1039/C4NJ02155J.

WALUNJ, Y.; MHASKE, P.; KULKARNI, P. Application, reactivity and synthesis of isoxazole derivatives. **Mini-Reviews in Organic Chemistry**, 18, n. 1, p. 55-77, 2021.

WANAT, K. Biological barriers, and the influence of protein binding on the passage of drugs across them. **Molecular biology reports**, 47, n. 4, p. 3221-3231, 2020.

WANG, S.; LIU, S.; ZHANG, Y.; HE, J. *et al.* Human Serum Albumin (HSA) and Its Applications as a Drug Delivery Vehicle. 03/09 2020.

WEBER, W. A. Positron emission tomography as an imaging biomarker. **Journal of Clinical Oncology**, 24, n. 20, p. 3282-3292, 2006.

WEINBERG, R. A. Oncogenes and the molecular biology of cancer. **The Journal of cell biology**, 97, n. 6, p. 1661-1662, 1983.

WHO. 2022. Disponível em: https://www.who.int/data. Acesso em: 07-25.

WU, A. M.; SENTER, P. D. Arming antibodies: prospects and challenges for immunoconjugates. **Nature biotechnology**, 23, n. 9, p. 1137-1146, 2005.

WU, J.-S.; LIU, W.-M.; ZHUANG, X.-Q.; WANG, F. *et al.* Fluorescence Turn On of Coumarin Derivatives by Metal Cations: A New Signaling Mechanism Based on C=N Isomerization. **Organic Letters**, 9, n. 1, p. 33-36, 2007/01/01 2007.

YADAV, P. Targeted cancer therapy; researchers reflection. **Int Peer-Rev J**, 1, p. 11-17, 2017.

YANG, L.; POWELL, D. R.; HOUSER, R. P. Structural variation in copper (I) complexes with pyridylmethylamide ligands: structural analysis with a new four-coordinate geometry index, τ 4. **Dalton Transactions**, n. 9, p. 955-964, 2007.

YANG, M.; QIU, F.; EL-SAYED, E.-S. M.; WANG, W. *et al.* Water-stable hydrazone-linked porous organic cages. **Chemical Science**, 12, n. 40, p. 13307-13315, 2021.

YOGEESWARI, P.; MENON, N.; SEMWAL, A.; ARJUN, M. *et al.* Discovery of molecules for the treatment of neuropathic pain: Synthesis, antiallodynic and antihyperalgesic activities of 5-(4-nitrophenyl)furoic-2-acid hydrazones. **European Journal of Medicinal Chemistry**, 46, n. 7, p. 2964-2970, 2011/07/01/ 2011.

YOGUIM, M. I.; GRANDINI, G. S.; BERTOZO, L. d. C.; CARACELLI, I. *et al.* Studies on the Interaction of Rose Bengal with the Human Serum Albumin Protein under Spectroscopic and Docking Simulations Aspects in the Characterization of Binding Sites. **Chemosensors**, 10, n. 11, p. 440, 2022.

ZUNSZAIN, P. A.; GHUMAN, J.; MCDONAGH, A. F.; CURRY, S. Crystallographic analysis of

human serum albumin complexed with 4Z,15E-bilirubin-IXalpha. **J Mol Biol**, 381, n. 2, p. 394-406, Aug 29 2008.

8. Appendix

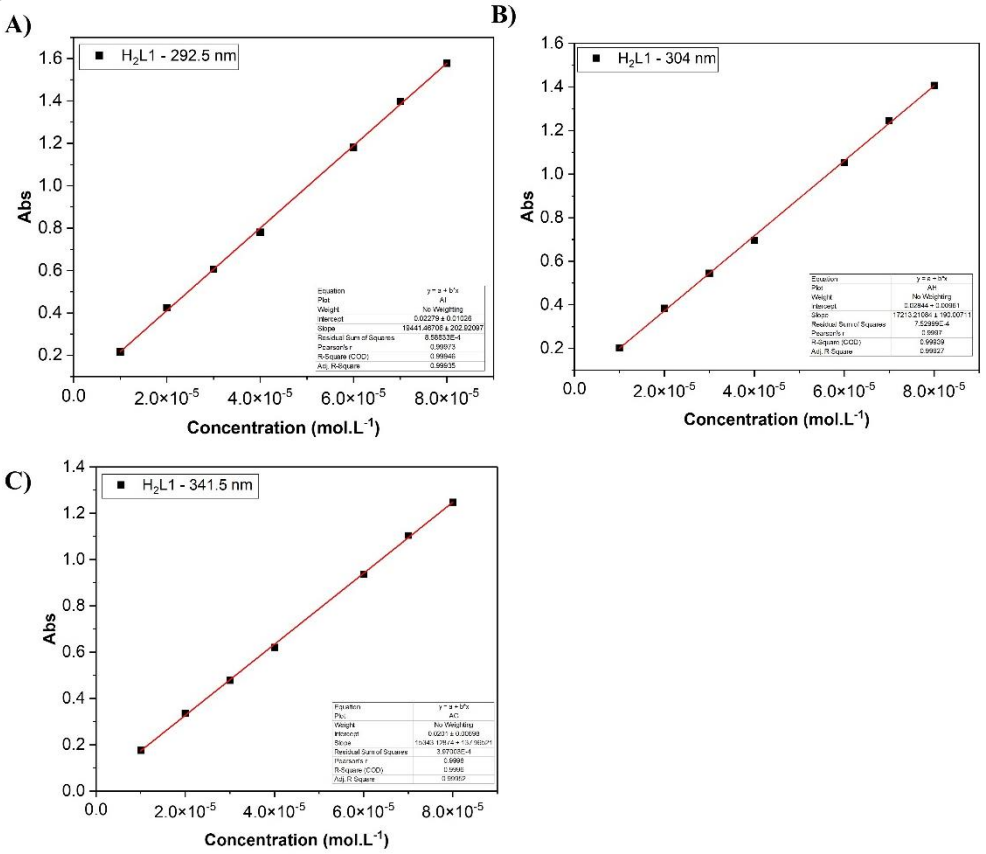

Appendix Figure 1. Absorbance (max) vs [C] for the ligand H_2L1. (A) – band at 292.5 nm, (B) – band at 304 nm, (C) – band at 341.5 nm.

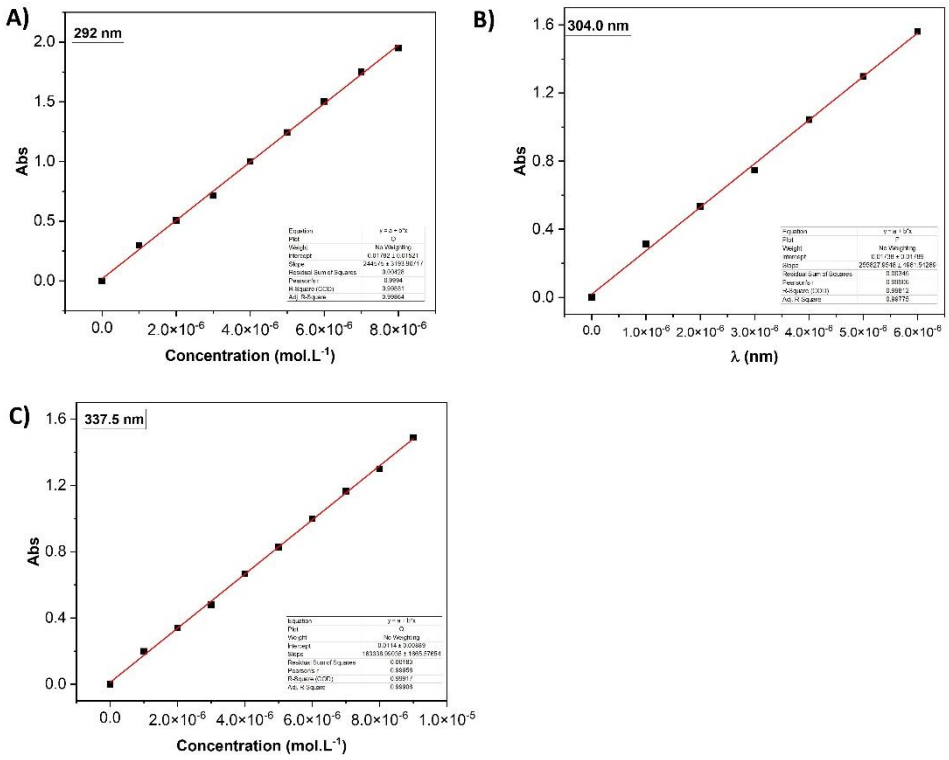

Appendix Figure 2. Absorbance (max) vs [C] for the ligand H_2L2. (A) – band at 292 nm, (B) – band at 304 nm, (C) – band at 337.5 nm.

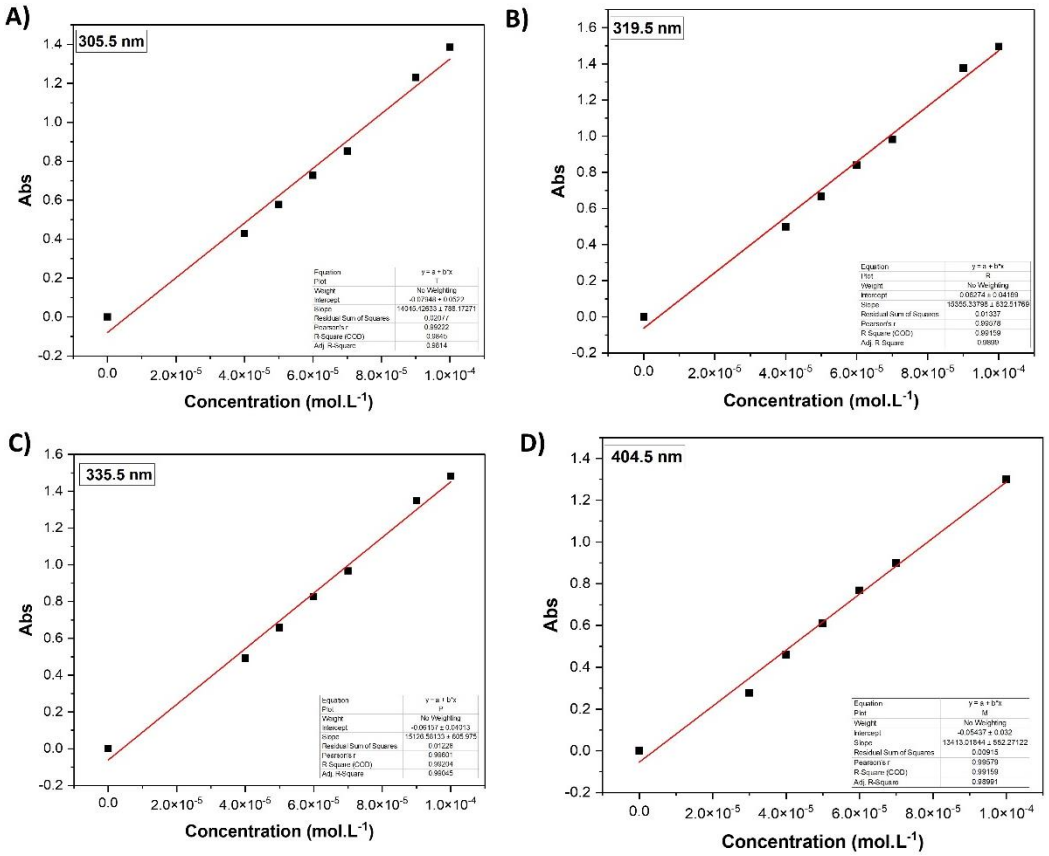

Appendix Figure 3. Absorbance (max) vs [C] for complex 2A. (A) – band at 305.5 nm, (B) –band at 319.5 nm, (C) – band at 335.5 nm and (D) - band at 404.5 nm.

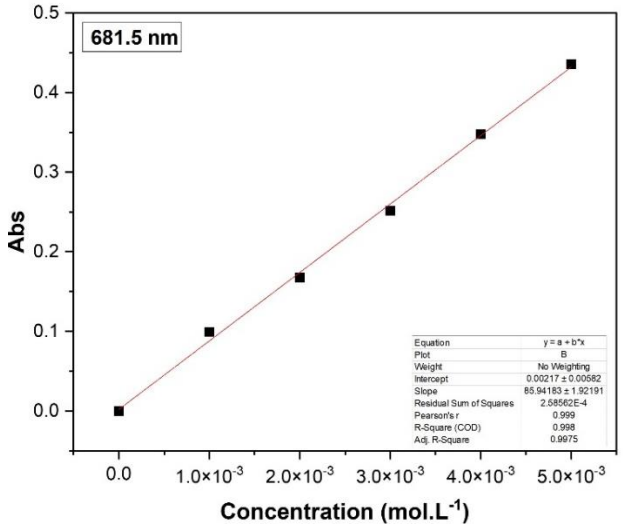

Appendix Figure 4. Absorbance (max) vs [C] for the d-d transition in 681.5 nm for complex 2A.

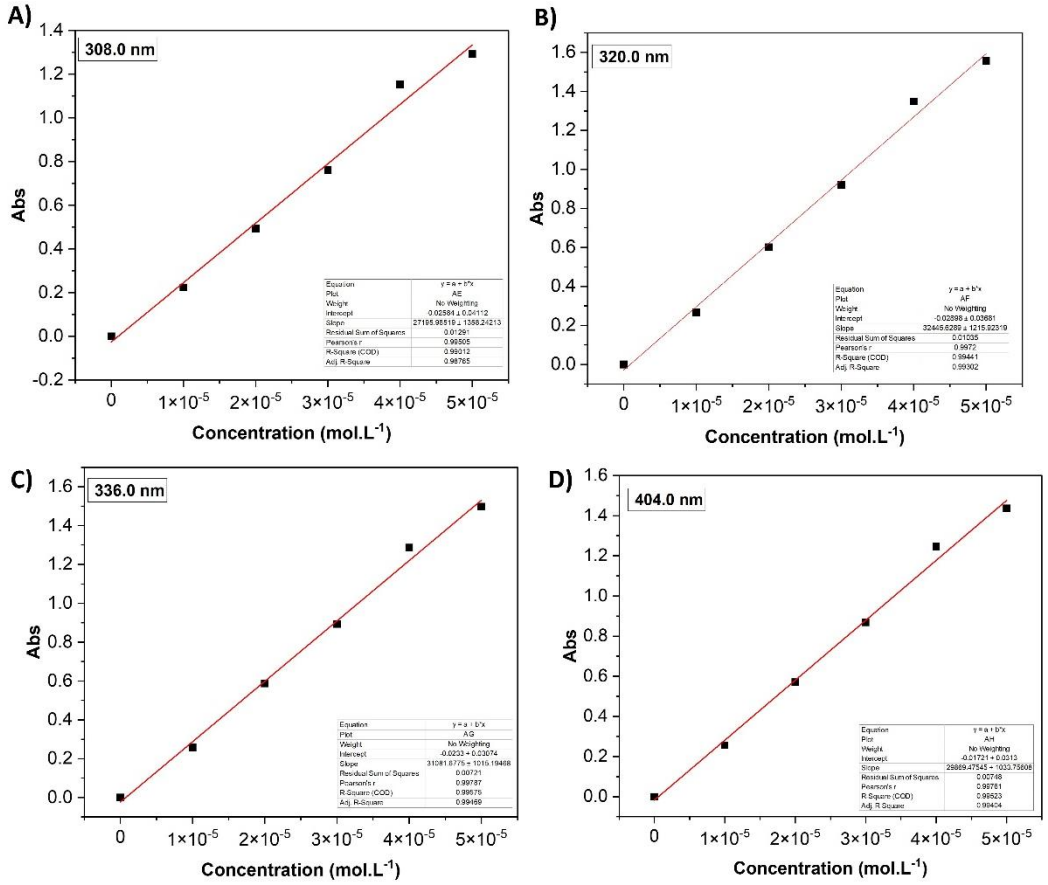

Appendix Figure 5. Absorbance (max) vs [C] for complex 2B. (A) – band at 308 nm, (B) –band at 320 nm, (C) – band at 336 nm and (D) - band at 404 nm.

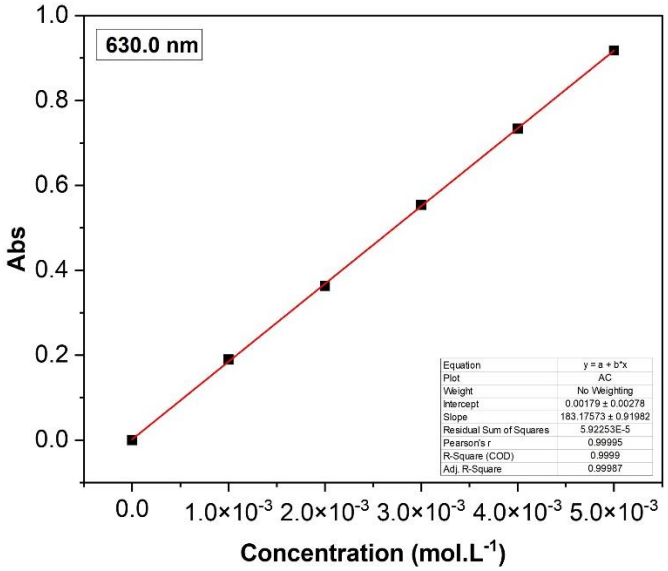

Appendix Figure 6. Absorbance (max) vs [C] for the d-d transition in 630 nm for complex 2B.

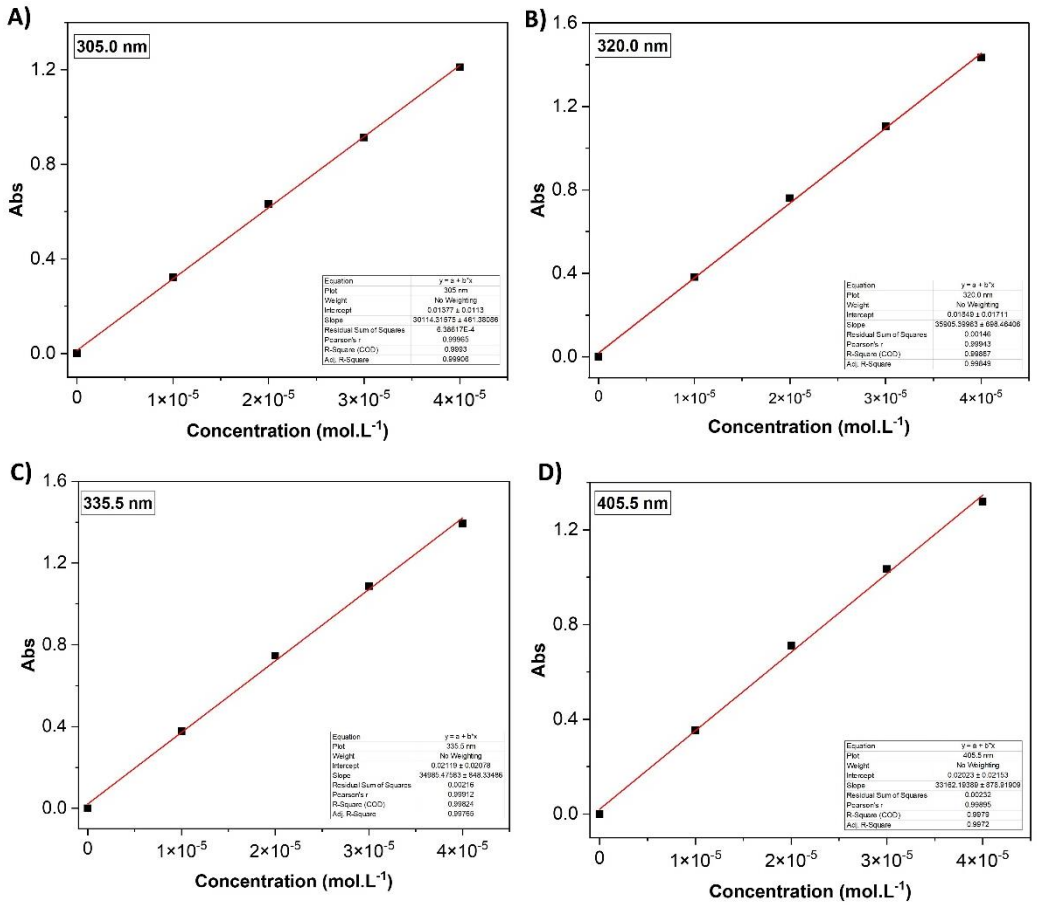

Appendix Figure 7. Absorbance (max) vs [C] for complex 2C. (A) – band at 305 nm, (B) –band at 320 nm, (C) – band at 335.5 nm and (D) - band at 405.5 nm.

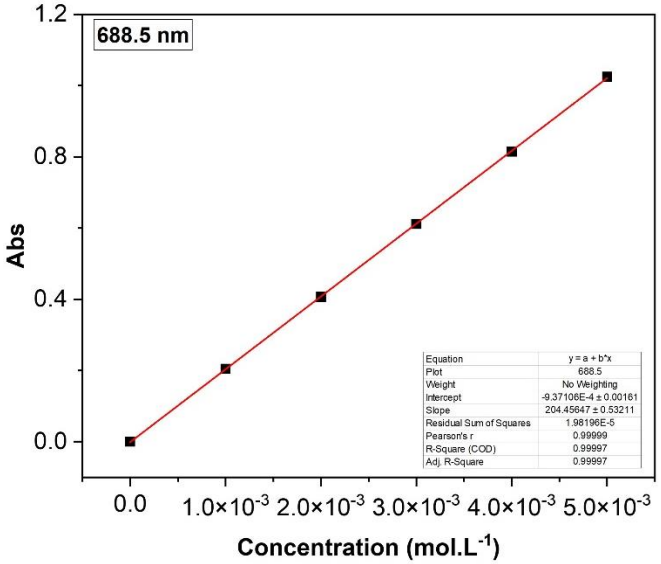

Appendix Figure 8. Absorbance (max) vs [C] for the d-d transition in 688.5 nm for complex 2C.

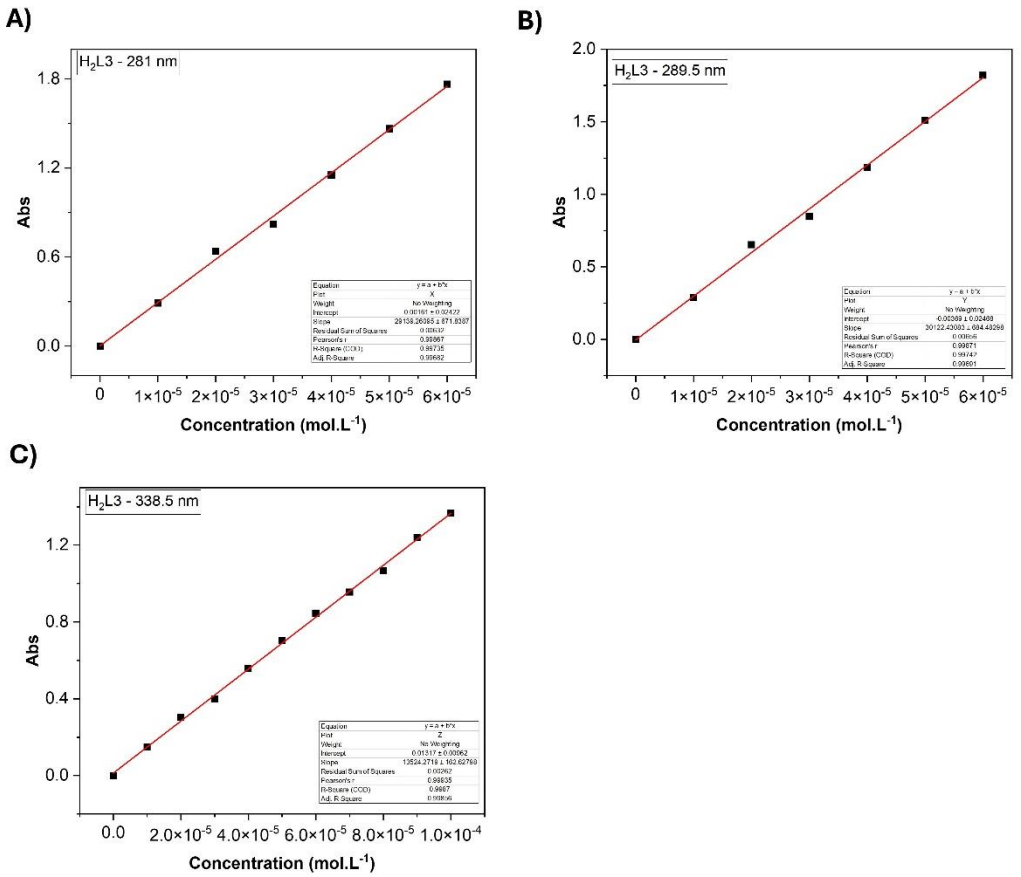

Appendix Figure 9. Absorbance (max) vs [C] for the ligand H_2L3. (A) – band at 281 nm, (B) – band at 289.5 nm, (C) – band at 338.5 nm.

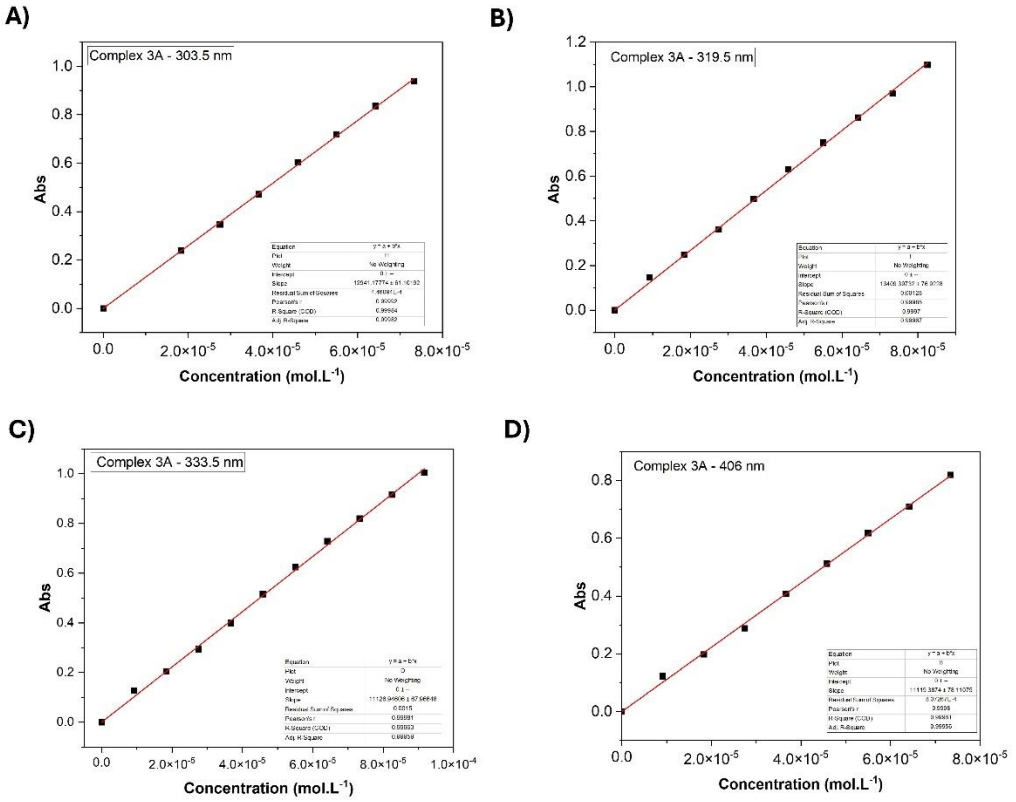

Appendix Figure 10. Absorbance (max) vs [C] for complex 3A. (A) – band at 303.5 nm, (B) – band at 319.5 nm, (C) – band at 333.5 nm and (D) - band at 406 nm.

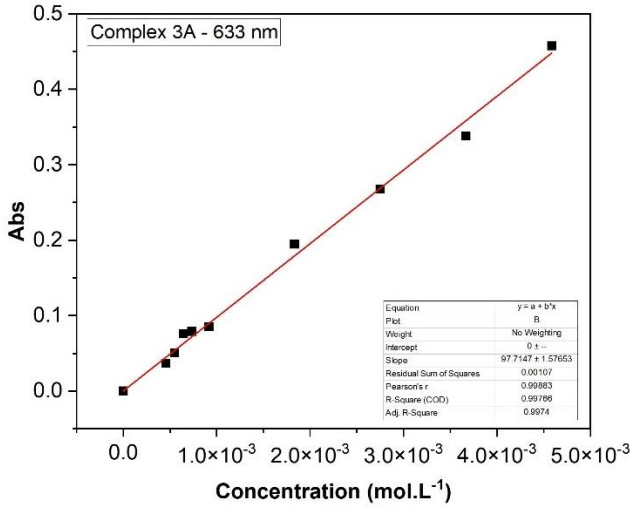

Appendix Figure 11. Absorbance (max) vs [C] for the d-d transition in 633 nm for complex 3A.

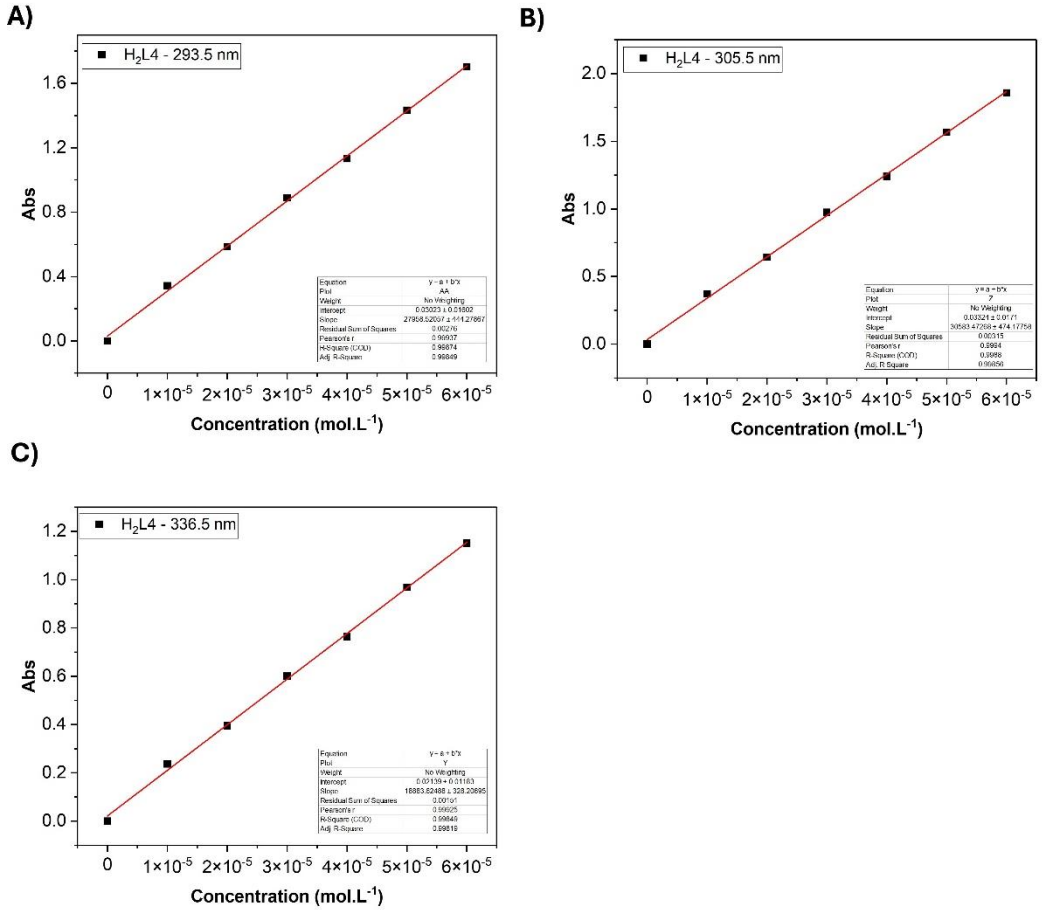

Appendix Figure 12. Absorbance (max) vs [C] for the ligand H_2L4. (A) – band at 293.5 nm, (B) – band at 305.5 nm, (C) – band at 336.5 nm.

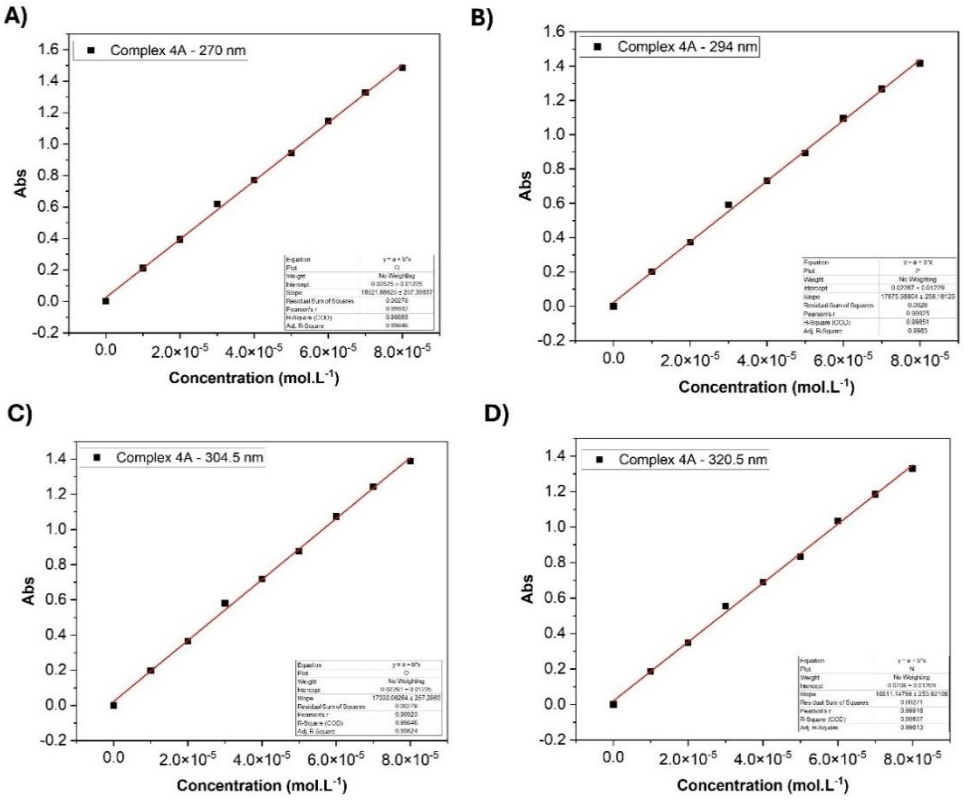

Appendix Figure 13. Absorbance (max) vs [C] for complex 4A. (A) – band at 270 nm, (B) –band at 294 nm, (C) – band at 304.5 nm and (D) - band at 320.5 nm.

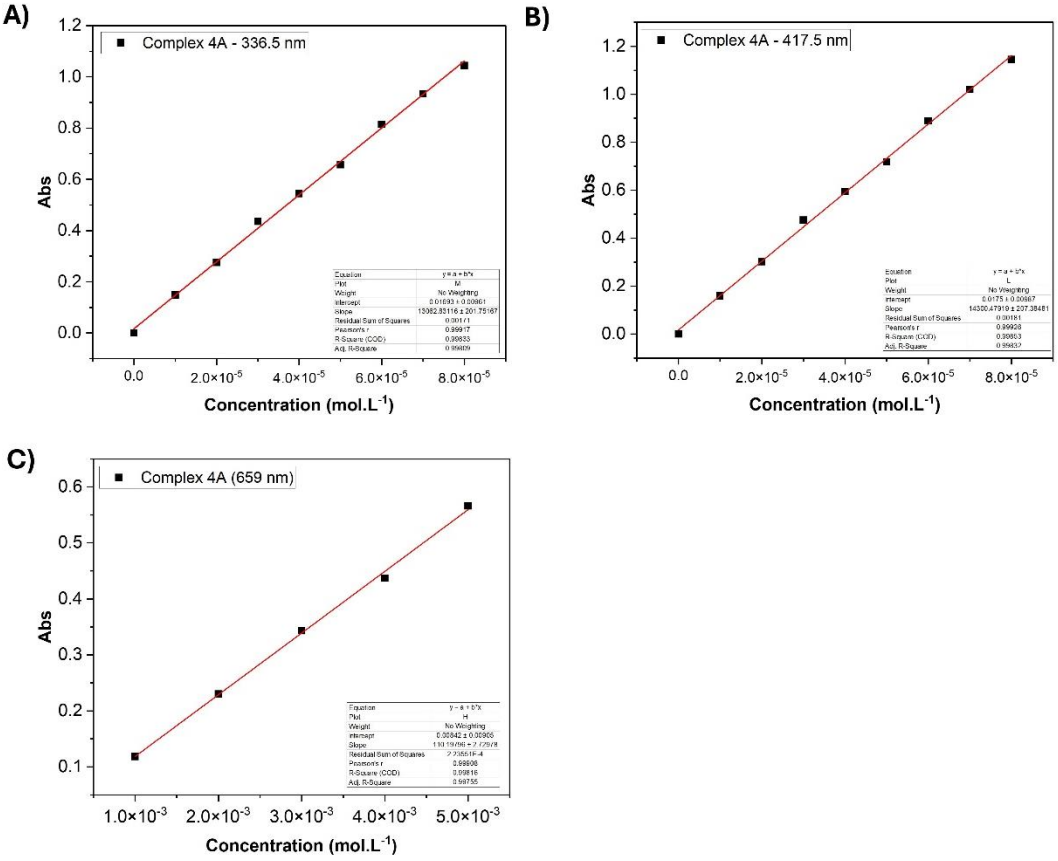

Appendix Figure 14. Absorbance (max) vs [C] for complex 4A. (A) – band at 336.5 nm, (B) – band at 417.5 nm, (C) – band at 659 nm d-d transition.

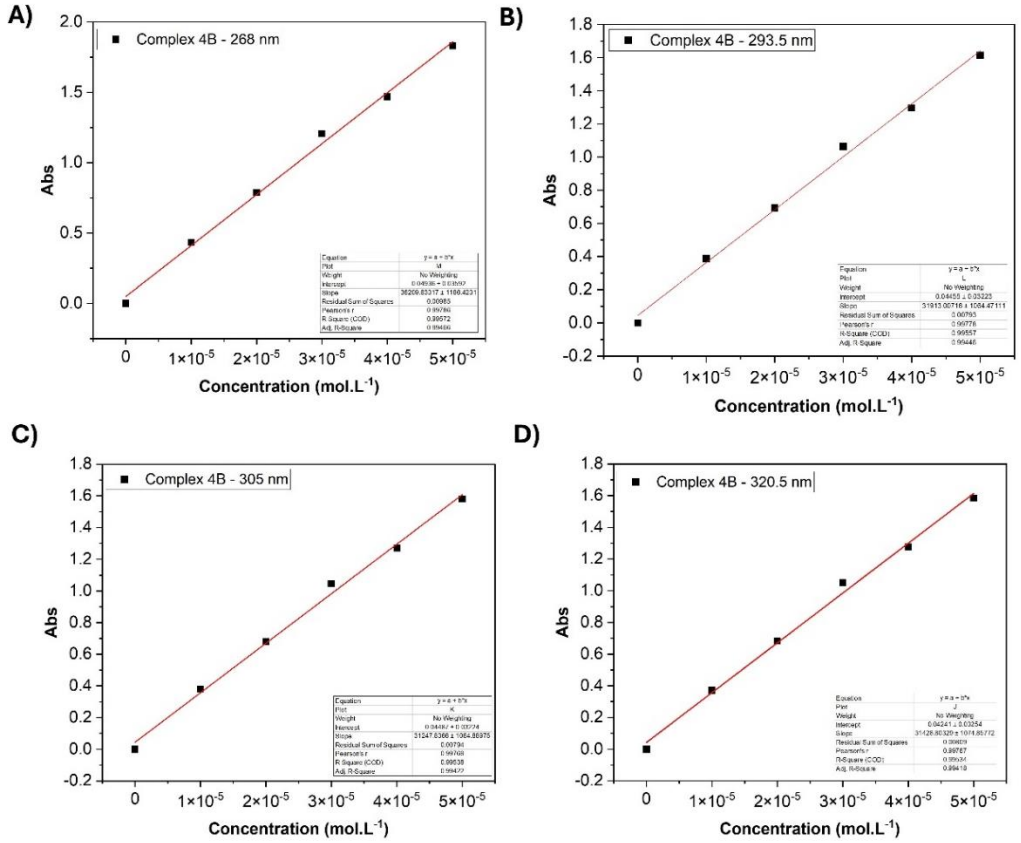

Appendix Figure 15. Absorbance (max) vs [C] for complex 4B. (A) – band at 268 nm, (B) –band at 293.5 nm, (C) – band at 305 nm and (D) - band at 320.5 nm.

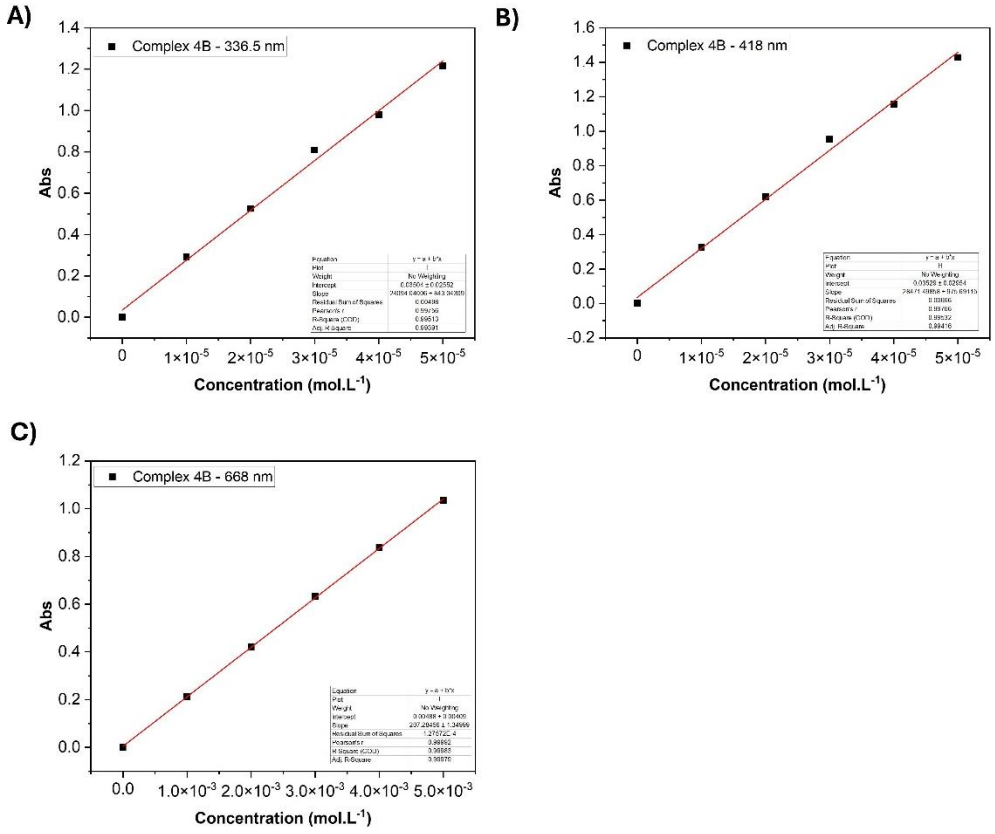

Appendix Figure 16. Absorbance (max) vs [C] for complex 4B. (A) – band at 336.5 nm, (B) – band at 418 nm, (C) – band at 668 nm d-d transition.

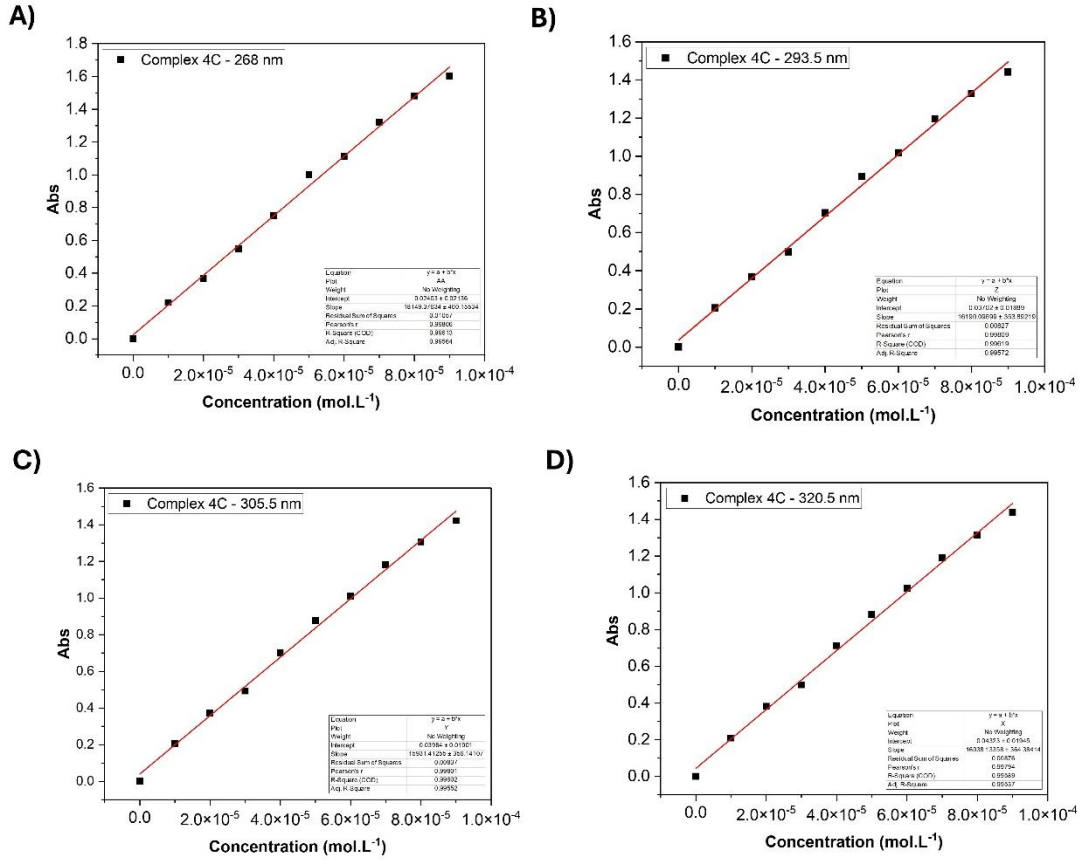

Appendix Figure 17. Absorbance (max) vs [C] for complex 4C. (A) – band at 268 nm, (B) –band at 293.5 nm, (C) – band at 305.5 nm and (D) - band at 320.5 nm.

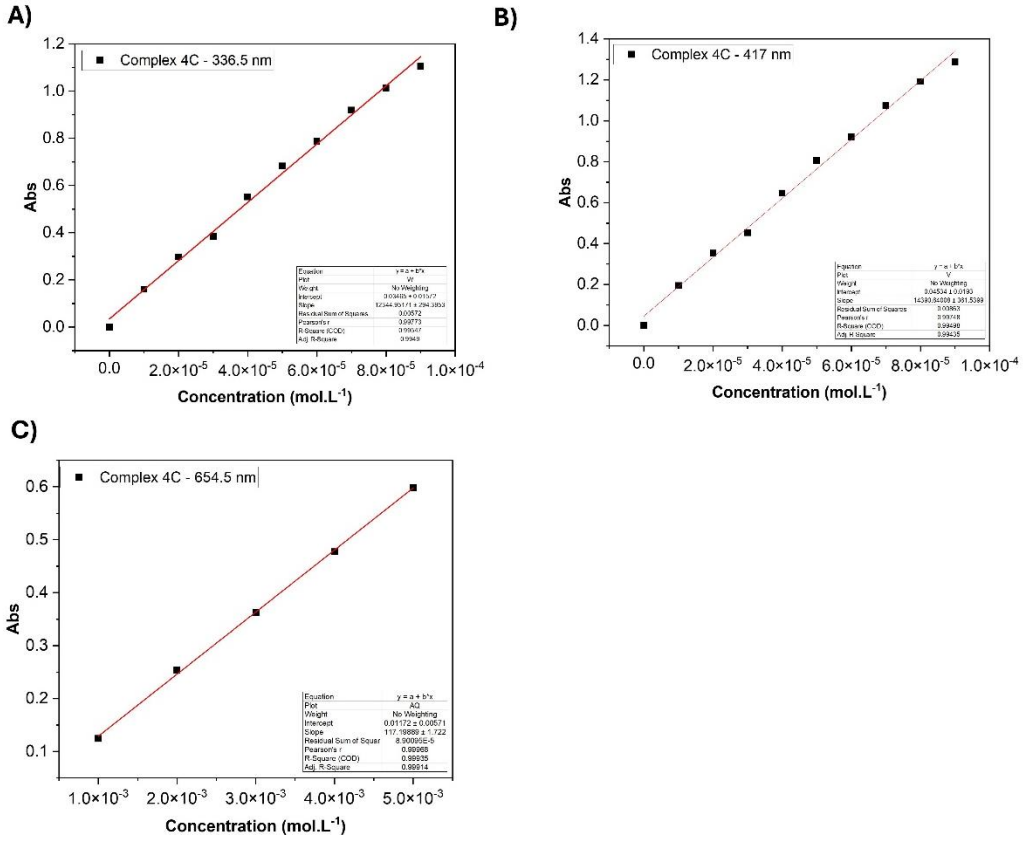

Appendix Figure 18. Absorbance (max) vs [C] for complex 4C. (A) – band at 336.5 nm, (B) – band at 417 nm, (C) – band at 664.5 nm d-d transition.

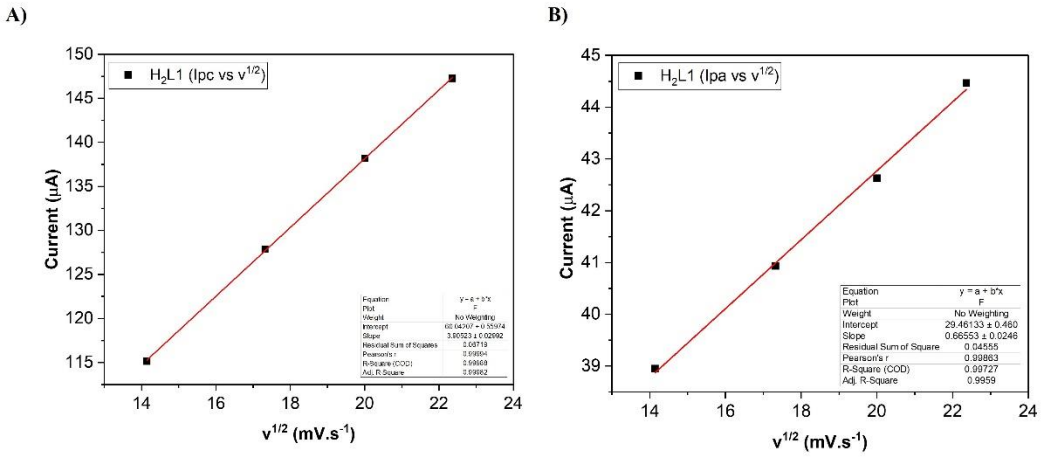

Appendix Figure 19. A) Linear relationship between the cathodic peak current and the square root of the scan rate for the H_2L1 ligand. **B)** Linear relationship between the anode peak current and the square root of the scan rate for the H_2L1 ligand.

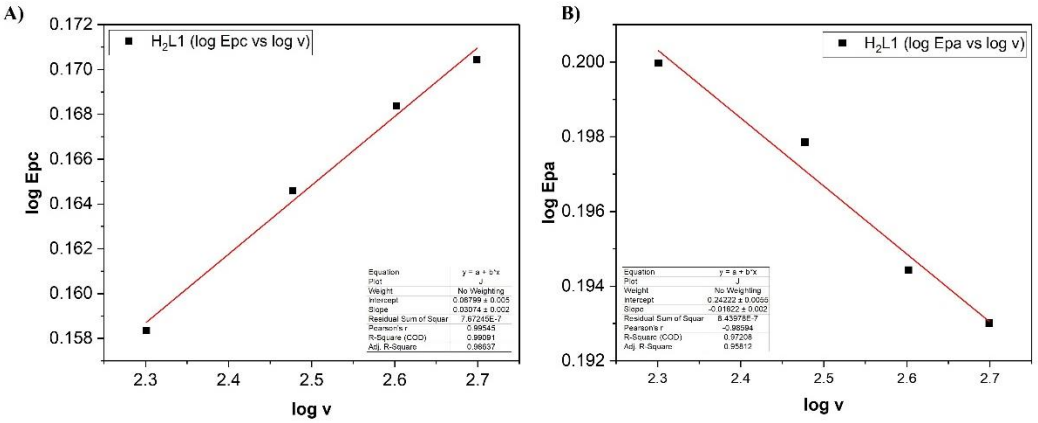

Appendix Figure 20. A) Linear relationship between the logarithm of the cathodic peak current and the logarithm of the scan rate for the H_2L1 ligand. **B)** Linear relationship between the logarithm of the anode peak current and the logarithm of the scan rate for the H_2L1 ligand.

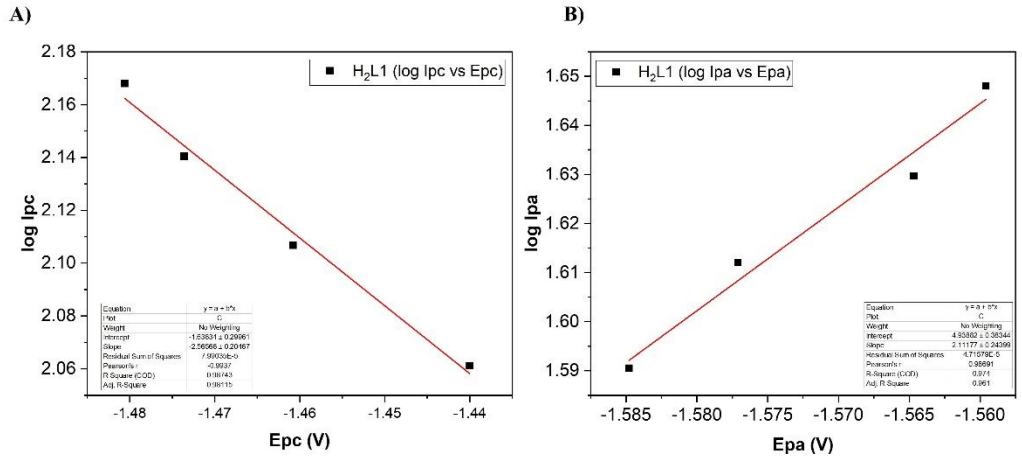

Appendix Figure 21. A) Linear relationship between the logarithm of the cathodic peak current and the cathodic potential for the H_2L1 ligand. **B)** Linear relationship between the logarithm of the anode peak current and the anode potential for the H_2L1 ligand.

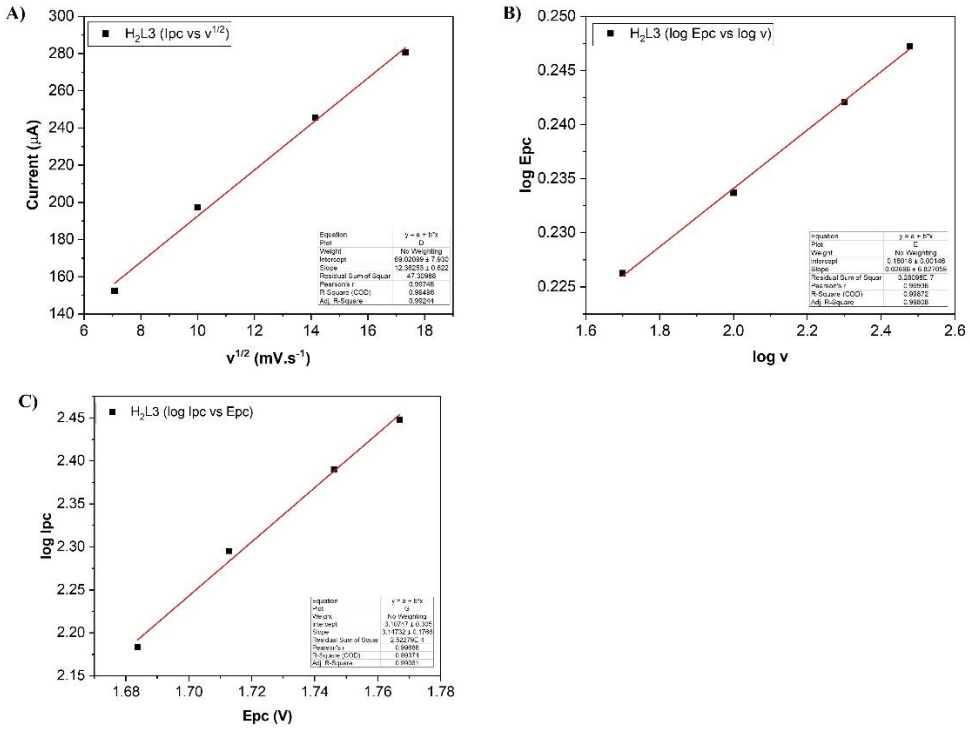

Appendix Figure 22. A) Linear relationship between the cathodic peak current and the square root of the scan rate for the H_2L3 ligand. **B)** Linear relationship between the logarithm of the cathodic peak current and the logarithm of the scan rate for the H_2L3 ligand. **C)** Linear relationship between the logarithm of the cathodic peak current and the cathodic potential for the H_2L3 ligand.

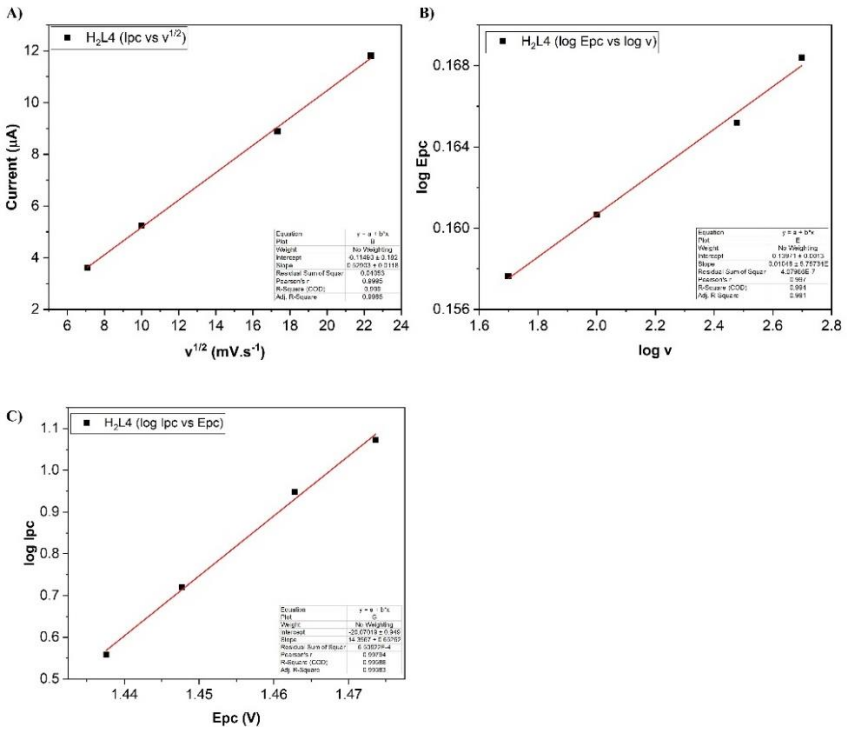

Appendix Figure 23. A) Linear relationship between the cathodic peak current and the square root of the scan rate for the H_2L4 ligand. **B)** Linear relationship between the logarithm of the cathodic peak current and the logarithm of the scan rate for the H_2L4 ligand. **C)** Linear relationship between the logarithm of the cathodic peak current and the cathodic potential for the H_2L4 ligand.

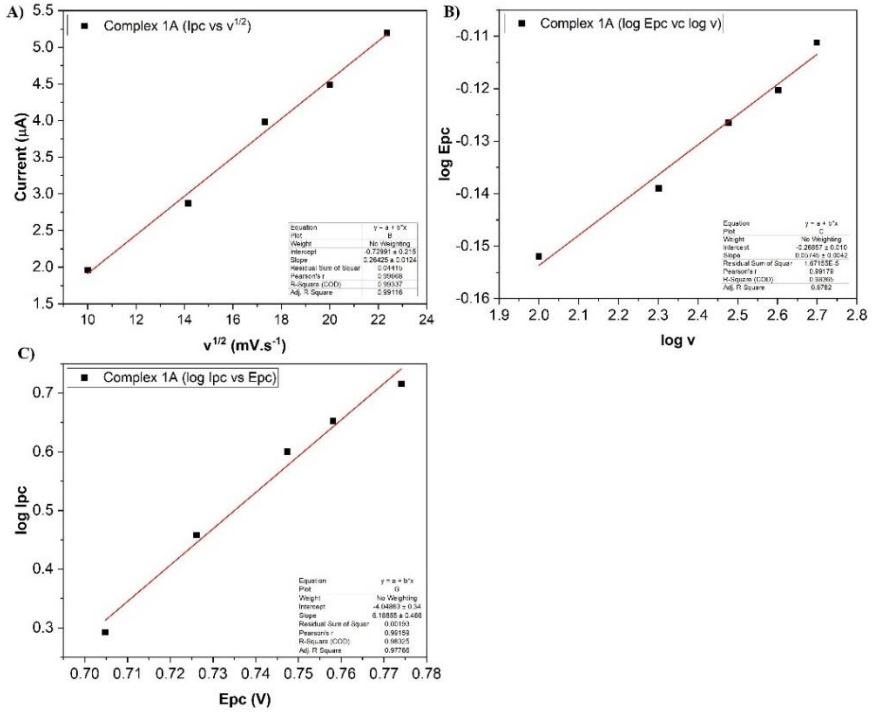

Appendix Figure 24. A) Linear relationship between the cathodic peak current and the square root of the scan rate for complex 1A. **B)** Linear relationship between the logarithm of the cathodic peak current and the logarithm of the scan rate for complex 1A. **C)** Linear relationship between the logarithm of the cathodic peak current and the cathodic potential for complex 1A.

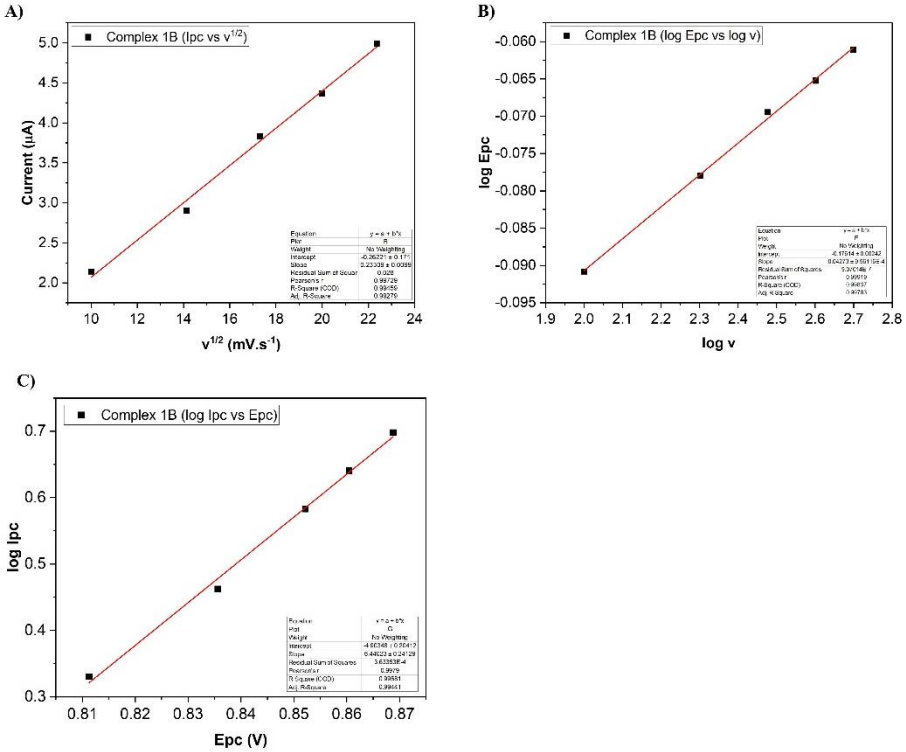

Appendix Figure 25. A) Linear relationship between the cathodic peak current and the square root of the scan rate for complex 1B. **B)** Linear relationship between the logarithm of the cathodic peak current and the logarithm of the scan rate for complex 1B. **C)** Linear relationship between the logarithm of the cathodic peak current and the cathodic potential for complex 1B.

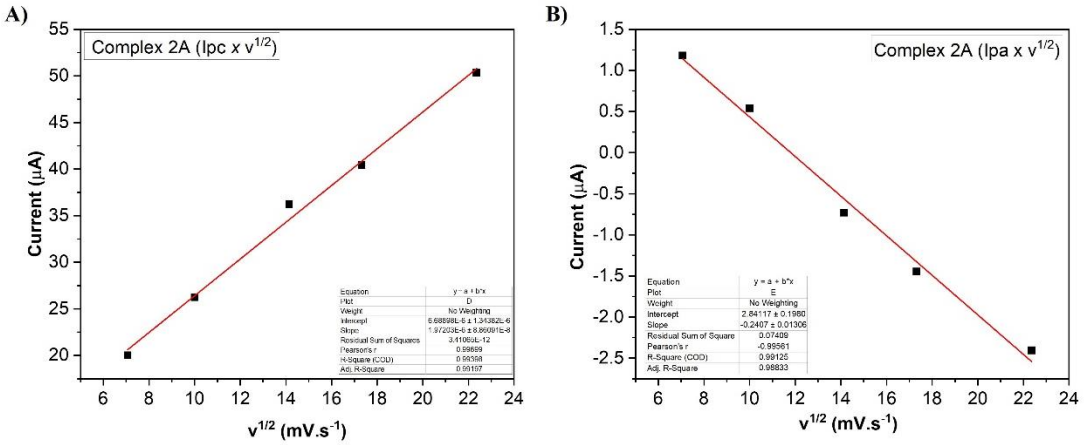

Appendix Figure 26. A) Linear relationship between the cathodic peak current and the square root of the scan rate for complex 2A. **B)** Linear relationship between the anode peak current and the square root of the scan rate for complex 2A.

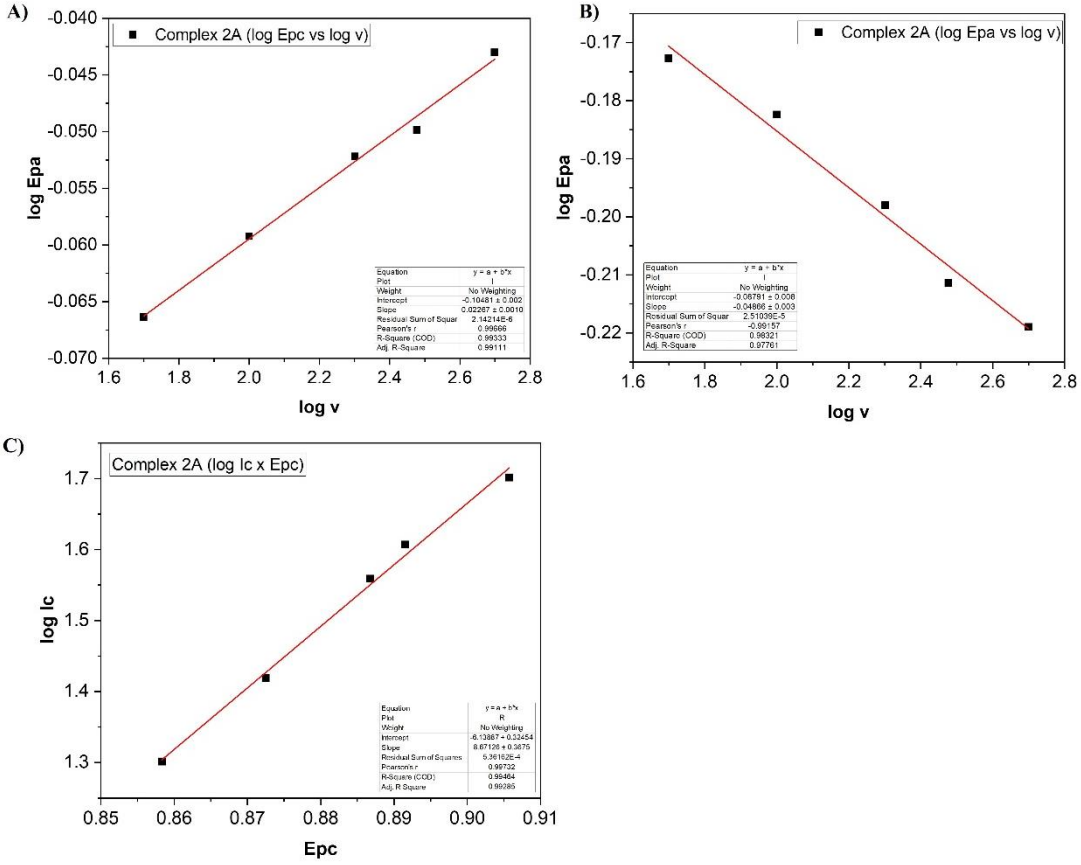

Appendix Figure 27. A) Linear relationship between the logarithm of the cathodic peak current and the logarithm of the scan rate for complex 2A. **B)** Linear relationship between the logarithm of the anode peak current and the logarithm of the scan rate for complex 2A. **C)** Linear relationship between the logarithm of the cathodic peak current and the cathodic potential for complex 2A.

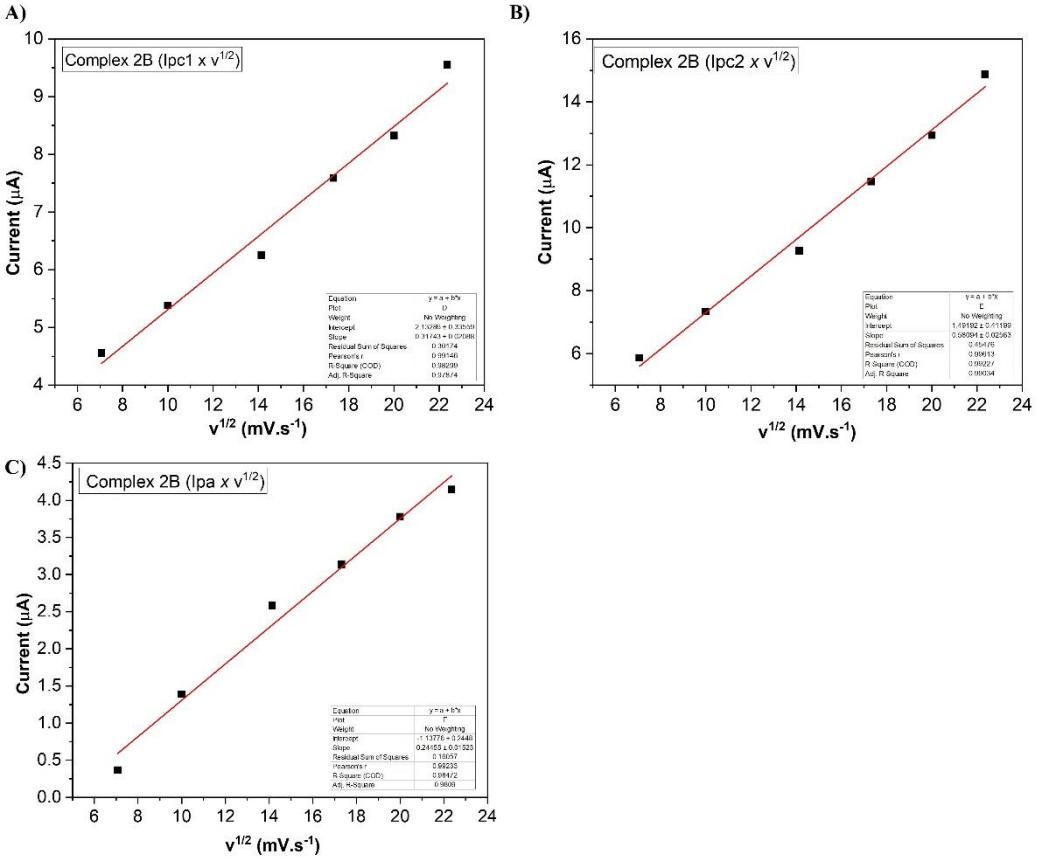

Appendix Figure 28. A) Linear relationship between the first cathodic peak current and the square root of the scan rate for complex 2B. **B)** Linear relationship between the second cathodic peak current and the square root of the scan rate for complex 2B. **C)** Linear relationship between the anode peak current and the square root of the scan rate for complex 2B.

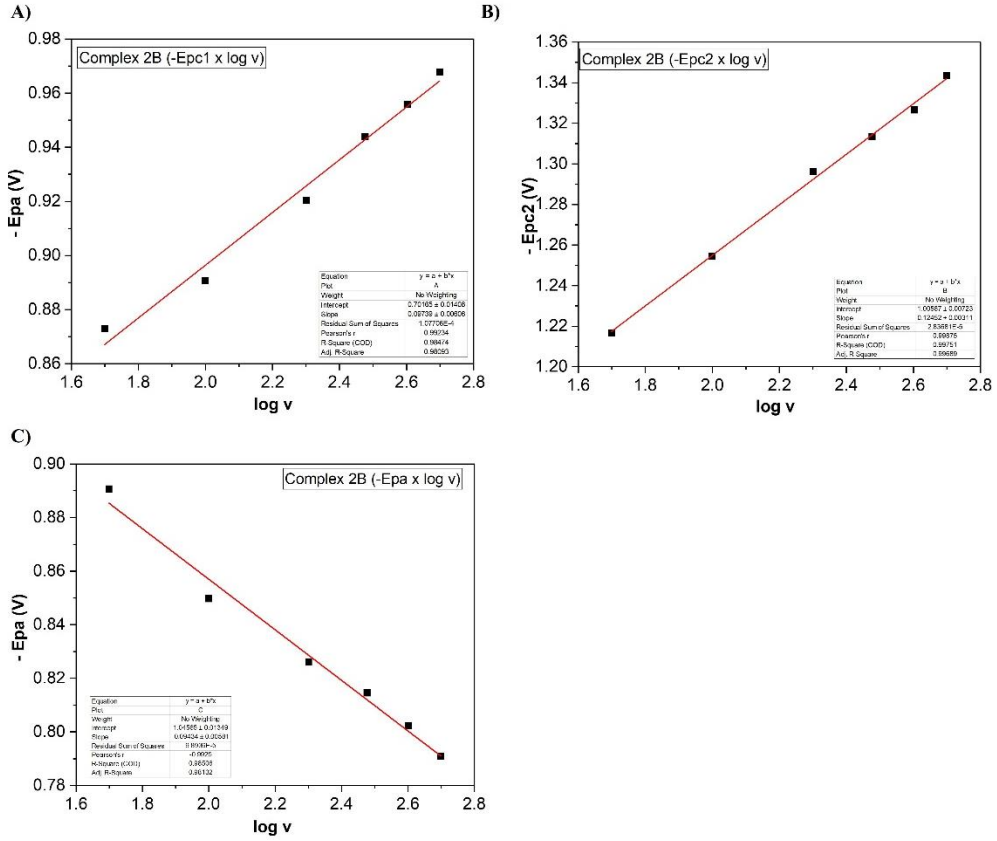

Appendix Figure 29. A) Linear relationship between the logarithm of the first cathodic peak current and the logarithm of the scan rate for complex 2B. **B)** Linear relationship between the logarithm of the second cathodic peak current and the logarithm of the scan rate for complex 2B. **C)** Linear relationship between the logarithm of the anode peak current and the logarithm of the scan rate for complex 2B.

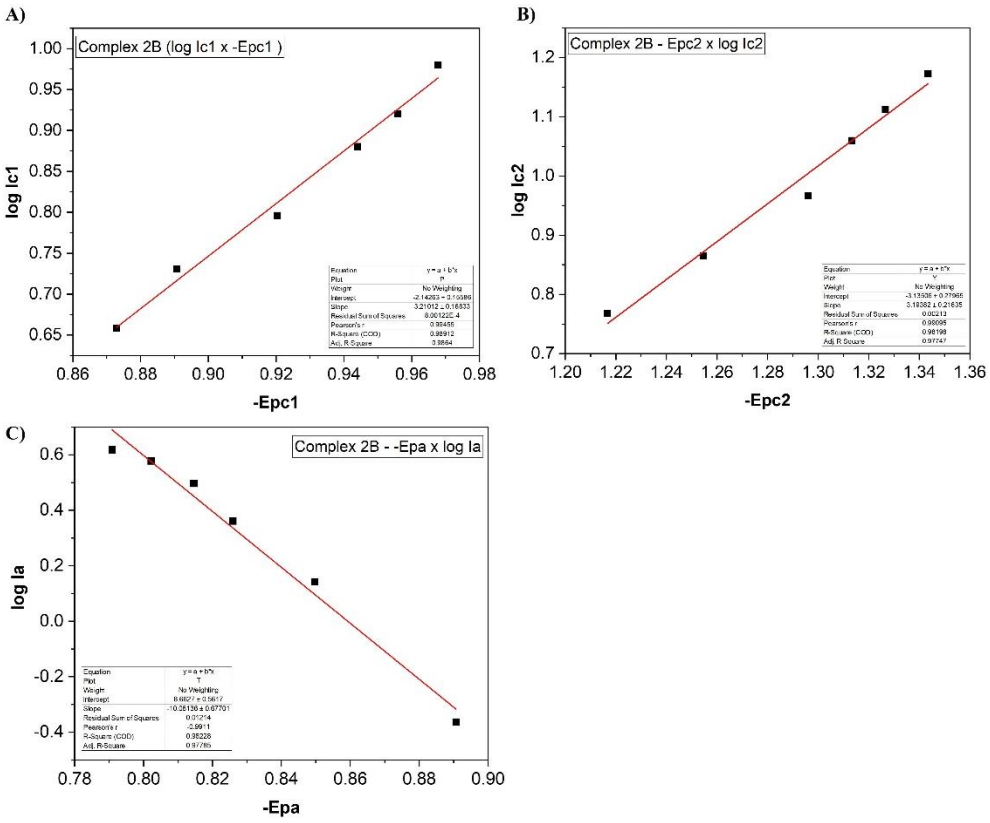

Appendix Figure 30. A) Linear relationship between the logarithm of the first cathodic peak current and the first cathodic potential for complex 2B. **B)** Linear relationship between the logarithm of the second cathodic peak current and the second cathodic potential for complex 2B. **C)** Linear relationship between the logarithm of anode peak current and the anode potential for complex 2B.

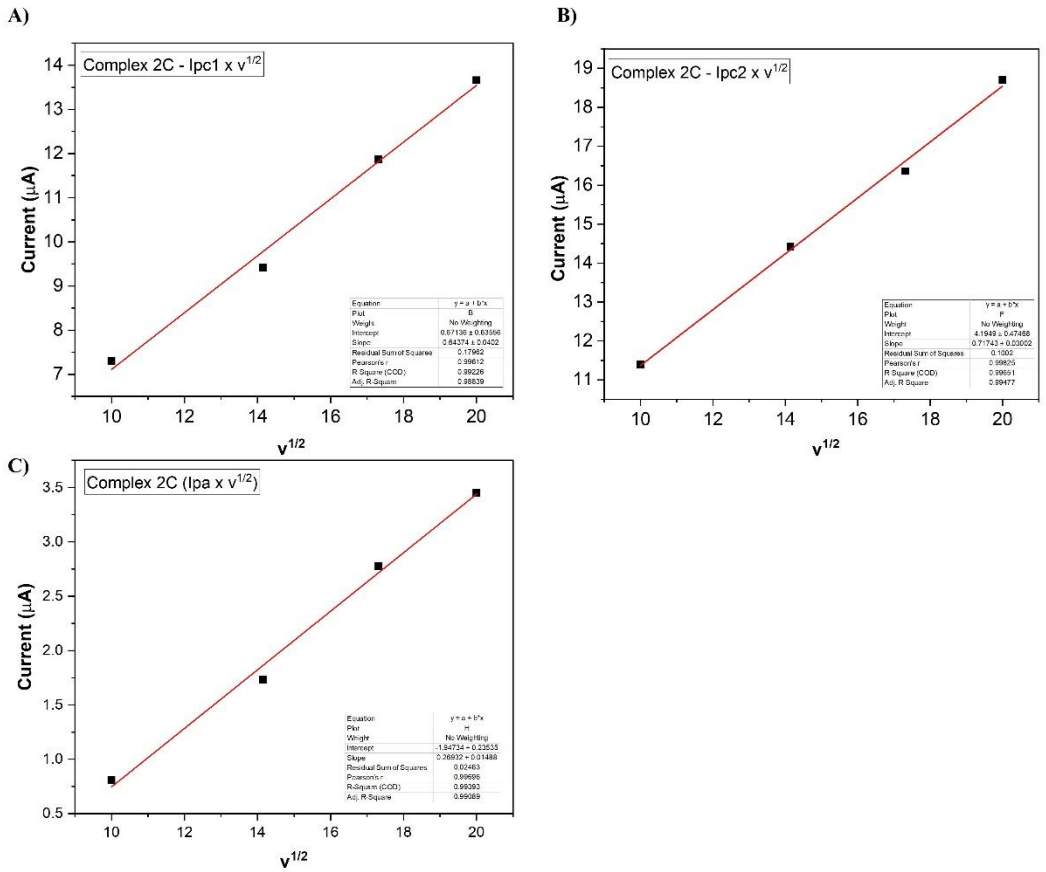

Appendix Figure 31. A) Linear relationship between the first cathodic peak current and the square root of the scan rate for complex 2C. **B)** Linear relationship between the second cathodic peak current and the square root of the scan rate for complex 2C. **C)** Linear relationship between the anode peak current and the square root of the scan rate for complex 2C.

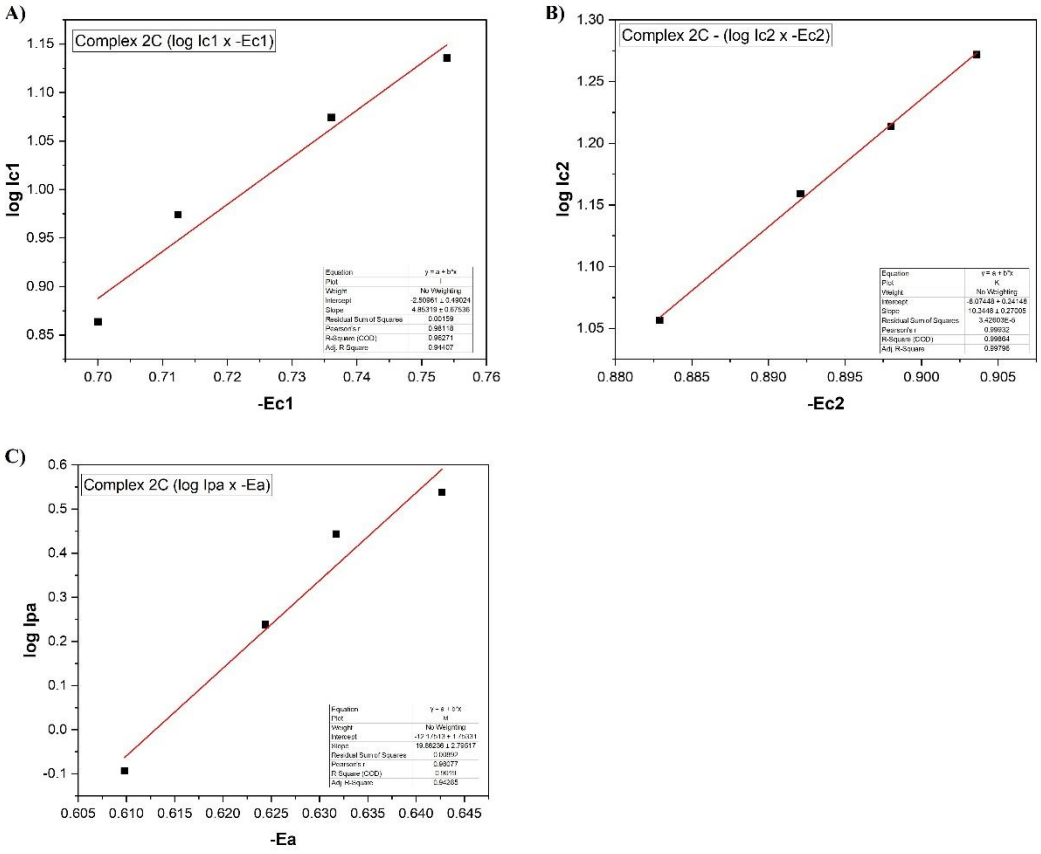

Appendix Figure 32. A) Linear relationship between the logarithm of the first cathodic peak current and the first cathodic potential for complex 2C. **B)** Linear relationship between the logarithm of the second cathodic peak current and the second cathodic potential for complex 2C. **C)** Linear relationship between the logarithm of the anode peak current and the anode potential for complex 2C.

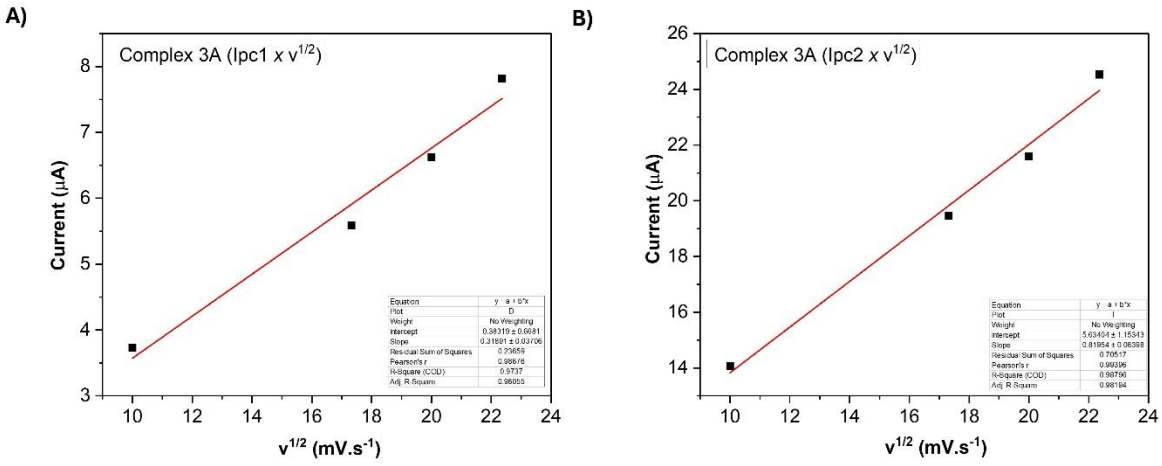

Appendix Figure 33. A) Linear relationship between the first cathodic peak current and the square root of the scan rate for complex 3A. **B)** Linear relationship between the second cathodic peak current and the square root of the scan rate for complex 3A.

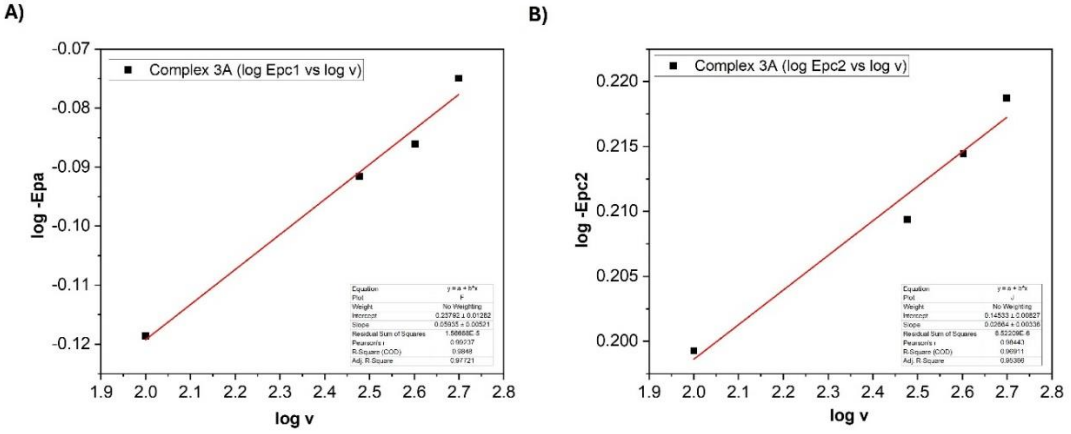

Appendix Figure 34. A) Linear relationship between the logarithm of the first cathodic peak current and the logarithm of the scan rate for complex 3A. **B)** Linear relationship between the logarithm of the second cathodic peak current and the logarithm of the scan rate for complex 3A.

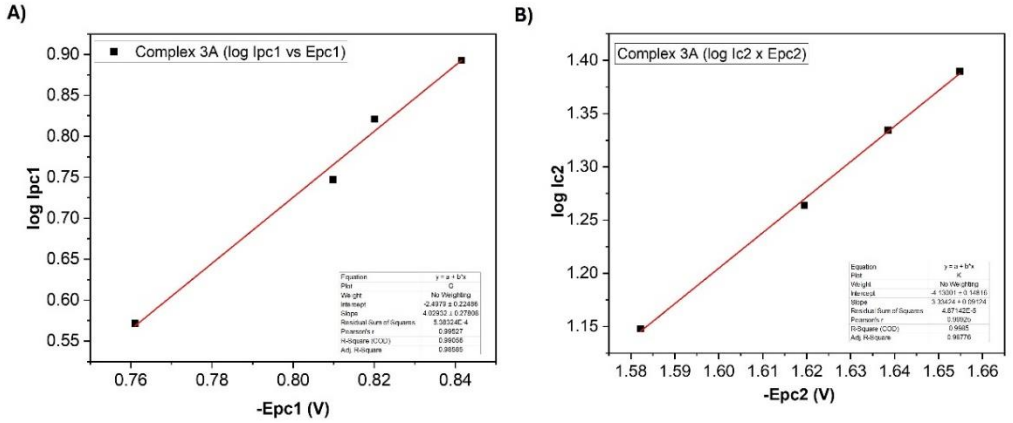

Appendix Figure 35. A) Linear relationship between the logarithm of the first cathodic peak current and the first cathodic potential for complex 3A. **B)** Linear relationship between the logarithm of the second cathodic peak current and the second cathodic potential for complex 3A.

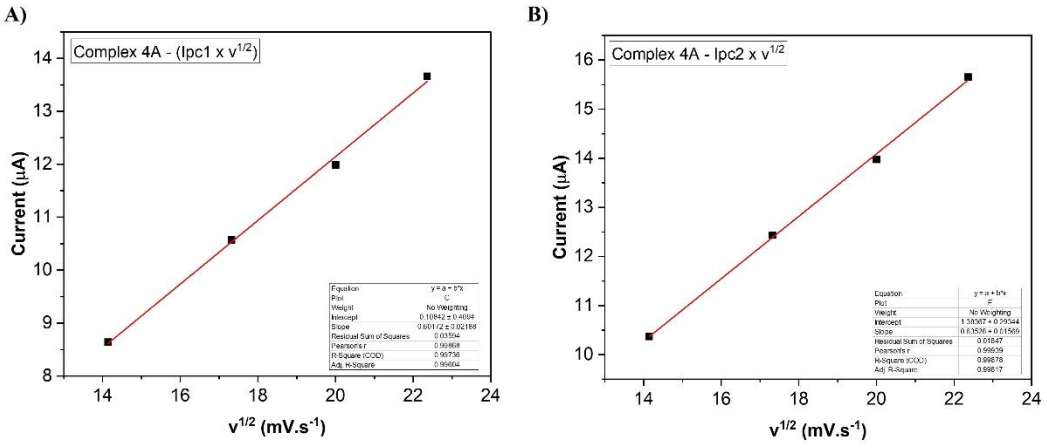

Appendix Figure 36. A) Linear relationship between the first cathodic peak current and the square root of the scan rate for complex 4A. **B)** Linear relationship between the second cathodic peak current and the square root of the scan rate for complex 4A.

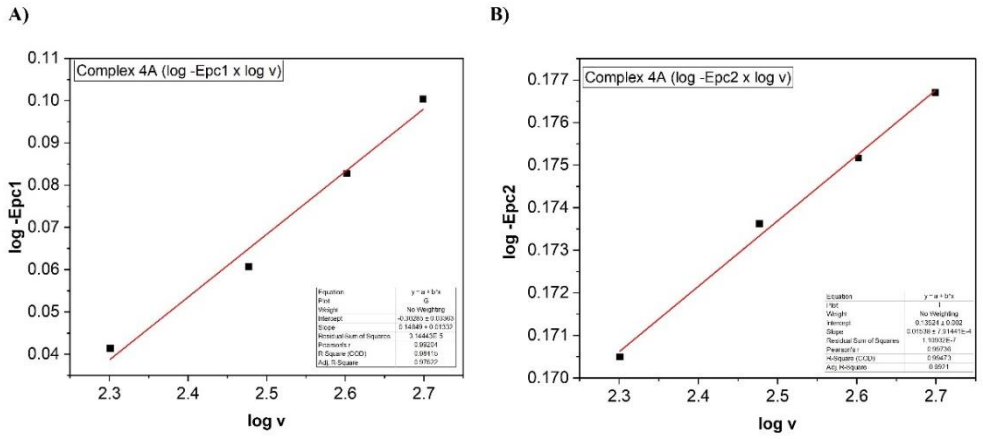

Appendix Figure 37. A) Linear relationship between the logarithm of the first cathodic peak current and the logarithm of the scan rate for complex 4A. **B)** Linear relationship between the logarithm of the second cathodic peak current and the logarithm of the scan rate for complex 4A.

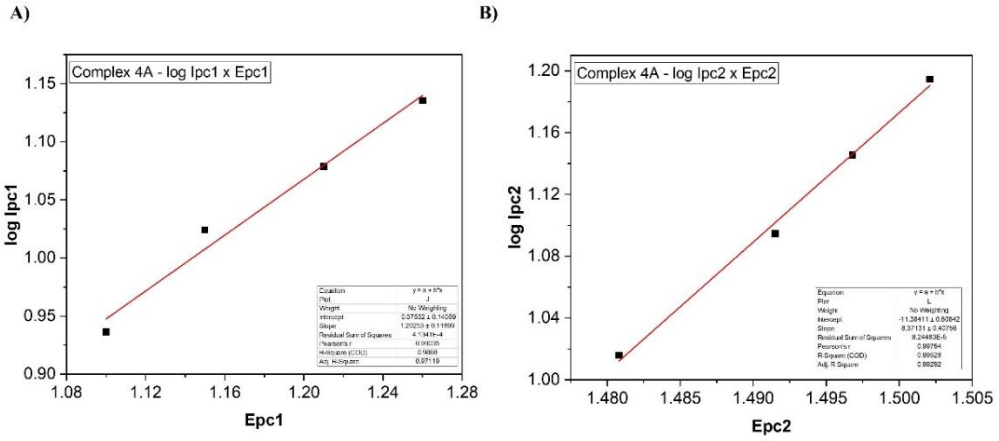

Appendix Figure 38. A) Linear relationship between the logarithm of the first cathodic peak current and the first cathodic potential for complex 4A. **B)** Linear relationship between the logarithm of the second cathodic peak current and the second cathodic potential for complex 4A.

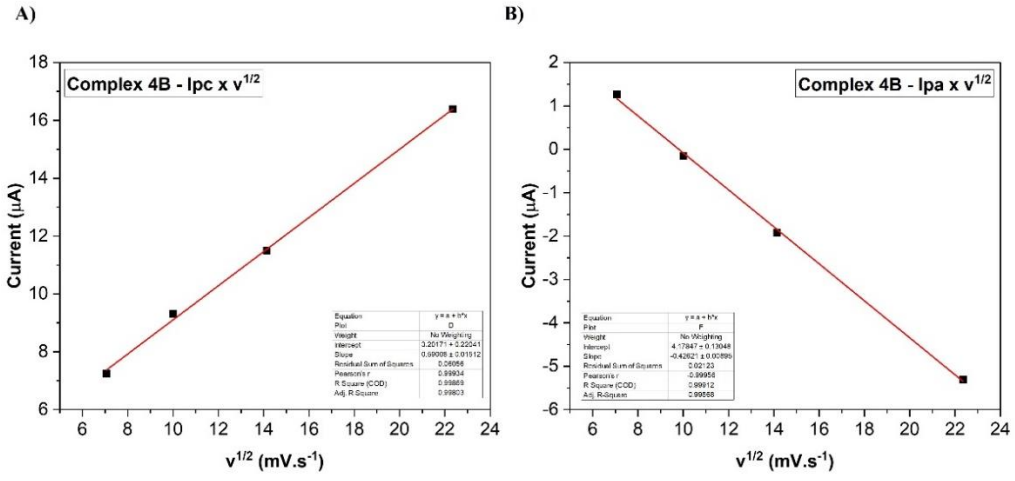

Appendix Figure 39. A) Linear relationship between the cathodic peak current and the square root of the scan rate for complex 4B. **B)** Linear relationship between the anode peak current and the square root of the scan rate for complex 4B.

A) B)

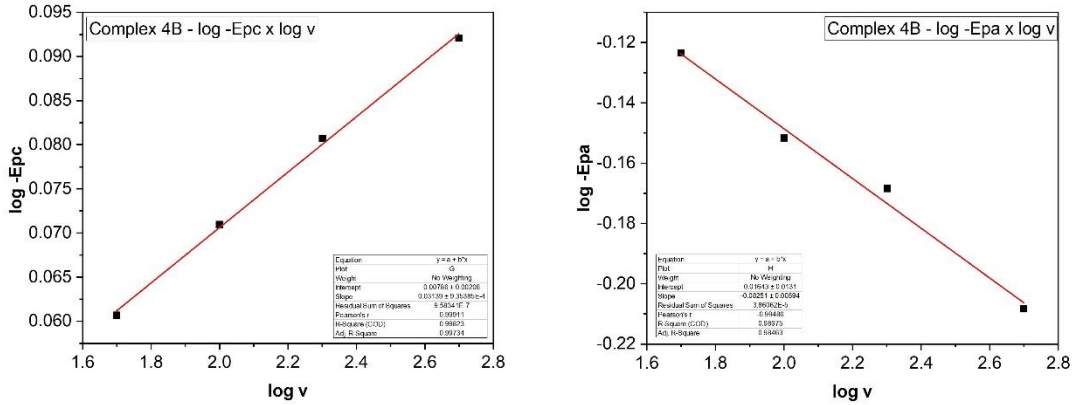

Appendix Figure 40. A) Linear relationship between the logarithm of the cathodic peak current and the logarithm of the scan rate for complex 4B. **B)** Linear relationship between the logarithm of the anode peak current and the logarithm of the scan rate for complex 4B.

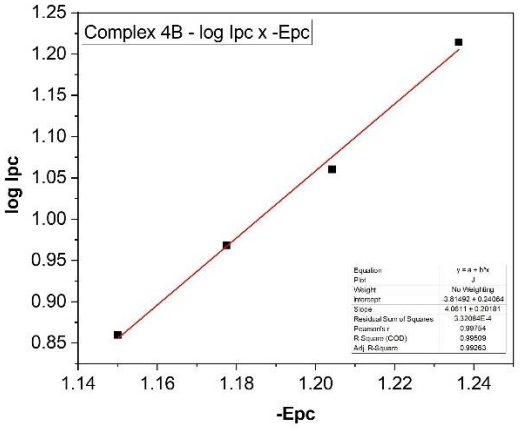

Appendix Figure 41. Linear relationship between the logarithm of the cathodic peak current and the first cathodic potential for complex 4B.

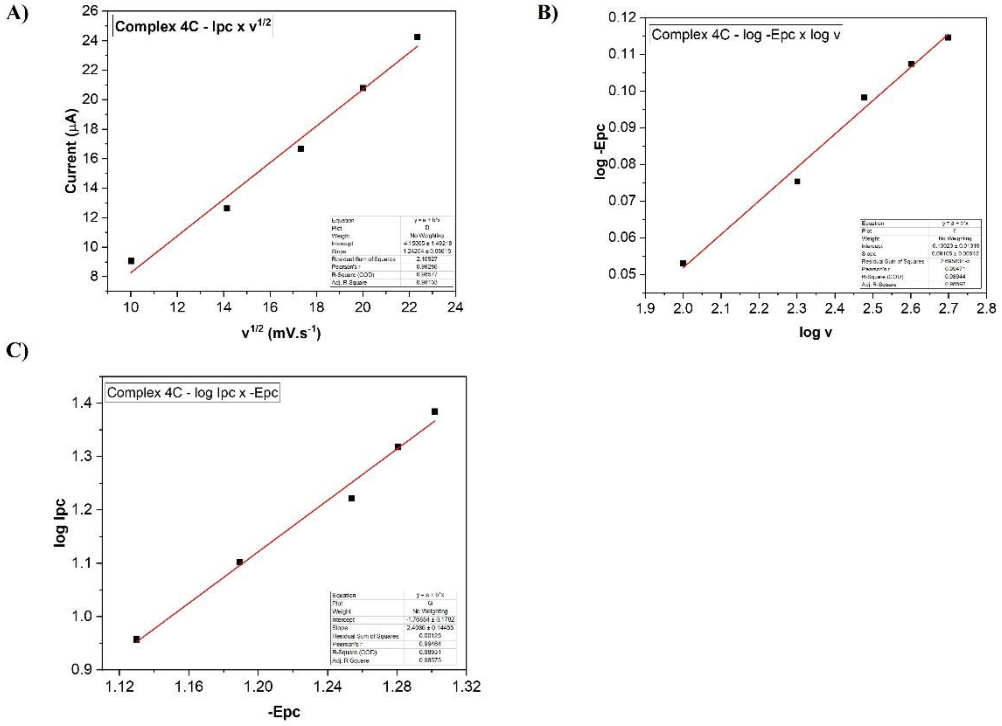

Appendix Figure 42. A) Linear relationship between the cathodic peak current and the square root of the scan rate for complex 4C. **B)** Linear relationship between the logarithm of the cathodic peak current and the logarithm of the scan rate for complex 4C. **C)** Linear relationship between the logarithm of the cathodic peak current and the cathodic potential for complex 4C.

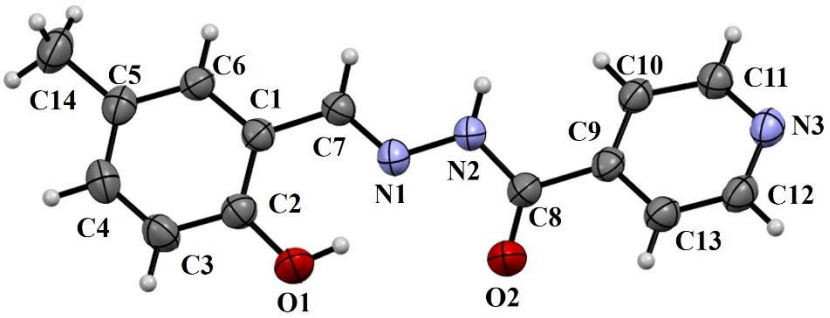

Appendix Figure 43. Molecular structure representations of H_2L1. The ellipsoids were drawn at the 50% probability level.

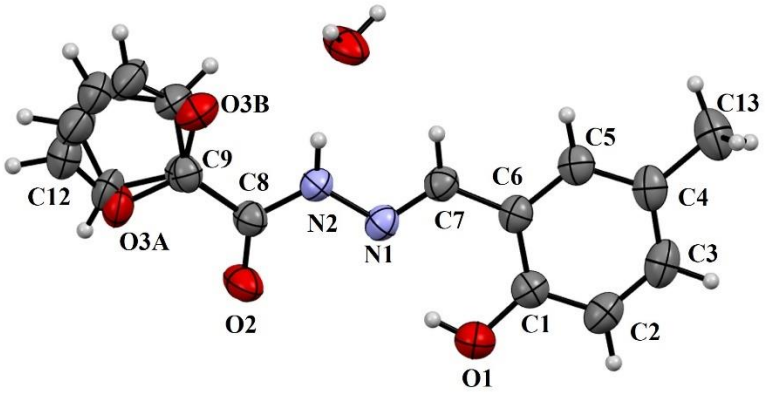

Appendix Figure 44. Molecular structure representations of H_2L2. The ellipsoids were drawn at the 50% probability level.

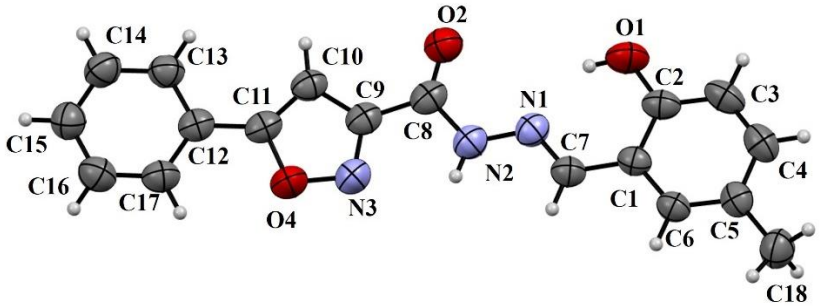

Appendix Figure 45. Molecular structure representations of H_2L3. The ellipsoids were drawn at the 50% probability level.

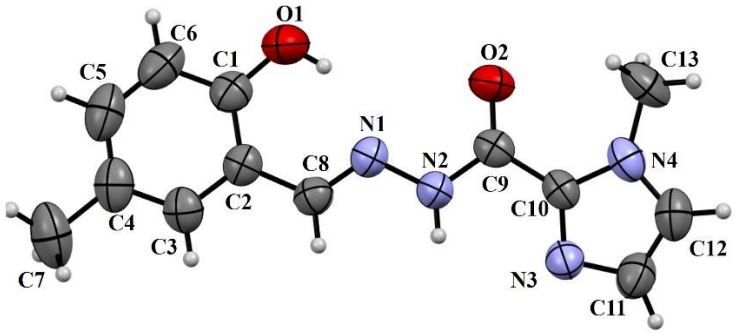

Appendix Figure 46. Molecular structure representations of H_2L4. The ellipsoids were drawn at the 50% probability level.

Appendix Table 1. Selected bond distances and angles for compounds H_2L1, H_2L2, H_2L3 and H_2L4.

Compound	H_2L1	H_2L2	H_2L3	H_2L4
Bond distances (Å)				
C2−O1 / C1−O1	1.361(2)	1.351(3)	1.353(3)	1.357(3)
C7−N1 / C8−N1	1.275(2)	1.287(3)	1.279(3)	1.277(2)
C8−O2 / C9−O2	1.215(2)	1.237(3)	1.215(3)	1.217(2)
N1−N2	1.369(19)	1.379(3)	1.366(3)	1.374(2)
C8−N2 / C9−N2	1.355(2)	1.343(3)	1.362(3)	1.357(2)
C1−C7 / C6−C7 C2−C8	1.448(2)	1.443(3)	1.450(3)	1.444(3)
C8−C9 / C9−C10	–	–	1.477(3)	1.469
C9−N3 / C10−N4	–	–	1.307(3)	1.355
N3−O3	–	–	1.389(2)	–
C10−N3	–	–	–	1.318
C11−O3	–	–	1.355(3)	–
Bond angle / °				
C3−C2−O1 / C2−C1−O1 / C2−C3−O1 /	118.20(15)	118.4(2)	118.74(19)	118.74
C6−C1−C7 / C2−C1−C7 / C1−C2−C8	119.94(13)	123.6(2)	122.22(18)	122.07(19)
C1−C7−N1 / C6−C7−N1 / C2−C8−N1	119.51(13)	122.9(2)	120.11(17)	121.2(2)
C7−N1−N2 / C8−N1−N2	120.23(13)	114.4(2)	117.47(17)	118.05(18)
N1−N2−C8 / N1−N2−C9	115.86(13)	120.1(2)	120.66(18)	117.78(17)
N2−C8−C9 / N2−C9−C10	116.80(14)	114.4(10)	113.3(2)	112.86(19)
N2−C8−O2 / N2−C9−O2 /	122.19(16)	123.7(2)	123.38(19)	123.28(19)

Appendix Table 1 (cont). Selected angles for compounds H_2L1, H_2L2, H_2L3 and H_2L4.

Compounds	H_2L1	H_2L2	H_2L3	H_2L4
Bond angle / °				
C8−C9−C13	117.52(14)	–	–	–
C8−C9−O3	–	116.0(17)	–	–
C8−C9−C10	124.53(14)	–	129.3(2)	–
C9−C10−N3	–	–	118.55(19)	124.46
C11−N3−C12	116.53(15)	–	–	–
C9−O3−C12	–	108.5(12)	–	–
C11−O3−N3	–	–	109.15(16)	–
C9−C10−N4	–	–	–	123.64
C12−C11−O3	–	–	116.15(16)	–
N3−C10−N4	–	–	–	111.96
C10−N4−C13	–	–	–	129.18

9. Scientific Production

This work was developed over 48 months of PhD research through the Program of the Department of Chemistry at the Pontifical Catholic University of Rio de Janeiro (PUC-Rio). I started my doctorate in the second semester of 2020 and, due to the pandemic situation imposed by COVID-19, the first 12 months of experimental work were significantly impacted. However, this research resulted in two full manuscripts (one already published, the other one submitted) in indexed scientific journal, with myself being the first author of one of them, which was featured on the back cover of the journal Dalton Transactions, and second author of another publication that is currently under review. The first page of one of these articles and the submission email, in chronological order, are presented below. The full published article can be downloaded from the publisher's website. Parts of this work have been presented at many national and international conferences, including oral presentations and posters.

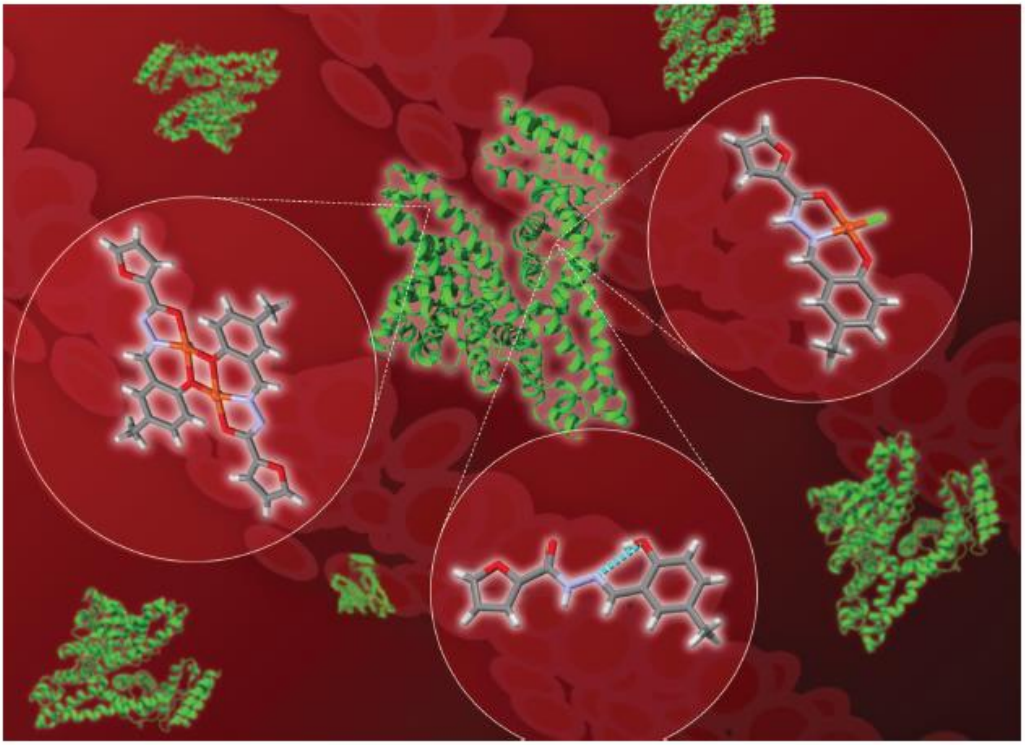

Showcasing research from Professor Nicolás A. Rey's laboratory (LABSO-Bio), Department of Chemistry, Pontifical Catholic University of Rio de Janeiro, Rio de Janeiro, Brazil.

Copper(II) complexes of a furan-containing aroylhydrazonic ligand: syntheses, structural studies, solution chemistry and interaction with HSA

A combined experimental–theoretical approach demonstrated that new mononuclear and dinuclear copper complexes of 5-methylsalicylaldehyde 2-furoyl hydrazone, as well as the ligand itself, are able to bind human serum albumin, although at different sites and with diverse stoichiometries.

As featured in:

See Nicolás A. Rey *et al.*, *Dalton Trans.*, 2023, **52**, 17731.

ROYAL SOCIETY OF CHEMISTRY

rsc.li/dalton

Registered charity number: 207890

Dalton Transactions

ROYAL SOCIETY OF CHEMISTRY

PAPER

View Article Online
View Journal

Cite this: DOI: 10.1039/d3dt02597g

Copper(II) complexes of a furan-containing aroylhydrazonic ligand: syntheses, structural studies, solution chemistry and interaction with HSA†

Fagner da Silva Moura,[a] Ygor S. Sobrinho,[a] Carolina Stellet,[a] Jilder D. P. Serna,[b] Carolina B. P. Ligiero,[c] Maurício I. Yoguim,[d] Daphne S. Cukierman,[a,e] Renata Diniz,[f] Odivaldo C. Alves,[c] Nelson H. Morgon,[g] Aguinaldo R. de Souza[d] and Nicolás A. Rey *[a]

Received 10th August 2023,
Accepted 31st October 2023

DOI: 10.1039/d3dt02597g

rsc.li/dalton

Copper(II) complexes have become a potential alternative to the use of platinum drugs in cancer therapy due to their multi-target mode of action. In this context, we report the syntheses of new mononuclear and dinuclear coordination compounds of this element, **1** and **2**, derived from the ligand 5-methyl-salicylaldehyde 2-furoyl hydrazone ($\mathbf{H_2L}$). All three compounds were structurally and spectroscopically characterized, both in the solid state and in solution. In **1**, Cu is coordinated by three donor-atoms from the hydrazonic ligand and one chloride ion. $\mathbf{H_2L}$ is deprotonated at the phenol oxygen. The dinuclear complex **2** is, on the other hand, a dimeric form of **1** in which the chloride ions of a pair of mononuclear units are lost and phenoxo bridges take their places, double-connecting the metal centres and resulting in a single species with the ligand fully deprotonated. The compounds were fairly stable in aqueous medium at room temperature. An experimental–theoretical combined approach demonstrated that all of them are able to bind human serum albumin (HSA), although at different sites and with diverse stoichiometries and affinities (as concluded by the calculated binding energies). In view of this, and due to the well-known antiproliferative activity of hydrazone-containing copper complexes, we consider the compounds presented in here promising, and believe that they deserve more profound studies regarding the assessment of their potential against tumour cell lines.

Acknowledgement of your Submission to Dalton Transactions - DT-ART-07-2024-002066

2 mensagens

Dalton Transactions <onbehalfof@manuscriptcentral.com> 17 de julho de 2024 às 14:13
Responder a: dalton@rsc.org
Para: ileon@biol.unlp.edu.ar
Cc: oliviaespindola@quimica.unlp.edu.ar, 92mourafagner@gmail.com, luciasantamaria@quimica.unlp.edu.ar, stelletcarol@gmail.com, jilderpea@gmail.com, dinizr@gmail.com, nicoarey@puc-rio.br, ileon@biol.unlp.edu.ar

17-Jul-2024

Dear Dr Leon:

TITLE: Antiproliferative activity of a series of copper(II) complexes derived from a furan-containing N-acylhydrazone. Monomer versus dimers, charged versus neutral, and cell mechanistic studies on triple negative breast cancer cells

Thank you for your submission to Dalton Transactions, published by the Royal Society of Chemistry. This is an automatic acknowledgement that you have uploaded your files to our online submission system. Your manuscript ID is: DT-ART-07-2024-002066

Your manuscript will be passed to an editor for initial assessment as soon as possible. If there are any problems with your submission we will contact you.

Please indicate the above manuscript ID when you contact us about this submission.

Do you have an ORCID iD? ORCID (Open Researcher and Contributor iD) is a unique researcher identifier that allows you to link your research output and other professional activities in a single record. We therefore encourage each researcher to sign up for their own ORCID account. Please edit your user account to link your ORCID iD or create a new one, ensuring that you have not linked your account to another researcher's ORCID iD. Please note that we are unable to do this on your behalf. If your article is accepted, you may choose to have your ORCID record updated automatically with details of the publication.

We already have the following information for authors of this manuscript: Espíndola-Moreno, Olivia - No ORCID iD Available, da Silva Moura, Fagner - No ORCID iD Available, Santa María de la Parra, Lucía - No ORCID iD Available, Stellet, Carolina - No ORCID iD Available, Serna, Jilder - No ORCID iD Available, Diniz, Renata - No ORCID iD Available, Rey, Nicolás - https://orcid.org/0000-0002-0624-7560, Leon, Ignacio - https://orcid.org/0000-0003-1010-3997
If this is not how you want your name to appear on an Accepted Manuscript, please amend your ScholarOne account.

The Royal Society of Chemistry is a member of CrossCheck. Your submission may be compared against the CrossCheck database using the iThenticate plagiarism detection software. For further information, please see here: https://rsc.li/plagiarism

This journal has a policy of sharing reviewer reports. Please note that the Editor's decision and copies of the reports will be shared with all reviewers who provide a recommendation on your manuscript.

Please contact us if we can be of any assistance.

Yours sincerely,
Dalton Transactions Editorial Office
dalton@rsc.org

If you need to contact the journal, please use the email address dalton@rsc.org